"For instance, on the planet Earth, man had always assumed that he was more intelligent than dolphins because he had achieved so much—the wheel, New York, wars and so on—whilst all the dolphins had ever done was muck about in the water having a good time. But conversely, the dolphins had always believed that they were far more intelligent than man—for precisely the same reasons."

-Douglas Adams,
The Hitchhiker's Guide to the Galaxy.

University of Alberta

Solid-State Spin-1/2 NMR Studies of Disorder, Bonding, and Symmetry

by

Kristopher Jon Harris

A thesis submitted to the Faculty of Graduate Studies and Research
in partial fulfillment of the requirements for the degree of

Doctor of Philosophy

Department of Chemistry

© Kristopher Jon Harris

Fall 2009

Edmonton, Alberta

Permission is hereby granted to the University of Alberta Libraries to reproduce single copies of this thesis and to lend or sell such copies for private, scholarly or scientific research purposes only. Where the thesis is converted to, or otherwise made available in digital form, the University of Alberta will advise potential users of the thesis of these terms.

The author reserves all other publication and other rights in association with the copyright in the thesis and, except as herein before provided, neither the thesis nor any substantial portion thereof may be printed or otherwise reproduced in any material form whatsoever without the author's prior written permission.

Library and Archives Canada

Published Heritage Branch

395 Wellington Street
Ottawa ON K1A 0N4
Canada

Bibliothèque et Archives Canada

Direction du Patrimoine de l'édition

395, rue Wellington
Ottawa ON K1A 0N4
Canada

Your file Votre référence
ISBN: 978-0-494-51227-2
Our file Notre référence

NOTICE:
The author has granted a non-exclusive license allowing Library and Archives Canada to reproduce, publish, archive, preserve, conserve, communicate to the public by telecommunication or on the Internet, loan, distribute and sell theses worldwide, for commercial or non-commercial purposes, in microform, paper, electronic and/or any other formats.

The author retains copyright ownership and moral rights in this thesis. Neither the thesis nor substantial extracts from it may be printed or otherwise reproduced without the author's permission.

AVIS:
L'auteur a accordé une licence non exclusive permettant à la Bibliothèque et Archives Canada de reproduire, publier, archiver, sauvegarder, conserver, transmettre au public par télécommunication ou par l'Internet, prêter, distribuer et vendre des thèses partout dans le monde, à des fins commerciales ou autres, sur support microforme, papier, électronique et/ou autres formats.

L'auteur conserve la propriété du droit d'auteur et des droits moraux qui protège cette thèse. Ni la thèse ni des extraits substantiels de celle-ci ne doivent être imprimés ou autrement reproduits sans son autorisation.

In compliance with the Canadian Privacy Act some supporting forms may have been removed from this thesis.

While these forms may be included in the document page count, their removal does not represent any loss of content from the thesis.

Conformément à la loi canadienne sur la protection de la vie privée, quelques formulaires secondaires ont été enlevés de cette thèse.

Bien que ces formulaires aient inclus dans la pagination, il n'y aura aucun contenu manquant.

Canada

Examining Committee

Roderick Wasylishen, Chemistry

Mariusz Klobukowski, Chemistry

Rik Tykwinski, Chemistry

Wolfgang Jäger, Chemistry

Frank Hegmann, Physics

Daniel Leznoff, Chemistry, Simon Fraser University

Abstract

This thesis is concerned with applications of modern solid-state NMR spectroscopy. Investigations of three quite different types are undertaken, each of which attempt to advance knowledge in the fields of chemistry and NMR. The goal of each project is to obtain insight into the effects of chemical environment, in particular bonding, on the NMR observables.

Carbon-13 and nitrogen-15 solid-state nuclear magnetic resonance has been used to study solid samples containing the dicyanoaurate(I) anion, $[Au(CN)_2]^-$, with n-butylammonium, potassium, and thallium counterions. Differences in Au-Tl metallophilic bonding are shown to cause a difference in the isotropic cyanide carbon-13 chemical shift of up to 15.7 ppm, while differences in Au-Au aurophilic bonding are found to be responsible for a change of up to 5.9 ppm. Disordered polymeric gold(I) monocyanide was also investigated, and a range of 7±2% to 25±5% of the AuCN chains are found to be "slipped" instead of aligned with the neighbouring chains at the metal position.

An investigation of the chemical shift tensors of the ^{13}C-labelled carbons in solid samples of $Ph^{13}C{\equiv}^{13}CPh$ and (η^2-$Ph^{13}C{\equiv}^{13}CPh)Pt(PPh_3)_2{\cdot}(C_6H_6)$ has also been carried out. Coordination of diphenylacetylene to platinum causes a change in the ^{13}C chemical shift tensor orientation and a net increase in the isotropic chemical shift. The carbon chemical shift tensors in the platinum complex bear a striking similarity to those of the alkenyl-carbons in *trans*-Ph(H)C=C(H)Ph, and a theoretical discussion of these observations is presented. Each of the fundamental NMR interaction tensors ($\underline{\boldsymbol{\sigma}}$, $\underline{\mathbf{J}}$, $\underline{\mathbf{D}}$ and $\underline{\mathbf{V}}$) may be decomposed into isotropic, symmetric, and antisymmetric components. Observations of all theoretically allowed components other than the antisymmetric portion of $\underline{\mathbf{J}}$ ($\underline{\mathbf{J}}^{\mathrm{anti}}$) have previously been published. Andrew and Farnell's theory (*Mol. Phys.* 15, 157 (1968)) for the effects of $\underline{\mathbf{J}}^{\mathrm{anti}}$ on NMR spectra has been extended to powdered samples, and methods for analyzing

the resultant line shapes have been determined. Finally, the first reported experimental attempts to measure $\underline{\mathbf{J}}^{anti}$ are presented, and experimental proof that no elements of $\underline{\mathbf{J}}^{anti}(^{119}Sn,^{119}Sn)$ in hexa(p-tolyl)ditin are larger than 2900 Hz is given.

Acknowledgements

There are many people who have contributed to my understanding of chemistry over my tenure as a student, and I gratefully acknowledge all of their efforts to chip away at my dull incomprehension. Special thanks go to the solid-state NMR research group at the University of Alberta for many helpful discussions. I would also like to thank Dr. Victor Terskikh for acquiring NMR spectra of AuCN at 21.14 T. Dr. Darren Brouwer, NRC Steacie Institute for Molecular Sciences, is also thanked for introducing me to dipolar-recoupling NMR experiments, and for helpful discussions. Of course, I would never have had the opportunity to undertake any of this research without the equipment and operating grants that fund my supervisor's research group, and I would also have been unable to focus on research without the aid of scholarships and teaching assistantships; specifically, I would like to acknowledge the funding provided by the Natural Sciences and Engineering Research Council of Canada, as well as the Canada Research Chairs Program (R.E. Wasylishen holds a Research Chair in Physical Chemistry at the University of Alberta), the Canadian Foundation for Innovation, the Province of Alberta, and the University of Alberta.

Contents

1 Introduction 1
- 1.1 Motivation . . . 1
- 1.2 Overview of Thesis . . . 4

2 NMR Theory for Bare Nuclei 8
- 2.1 NMR and Gyroscopes . . . 8
- 2.2 Quantum Mechanical Description of Spin Angular Momentum . . . 10
- 2.3 Spin-$\frac{1}{2}$ Particle in an Externally Applied Magnetic Field . . . 12
- 2.4 Ensemble of Spin-$\frac{1}{2}$ Nuclei in a Magnetic Field . . . 14
- 2.5 Observation of the NMR Signal: Case of Spin-$\frac{1}{2}$ Nuclei . . . 16
- 2.6 Analyzing the NMR Signal: Fourier Transforms . . . 19
  - 2.6.1 Theory of Fourier Transforms . . . 20
  - 2.6.2 The Discrete Fourier Transform . . . 23
- 2.7 Summary . . . 24

3 The NMR Interactions and NMR Spectral Analysis 25
- 3.1 Magnetic Shielding . . . 26
  - 3.1.1 The Shielding Interaction . . . 26
  - 3.1.2 Effects of Shielding on NMR Spectra . . . 28
  - 3.1.3 Setting a Zero on the Scale: Chemical Shifts . . . 32
- 3.2 Direct Dipolar Coupling . . . 34
- 3.3 Indirect Coupling . . . 38
- 3.4 Electric Quadrupole Coupling . . . 40
- 3.5 Theoretical Frameworks in NMR . . . 41
- 3.6 Multiple Interaction NMR Lineshapes . . . 43
  - 3.6.1 Powder Lineshapes from AX Spin Systems . . . 43
  - 3.6.2 Powder Lineshapes from AB Spin Systems . . . 46
- 3.7 Common Experimental Techniques . . . 48
- 3.8 Dipolar Recoupling Spectroscopy . . . 51

4 A ^{15}N and ^{13}C NMR Investigation of Cyanoaurate Salts 56
- 4.1 Introduction . . . 56
- 4.2 NMR Terminology and Theory . . . 59

4.3 Experimental 61
4.3.1 Sample Preparation 61
4.3.2 SSNMR 63
4.4 Results and Discussion 64
4.4.1 ^{13}C NMR of Gold(I) Dicyanides 64
4.4.2 ^{15}N NMR of Gold(I) Dicyanides 76
4.4.3 ^{13}C and ^{15}N NMR of a Gold(III) Tetracyanide 79
4.5 Conclusions 82

5 A ^{15}N and ^{13}C NMR Study of Disorder in Polymeric Gold Monocyanide 83
5.1 Introduction 83
5.2 Experimental 86
5.2.1 Sample Preparation 86
5.2.2 SSNMR 88
5.3 Results and Discussion 89
5.3.1 ^{13}C NMR of Gold(I) Monocyanide 89
5.3.2 ^{13}C NMR Linewidths in Gold(I) Monocyanide 98
5.3.3 ^{15}N NMR of Gold(I) Monocyanide 103
5.3.4 Hydrothermal treatment of AuCN(A) 105
5.3.5 Analysis of the Intermediates 106
5.4 Conclusions 116

6 Acetylenic Carbon-13 Chemical Shift Tensors for Diphenylacetylene and (η^2-Diphenylacetylene)Pt(PPh_3)$_2$: A Solid-State NMR and Theoretical Study 118
6.1 Introduction 118
6.2 Experimental 121
6.2.1 Sample Preparation 121
6.2.2 X-ray Crystallography 122
6.2.3 NMR Spectroscopy 122
6.2.4 DFT Calculations 123
6.3 Results and Discussion 125
6.3.1 Diphenylacetylene-α,β-$^{13}C_2$ 125
6.3.2 (η^2-Diphenylacetylene-α,β-$^{13}C_2$)Pt(PPh_3)$_2$ 129
6.3.3 Summary of the Effects of η^2-Bonding to Pt(0) on Unsaturated-Carbon CS Tensors 140
6.3.4 A Comparison of the Alkynyl-Carbon CS tensors for (η^2-Diphenylacetylene)Pt(PPh_3)$_2$ and *trans*-Stilbene 142
6.4 Conclusions 146
6.5 Appendix 147

7 NMR Line Shapes from AB Spin Systems in Solids: The Role of Antisymmetric Spin-Spin Coupling **151**
7.1 Introduction 151
7.2 Theory 156
7.2.1 The Antisymmetric J-coupling Hamiltonian 157
7.2.2 The $A(\Theta)$ Distribution 161
7.2.3 NMR Spectra from a Single Crystal 163
7.2.4 NMR Spectra from Powdered Samples 167
7.3 Selection of Appropriate Spin Systems and Compounds 168
7.4 Data Collection and Analysis 172
7.4.1 Tin-119 Solid-State NMR Spectroscopy of Hexa(*p*-tolyl)ditin 172
7.5 Experimental and Theoretical Implications 177
7.6 Conclusions 179
7.7 Experimental Details 180

8 Concluding Remarks and Future Outlook **182**
8.1 Future Studies 184

List of Tables

3.1 Symmetry Requirements for $\underline{\sigma}$ Elements 29

3.2 Symmetry Requirements for $\underline{J}$ Elements 39

4.1 Local Structural Parameters for Gold(I) Cyanides 64

4.2 Parameters Derived from Simulations of Carbon-13 SSNMR Spectra 67

4.3 Parameters Derived from Simulations of Nitrogen-15 SSNMR Spectra 77

5.1 Carbon-13 NMR Parameters of AuCN 90

5.2 Nitrogen-15 NMR Parameters of AuCN 105

5.3 Carbon-13 NMR Parameters for Annealed AuCN 107

5.4 Carbon-13 NMR parameters for Intermediate (A) and (A′) 110

5.5 Carbon-13 Isotropic Chemical Shifts for Amorphous Cyanide Materials from SSNMR Spectra 113

6.1 Experimental and Calculated Alkynyl-Carbon Chemical Shift Tensors for Diphenylacetylene and (η^2-Diphenylacetylene)Pt(PPh_3)$_2$ 127

6.2 Crystallographic Data for (η^2-Diphenylacetylene)Pt(PPh_3)$_2$ and Solvates 131

6.3 ^{13}C and ^{31}P NMR Parameters of (η^2-Diphenylacetylene)Pt(PPh_3)$_2$. 135

7.1 Energy levels and wavefunctions for an AB spin system under MAS, including the effects of $\underline{\mathbf{J}}^{\mathrm{anti}}$ 165
7.2 Transition frequencies and intensities for an AB spectrum, incorporating isotropic chemical shifts and the full $\underline{\mathbf{J}}$ tensor. 165
7.3 Number of independent components of $\underline{\mathbf{J}}^{\mathrm{anti}}$ for each point group, assuming the two nuclei are not exchanged by a symmetry operation (condensed from Table 3.2). 172
7.4 Tin-119 NMR parameters determined for hexa(*p*-tolyl)ditin. 175
7.5 Relationships between the mechanisms which contribute to $\underline{\mathbf{J}}$ and the symmetry properties of $\underline{\mathbf{J}}^{311}$ 179

List of Figures

2.1 A. A child's top demonstrating the relationship between rotational motion and the resultant angular momentum. B. Tipping of the rotating top results in the torque produced by gravity inducing the depicted precession 9

2.2 A. Representation of the state $|\psi_\theta\rangle = cos(\theta/2)\,|+1/2\rangle + sin(\theta/2)\,|-1/2\rangle$, in which $\langle \hat{I}_z \rangle = cos(\theta)\frac{1}{2}\hbar$, $\langle \hat{I}_x \rangle = sin(\theta)\frac{1}{2}\hbar$, $\langle \hat{I}_y \rangle = 0$. B. Under the effect of a magnetic field along the z-axis, $\langle \hat{\boldsymbol{I}} \rangle$ precesses about the applied field, with the tip following the depicted circular path. Indicated direction of precession is for a nucleus with positive γ. 13

2.3 The nuclear magnetic moment orientations for an ensemble of spin-$\frac{1}{2}$ nuclei is the sum of the sets of vectors shown. 15

2.4 A. Orientation of the cylindrical sample, coil, and external magnetic field, B^0. B. The two components of the B^1 field are depicted in a horizontal slice through the centre of the coil and sample shown in part A. C. Demonstration of the fixed relationship between the orientation of the nuclear magnetic moments, $\langle \hat{\boldsymbol{\mu}} \rangle(t)$, and one component of the B^1 field. 18

2.5 Example of a Fourier transform, where Re$\{f\}$ indicates the real part of the function f, while Im$\{f\}$ is the corresponding imaginary component. In this example, the frequency representation is much simpler than the time-domain signal. For definitions of the functions, see Section 2.6.1. 20

3.1 Theoretical ^{13}C NMR spectrum of a glassy sample of ethanol; absolute frequency scale. 32

3.2 Theoretical ^{13}C NMR spectrum of a glassy sample of ethanol; chemical shift scale. 34

3.3 Axis system used to express the dipolar coupling, Equation 3.18; B^0 is along the z-axis, and $\boldsymbol{r}$ is the vector joining nucleus I (at the origin) to nucleus S. 37

3.4 Axis system used in Equation 3.31 where the orientations of B^0 and $\boldsymbol{r}_{\mathrm{AX}}$ are described as shown. Note that $\boldsymbol{r}_{\mathrm{AX}}$ is a vector joining nucleus A with nucleus X. 45

3.5 Example A-spin spectrum from an AX spin system. Here, a ^{13}C anisotropic shielding lineshape including coupling to ^{31}P is shown. Specific details: $\nu_{\mathrm{L}} = 100$ MHz, $\delta_{11} = 175$ ppm, $\delta_{22} = 100$ ppm, $\delta_{33} = -175$ ppm, $R_{\mathrm{eff}} = 1.5$ kHz, $\alpha = 50°$, $\beta = 30°$, $J_{\mathrm{iso}} = 0$. 47

3.6 Example of the effects of MAS on a shielding-only powder pattern, the theoretical system has a shielding anisotropy of approximately 28 kHz and an MAS frequency of 2 kHz was used. 50

3.7 A. Symbolic display of a one-dimensional, single-channel ^{13}C $SR26_4^{11}$ homonuclear dipolar recoupling pulse sequence; pulses in one $R26_4^{11}$ block are shown using the $(\text{Pulse Angle})_{\text{Phase}}$ convention. B. Two dimensional, two-channel version of the $SR26_4^{11}$ sequence, with signal enhancement via ^{1}H → ^{13}C CP followed by a flip-back pulse, and heteronuclear decoupling during both homonuclear recoupling and acquisition. 52

3.8 Theoretical behaviour of intensity versus time for the DQ signal intensity from an $SR26_4^{11}$ experiment, see Equation 3.42. Curves for two example distances, *i.* and *ii.*, from idealized propane and *trans*-2-butene are shown. Vertical gray lines in the graph indicate the allowed values of $\tau = n \cdot 3.2$ ms at a rotor spinning frequency of 5 kHz. 53

3.9 2D carbon-13 CP-$SR26_4^{11}$ spectrum of 1-^{13}C-glycine probing intermolecular dipolar couplings ($|\boldsymbol{r}_{CC}| = 3.104$ Å, and $R_{\text{eff}} = 254$ Hz); spectrum collected using a 75.1 MHz transmitter frequency, with $\nu_{rot} = 8.097$ kHz, and $\tau = 3.95$ ms; high power TPPM decoupling was applied during signal acquisition. The spectrum from the analogous 1D CP-$SR26_4^{11}$ sequence is shown above the 2D spectrum. Note that because the 1D peak occurs at +12.5 ppm from the transmitter frequency, the self-correlation peak (correlating two nuclei at the same chemical shift) occurs at +25 ppm in the indirect dimension. . 55

4.1 Simulated (upper trace) and experimental (lower trace) ^{13}C NMR spectra of a stationary sample of $K[Au(CN)_2]$ at 11.75 T. 66

4.2 Carbon-13 T1 and T2 relaxation data and theoretical fits from $K[Au(CN)_2]$ and the low-frequency site of $Tl[Au(CN)_2]$. See text for details of experiments. 68

4.3 Local structure of $Tl[Au(CN)_2]$ depicting the intersection of the two Au chains, where Au atoms 1, 2, and 3 are numbered; and metallophilic bond lengths are given in Angstroms. Cyanide ligands are oriented with carbon bonded to the gold atoms. 70

4.4 A. ^{13}C NMR spectrum of $Tl[Au(CN)_2]$ under MAS, $\nu_{rot} = 10$ kHz, acquired at 7.05 T. B. ^{13}C NMR spectrum of $Tl[Au(CN)_2]$ under MAS, $\nu_{rot} = 12$ kHz, acquired at 11.75 T. 71

4.5 Experimental (lower trace) and simulated (upper trace) ^{13}C NMR spectra of a stationary sample of $Tl[Au(CN)_2]$ at 11.75 T. 75

4.6 Simulated (upper trace) and experimental (lower trace) ^{15}N cross-polarized NMR spectra acquired from a stationary sample of $[(n\text{-}C_4H_9)_4N][Au(CN)_2]\cdot H_2O$ at 4.70 T. 76

4.7 Experimental (A.) and simulated (B.) slow-spinning ^{15}N NMR spectra of $K[Au(CN)_2]$ at 11.75 T ($\nu_{rot} = 2.5$ kHz). 78

4.8 Experimentally observed ^{15}N NMR spectrum of $Tl[Au(CN)_2]$ at 11.75 T under MAS ($\nu_{rot} = 10$ kHz). 79

4.9 Experimental (lower trace) and simulated (upper trace) ^{13}C NMR spectra of a stationary sample of $K[Au(CN)_4]$ at 11.75 T. 80

5.1 Two unit cells of AuCN; carbon and nitrogen atoms are not distinguished by the neutron diffraction experiment and are therefore represented using the same shade. See text for further discussion of the structure. 84

5.2 Upper spectrum: ^{13}C NMR spectrum of AuCN(A) under MAS, $\nu_{rot} = 13$ kHz, acquired at 11.75 T. Lower spectrum: ^{13}C NMR spectrum of AuCN(B) under MAS, $\nu_{rot} = 10$ kHz, also acquired at 11.75 T. Peaks marked with a † in the spectrum of AuCN(B) have been assigned as impurities (see text). 91

5.3 Carbon-13 $SR26_4^{11}$ homonuclear dipolar correlation spectrum of AuCN(A) acquired under MAS, $\nu_{rot} = 9.615$ kHz, at 7.05 T; spectrum resulted from 6 days of experimental time. The corresponding 1D Bloch-decay experiment is placed at the top of the spectrum. In the presented expansion, self-correlation appears on the diagonal, while inter-site correlations occur as pairs of peaks off the diagonal. Spectral artifacts have no frequency dependence in t_1, and occur at 0 ppm in the indirect dimension. 92

5.4 IR spectra of the CN stretching region, upper spectrum from AuCN(A), and lower spectrum from AuCN(B). 94

5.5 Powder X-ray diffraction spectra of different AuCN samples. The spectrum from AuCN(A) is shown as trace A. and that of AuCN(B) is shown as B., while powder patterns from AuCN(A′) are shown both before, in C., and after, in D., mineralization at high temperature with an aqueous solution of KCN. Peaks marked with a * in C. and D. are assigned to metallic Au. See text for preparation details of each sample. 96

5.6 Experimental (lower trace) and simulated (upper trace) ^{13}C NMR spectra of a stationary sample of AuCN(B) at 4.70 T. 98

5.7 Comparison ^{13}C MAS NMR spectra obtained for AuCN(A) and AuCN(B). A. Spectra from both samples acquired at 11.75 T, plotted on a chemical shift scale. B. Spectra from AuCN(A) acquired at 7.05 and 11.75 T, plotted on a frequency scale. C. Spectra from AuCN(B) acquired at 7.05 and 11.75 T, plotted on a frequency scale. 100

5.8 Carbon-13 MAS NMR spectra obtained at 4.70 T for $AuCN$,[190] before and after heating to 180 °C. 101

5.9 Upper spectrum: ^{15}N NMR spectrum of AuCN(A) under MAS, ν_{rot} = 13 kHz, acquired at 11.75 T. Lower spectrum: ^{15}N NMR spectrum of AuCN(B) under MAS, ν_{rot} = 10 kHz, also acquired at 11.75 T - spinning sidebands marked with a *. 104

5.10 Carbon-13 NMR spectrum of annealed AuCN(A) under MAS, ν_{rot} = 19 kHz, acquired at 11.75 T; a small spectral artifact (quadrature image) is marked with a †. 106

5.11 Carbon-13 NMR spectra acquired at 11.75 T under MAS, ν_{rot} = 13 – 19 kHz; spectra of Intermediate(A) and (A′) are superimposed on those of the corresponding washed samples. Peaks are labelled 1 to 5 for simplicity (see text). 109

5.12 Carbon-13 NMR spectra, acquired at 11.75 T under MAS, of a variety of materials expected as possible impurities in the AuCN(A) and (A′) synthesis superimposed on the spectrum obtained from AuCN(A) at the same field. See Table 5.5 for isotropic chemical shifts. 110

5.13 Carbon-13 $SR26_4^{11}$ homonuclear dipolar-recoupling spectrum of Intermediate(A) acquired over 6 days under MAS, $\nu_{rot} = 9.615$ kHz, at 7.05 T. Peaks on either side of the 0 ppm line in the indirect dimension are small dispersion-shaped spectral artifacts. Short acquisition time in t_1 causes peaks to have the typical $\sin(x)/x$ shape in the indirect dimension, where the "feet" are a few percent of the main peak height. These features can be seen for the very intense peak from site 1, and have been marked with a dashed vertical line. Self-correlation peaks occur along the solid diagonal line, while inter-site correlation peaks occur in pairs off of the line. Peaks from self correlations for each of the sites numbered 1 - 5 are marked (expected location for site 2), and the correlations between sites 1 and 4 assigned to AuCN are indicated. An arrow highlights the inter-site correlation involving site 5. 112

5.14 IR spectra of the CN stretching region, from Intermediate(A). 114

5.15 Nitrogen-15 NMR spectrum of Intermediate(A) under MAS, $\nu_{rot} = 13$ kHz, acquired at 11.75 T. 115

5.16 Nitrogen-15 NMR spectrum of Intermediate(A) under MAS, $\nu_{rot} = 13$ kHz, acquired at 11.75 T. 115

6.1 Simulated and experimental ^{13}C NMR spectra of the alkynyl carbons from stationary samples of DPA. Experimental spectra were recorded at applied field strengths of 9.4 (A) and 4.7 (C) T. The corresponding simulations are presented as traces B and D. 126

6.2 Principal axis system of the alkynyl-carbon CS tensor of DPA. The unlabelled principal component directed out of the page is δ_{11}. . . . 129

6.3 ORTEP[250] plot of PtDPA·C_6H_6 (50% probability ellipsoids) with hydrogen atoms and all but *ipso* carbons of the PPh_3 phenyl rings removed for clarity. 132

6.4 Simulated and experimental ^{13}C NMR spectra acquired from a sample of (η^2-diphenylacetylene)Pt(PPh_3)$_2$ dissolved in CD_2Cl_2. Simulated spectra are shown without (A) and with (B) ^{195}Pt ($I = \frac{1}{2}$, N.A. = 33.8 %). The sum of the subspectra is also shown (C) for comparison with the experimental spectrum (D), which has been corrected to show only alkynyl-carbons through subtraction of the spectrum from a non ^{13}C-labelled sample. The small distortions and negative peaks in the experimental spectrum arise from imperfections in the subtraction. . 133

6.5 Simulated and experimental ^{13}C NMR spectra of the alkynyl carbons from PtDPA at 7.05 T, acquired with MAS ($\nu_{rot} = 8$ kHz). Simulated spectra are shown with (A) and without (B) ^{195}Pt ($I = \frac{1}{2}$, N.A. = 33.8 %). The sum of the subspectra is also shown (C) for comparison with the experimental spectrum (D). 136

6.6 Simulated and experimental ^{13}C NMR spectra of the alkynyl carbons from stationary samples of PtDPA. Experimental spectra were recorded at applied field strengths of 11.75 (A) and 7.05 (C) T. The corresponding simulations are presented as traces B and D. 138

6.7 Principal axis systems for the alkynyl-carbon CS tensors of PtDPA. δ_{11} and δ_{22} are labelled, while δ_{33} is directed out of the page. For clarity, all phenyl rings are removed except the *ipso* carbons of the diphenylacetylene rings. 139

6.8 Summary of the effects on the CS tensors of alkenyl and alkynyl carbons caused by η^2-bonding with platinum(0). In the diagram for DPA forming PtDPA, dashed lines link orientationally similar principal components. 142

6.9 Abbreviated energy level diagram of the MOs of (η^2-acetylene)Pt(PMe_3)$_2$ on a nonlinear energy scale. We label the orbitals counting down from the HOMO, and counting up from the LUMO. The displayed molecular orbitals, HOMO-5 and LUMO+1, couple to produce a +45 ppm $\sigma_{ij}^{p,oc-vir}$ term directed out of the page for the alkynyl-carbon magnetic shielding (see text). 146

7.1 A. Coordinate system and conventions used in the expressions for the $A(\Theta)$ distribution. The lab frame is defined by the axes X, Y, Z; the axis of sample rotation is $\vec{r}_{rot}$, which is at the "magic angle" of $\cos^{-1}(1/\sqrt{3})$ relative to the Z axis; and the crystallite axis system in which $\underline{\mathbf{J}}$is represented is described with the vectors x, y, z. Angles given as ξ_a are those between axis a of the crystallite frame and $\vec{r}_{rot}$. B. Normalized projections of the crystallite axes x, y, z on the plane perpendicular to $\vec{r}_{rot}$ shown in A are labelled p_x, p_y, and p_z. Rotation of these projected vectors by -90°about $\vec{r}_{rot}$ are annotated as the corresponding primed vectors p'_x, p'_y, p'_z; and angles given as $\varepsilon_{ab'}$ are those between p_a and p'_b ($\varepsilon_{yx'}$ is shown as an example). . . . 160

7.2 A. Numerically generated plots of $f_{zy}(\Theta; c_{yx}, c_{zx})$ versus fraction of crystallites displaying that value. (i) The smallest range of the f_{zy} distribution, $\pm 1/\sqrt{3}$, is found with the parameters $c_{yz} = c_{zx} = 0$. (ii) The largest range of the f_{zy} distribution, ± 1, occurs when $c_{yz} = c_{zx} = 1$. (iii) Example of the range found for the f_{zy} distribution with intermediate values of the c_{ij} constants, in this plot, $c_{yz} = 0$ and $c_{zx} = 0.8$. B. Plot of $f^2_{zy}(\Theta; c_{yx}, c_{zx})$, with parameters $c_{yz} = c_{zx} = 1$, the same as in A(ii). 163

7.3 A. Numerically generated plots of $f_{zy}(\Theta; c_{yx}, c_{zx})$ versus fraction of crystallites displaying that value. (i) The smallest range of the f_{zy} distribution, $\pm 1/\sqrt{3}$, is found with the parameters $c_{yz} = c_{zx} = 0$. . . 166

7.4 Structure of hexa(*p*-tolyl)ditin. A. View along the tin-tin bond. B. Side view. Hydrogen atoms are omitted for clarity. 173

7.5 A. Tin-119 VACP/MAS spectrum of hexa(*p*-tolyl)ditin obtained at 7.05 T. The two dominant peaks result from the uncoupled nuclei, and are therefore far more intense than peaks from the coupled isotopomers. The splitting (i) is equal to $^1J_{iso}(^{119}Sn,^{117}Sn)$ for site 1 and the splitting (ii) is $^1J_{iso}(^{119}Sn,^{117}Sn)$ for site 2. The splitting corresponding to $C_0 - |J_{iso}(^{119}Sn,^{119}Sn)|$ is also marked in the figure. B. Tin-119 POST-C7 spectrum of hexa(*p*-tolyl)ditin also obtained at 7.05 T under MAS, where the double-quantum pulse sequence filters out all but homonuclear spin pairs, leaving only the central part of the AB pattern. The edges of the lineshape provide a maximum value for $C_0 - |J_{iso}(^{119}Sn,^{119}Sn)|$, and therefore of the largest component of $\underline{\mathbf{J}}^{anti}$. 173

7.6 2D J-resolved ^{119}Sn CP/MAS NMR spectrum of hexa(p-tolyl)ditin obtained at 4.70 T. The splitting $C_0 - |J_{iso}(^{119}Sn,^{119}Sn)|$ is easily resolved in the second dimension. 176

List of Symbols and Abbreviations

α, β, γ	Euler angles for specifying relative coordinate-system orientations
$\underline{\boldsymbol{\sigma}}$	magnetic shielding tensor
σ_{iso}	isotropic component of the magnetic shielding tensor
σ_{11}, σ_{22}, σ_{33}	magnetic shielding tensor elements in its principal axis system
$\boldsymbol{\sigma}^d$	theoretical diamagnetic contribution to the magnetic shielding
$\boldsymbol{\sigma}^p$	theoretical paramagnetic contribution to the magnetic shielding
$\underline{\boldsymbol{\delta}}$	chemical shift tensor
δ_{iso}	isotropic component of the chemical shift tensor
δ_{11}, δ_{22}, δ_{33}	elements of the chemical shift tensor in its principal axis system
γ	magnetogyric (also gyromagnetic) ratio
$\hat{\boldsymbol{\mu}}$	magnetic dipole moment vector operator
ν	frequency in Hz
ω	frequency in rad/s
η_Q	asymmetry of the electric field gradient tensor
Ω	span of the magnetic shielding/chemical shift tensors
κ	skew of the magnetic shielding/chemical shift tensors
AO	atomic orbital
$A(\Theta)$	effective antisymmetric indirect nuclear spin-spin coupling constant
A_{max}	maximum value in the $A(\Theta)$ distribution
$\mathbf{B}^0$	externally applied static magnetic field
$\mathbf{B}^1$	externally applied pulsed magnetic field
CP	cross polarization
CS	chemical shift
C_Q	nuclear quadrupolar coupling constant
$\underline{\mathbf{D}}$	direct nuclear spin-spin coupling tensor

DFT	density functional theory
DQ/DQC	double quantum / double-quantum coherence
GIAO	gauge-including atomic orbital
$\hat{\mathscr{H}}$	Hamiltonian operator
HOMO	highest occupied molecular orital
$\hat{\mathbf{I}}$, $\hat{\mathbf{S}}$	vector operators for spin angular momentum
$\hat{I}_{x(y,z,+,-)}$, $\hat{S}_{x(y,z,+,-)}$	vector spin angular momentum operator components
$\underline{\mathbf{J}}$	indirect nuclear spin-spin coupling tensor
J_{iso}	isotropic component of $\underline{\mathbf{J}}$
$\underline{\mathbf{J}}^{\mathrm{sym}}$	symmetric component of $\underline{\mathbf{J}}$
$\underline{\mathbf{J}}^{\mathrm{anti}}$	antisymmetric component of $\underline{\mathbf{J}}$
J_{11}, J_{22}, J_{33}	the elements of $\underline{\mathbf{J}}^{\mathrm{sym}}$ in its principal axis system
LUMO	lowest occupied molecular orbital
MAS	magic angle spinning
MO	molecular orbital
NMR	nuclear magnetic resonance
NQR	nuclear quadrupole resonance
PAS	principal axis system (diagonalizes symmetric tensor)
PtDPA	(η^2-diphenylacetylene)Pt(PPh_3)$_2$
POST-C7	modified C7 dipolar recoupling NMR pulse sequence
Q	nuclear quadrupole moment
rf	radiofrequency
R_{DD}	direct-dipolar coupling constant
R_{eff}	effective direct-dipolar coupling constant
$\mathrm{SR26}_4^{11}$	symmetry-derived dipolar recoupling pulse sequence
SSNMR	solid-state nuclear magnetic resonance

T_1	the nuclear longitudinal relaxation time constant
T_2	the nuclear transverse relaxation time constant
TSB	*trans*-stilbene
$\underline{\mathbf{V}}$	the electric field gradient (at the nucleus) tensor
VACP	variable-amplitude cross polarization
ZORA	zeroth-order regular approximation (in density functional theory)

Chapter 1

Introduction

1.1 Motivation

Fascination with the underlying structure of matter probably predates all of our written records. Long before modern ideas about the atomic nature of matter, greek philosophers deduced from the manner in which natural objects break into pieces that matter, in some format, must be composed of tiny elementary particles and enough void space to allow these elementary particles to move and rearrange. The idea of atomism is credited to the Greek school of thought founded by Leucippus of Abdera (~530 B.C.). Unfortunately, Leucippus left behind no written treatise of his philosophy; however, he was influential enough that later philosophers described at least some details of his theories. For example, one of Aristotle's works summarizes the philosophy of one of Leucippus' pupils, Democritus of Abdera, in a later incarnation of the doctrine:[1]

> "According to the theory of Democritus it is the nature of the eternal objects to be tiny substances infinite in number. Accordingly he postulates also a place for them that is infinite in magnitude, which he designates by these names - *the void, the nothing,* and *the infinite*;

whereas he speaks of each individual atom as *the yes-thing, the dense,* and *being.* He conceives them as so small as to elude our senses, but as having all sorts of forms, shapes, and different sizes. Treating these as elements, he conceives of them as combining to produce visible and otherwise perceptible objects.

As they move about in the void the particles are at variance with one another because of their dissimilarity and the other mentioned differences; hence in their motion, as they bump or even as they brush against one another, they tend to get ensnarled and interlocked. The process of interlocking never makes them into a single nature however, for it would be absurd to think that two or more things could ever become one. When these substances remain joined for some time, it is explained by the fact that they fit snugly and so catch firm hold of one another; for some bodies are scalene while others are sharply hooked, some are concave, others convex, and there are numerous other differences. His theory is that they cling together and remain in certain combinations until they are shaken apart and separated by outside forces."

While the details seem simplistic today, the essence of this depiction is incredibly accurate. It also captures one of the features of chemistry that originally drew my interest in the field - chemistry provides one with problems that can be solved mathematically and solutions that yield an intuitive understanding. For example, development of the kinetic model of gases allows one to equate pressure on the side of a container with the average speed of gas molecules hitting it. I am the type of person who finds particular satisfaction in the type of puzzle solving where a mathematical and intuitive picture results, so chemistry was a natural fit. Once I realized this, I needed only choose a tool with which to investigate.

It is probably past the point where one need justify the importance and utility of NMR spectroscopy in studying chemistry. We are now in a state where NMR is ubiquitous and nearly all chemists, as well as researchers in many other fields, use NMR in a routine manner. Beyond the well-known nature of NMR as a workhorse method for problem solving, it is a fundamentally interesting area of science. There is real beauty in the details of NMR experiments - when sitting in on one of our group meetings during his visit to the University of Alberta, Prof. Mark Ratner, author of the popular *Introduction to Quantum Mechanics in Chemistry*, remarked on the impressive sensitivity and resolution of one particular experiment, saying "NMR: it's God's own science". Because lifetimes of the coherent states used in NMR spectroscopy are unusually long, incredibly complicated experiments can be performed. However, there are usually only a small number of particles and basis functions, so the experiments can still be understood in a way that is sufficiently intuitive to be satisfying. NMR therefore provided me with a method to answer chemical problems, and one where I was interested in the day-to-day details.

Once settled on NMR, there were still a plethora of subtopics and research projects that I could have focussed on, for example, there are several journals dedicated exclusively to NMR, and the Encyclopedia of NMR contains approximately 7500 pages describing background information on the current state of the field. In this selection process, my supervisor Prof. Wasylishen was able to provide most of the logic for narrowing the scope of possible projects. Of course, one criterion that I had for a research program was that it should attempt to solve problems important to the field of chemistry, through provision of useful information and insights. I also made every attempt to spend most of my time on projects that I thought would teach me something I wanted to know about interpreting the science of NMR. In particular, I was concerned with "how to think about" quantum mechanics, NMR observables, and chemical bonding.

1.2 Overview of Thesis

The first project I became involved in was an experimental NMR investigation into the modes of disorder in AuCN, a topic with some history in the Wasylishen research group. However, we soon found that it was necessary to investigate a series of related materials to form a body of data with which to interpret our results; Chapter 4 details the work on these related materials, and has been published as a refereed journal article.[2] A series of ionic salts containing the linear dicyanoaurate anion, $[NC\text{-}Au\text{-}CN]^-$, were investigated in the solid state using ^{13}C and ^{15}N NMR. These materials form an interesting topic within chemistry as they involve "metallophilic" bonds, which are sometimes formed between closed-shell heavy metal atoms. The combined abilities of metallophilic bonds and cyanide ligands to create a network of these anions makes them building blocks for an array of interesting materials with novel properties. Several salts with differing counterions, $K[Au(CN)_2]$, $[(n\text{-}C_4H_9)_4N][Au(CN)_2]\cdot H_2O$, and $Tl[Au(CN)_2]$, were investigated. One of the interesting results of this investigation is that these metallophilic interactions between dicyanoaurate anions cause a measurable effect on the ^{13}C chemical shift. We also investigated one gold(III) salt, $K[Au(CN)_4]$, to determine the effects of the formal oxidation state of gold on the NMR parameters.

With this background NMR data in hand, we then went on to investigate the question of disorder in AuCN, and this study is reported in Chapter 5, most of which has been published as a journal article.[2] At first, difficulties with sample preparation prevented interpretation of the NMR spectra - how can a peak be assigned if the composition of the sample is unknown? We were able to solve this problem using a combination of powder X-ray diffraction and 2D ^{13}C-^{13}C correlation NMR spectroscopy. Once a trusted and reproducible sample was obtained, a synthesis of NMR, IR, and X-ray diffraction data was used to help build up a picture of the disorder present, as well as the differences between samples. One of the important

results of this investigation was the determination of one type of disorder which had been proposed in the literature, but not measured definitively: slipping of the linear $\cdots$CNAuCNAu$\cdots$ chains with respect to each other. We were able to quantify the fraction of disordered sites and measure differences in the amount of the disorder produced by different synthetic methods.

I was also involved in a collaboration with Dr. Guy Bernard, a research associate in the Wasylishen group, concerning changes in the ^{13}C NMR parameters of unsaturated carbon centres induced by metal coordination. Dr. Bernard had previously investigated the ^{13}C NMR parameters from a sample of diphenylacetylene, isotopically labelled with ^{13}C at both the alkynyl positions. The next step was to measure the effect on these ^{13}C NMR observables from η^2-coordination to a Pt(II) centre, forming (η^2-diphenylacetylene)Pt(PPh_3)$_2$. The effect of this coordination on the alkynyl carbon's isotropic (orientationally averaged) chemical shift was well known from solution NMR; however, the change in the full orientation-dependent chemical shift interaction was not known. I therefore prepared a sample of this material and structures of several forms were determined using X-ray diffraction by my collaborators Dr. Robert McDonald and Dr. Micheal Ferguson. With this structural information in hand, I prepared a doubly ^{13}C labelled version of the material, using an isotopically labelled version of the starting material, diphenylacetylene, prepared by Chris McDonald. This allowed me to analyze the solid-state NMR spectra from (η^2-diphenylacetylene)Pt(PPh_3)$_2$, and the results of this investigation are presented in Chapter 6, which has also been published as an article in a refereed journal.[3]

An interesting feature of the alkynl-carbon ^{13}C chemical shift tensor from (η^2-diphenylacetylene)Pt(PPh_3)$_2$ is the apparent congruency with well-known chemical bonding models. The Dewar-Chatt-Duncanson model predicts that, upon η^2-coordination to a metal centre, a carbon-carbon triple bond becomes similar to a carbon-carbon double bond. The experimental results reported here show that the

alkynyl-carbon ^{13}C chemical shift tensor in diphenylacetylene becomes, upon coordination with Pt(II), very similar to the chemical shift tensor of an alkenyl carbon. In order to investigate the source of this similarity, I undertook a theoretical examination of the chemical shifts in these two systems, and the conclusions of this study are reported in Chapter 6. This analysis uncovers the fact that similarities in chemical shift tensors for alkenyl carbons versus η^2-bound alkynyl carbons is not due to a similarity of molecular orbitals. Not surprisingly, the electron current density, which gives rise to the chemical shift, is heavily affected by the platinum atom - thereby negating any simplistic comparison of chemical shift contributions. This theoretical study was also presented in the corresponding journal article.[3]

The final experimental chapter of this thesis details some work characterizing indirect spin-spin coupling, $\underline{\mathbf{J}}$, tensors, in collaboration with Dr. David Bryce (Wasylishen group alumnus, now Assistant Professor at the University of Ottawa). Similar to the other NMR interaction tensors, $\underline{\mathbf{J}}$ can be divided into components with different symmetry properties: the isotropic component, J_{iso}, the anisotropic symmetric component, $\underline{\mathbf{J}}^{\text{sym}}$, and the anisotropic antisymmetric component, $\underline{\mathbf{J}}^{\text{anti}}$. Effects from the antisymmetric component of $\underline{\mathbf{J}}$ on NMR spectra are generally ignored, and no experimental characterization of $\underline{\mathbf{J}}^{\text{anti}}$ has ever been reported. This makes $\underline{\mathbf{J}}^{\text{anti}}$ somewhat of an anomaly, as all other components of the fundamental NMR interaction tensors (unless theoretically required to be zero), have been experimentally observed. Rather than some esoteric quest, there is real potential benefit in learning to characterize $\underline{\mathbf{J}}^{\text{anti}}$. Given the demonstrated utility of the other $\underline{\mathbf{J}}$ components for solving problems and providing chemical insight, it is anticipated that the elements of $\underline{\mathbf{J}}^{\text{anti}}$ will provide a profitable source of data.

While effects from $\underline{\mathbf{J}}^{\text{anti}}$ are generally ignored, as far back as 1968 Andrew and Farnell published a theory including such effects for NMR spectra.[4] Specifically, they delineated the form of the NMR spectrum from an AB pair of spin-$\frac{1}{2}$ nuclei in a single

crystal spinning rapidly at the magic angle. Given that modern quantum chemical calculations have shown that the elements of $\underline{\mathbf{J}}^{\mathrm{anti}}$ can be of significant magnitude, and there is a published theory predicting observable effects on spectra, it might be expected that one need worry about the validity of published data extracted from AB spin systems without consideration of antisymmetric $\underline{\mathbf{J}}$ coupling. With this in mind, I reinvestigated the theoretical framework, and extended the theory of Andrew and Farnell to include the orientational averaging expected for samples. The most probable values of the transition frequencies are for those crystallites where the transition frequency is unaffected by $\underline{\mathbf{J}}^{\mathrm{anti}}$; accordingly, analyzing the highest point of each NMR peak allows one to extract data completely independent of $\underline{\mathbf{J}}^{\mathrm{anti}}$. However, the shape and characteristic features of the peaks do reflect the magnitude of $\underline{\mathbf{J}}^{\mathrm{anti}}$ elements, and I was able to determine a method for analyzing the line shapes to determine a measure of the largest element of $\underline{\mathbf{J}}^{\mathrm{anti}}$. Given this theoretical framework, we worked towards determining practical considerations for the conditions under which an observation of $\underline{\mathbf{J}}^{\mathrm{anti}}$ is probable. Dr. David Bryce had extensive experience with quantum chemical calculations involving $\underline{\mathbf{J}}^{\mathrm{anti}}$ and was instrumental in narrowing down the possible candidates and helping to provide a detailed background for the discussion. The conditions for a successful experiment are quite stringent, but we determined that hexa(p-tolyl)ditin was a molecule which possesses an unusually high probability of yielding positive results for antisymmetry in the $^{1}\underline{\mathbf{J}}(^{119}\mathrm{Sn},^{119}\mathrm{Sn})$ indirect coupling tensor. I therefore synthesized a sample of this material, and collected a solid-state NMR spectrum enabling us to provide a definite upper limit of 2900 Hz (but no lower limit) on the elements of $\underline{\mathbf{J}}^{\mathrm{anti}}$ in this molecule.[5] An exact measure of $\underline{\mathbf{J}}^{\mathrm{anti}}$ still remains elusive, but for the first time, we can say that its elements are definitely less than a specific number. More important, a general approach for obtaining information on $\underline{\mathbf{J}}^{\mathrm{anti}}$ has been developed.

Chapter 2

NMR Theory for Bare Nuclei

2.1 NMR and Gyroscopes

Nuclear magnetic resonance is the study of charged particles with spin angular momentum under the influence of external magnetic fields. It therefore seems best to start with an exploration of angular momentum in a more familiar setting. I will then move on to a quick rationale of why NMR works and how it provides chemical information to the researcher. Hopefully, this tangible model will improve the clarity of the quantum mechanical descriptions in the following sections of this chapter.

Spin angular momentum of subatomic particles is another in the list of quantum phenomena whose comprehension benefits greatly from comparisons to the macroscopic world. Consider the top, a popular children's toy, depicted in Figure 2.1A. The energy put into spinning the top is stored as angular momentum, which is represented as a vector perpendicular to the plane of circular motion, in the direction defined by the right-hand rule. This may not seem like a particularly engrossing toy, but the allure of these tops is their extraordinary stability once rotating. If a spinning top were set down at the angle depicted in Figure 2.1B, one would expect it to simply fall over. However, the top does not fall but instead maintains a constant

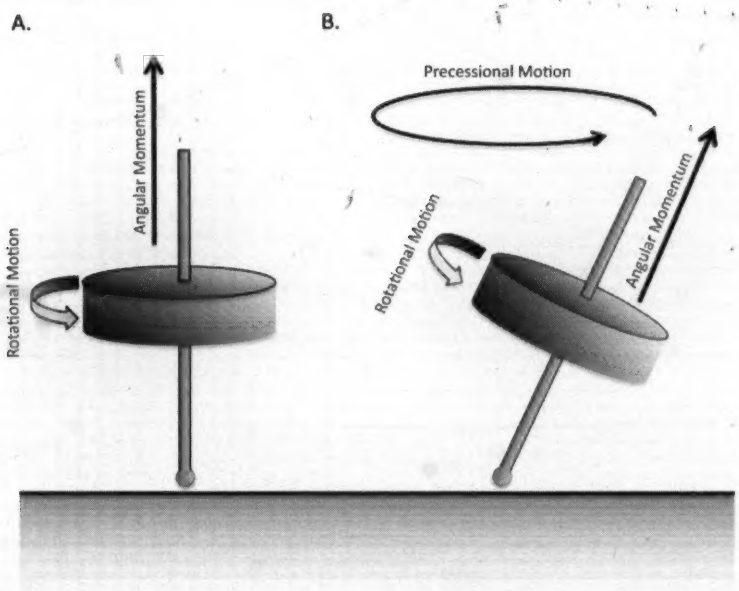

Figure 2.1: A. A child's top demonstrating the relationship between rotational motion and the resultant angular momentum. B. Tipping of the rotating top results in the torque produced by gravity inducing the depicted precession

angle with respect to the surface it is spinning on. The downward force of gravity (which would act to rotate the top about its contact point with the surface were it not spinning) is converted into the horizontal motion of precession - the upward tip of the gyroscope inscribes a circle as shown in Figure 2.1B. As will be shown momentarily, this precessional motion of a child's top is an interesting analogy to NMR, and provides a tangible handhold from which to approach the topic.

Many of the elementary particles that compose our world possess an intrinsic angular momentum, known as *spin angular momentum.* In an interesting break from the classical angular momentum of a top, spin angular momentum is simply a property of the particle, it does not arise from some rotation of matter forming the particle. Just as a proton has an electric charge of $\sim -1.6 \times 10^{-19}$ Coulombs, it has an intrinsic spin angular momentum of $\sim 9.1 \times 10^{-35}\ kg \cdot m^2 \cdot s^{-1}$. Nuclei with spin

angular momentum are analogous to the top described above, e.g., the two protons in a water molecule have an orientation: their spin angular momentum vectors point in some specific direction. This is probably what most NMR spectroscopists picture when they think of matter: intangibly small tops afloat in a sea of fast-moving electrons.

Elementary particles possess another important property directly associated with their spin: any particle with spin angular momentum also possesses a magnetic dipole moment that is parallel or antiparallel to the spin angular momentum vector. In the example of a child's top shown above, the torque due to gravity causes the gyroscope to precess around the direction defined by the force of gravity. For a nucleus with spin angular momentum, an analogous torque is supplied by an external magnetic field acting on the nuclear magnetic moment, which results in the spin angular momentum vector precessing around the external field. NMR experiments are simply the measurement of this precession frequency. Nearly the entire power of NMR to chemists is hidden in this last sentence: the electronic environment and neighbouring nuclei cause the local field to deviate from the external field, thereby altering the precession frequency for each nucleus. It is this encoding of the local environment in the precession frequency that allows NMR measurements to provide chemical information.

2.2 Quantum Mechanical Description of Spin Angular Momentum

The theory of NMR begins with describing the set of operators that can be used to build the Hamiltonian. The spin angular momentum is a directional quantity, and is therefore described by a vector operator, $\hat{\boldsymbol{I}} = (\hat{I}_x, \hat{I}_y, \hat{I}_z)$, the scalar magnitude of which is given in the usual way: $||\hat{\boldsymbol{I}}|| = \sqrt{\hat{I}_x^2 + \hat{I}_y^2 + \hat{I}_z^2}$. The commutation relation-

ships for the components of $\hat{\boldsymbol{I}}$ can be used to determine the possible eigenvalues for total spin angular momentum;[6] the final result is that this observable can only take on certain, quantized values. The eigenvalues of $||\hat{\boldsymbol{I}}||$ that represent these values are

$$[I(I+1)]^{1/2}\hbar \qquad (\text{where } I = 0, \frac{1}{2}, 1, \frac{3}{2}, 2, \frac{5}{2}, ...) \ . \tag{2.1}$$

The total spin angular momentum of each elementary particle is a fixed property (at the energy levels used in NMR), and the quantum number I which describes this value is usually denoted as a particle's *spin*. For example, protons and electrons are both spin-$\frac{1}{2}$ particles: they are characterized by $I = \frac{1}{2}$, and their total spin angular momentum is $\frac{\sqrt{3}}{2}\hbar$.

While the total spin angular momentum of a particle is fixed, the orientation of this vector is free to move. I will start here with an isolated spin-$\frac{1}{2}$ particle, focusing first on the z-component of the vector. The commutation relationships can be used to show that $\hat{I}_z$ has two eigenvalues:[6] $m\hbar$; where $m = +\frac{1}{2}$ or $-\frac{1}{2}$. What exactly the two eigenfunctions that produce these eigenvalues are is less than clear; however, this turns out to be not too important for NMR, and we can simply call the function by the value of the quantum number m, i.e., the eigenfunctions are denoted as $|+1/2\rangle$ and $|-1/2\rangle$. We have thus determined two possible states for the system, where the two wave functions are eigenfunctions of both $\hat{\boldsymbol{I}}$ and $\hat{I}_z$. Measurement of $||\hat{\boldsymbol{I}}||$ yields $\frac{\sqrt{3}}{2}\hbar$ for either state, while measurement of $\hat{I}_z$ produces a different value for each: $+\frac{1}{2}\hbar$ for $|+1/2\rangle$ but $-\frac{1}{2}\hbar$ for $|-1/2\rangle$.

At this point it appears as if we are building up a picture of the orientation of $\boldsymbol{I}$ for this spin-$\frac{1}{2}$ particle, as we have a state for which we know the length of the vector and its z-component. However, a conceptual difficulty arises when we attempt to derive expectation values for the other two components of $\hat{\boldsymbol{I}}$ and find that both are zero when the particle is in the state $|+1/2\rangle$ or $|-1/2\rangle$, i.e., $\langle\hat{I}_x\rangle = \langle\hat{I}_y\rangle = 0$. What

does this mean then, that we have determined a possible state where we know both the length and z-component of $\hat{\boldsymbol{I}}$, but the average measurements of $\hat{I}_x$ and $\hat{I}_y$ will equal 0? In a classical system, the only way for this to be true in a fully specified system would be if $||\boldsymbol{I}|| = I_z$, but here we know $\langle \hat{I}_z \rangle = \pm\frac{1}{2}\hbar < \frac{\sqrt{3}}{2}\hbar = \langle \hat{I}^2 \rangle^{\frac{1}{2}}$. This is a general result in the quantum mechanical treatment of spin angular momentum: the particle has a well defined total spin angular momentum, but we can only observe a portion of this total.

It is an important point that $|+1/2\rangle$ and $|-1/2\rangle$ are not the only states a spin-$\frac{1}{2}$ particle can be in. For example, the wave function $|\psi_x\rangle = \frac{1}{\sqrt{2}}|+1/2\rangle + \frac{1}{\sqrt{2}}|-1/2\rangle$ is an eigenfunction of $\hat{I}_x$: measurement of $\boldsymbol{I}$ in the x direction is certain to yield $+\frac{1}{2}\hbar$, while $\langle \hat{I}_z \rangle = \langle \hat{I}_y \rangle = 0$. There is, of course, nothing special about the Cartesian axes, and it is possible to determine a wave function for which there is an expectation value of $+\frac{1}{2}\hbar$ in any selected direction, and indeterminate angular momentum in the perpendicular directions. An important example, that I will make use of in the next section, is the state $|\psi_\theta\rangle = cos(\theta/2)\,|+1/2\rangle + sin(\theta/2)\,|-1/2\rangle$ depicted in Figure 2.2A, which is an eigenfunction of the angular momentum operator along the vector in the x,z plane, at an angle θ to the z-axis. A useful piece of terminology is to say that the system is *quantized* or *polarized* along the direction for which measurement of angular momentum is an eigenvalue.

2.3 Spin-$\frac{1}{2}$ Particle in an Externally Applied Magnetic Field

As always, we begin a problem in quantum mechanics by writing the Hamiltonian operator. The first step is to define the magnetic dipole moment of the particle, as this is what interacts with the externally applied magnetic field. For a nucleus with spin, the magnetic dipole moment is a simple multiple of the spin angular

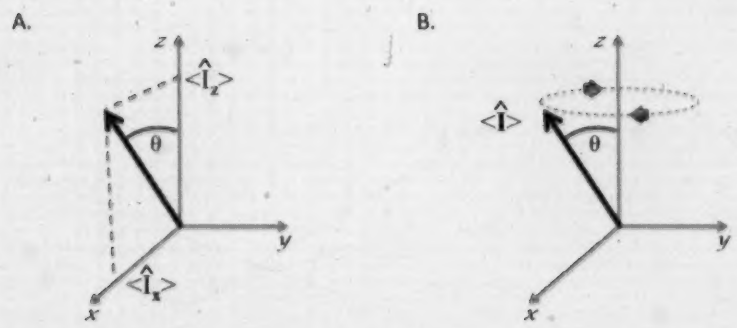

Figure 2.2: A. Representation of the state $|\psi_\theta\rangle = cos(\theta/2)\,|+1/2\rangle + sin(\theta/2)\,|-1/2\rangle$, in which $\langle \hat{I}_z \rangle = cos(\theta)\frac{1}{2}\hbar$, $\langle \hat{I}_x \rangle = sin(\theta)\frac{1}{2}\hbar$, $\langle \hat{I}_y \rangle = 0$. B. Under the effect of a magnetic field along the z-axis, $\langle \hat{\boldsymbol{I}} \rangle$ precesses about the applied field, with the tip following the depicted circular path. Indicated direction of precession is for a nucleus with positive γ.

momentum:

$$\hat{\boldsymbol{\mu}} = \gamma \hat{\boldsymbol{I}}\,, \tag{2.2}$$

where $\hat{\boldsymbol{\mu}}$ is the magnetic dipole moment operator, and γ is the magnetogyric ratio (a rather unimaginative name for this proportionality constant which, incidentally, is different for each nuclear isotope that possesses spin). The Hamiltonian operator is given by:

$$\begin{aligned} \hat{\mathscr{H}} &= -\hat{\boldsymbol{\mu}} \cdot \boldsymbol{B}^0 \\ &= -\gamma \hat{\boldsymbol{I}} \cdot \boldsymbol{B}^0\,, \end{aligned} \tag{2.3}$$

where $\boldsymbol{B}^0$ is the externally applied field.

As an example, I will now examine the time behaviour of a spin-$\frac{1}{2}$ particle that is initially quantized along the direction shown in Figure 2.2A, i.e., $|\psi\rangle\,(t=0) = cos(\theta/2)\,|+1/2\rangle + sin(\theta/2)\,|-1/2\rangle$, when exposed to a magnetic field defined by $\boldsymbol{B}^0 = (0, 0, B^0)$. The initial wavefunction is not an eigenfunction of the Hamiltonian,

so the system is time dependent, and it can be shown that the expectation values for angular momentum are given by:[6]

$$\begin{aligned} \langle \hat{I}_x \rangle(t) &= \tfrac{1}{2}\hbar \, sin(\theta) cos(\omega t) \\ \langle \hat{I}_y \rangle(t) &= \tfrac{1}{2}\hbar \, sin(\theta) sin(\omega t) \\ \langle \hat{I}_z \rangle(t) &= \tfrac{1}{2}\hbar \, cos(\theta) \, . \end{aligned} \tag{2.4}$$

In Equation 2.4, θ is defined as shown in Figure 2.2A, and ω is the angular frequency $\omega = -\gamma B^0$. This is an interesting solution: we find that the z-component is stationary, while the expectation values for $\langle \hat{I}_x \rangle(t)$ and $\langle \hat{I}_y \rangle(t)$ rotate about the applied field. Note that for a nucleus with positive γ, the spin angular momentum vector precesses about the applied magnetic field in the direction that the fingers of the left hand curl when the thumb is aligned with the field (see Figure 2.2B). This quantum system behaves analogously to the classical one: a torque acting on a system possessing angular momentum leads to precession. The difference in this quantum system is that it is the vector of expectation values that precesses, rather than the total angular momentum vector itself. It is apparent from these solutions that the rate of precession depends on the strength of the coupling with the applied field, which depends on *(a)* the particle's identity, because different particles of the same total spin angular momentum have different magnetic dipole moments, see Equation 2.2, and *(b)* the effective field, because different chemical environments will be characterized by unique local fields, see Chapter 3.

2.4 Ensemble of Spin-$\frac{1}{2}$ Nuclei in a Magnetic Field

Up to this point I've discussed only an isolated nuclear spin, but a sample used for NMR experiments contains something more on the order of Avogadro's number of these spins. The lone spin-$\frac{1}{2}$ solution given in equation 2.4 describes how a spin,

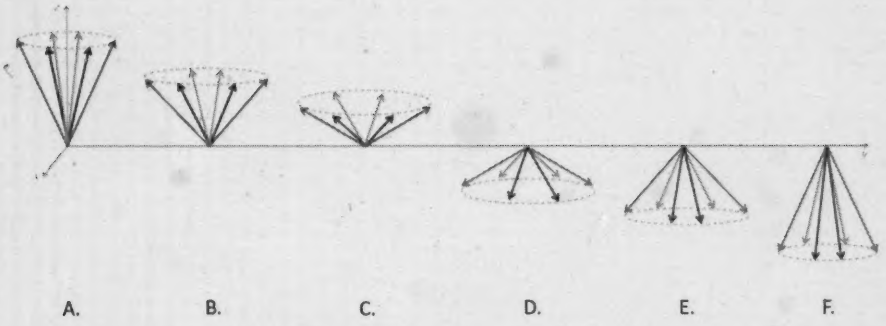

Figure 2.3: The nuclear magnetic moment orientations for an ensemble of spin-$\frac{1}{2}$ nuclei is the sum of the sets of vectors shown.

initially polarized in the z,x plane at an angle θ to the z-axis, precesses about the applied magnetic field. This precession behaviour will be followed by all the other spins in the sample except that their initial polarization direction will be related by a rotation around the z-axis, and a different value of θ. An important point to note is that because the magnetic field is invariant to rotations about the z-axis, the distribution of magnetic dipoles must also be, i.e., $\langle \hat{I}_x \rangle_{(ensemble)} = \langle \hat{I}_y \rangle_{(ensemble)} = 0$. The total distribution is illustrated in rough form in Figure 2.3: for each value of θ, there is an even distribution of magnetic dipoles over a circle. Of course, in a real system, each circle is populated by many more dipoles, and θ is a smooth, not a stepwise, distribution. Also, the set of orientations depicted in Figure 2.3 are *initial* orientations—the whole set precesses around the z-axis at the same rate.

Unlike the even distribution in the x and y directions, the θ distribution is biased because the total energy depends on this angle: the orientations[a] aligned partially with the field (Figure 2.3A-C) are more heavily populated than those aligned against it (Figure 2.3D-F). Because density matrix theory is naturally adapted to working with large numbers of spins, it is the standard method to determine this ratio, and

[a] Note that I am referring to the orientation of the nuclear magnetic moment here, the orientation of the related spin angular momentum can be parallel or antiparallel to this, depending on the sign of γ.

it can be shown that the competing influences of orientation energy and thermal energy result in a very small net polarization along the applied field.[7] The magnetic dipole moment of a single spin-$\frac{1}{2}$ nucleus polarized along the z-axis is different from that of an ensemble average of these spins:

$$\langle \hat{u}_z \rangle = \quad \tfrac{1}{2}\gamma\hbar \qquad \text{isolated spin in } |+1/2\rangle \text{ state;} \tag{2.5}$$

$$\langle \hat{u}_z \rangle = \tfrac{1}{2}\gamma\hbar \cdot \left(\tfrac{\hbar\gamma B_0}{2k_B T}\right) \qquad \text{per spin in equilibrium ensemble of spins.} \tag{2.6}$$

For example, an ensemble of protons at room temperature in an 11.75 T magnet behaves as if each nucleus was polarized with $\sim 4 \times 10^{-5}$ the net magnetic moment of a single proton in the $|+1/2\rangle$ state. Alternatively, and more commonly in introductory courses, this ensemble could be viewed as if for every 25,001 protons, 12500 are aligned against the field, and 12501 are aligned with the field.[b] However, it should be realized that the axis of polarization is unique for each spin, and the ensemble of spins have their orientations arrayed over a sphere, with a slight bias towards the lower energy end of the sphere.

2.5 Observation of the NMR Signal: Case of Spin-$\frac{1}{2}$ Nuclei

We now have a description of an ensemble of spin-$\frac{1}{2}$ nuclei in a magnetic field, the net result being a static polarization of the magnetic dipoles along the z-axis. However, this nuclear magnetization is difficult to observe. The usual method of extracting the frequency information is to rotate the macroscopic nuclear magnetic

[b] The picture of a spin ensemble as an array of orientations happens to be the one I prefer, and I've included it here (and designed the preceding sections) in an attempt to provide some background and a little bit more rigour to the analogous pictorial description in Levitt's textbook, *Spin Dynamics*.[8] Hopefully, this description also leads naturally into the density matrix theory discussion of individual spin polarization versus coherence in Appendix 8 of Hore, Jones, and Wimperis' primer.[9]

polarization perpendicular to the axis of the external field, where, by the arguments in the preceding sections, it will precess at the rate $\omega = -\gamma B^0$ (which is in the tens to hundreds of MHz in most applications of NMR). Ignoring the mechanism of this rotation for a moment, the ω precession frequency is measured as an alternating current, induced by the rotating bulk nuclear magnetic dipole moment, in a cylindrical coil of wire wrapped around the sample. This entire process can be accomplished using some complicated, but commercial, hardware. Because the electronic components of an NMR spectrometer (and their inter-operation) are explained lucidly by many authors, e.g., reference 8, I will not reproduce all of the details here. However, I will present some justification for the mechanism used in rotating the macroscopic nuclear magnetic polarization in this Section, and some details of signal analysis in Section 2.6.

The rotation of polarization is performed using the coil of wire, mentioned above as a detector, to perturb the sample. A radiofrequency pulse of alternating current passed through the coil induces a time-dependent magnetic field, B^1, in the volume contained by the coil. Note that this B^1 field is much weaker than the still-present B^0 field, whose time independence leads to its usual name as the static field. With the geometry shown in Figure 2.4A, the generated B^1 field is the same at every point in the y-direction. We can therefore focus on just one horizontal slice (i.e., a slice in the x,y plane) through the coil, and the time dependence of the field in one such slice is shown in Figure 2.4B. Note that I haven't drawn an entire cross-section, just a circle in the centre of the sample. In Figure 2.4B, it is shown how the B^1 field is described as the sum of two magnetic field vectors, constant in length, that rotate in opposite directions. In an NMR experiment, we match the rotation frequency of the B^1 field to the precession frequency of the nuclear magnetic moments. This matching of frequencies results in the situation displayed in Figure 2.4C, where the constant relative orientation between the nuclear spin quantization axis and one

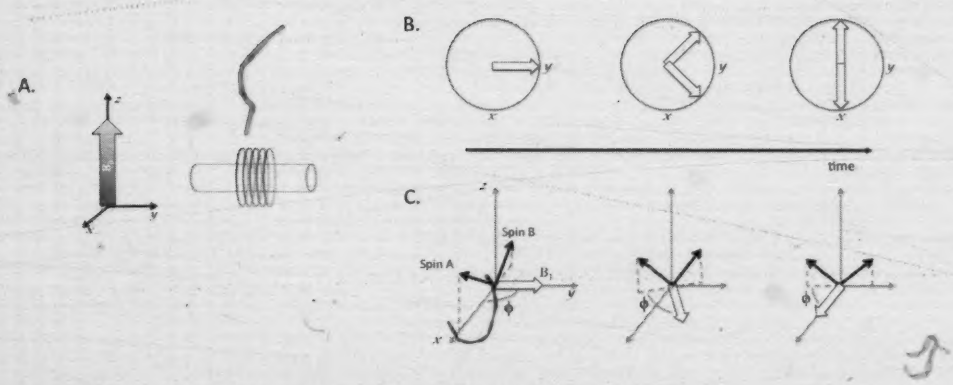

Figure 2.4: A. Orientation of the cylindrical sample, coil, and external magnetic field, B^0. B. The two components of the B^1 field are depicted in a horizontal slice through the centre of the coil and sample shown in part A. C. Demonstration of the fixed relationship between the orientation of the nuclear magnetic moments, $\langle\hat{\boldsymbol{\mu}}\rangle(t)$, and one component of the B^1 field.

component of the B^1 field is demonstrated. Note that the second, counter-rotating B^1 component is omitted from Figure 2.4C because it is ineffectual (the second component is off-resonance: the orientation with respect to $\langle\hat{\boldsymbol{\mu}}\rangle(t)$ is continually changing).

Because of the fixed orientation between $\langle\hat{\boldsymbol{\mu}}\rangle(t)$ and $B^1(t)$, there is a constant torque on the nuclear spin, and therefore $\langle\hat{\boldsymbol{\mu}}\rangle(t)$ precesses about the B^1 field. Recalling the left-handed sense of precession described in Section 2.3 for a spin with positive γ, Spin A of Figure 2.4C is constantly being pushed up towards the $+z$-axis, while Spin B is pushed downwards to the $-z$-axis. Because Spin A and Spin B are really just two members forming the "ring" of spins in Figure 2.3A, one period of precession around B^0 will result in the ring formed by these vector tips being tilted downwards toward the $-x$ axis. And, of course, the same thing will happen to each of the "rings" in Figure 2.3. The result of a radiofrequency pulse is thus to tilt the z-axis magnetization downwards toward the $-z$-axis. The expression for the rate of this precession around the B^1 field is the same as that shown above for precession

around the static external field:

$$\omega_{pulse} = -\gamma B^1 \,. \tag{2.7}$$

Therefore, the z-magnetization can be placed in the x,y plane using pulsed rf radiation of a suitable magnitude and pulse length. This 90 degree rotation of the polarization has lead to the familiar term "$\pi/2$ pulse." Once in the x,y plane, the precessing bulk magnetic moment will induce a detectable current in the coil as the magnetization precesses around the static field. As one final side note, a pulse length double that of a $\pi/2$ pulse yields polarization along the $-z$-axis, which is a population inversion of the initial thermal-equilibrium magnetization.

2.6 Analyzing the NMR Signal: Fourier Transforms

The NMR signal, an alternating current that is detected in a circuit attached to the coil, is passed on to the spectrometer computer in the format of amplitude versus time, $a(t)$, generally as a series of complex (real + imaginary) data points. Different nuclear sites precess at different frequencies, so interpretation of the signal is greatly facilitated through determination of its frequency components. A Fourier transform, or FT, is the usual method used to extract the frequency contributions to the time-domain signal, and this procedure is depicted symbolically in Figure 2.5. The following discussion provides a mathematical explanation of the FT, a more conceptual approach has been given by Levitt, in *Spin Dynamics*.[8] While the mathematics involved are nothing new, I think that some insight can be gained by working through the derivation. In particular, I think it is enlightening to derive the theory using the terminology and proofs of linear algebra that are familiar to chemists from electronic structure theory.

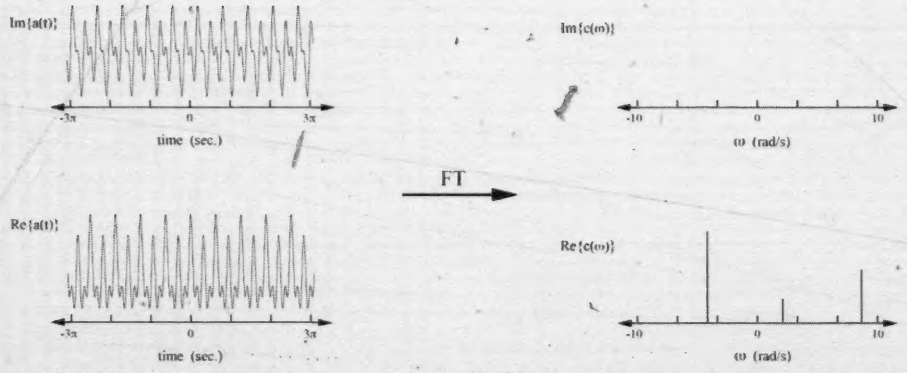

Figure 2.5: Example of a Fourier transform, where $\mathrm{Re}\{f\}$ indicates the real part of the function f, while $\mathrm{Im}\{f\}$ is the corresponding imaginary component. In this example, the frequency representation is much simpler than the time-domain signal. For definitions of the functions, see Section 2.6.1.

2.6.1 Theory of Fourier Transforms

Fourier transformation is an example of the change of basis seen frequently in quantum mechanics. Specifically, we use as a basis for the function space that $a(t)$ resides in, the set of functions:[c]

$$\begin{aligned} b_\omega(t) &= \frac{1}{\sqrt{2\pi}}[cos(\omega t) + i\, sin(\omega t)] \qquad \text{where } \omega \in \mathbb{R} \\ &= \frac{1}{\sqrt{2\pi}} e^{+i\omega t}. \end{aligned} \tag{2.8}$$

This choice of basis is useful because these are periodic functions with different frequencies, ω, and expression in this basis will therefore provide us with a measure of the frequency distribution in $a(t)$. In the following, note that I will use both function notation and Dirac notation: $a(t) \equiv |a\rangle$, and $b_\omega(t) \equiv |b_\omega\rangle$. Expansion of a vector in terms of a *discrete* basis would be given by a sum over the basis functions,

[c] See pages 100 - 103 of D. J. Griffiths for a similar derivation, albeit one in a different context, including some notes on the mathematical validity of using non-normalizable functions as the basis for a function space.[6]

e.g.,

$$|v\rangle = \sum_{i=0}^{n} c_i \, |i\rangle \ , \tag{2.9}$$

but here we have a continuous set of basis functions, so the sum becomes an integral:

$$|a\rangle = \int_{-\infty}^{\infty} c_\omega \, |b_\omega\rangle \, \mathrm{d}\omega \, . \tag{2.10}$$

Equation 2.10 expresses the formal definition of the signal amplitude, $a(t)$, in terms of frequency components, $b_\omega(t)$. The task of a Fourier transform is to determine the coefficients, c_ω, as these encode the contributions of the different basis functions, which are at different frequencies, to the signal. For example, if we want to know the contribution of the function $\frac{1}{\sqrt{2\pi}}[cos(\lambda t) + i\, sin(\lambda t)]$, at frequency λ rad/s, we need to calculate the coefficient c_λ. The general coefficient c_λ can be calculated through multiplication of Equation 2.10 from the left by $\langle b_\lambda|$, i.e.,

$$\langle b_\lambda | a \rangle = \int_{-\infty}^{\infty} c_\omega \, \langle b_\lambda | b_\omega \rangle \, \mathrm{d}\omega \, , \tag{2.11}$$

and simplifying by exploiting the "orthonormality"[6] of the basis functions:

$$\begin{aligned} \langle b_\lambda | b_\omega \rangle &= \int_{-\infty}^{\infty} b_\lambda^*(t) \, b_\omega(t) \, \mathrm{d}t \\ &= \int_{-\infty}^{\infty} \frac{1}{\sqrt{2\pi}} e^{-i\lambda t} \, \frac{1}{\sqrt{2\pi}} e^{+i\omega t} \, \mathrm{d}t \\ &= \delta(\omega - \lambda) \, , \end{aligned} \tag{2.12}$$

which results in Equation 2.11 being reduced to

$$\begin{aligned} \langle b_\lambda | a \rangle &= \int_{-\infty}^{\infty} c_\omega \delta(\omega - \lambda) \, \mathrm{d}\omega \\ &= c_\lambda \, . \end{aligned} \tag{2.13}$$

This simple equation is the final answer, but I'll write it out in a more familiar form and spell out what it means a little more clearly. Switching back to the more common ω for the index, Equation 2.13 becomes the familiar expression for the Fourier transform:

$$\begin{aligned} c_\omega \equiv c(\omega) &= \langle b_\omega | a \rangle \\ c(\omega) &= \int_{-\infty}^{\infty} \frac{1}{\sqrt{2\pi}} e^{-i\omega t}\, a(t)\, \mathrm{d}t\,. \end{aligned} \tag{2.14}$$

I've also swapped out c_ω in favour of $c(\omega)$, because Equation 2.14 is valid for any ω: evaluation of the integral yields the complete set of coefficients as a function of ω.

To make this a little clearer, let us define an example signal amplitude, $a_{ex}(t)$, as a sum of polynomials:

$$a(t) = \sum_{n=0}^{\infty} k_n\, t^n\,. \tag{2.15}$$

Let us imagine that $a_{ex}(t)$ is defined by some set of thousands of k_n coefficients such that when we solve Equation 2.14, i.e., the FT of $a_{ex}(t)$, we find

$$c(\omega) = \begin{cases} 3 & \text{if } \omega = -4 \\ 1 & \text{if } \omega = +2 \\ 2 & \text{if } \omega = +8 \\ 0 & \text{otherwise}\,. \end{cases} \tag{2.16}$$

These coefficients, by Equation 2.10, show that an alternate representation of our example signal amplitude is given by:

$$a_{ex}(t) = 3\, e^{-i4t} + 1\, e^{+i2t} + 2\, e^{+i8t}\,. \tag{2.17}$$

In other words, $a(t)$ can be expressed as the sum of three functions which are periodic, and which oscillate at the rates -4, 2 and 8 rad/s. The Fourier transform

of $a_{ex}(t)$ is the one depicted graphically in Figure 2.5. It is often stated that a FT converts a function of time into a function of frequency, and the above example illustrates more clearly what this means: a Fourier transform does correlate a function of frequencies, $c(\omega)$, with a function of time, $a(t)$, but $c(\omega)$ is really just a set of coefficients for time functions, Equation 2.8, which recreate the original $a(t)$.

2.6.2 The Discrete Fourier Transform

The theory outlined above applies to a time-domain signal that is defined at all times ($t = -\infty$ to $+\infty$), and is measured continuously in time—an obvious impossibility. In practice, the signal is digitized with one (complex-valued) intensity point collected every sampling interval, τ_d. The obvious treatment of such data is to replace the improper integral of Equation 2.14 with a finite sum, and calculate one of these sums for each value of frequency (ω) desired. This is indeed the approach that is taken, but the ramifications in terms of the information lost or retained are not completely obvious. One important point is that only a certain *bandwidth*, B, of frequencies is defined when a sampling interval τ_d is used:[10]

$$B = \tau_d^{-1} \quad , \tag{2.18}$$

(assuming complex data pairs are acquired). Any frequency functions outside of this bandwidth still contribute to the discrete $c(\omega)$, but are aliased to a different position. A second important note is that, using a specific sampling interval, increasing the total time the signal is acquired has the effect of more accurately resolving the resultant spectrum–a simple restating of the fact that a complicated, multi-frequency spectrum cannot be fully represented if only a handful of time-domain data is acquired.

2.7 Summary

The preceding sections of this chapter provide a description of the fundamentals of NMR spectroscopy. It is hoped that this discussion is helpful when viewing later chapters, despite the fact that space considerations limited the description to an extremely brief version. The simplified picture can be summarized as follows: a sample of nuclei possessing spin is placed in an external magnet, where a delay time allows bulk nuclear polarization to develop, after which a radio frequency pulse causes the polarization axis to tilt downwards into the plane perpendicular to the applied field, where precession of this state leads to a time-domain signal that is analyzed in terms of frequency components using a Fourier transform. With this schematic in hand, I will now move on in the next chapter to discuss how the fundamental NMR interactions act as perturbations on the system, and how this provides chemical information to the spectroscopist - specifically, the type of information obtained in the experimental chapters of the thesis. Further details regarding magnetic resonance theory and spectrometer operation/construction that I was not able to capture in the length of this chapter can be found in any one of a number of introductory textbooks.[8,10–16]

Chapter 3

The NMR Interactions and NMR Spectral Analysis

The discussion in the previous chapter dealt with completely isolated, non-interacting nuclei in a strong external magnetic field. In this chapter, I will introduce the other interactions that affect the nucleus: shielding of the nucleus from the external magnetic field, two mechanisms for coupling between nuclei, and interaction of the nuclear electric quadrupole moment with the electric field gradient of the molecular environment. The main objective of the research chapters of this thesis is measurement of these interactions, coupled in ideal cases with an improved understanding of the interaction itself or the chemistry of the system. In the remainder of this chapter, the physics of each interaction are described, as are conventions used to report them. Limited examples designed to clarify either the interaction descriptions or the methods of spectral analysis will also be included. A brief summary of some NMR experimental techniques and the results of their application are also included.

3.1 Magnetic Shielding

3.1.1 The Shielding Interaction

For the purposes of discussing magnetic shielding, a molecule in which only one nucleus has spin angular momentum will be used as the system. Furthermore, only molecules in which all the electrons are spin paired, i.e., diamagnetic molecules, will be considered here. When such a molecule is placed in a magnetic field, the electron's charge and momentum causes them to be subject to the Lorentz force. The net result of this force is the induction of an electric current density in the molecule, which leads to a *response* magnetic field, according to the Biot-Savart law. Because this response field most often opposes the externally applied one (thereby lowering the total field), the effect is commonly termed magnetic shielding. In this Section, I will focus on the effects of magnetic shielding; further discussion and references regarding the physics of the electronic current density is provided in Chapter 6.

Theoretical derivation of the effect of an external magnetic field on the electronic wavefunction shows that each of the three components of the response magnetic field vector, $\boldsymbol{B}^R$, have a contribution which is linearly proportional to each of the three components of the applied magnetic field, $\boldsymbol{B}^0$. This makes nine total proportionality constants, which form a 3×3 matrix, known as a 2^{nd}-rank tensor. This magnetic shielding tensor is labelled with the symbol $\underline{\boldsymbol{\sigma}}$, and the response magnetic field is therefore given by:[11]

$$\boldsymbol{B}^R = -\underline{\boldsymbol{\sigma}}\boldsymbol{B}^0 \tag{3.1}$$

$$(B_x^R, B_y^R, B_z^R) = -\begin{pmatrix} \sigma_{xx} & \sigma_{xy} & \sigma_{xz} \\ \sigma_{yx} & \sigma_{yy} & \sigma_{yz} \\ \sigma_{zx} & \sigma_{zy} & \sigma_{zz} \end{pmatrix} \begin{pmatrix} B_x^0 \\ B_y^0 \\ B_z^0 \end{pmatrix}.$$

Making the total magnetic field:

$$\begin{aligned} \boldsymbol{B}^T &= \boldsymbol{B}^0 + \boldsymbol{B}^R \\ &= (1 - \underline{\boldsymbol{\sigma}})\boldsymbol{B}^0 . \end{aligned} \tag{3.2}$$

Note that this means the Hamiltonian operator, and therefore the behaviour of the system, is really the same as that discussed in Chapter 2 for a spin in a vacuum, the only difference being that we first have to calculate the static field present using Equation 3.2. The spin still precesses about the field, but the precession frequency is slightly different from the precession frequency of a bare nucleus. In anticipation of the chemical usefulness of the components of $\underline{\boldsymbol{\sigma}}$, I will now go on to discuss some features of this tensor.

It can usually be assumed that the magnetic shielding tensor is symmetric across the lead diagonal, i.e., $\sigma_{ij} = \sigma_{ji}$ (see Chapter 7 for a discussion of when this assumption is not valid). Like any real, symmetric matrix, $\underline{\boldsymbol{\sigma}}$ can be diagonalized through a change of basis. This means that in a specific axis system, known as the principal axis system or PAS, all off-diagonal elements of the tensor are zero. By convention,[17] the three tensor elements in the PAS are given the labels $\sigma_{xx}^{\mathrm{PAS}} = \sigma_{11}$, $\sigma_{yy}^{\mathrm{PAS}} = \sigma_{22}$, $\sigma_{zz}^{\mathrm{PAS}} = \sigma_{33}$, where $\sigma_{11} \leq \sigma_{22} \leq \sigma_{33}$. The tensor is not fully specified unless the three angular degrees of freedom required to express the orientation of the PAS are given. An interesting note is that the three tensor elements in the PAS are the eigenvalues of the tensor; accordingly, if the external field is applied along any one axis of the PAS, the response field defined by Equation 3.1 is parallel to it. This behaviour is in contrast to the general case, where $\boldsymbol{B}^R$ is at some angle to $\boldsymbol{B}^0$.

There are six independent pieces of data in a symmetric tensor, and a multitude of systems are in use for reporting the principal components of $\underline{\boldsymbol{\sigma}}$. Part of the reason for having multiple convention systems is likely the different preferences of

each spectroscopist, but there are also benefits to having more than one system. For example, in systems of higher symmetry, one may choose to use the equivalent set of three variables:[17] the isotropic (orientationally averaged) value, $\sigma_{\text{iso}} = \frac{1}{3}(\sigma_{11} + \sigma_{22} + \sigma_{33})$, the span, $\Omega = \sigma_{33} - \sigma_{11}$, and the skew, $\kappa = 3(\sigma_{\text{iso}} - \sigma_{22})/\Omega$.

Often, the goal of an NMR experiment is to measure each component (σ_{11}, σ_{22}, and σ_{33}), as well as the orientation of the PAS. Site symmetry may further reduce the total number of data points needed to describe the magnetic shielding, e.g., a spherically symmetric environment produces the same shielding for any orientation of the applied magnetic field and therefore the shielding tensor has only one independent component ($\sigma_{11} = \sigma_{22} = \sigma_{33}$). Symmetry rules can also provide information about the orientation of the PAS. Constraints on the number of independent elements of $\underline{\boldsymbol{\sigma}}$ in environments exhibiting any symmetry element may be derived from Neumann's principle,[18] and the well known rules are reproduced in Table 3.1.[19–21] Listings in the Table also show when off-diagonal elements are zero in the axis system of convention for each point group; therefore, the listings provide information about the orientation of the PAS (of the symmetric portion of $\underline{\boldsymbol{\sigma}}$).

3.1.2 Effects of Shielding on NMR Spectra

Because the analysis in Chapter 2 shows that the nuclear spin angular momentum axis precesses at the frequency $\omega = -\gamma\,||\boldsymbol{B}||$, we would like to find the value of $||\boldsymbol{B}||$ including the magnetic shielding. In the PAS of the shielding tensor, Equation 3.2 allows us to determine the magnitude of $\boldsymbol{B}^T$ as

$$||\boldsymbol{B}^T|| = \left[\left(B_x^0(1-\sigma_{11})\right)^2 + \left(B_y^0(1-\sigma_{22})\right)^2 + \left(B_z^0(1-\sigma_{33})\right)^2\right]^{\frac{1}{2}} . \qquad (3.3)$$

Switching to spherical coordinates for the components of $\boldsymbol{B}^0$, and dropping any terms involving the very small products of the form $\sigma_{ii}\sigma_{jj}$, leads to a simpler form

Table 3.1: Symmetry Requirements for $\underline{\boldsymbol{\sigma}}$ Elements

Point Group[a]	Number of Elements		Non-zero Elements[b]
	Total	Independent	
T, T_h, T_d, O, O_h, K_h	3	1	$\sigma_{zz} = \sigma_{yy} = \sigma_{xx}$
D_4, D_{4h}, D_6, D_{6h}, $D_{\infty h}$, D_{2d}, D_3, D_{3d}, D_{3h}, C_{3v}, C_{4v}, C_{6v}, $C_{\infty v}$	3	2	σ_{zz}, $\sigma_{yy} = \sigma_{xx}$
C_{2v}, D_2, D_{2h}	3	3	σ_{zz}, σ_{yy}, σ_{xx}
C_3, C_{3h}, C_4, C_6, C_{6h}, S_4, S_6	5	3	σ_{zz}, $\sigma_{yy} = \sigma_{xx}$, $\sigma_{yx} = -\sigma_{xy}$
C_2, C_s, C_{2h}	5	5	σ_{zz}, σ_{yy}, σ_{xx}, σ_{yx}, σ_{xy}
C_1, C_i	9	9	all

[a]Symmetries defined in relation to the nucleus to be observed, not the total symmetry of the molecule or environment.

[b]When represented in the usual axis system for each point group. The full antisymmetric nature of the tensor is considered.

of the equation,

$$||\boldsymbol{B}^T|| = ||\boldsymbol{B}^0|| \left[1 - (\sin^2\theta\cos^2\phi)\sigma_{11} + (\sin^2\theta\sin^2\phi)\sigma_{22} + (\cos^2\theta)\sigma_{33}\right] , \quad (3.4)$$

where θ is the polar angle and ϕ is the azimuthal angle. The precession frequency can therefore be given as:[11]

$$\begin{aligned} \omega(\theta,\phi) &= -\gamma||\boldsymbol{B}^T|| \\ &= \omega_{\text{L}} - \omega_{\text{L}}\left[(\sin^2\theta\cos^2\phi)\sigma_{11} + (\sin^2\theta\sin^2\phi)\sigma_{22} + (\cos^2\theta)\sigma_{33}\right] , \end{aligned} \quad (3.5)$$

where ω_{L} is the Larmor frequency, i.e., the precession frequency in the absence of shielding, $-\gamma\,||\boldsymbol{B}^0||$. Equation 3.5 shows how, for any specific orientation of $\boldsymbol{B}^0$ in the molecule, the frequency is shifted from the natural precession frequency of the

nucleus by $\underline{\sigma}$. It is also worth noting that the form of Equation 3.5 demonstrates that the amount the peaks are shifted is directly proportional to the applied field.

Now that we have covered how magnetic shielding affects the observed frequency, we can discuss how the components of $\underline{\sigma}$ can be determined from an experiment. As a thought experiment, let us take a powder of microcrystals as our sample, specifically, one with only one nmr-active nucleus in a single unique site. Let us imagine that we place this sample in a suitable NMR spectrometer, allow it come to thermal equilibrium polarization, and finally operate on it with a $\pi/2$ pulse and record the precession signal. Furthermore, let us also assume that this sample is big enough, as is the usual case, that each θ,ϕ orientation of the molecule is populated by enough sites that the description of total magnetization developed in Chapter 2 is valid. The contribution to the signal from each orientation of the molecule in the magnetic field is given by Equation 2.4, i.e.,

$$\langle \hat{I}_x \rangle(t) + i\langle \hat{I}_y \rangle(t) = A\left[\cos\left(\omega(\theta,\phi)t\right) + i\sin\left(\omega(\theta,\phi)t\right)\right] . \tag{3.6}$$

Here, we are assuming that the signal amplitude, A, produced from each orientation is the same, because there are no preferential alignments. The total signal is then given by integrating over θ and ϕ:

$$a(t) = \int_0^{\pi}\int_0^{2\pi} Ae^{+i\omega(\theta,\phi)t}\,\sin\theta\,\mathrm{d}\theta\mathrm{d}\phi\,. \tag{3.7}$$

Fourier transformation of this signal, following Equation 2.14, yields:

$$c(\lambda) = \int_{-\infty}^{\infty} \frac{1}{\sqrt{2\pi}} e^{-i\lambda t}\left[\int_0^{\pi}\int_0^{2\pi} Ae^{+i\omega(\theta,\phi)t}\,\sin\theta\,\mathrm{d}\theta\mathrm{d}\phi\right]\mathrm{d}t\,, \tag{3.8}$$

which, by Equation 2.12, is equal to:

$$c(\lambda) = A\sqrt{2\pi}\int_0^{\pi}\int_0^{2\pi} \delta\Big(\lambda - \omega(\theta,\phi)\Big)\,\sin\theta\,\mathrm{d}\theta\mathrm{d}\phi\,. \tag{3.9}$$

Equation 3.9 is the not very surprising result that the graph of $c(\lambda)$ has a peak of height A for each frequency in the range of $\omega(\theta,\phi)$, but is zero otherwise.

I'll use a concrete example to make this a little clearer, choosing everyone's favourite molecule, ethanol, as the material. To simplify the problem, I'll assume we have engineered the system in such a way that the methyl carbon is the spin-$\frac{1}{2}$ nucleus ^{13}C, while all other nuclei do not affect the spectrum. In Figure 3.1 is presented a theoretical spectrum of a frozen glassy sample of ethanol, i.e., one containing all possible orientations of the molecule. In preparing this Figure, I've switched out of angular frequency to the more common Hz, and used a theoretical magnetic field such that $\nu_{\mathrm{L}} = 100$ MHz. The components of the shielding tensor for this molecule have been published[22,23] as $\sigma_{11} = 149$ ppm, $\sigma_{22} = 165$ ppm, and $\sigma_{33} = 180$ ppm (where ppm = parts per million $\equiv 10^{-6}$). The NMR spectrum, $c(\lambda)$ of Equation 3.9, is plotted via numerical integration[24] to yield Figure 3.1. Note how the molecular environment causes the peak from each crystallite to be shifted to lower absolute frequency than what would be observed for the same nucleus in a vacuum, ν_{L}. Furthermore, the three discontinuities in the lineshape, labelled ν_{11}, ν_{22} and ν_{33}, are the frequencies observed when the magnetic field is along each of the three vectors that compose the principal axis system of $\underline{\boldsymbol{\sigma}}$:

$$\nu_{ii} = \nu_{\mathrm{L}} - \nu_{\mathrm{L}}\sigma_{ii}\,. \tag{3.10}$$

This form of the spectrum makes it easy to very simply determine the values of the three principal components of the magnetic shielding tensor, providing ν_{L} is known.

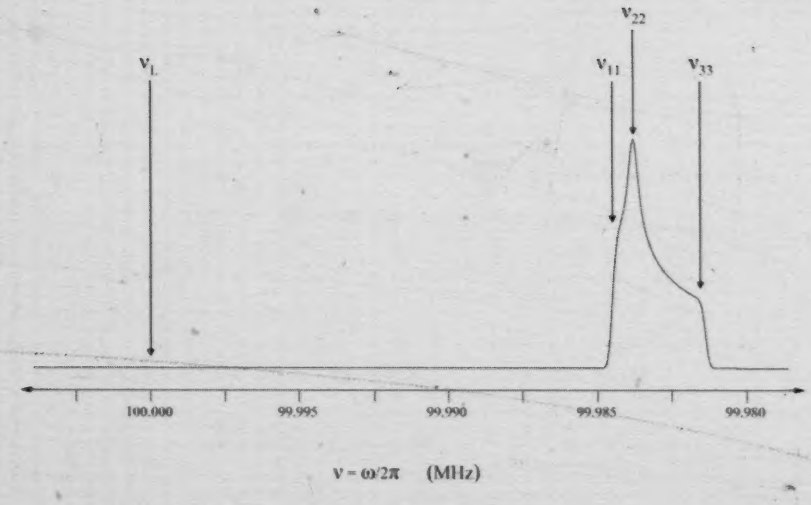

Figure 3.1: Theoretical ^{13}C NMR spectrum of a glassy sample of ethanol; absolute frequency scale.

3.1.3 Setting a Zero on the Scale; Chemical Shifts

Rather than plotting NMR spectra in terms of absolute frequency, it is more common to display spectra in terms of the fractional difference from a reference signal. Continuing with the example of a ^{13}C spectrum of ethanol, the accepted reference compound is neat, liquid tetramethylsilane (TMS), which produces a single sharp resonance. Consider what happens if, instead of plotting ν^{sample} directly, we plot the *chemical shift*, δ, using the definition:[17]

$$\delta(^{13}\mathrm{C}) = \frac{\nu^{sample} - \nu^{TMS}}{\nu^{TMS}}, \tag{3.11}$$

where ν^{TMS} is the frequency of the ^{13}C resonance from TMS. Because the fractional differences in frequency are very small, plots of δ usually use a ppm scale. Displayed in Figure 3.2 is the spectrum from Figure 3.1, but using the chemical shift scale. Because the reference sample is a liquid, it exhibits only one peak at ν^{TMS} =

$\nu_L - \nu_L\sigma^{TMS}$; furthermore, Equation 3.5 shows that any peaks from the sample occur at $\nu^{sample}(\theta,\phi) = \nu_L - \nu_L\,\sigma^{sample}(\theta,\phi)$. Therefore, NMR peaks occur on the chemical shift plot at

$$\delta(^{13}\mathrm{C}) = \frac{\sigma^{TMS} - \sigma^{sample}(\theta,\phi)}{1 - \sigma^{TMS}}\,. \tag{3.12}$$

Because the magnitude of σ^{TMS} is much, much smaller than 1, Equation 3.12 can often be approximated as

$$\delta(^{13}\mathrm{C}) \approx \sigma^{TMS} - \sigma^{sample}\,. \tag{3.13}$$

The form of Equation 3.13 highlights the fact that a chemical shift measures the difference in magnetic shielding from the reference compound. One benefit of using chemical shifts is that differences in frequency (see Equation 3.11) can be determined much more accurately than can absolute shieldings, given that the latter depends on the much less accurate value of ν_L. Since most of the chemical information contained in magnetic shieldings is derived from differences in shielding between environments anyway, the chemical shift scale is a natural choice.

From the above discussion, it may be surmised that the magnetic shielding tensor, $\underline{\boldsymbol{\sigma}}$, can be replaced by the alternate chemical shift tensor, $\underline{\boldsymbol{\delta}}$, where the components of one tensor are related to the other by

$$\delta_{ij}^{sample} = \frac{\sigma^{ref.} - \sigma_{ij}^{sample}}{1 - \sigma^{ref.}}\,. \tag{3.14}$$

Furthermore, $\underline{\boldsymbol{\delta}}$ can generally be assumed to be symmetric, just as $\underline{\boldsymbol{\sigma}}$ is, and both tensors are diagonal in the same PAS. The three elements in the PAS are also ordered according to magnitude: $\delta_{xx}^{\mathrm{PAS}} = \delta_{11}$, $\delta_{yy}^{\mathrm{PAS}} = \delta_{22}$, $\delta_{zz}^{\mathrm{PAS}} = \delta_{33}$, where $\delta_{11} \geq \delta_{22} \geq \delta_{33}$.[17] Note that the order is reversed from that used in labelling the principal

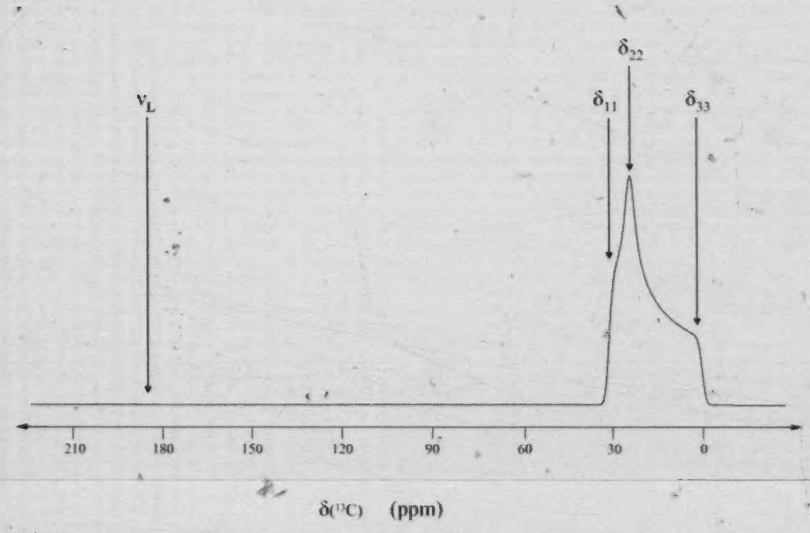

Figure 3.2: Theoretical ^{13}C NMR spectrum of a glassy sample of ethanol; chemical shift scale.

components of $\underline{\boldsymbol{\sigma}}$, so that both δ_{11} and σ_{11} label the high-frequency component of the two tensors. Also, the same alternate notation is often useful: $\delta_{\text{iso}} = \frac{1}{3}(\delta_{11}+\delta_{22}+\delta_{33})$, the span, $\Omega = \delta_{11} - \delta_{33}$, and the skew, $\kappa = 3(\delta_{22} - \delta_{\text{iso}})/\Omega$.[17]

3.2 Direct Dipolar Coupling

In most solid samples, the magnetic moment of the nuclear spin interacts not only with the externally applied field, but also with the magnetic moment of other spin-active nuclei in the sample. If we ignore any effects from intervening electrons, the coupling is called the direct dipolar coupling, and the Hamiltonian operator follows from the classical energy of interaction for two magnetic dipoles. The interaction energy for two magnetic dipole moments, $\boldsymbol{\mu}_A$ and $\boldsymbol{\mu}_B$, separated by the vector $\mathbf{r}$,

whose magnitude is r, is given by[10]

$$E = \frac{\mu_0}{4\pi}\left[r^{-3}(\boldsymbol{\mu}_A \cdot \boldsymbol{\mu}_B) - 3r^{-5}(\boldsymbol{\mu}_A \cdot \mathbf{r})(\boldsymbol{\mu}_B \cdot \mathbf{r})\right] . \tag{3.15}$$

The Hamiltonian operator can be built from this expression by making use of the relationship $\hat{\boldsymbol{\mu}}_A = \gamma\hbar\hat{\boldsymbol{I}}_A$.[a] Therefore, the direct dipolar coupling Hamiltonian between two nuclear spins I and S is

$$\hat{\mathscr{H}}_{DD} = hR_{DD}\left[(\hat{\boldsymbol{I}} \cdot \hat{\boldsymbol{S}}) - 3r^{-2}(\hat{\boldsymbol{I}} \cdot \mathbf{r})(\hat{\boldsymbol{S}} \cdot \mathbf{r})\right] , \tag{3.16}$$

where

$$R_{DD} = \frac{\gamma_A\gamma_B\mu_0 h}{16\pi^3 r^3} \tag{3.17}$$

is in frequency units, and is known as the direct dipolar coupling constant. It is often convenient to expand the dot products and convert to spherical coordinates, resulting in the so-called dipolar alphabet:[10]

$$\hat{\mathscr{H}}_{DD} = hR_{DD}[A + B + C + D + E + F] , \tag{3.18}$$

[a] Note that I have switched conventions here as it is more convenient to write the coupling Hamiltonian with angular momentum operators that do not include $\hbar$ in their eigenvalues, i.e., this $\hat{\boldsymbol{I}}$ is related to the one used heretofore by $1/\hbar$

where

$$A = -\hat{I}_z\hat{S}_z(3\cos^2\zeta - 1)\,, \tag{3.19}$$

$$B = \frac{1}{4}\left[\hat{I}_+\hat{S}_- + \hat{I}_-\hat{S}_+\right](3\cos^2\zeta - 1)\,, \tag{3.20}$$

$$C = -\frac{3}{2}\left[\hat{I}_z\hat{S}_+ + \hat{I}_+\hat{S}_z\right]\sin\zeta\,\cos\zeta\,e^{-i\varphi}\,, \tag{3.21}$$

$$D = -\frac{3}{2}\left[\hat{I}_z\hat{S}_- + \hat{I}_-\hat{S}_z\right]\sin\zeta\,\cos\zeta\,e^{i\varphi}\,, \tag{3.22}$$

$$E = -\frac{3}{4}\left[\hat{I}_+\hat{S}_+\right]\sin^2\zeta\,e^{-2i\varphi}\,, \tag{3.23}$$

$$F = -\frac{3}{4}\left[\hat{I}_-\hat{S}_-\right]\sin^2\zeta\,e^{2i\varphi}\,. \tag{3.24}$$

See Figure 3.3 for definitions of the angles ζ and φ. Equation 3.18 is organized according to the form of the operators, which is convenient because we don't generally need to include all of the terms A-F. For example, operators C-F do not affect the nuclear energy levels and are therefore usually ignored.[8,11] Term B may also be dropped when the two coupled nuclei have Larmor frequencies which differ by significantly more than the magnitude of their dipolar coupling.[8,11] One important characteristic of the direct dipolar coupling is that terms A and B, the only terms affecting energy levels, depend on ζ but not φ; accordingly, the coupling energy does not change under rotation of the molecule around the internuclear vector (or the equivalent rotation of the environment for non-molecular systems).

It is also possible to cast Equation 3.16 in matrix form:[25]

$$\hat{\mathscr{H}}_{DD} = hR_{DD}\,\hat{\boldsymbol{I}}\cdot\underline{\mathbf{D}}\cdot\hat{\boldsymbol{S}}\,, \tag{3.25}$$

where $\underline{\mathbf{D}}$ is the direct dipolar tensor. In the PAS of the direct dipolar tensor, in

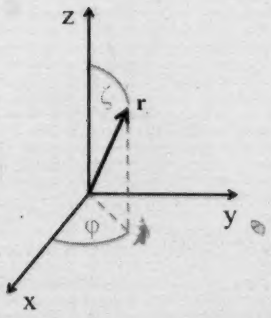

Figure 3.3: Axis system used to express the dipolar coupling, Equation 3.18; B^0 is along the z-axis, and $\boldsymbol{r}$ is the vector joining nucleus I (at the origin) to nucleus S.

which the internuclear vector $\boldsymbol{r}$ is along the z axis, $\underline{\mathbf{D}}$ takes the very simple format

$$\underline{\mathbf{D}}^{\mathrm{PAS}} = \begin{pmatrix} 1 & 0 & 0 \\ 0 & 1 & 0 \\ 0 & 0 & -2 \end{pmatrix}, \tag{3.26}$$

from which it is obvious that the tensor is both symmetric and traceless.

Experiments that allow one to determine dipolar couplings are useful for several reasons. The value of R_{DD} provides internuclear distances which may be used for structural constraints or assisting in peak assignments. Because NMR spectra that include the effects of dipolar coupling encode the relative orientation of $\underline{\mathbf{D}}$ to the other interaction tensors, it is possible to use the known orientation for the PAS of $\underline{\mathbf{D}}$ to determine the orientation of the other interaction tensors in the molecular frame. It should also be noted that the internuclear distance in the definition of R_{DD} will be averaged over whatever motions are faster than the NMR time scale, i.e., $r^{-3} \rightarrow \langle r^{-3} \rangle$. Also, vibrational averaging affects the NMR observable $\langle r^{-3} \rangle$ differently than an X-ray diffraction measurement of a bond length; consequently, the two measurements typically differ by a few percent.[26–28]

3.3 Indirect Coupling

In discussing the direct coupling mechanism in the previous section, it was noted that molecular electrons were ignored. However, the intervening electrons can have a significant effect, because the magnetic moments associated with the electron's spin and orbital angular momenta can interact with the nuclear magnetic dipole moments. Interaction with a perturbing nucleus causes the net magnetic moment from the electrons, usually assumed to be zero in a closed-shell molecule, to be significantly polarized. A second, responding, nucleus in the sample will have an interaction energy with the magnetically polarized electrons. The Hamiltonian that describes this indirect nuclear coupling energy has a format similar to that of the direct coupling interaction:[25,29]

$$\hat{\mathscr{H}}_J = h\,\hat{\boldsymbol{I}}_A \cdot \underline{\mathbf{J}} \cdot \hat{\boldsymbol{I}}_B\,, \tag{3.27}$$

where $\underline{\mathbf{J}}$ is a second-rank tensor whose elements are in frequency units. The difference from direct coupling is that the components of $\underline{\mathbf{J}}$ are not described by a simple equation, but are rather response parameters that must be calculated from first principles. A common name used for the indirect coupling, due to the symbol for the governing tensor, is the J-coupling interaction. Because the indirect coupling arises from a perturbation of the electronic structure of the molecule, the components of $\underline{\mathbf{J}}$ are extremely sensitive to the chemical environment around the two interacting nuclei.

The indirect spin-spin coupling tensor is a 2^{nd}-rank tensor, and is composed of up to nine independent components. In most cases, we can assume that the tensor is symmetric across the lead diagonal; however, there are rare cases, see Chapter 7, where this assumption fails. Similar to $\underline{\boldsymbol{\sigma}}$, $\underline{\mathbf{J}}$ is diagonal in its PAS with three principal components (J_{11}, J_{22} and J_{33}); the orientational (isotropic)

Table 3.2: Symmetry Requirements for $\underline{\mathbf{J}}$ Elements

Point Group[a]	Number of Elements		Non-zero Elements[b]
	Total	Independent	
C_{3v}, C_{4v}, C_{6v}, $C_{\infty v}$	3	2	J_{zz}, $J_{yy} = J_{xx}$
C_{2v}	3	3	J_{zz}, J_{yy}, J_{xx}
C_3, C_4, C_6	5	3	J_{zz}, $J_{yy} = J_{xx}$, $J_{yx} = -J_{xy}$
C_2, C_s	5	5	J_{zz}, J_{yy}, J_{xx}, J_{yx}, J_{xy}
C_1	9	9	all

[a]Symmetries defined in relation to the nucleus to be observed, not the total symmetry of the molecule or environment. Only point groups where the two nuclei coupled by $\underline{\mathbf{J}}$ are not exchanged by one of the symmetry operations are considered.

[b]When represented in the usual axis system for each point group. The full antisymmetric nature of the tensor is considered.

average, which would be observed in solutions, is given by one third the trace of the tensor: $J_{\text{iso}} = \frac{1}{3}(J_{11} + J_{22} + J_{33})$. By convention,[29] the three principal components are labelled according to their deviation from the isotropic average: $|J_{33} - J_{\text{iso}}| \geq |J_{11} - J_{\text{iso}}| \geq |J_{22} - J_{\text{iso}}|$. Both positive and negative values are possible for the tensor components, because favourable energetics may result when the nuclear dipole moments of the involved spins are polarized in the same, or in opposite directions. Symmetry arguments[18] regarding the number of independent elements in $\underline{\mathbf{J}}$ and constraints on the PAS orientation are similar to those involving $\underline{\boldsymbol{\sigma}}$, and result in the rules shown in Table 3.2.[20,30]

When attempting to measure $\underline{\mathbf{D}}$, it is important to consider that the similarity of the Hamiltonians governing the indirect and direct couplings, Equations 3.25 and 3.27, prevents separation of the portion of $\underline{\mathbf{J}}$ that has the same orientation dependence as $\underline{\mathbf{D}}$. However, prior knowledge of approximate magnitudes for each mechanism can sometimes be used to separate the two interactions.

3.4 Electric Quadrupole Coupling

All of the interactions described to this point have involved coupling of the nuclear magnetic dipole moment with an external or internal magnetic field; however, any nucleus with spin quantum number, I, greater than $\frac{1}{2}$ possesses an electric quadrupole moment. The nuclear electric quadrupole moment is described by the scalar variable Q, which is in units of m^{-2}. Interaction of this nuclear quadrupole moment with an electric field gradient, EFG, created by an anisotropic distribution of electric charges in a molecule, is described by the Hamiltonian[12]

$$\hat{\mathscr{H}}_Q = \frac{eQ}{2s(2s-1)} \hat{\boldsymbol{I}} \cdot \underline{\mathbf{V}} \cdot \hat{\boldsymbol{I}} \,, \tag{3.28}$$

where e is the elementary charge, and $\underline{\mathbf{V}}$ is the EFG tensor, whose elements are the gradients of the electric field:[31]

$$V_{ij} = \frac{\partial^2 U}{\partial i \, \partial j} \,. \tag{3.29}$$

Here, U is the electrostatic potential at the nucleus, and i, j are any two axes of a Cartesian coordinate system. The EFG tensor is a symmetric 2^{nd}-rank tensor, and is therefore diagonal in its PAS, with elements $|V_{zz}^{\text{PAS}}| \geq |V_{yy}^{\text{PAS}}| \geq |V_{xx}^{\text{PAS}}|$.[31] Because the tensor is traceless, the three components of $\underline{\mathbf{V}}^{\text{PAS}}$ must sum to zero; therefore, the three principal components are not linearly independent and there are only two unique elements in $\underline{\mathbf{V}}^{\text{PAS}}$. Accordingly, an alternative representation of the principal components can be given as the pair of constants V_{zz}^{PAS} and η_{Q}; this last constant is known as the asymmetry of $\underline{\mathbf{V}}$ and is defined by:[31]

$$\eta_Q = \frac{V_{xx}^{\text{PAS}} - V_{yy}^{\text{PAS}}}{V_{zz}^{\text{PAS}}} \,. \tag{3.30}$$

As with the other interaction tensors, point group symmetry can constrain the orientation of the PAS and the values of η_Q. Most notably, in some highly symmetric environments, all elements of $\underline{\mathbf{V}}$ are 0, and no quadrupolar coupling interaction is present. Because it is a measure of the electric field gradient at the nucleus, the quadrupole interaction is extremely sensitive to the area around the nucleus, and can provide a wealth of information about the nuclear environment.

3.5 Theoretical Frameworks in NMR

In the preceding discussion, only one method for predicting and understanding NMR spectra was presented; however, there are a plethora of methodologies, each of which has a multitude of sub-formats. Just as one may opt to calculate the motion of a system of particles using Newton's formulation of classical mechanics, but apply Lagrange's formulation to solve the same problem under geometrical constraints, it is often beneficial to apply different theoretical methods to each problem in NMR. The approach described previously is useful when analyzing single spin-$\frac{1}{2}$ nuclei: the similarity to classical mechanics and the ability to easily picture results is of obvious benefit. In particular, I think this solution method is particularly valuable in how it allows a solid understanding of the magnetic shielding interaction unencumbered by the details of a more complicated quantum treatment. Similarly, this vector picture is particularly efficient for analyzing simple experiments such as Hahn echoes or the attached proton test (APT).[8,10] However, understanding more complicated spin states and interaction Hamiltonians, or time evolution under delays and rf pulses, benefits from other methods of analysis which I will mention briefly here.

For a Hamiltonian that is a sum of the previously described interactions, one convenient way to understand the system is to diagonalize the Hamiltonian in order to determine its eigenfunctions (stationary states), and the energies of each state. The NMR spectrum can then be predicted using time-dependent perturbation the-

ory to determine the probability of an rf pulse exciting each of the transitions. The result of this analysis is therefore an energy level diagram and, in favourable cases, a simple understanding of how the interaction parameters affect the peak positions and splittings. An example including all details from the form of the Hamiltonian to the final spectrum is presented as part of Chapter 7. Lineshapes of the type given in Chapters 4, 5, and 6 benefit from this type of analysis, and the specifics of this methodology are described in the next Section.

Density matrix theory is a third alternative that allows one to derive all the results of the above two methods, and can also be used to analyze more complicated experiments and spin systems. Because nearly all of the results contained in later chapters are derived by calculating the eigenfunctions, rather than using density matrix theory, I've largely excluded details of the latter treatment. However, this should not be interpreted as reflecting the importance of density matrix theory to the field, because it is really the engine that drives much of modern NMR research. One of the important features of density matrix theory is that it allows one to treat time dependence in either the interaction or rf Hamiltonians in a natural way. This provides a path to designing complicated experiments where, e.g., one can tailor the Hamiltonian to express only certain interactions as the system evolves in orthogonal time dimensions. Also, because the formulation is general, a variety of numerical density matrix theory software packages now exist that allow researchers to investigate and develop NMR experiments of nearly any variety in a relatively straightforward manner. Textbooks introducing density matrix theory are now quite common—each individual will no doubt have their favourite, but I find particular clarity in the works of Farrar and Harriman;[7] Hore, Jones, and Wimperis;[9] and Levitt.[8]

3.6 Multiple Interaction NMR Lineshapes

In NMR, one often has to deconvolve a lineshape in terms of the interactions mentioned in the previous sections of this chapter. The first step in this process is to determine, given a set of parameters, the theoretical lineshape. In some cases the lineshape has simple, distinctive features that allow the experimenter to directly determine the parameters, while more complicated spectra require an interactive trial-and-error fitting procedure. I will now present a discussion of the details involved in analyzing NMR lineshapes from stationary powder samples of AX and AB spin-$\frac{1}{2}$ systems, the method with which most of the information reported in this thesis was determined. As noted in the preceding section, these expressions can all be obtained by diagonalizing the Hamiltonian and evaluating the allowed transitions using time-dependent perturbation theory.

3.6.1 Powder Lineshapes from AX Spin Systems

Many of the experimental spectra presented later on in this thesis are acquired from samples that contain relatively isolated pairs of spin-$\frac{1}{2}$ nuclei. In this Section, I will focus on spin pairs for which the difference in Larmor frequency between the the two nuclei is much greater than any other interaction, commonly known as AX spin systems. Because the related experimental spectra were acquired from systems that have significant magnetic shielding anisotropy and dipolar coupling magnitudes, but negligible indirect couplings, I will present the theory and analysis of spectra in this same regime. Using the angular definitions from the preceding discussion of magnetic shielding and dipolar coupling, the NMR transition frequency of the A spin in any one crystallite is given by:[32,33]

$$\begin{aligned}\nu_{\mathrm{A}}(\theta,\phi) = \; & \nu_{\mathrm{L}}\left[1 - \left((\sin^2\theta\cos^2\phi)\sigma_{11} + (\sin^2\theta\sin^2\phi)\sigma_{22} + (\cos^2\theta)\sigma_{33}\right)\right] \\ & \pm m_X R_{\mathrm{eff}}\left[3\cos^2\zeta - 1\right], \end{aligned} \tag{3.31}$$

where m_X is the azimuthal spin quantum number for nucleus X. Equation 3.31 must include m_X because the sign of the dipolar coupling depends on the orientation of the X spin, which may be aligned with or against the external magnetic field. The portion of Equation 3.31 that encodes the dipolar coupling interaction is of a relatively simple nature, because only term A of the dipolar coupling alphabet is involved in determining the energy levels of an AX spin system.

It is slightly easier to work with the expression for the transition frequencies if ζ is expressed in terms of θ and ϕ. Using the axis system and definitions shown in Figure 3.4, the AX NMR transition frequencies are

$$\nu_A(\theta,\phi) = \nu_L \left[1 - \left((\sin^2\theta\cos^2\phi)\sigma_{11} + (\sin^2\theta\sin^2\phi)\sigma_{22} + (\cos^2\theta)\sigma_{33}\right)\right] \pm m_X R_{eff}\left[3\left(\sin\beta\sin\theta\cos(\alpha-\phi) + cos\beta\cos\theta\right)^2 - 1\right]. \quad (3.32)$$

Note that θ and ϕ define the orientation of the applied field in the PAS of $\underline{\sigma}$, while α and β are constants that define the fixed orientation of the dipolar vector in this same coordinate system. Different crystallites will therefore be characterized by different values of θ and ϕ and the total powder pattern can once again be found by integrating over these two angles. The expression for the X-spin spectrum is basically the same, but it is well separated from the A-spin spectrum (by definition) so we can ignore it for now. If the shielding tensor for the X spin is desired, we could go on to examine the X-spin spectrum with the same method described below for the A-spin spectrum.

It is possible to gain some intuitive insight into analysis of the A-spin powder patterns by considering the form of the pair of subspectra created by the two spin states of the X nucleus. If R_{eff} is 0, the two subspectra are identical and the lineshape simply reduces to the magnetic-shielding only lineshape discussed above. In the experimental spectra from AX spin pairs shown in Chapters 4 and 5, R_{eff} is a few

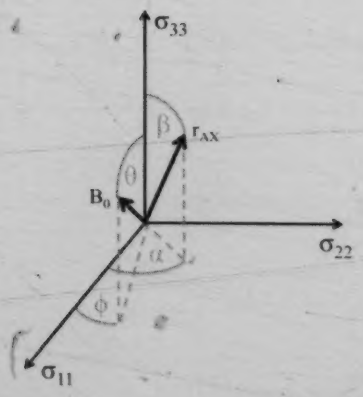

Figure 3.4: Axis system used in Equation 3.31 where the orientations of B^0 and r_{AX} are described as shown. Note that r_{AX} is a vector joining nucleus A with nucleus X.

percent of the total shielding anisotropy; therefore, the two subspectra are similar to the shielding-only lineshape, with a small modulation from the dipolar coupling term. This leads to a lineshape that looks like an overlay of two different shielding-only powder patterns, in which the splittings encode the value of R_{eff} and the angles α and β. For example, two peaks will be produced when $\boldsymbol{B}^0$ is along the y-axis, ν_{22} in Figure 3.1, and each is at a different position due to the opposite sign of the dipolar coupling term in Equation 3.31. The frequency differences between the subspectra when $\boldsymbol{B}^0$ is along the three axes of the PAS are displayed in Figure 3.5, and are given by:[33]

$$\begin{aligned} \Delta_{11} &= |R_{\text{eff}}(3\sin^2\beta\cos^2\alpha - 1)|\,, \\ \Delta_{22} &= |R_{\text{eff}}(3\sin^2\beta\sin^2\alpha - 1)|\,, \\ \Delta_{33} &= |R_{\text{eff}}(3\cos^2\beta - 1)|\,. \end{aligned} \tag{3.33}$$

These expressions are given in terms of absolute values because there is no way to tell which subspectrum is associated with which spin state of the X nucleus, and

this leads to several possible solutions for α and β.

As the internuclear vector is a fixed feature of the molecule (often a bond), an AX powder pattern provides information about the orientation of $\underline{\sigma}$ in the molecule. However, because of the cylindrical symmetry of the dipolar interaction, any solution of Equation 3.33 remains valid under any rotation about r_{AX}. This is clear if we consider the axis system shown in Figure 3.4: the experimental spectrum allows us to determine the orientation of r in the PAS of $\underline{\sigma}$ (via α and β); however, if we try and place the molecule in this coordinate system we will see the orientational information is incomplete: nucleus A is at the origin and nucleus X at the end of r_{AX}, but where do we position the other nuclei? We need one more dihedral angle to affix the rotation of the molecule about r_{AX}. Often, symmetry requirements on the tensor orientations can be used to remove or eliminate orientational ambiguities, while in other cases, quantum chemical calculations or empirical observations can be used to complete the orientational solution.

3.6.2 Powder Lineshapes from AB Spin Systems

In addition to an examination of samples comprised of isolated AX spin pairs, analogous spin pairs where the difference in Larmor frequency of the two nuclei is small compared to the coupling interactions are also presented below. Such systems are commonly termed AB spin pairs, following the convention that the distance along the alphabet between the two spins is correlated with the difference in Larmor frequencies of the nuclei. As before, I will limit expressions describing spectra from AB spin systems to the same regime as the experimental spectra presented later in the thesis. Therefore, only the isotropic portion of $\underline{\mathbf{J}}$ is included, as the orientation dependence of the dipolar coupling is assumed to dwarf that of the indirect coupling; however, note that the expressions are still given in terms of the effective dipolar coupling constant, R_{eff}. Also, only pairs of spin-$\frac{1}{2}$ nuclei are considered.

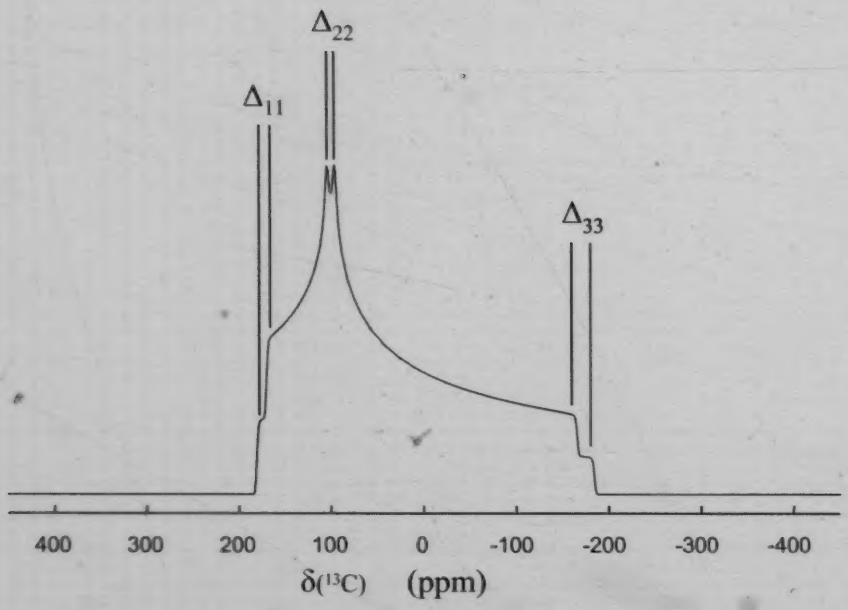

Figure 3.5: Example A-spin spectrum from an AX spin system. Here, a ^{13}C anisotropic shielding lineshape including coupling to ^{31}P is shown. Specific details: $\nu_L = 100$ MHz, $\delta_{11} = 175$ ppm, $\delta_{22} = 100$ ppm, $\delta_{33} = -175$ ppm, $R_{eff} = 1.5$ kHz, $\alpha = 50°$, $\beta = 30°$, $J_{iso} = 0$.

In these types of AB spin systems, the NMR transition frequencies encode the orientation dependence of both shielding tensors, the dipolar coupling, and the isotropic indirect coupling. For each crystallite of a powder there are four precession frequencies, ν_i, each with signal amplitude, A_i:[34-36]

$$\nu_1 = 1/2\,(\nu_A + \nu_B + X + Y), \quad \text{with } A_1 = 1 - Z/D; \tag{3.34}$$

$$\nu_2 = 1/2\,(\nu_A + \nu_B + X - Y), \quad \text{with } A_2 = 1 + Z/D; \tag{3.35}$$

$$\nu_3 = 1/2\,(\nu_A + \nu_B - X + Y), \quad \text{with } A_3 = 1 + Z/D; \tag{3.36}$$

$$\nu_4 = 1/2\,(\nu_A + \nu_B - X - Y), \quad \text{with } A_4 = 1 - Z/D. \tag{3.37}$$

Equations 3.34 - 3.37 are written in terms of the following constants:

$$X = \left[(\nu_A - \nu_B)^2 + Z^2\right] , \tag{3.38}$$

$$Y = J_{\text{iso}} - R_{\text{eff}}(3\cos^2\zeta - 1) , \tag{3.39}$$

$$Z = J_{\text{iso}} + 1/2\ R_{\text{eff}}(3\cos^2\zeta - 1) , \tag{3.40}$$

where ν_A and ν_B are the magnetically shielded Larmor frequencies, and Ω is the angle between the applied magnetic field and $\boldsymbol{r}_{AB}$.

In order to fully specify the system, it is necessary to detail all of the interactions in the same frame, or at least specify each interaction in their own frame and also how the coordinate systems are related. The method applied in later chapters is to select the PAS of $\underline{\mathbf{D}}$ as the reference frame. Orientations for each shielding tensor are then specified using the three Euler angles that rotate their PAS into that of $\underline{\mathbf{D}}$. The convention used here is three successive right-handed rotations about: the reference z-axis (α), the new y'-axis this generates (β), and the z''-axis that was generated by the first two rotations (γ).[37]

Because the shielding interaction scales with the applied field strength (in frequency units), while the coupling interactions do not, fitting the lineshape at multiple field strengths greatly increases the confidence of any extracted parameters. As mentioned above for AX spin systems, the cylindrical symmetry of the dipolar interaction places some limits on the absolute determination of the orientation of the PAS for each interaction tensor. And, as before, symmetry and/or quantum chemical calculations can be very useful in narrowing down the solution space.

3.7 Common Experimental Techniques

A myriad of experiments are available to the modern NMR spectroscopist. In favourable cases, the researcher can choose which interactions are expressed in each

dimension of the final spectrum. Most of these techniques are well known, so I will simply list key features of a few methods integral to the results presented in later chapters. In some samples, large dipolar couplings between protons and the nucleus of interest prevent resolution of the smaller interactions we desire to measure. The solution to this problem is the application of high-power ^{1}H decoupling using one of a library of pulse sequences, as this usually removes nearly all of the line broadening.[38] While hampering resolution during acquisition, protons in the sample can also provide an advantage: polarization of the observed spins can be enhanced via the technique of cross polarization, CP. An increase in signal intensity of the observed A spin, by performing CP from an X spin, in the amount γ_X/γ_A is theoretically possible.[39] In the case of ^{1}H$\rightarrow^{13}$C CP, this can provide up to a fourfold increase in sensitivity. A secondary benefit of using CP is that the time between scans can be reduced to the often much shorter longitudinal relaxation time of the X nucleus. Often, the reduction in recycle time is just as beneficial as the increased signal intensity. CP is only effective when the A and X spins are strongly coupled; furthermore, the Hartmann-Hahn match condition must be satisfied in that the rf-induced nutation frequencies on both spectrometer channels must match:[39]

$$\gamma_A B_A^1 = \gamma_X B_X^1 , \tag{3.41}$$

where B_i^1 is the magnetic field strength of the rf pulse at the frequency of nucleus i. A variety of functions can be used to control the shape of the B^1 sweep, with different functions producing optimal results under different experimental conditions. In summary, decoupling is used to isolate the spins of interests, while CP increases the signal to noise ratio of the experiment.

For powdered samples, the orientation dependence of the various interactions creates broad spectra. While a plethora of information is contained in this line shape,

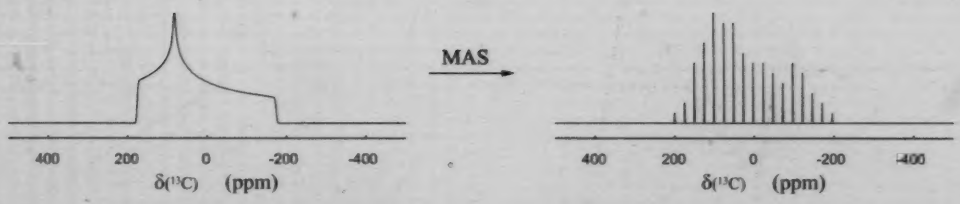

Figure 3.6: Example of the effects of MAS on a shielding-only powder pattern, the theoretical system has a shielding anisotropy of approximately 28 kHz and an MAS frequency of 2 kHz was used.

multiple sites may be obscured, and it is not always possible to analyze a lineshape for all the interaction parameters at once. The dipolar interaction, as well as the anisotropic portions of $\underline{\boldsymbol{\sigma}}$ and $\underline{\mathbf{J}}$, can be effectively averaged by spinning the sample in a rotor inclined at the so-called magic angle, 54.74°, to the applied magnetic field—a technique called magic angle spinning, MAS.[40] Further details and references regarding the mechanism of this line narrowing technique are given in Chapter 7. If the sample is spun at a sufficiently fast rate, the anisotropic portions of $\underline{\boldsymbol{\sigma}}$, $\underline{\mathbf{J}}$, and $\underline{\mathbf{D}}$ are averaged to zero, e.g., the broad lineshape from anisotropies in shielding and couplings are narrowed to single lines, split only by J_{iso}. In the intermediate regime, when the spinning rate approximately equals the breadth of the interaction in frequency units, the averaging is not complete, and the broad lineshapes are instead broken up into a series of spikelets. These spikelets are separated by an interval equal to the spinning rate, and the intensities of the spikelet pattern encode the anisotropic portion of the interactions. The prototypical case is displayed in Figure 3.6, where a magnetic shielding powder pattern is broken up into a series of peaks by MAS (at a rate equal to about 1/10 of the shielding anisotropy). When magnetic shielding is the only interaction, there is a complicated, but closed-form expression relating the shielding tensor components to the spikelet peak heights;[41] therefore, it is relatively straightforward to determine the components of $\underline{\boldsymbol{\sigma}}$ from the

spectrum. However, when couplings to other nuclei are involved, the peak heights are modulated by the interactions in a more complicated fashion, and a brute-force numerical simulation method must be used to re-create the spectrum from trial parameters.[42] In general, significant quadrupolar interactions can limit the ability of MAS to narrow the spectrum, but MAS is often still useful for samples containing quadrupolar nuclei.[12]

3.8 Dipolar Recoupling Spectroscopy

There are a library of techniques in spin-$\frac{1}{2}$ NMR spectroscopy which make use of the resolution afforded by MAS, but retain information from homonuclear dipolar couplings.[43,44] Chapter 5 contains some NMR spectra obtained using the supercycled $SR26_4^{11}$ pulse sequence, which has been tailored, using symmetry principles,[45] for the combination of a small R_{eff}, but large chemical shift anisotropy.[46,47] The $SR26_4^{11}$ pulse sequence acts as a filter: spectra only include signals from homonuclear spin pairs with significant dipolar couplings. A one-dimensional version of this pulse sequence is displayed in Figure 3.7A. The first half of the sequence excites a double-quantum coherence, DQC, using a long train of composite 180° pulses, which are phased according to the $R26_4^{11}$ protocol.[46,47] This block of pulses is then phase shifted and repeated 4 times, according to literature methods, creating the supercycled $SR26_4^{11}$ pulse sequence.[46,47] Rotor synchronization requires that one $SR26_4^{11}$ block exactly fill 16 rotor periods, thereby necessitating an rf nutation frequency 6.5 times the rotor spinning frequency. The DQC created by the first block of pulses has an intensity proportional to the dipolar coupling of the two involved homonuclear spins, and may be measured by first converting it back into longitudinal magnetization with a second train of $SR26_4^{11}$ pulses, and then observing it with a $\pi/2$ read pulse. Only the portion of the magnetization passing through a DQC is desired, so a standard DQC-filtering phase cycle must be applied to the second half of the pulse

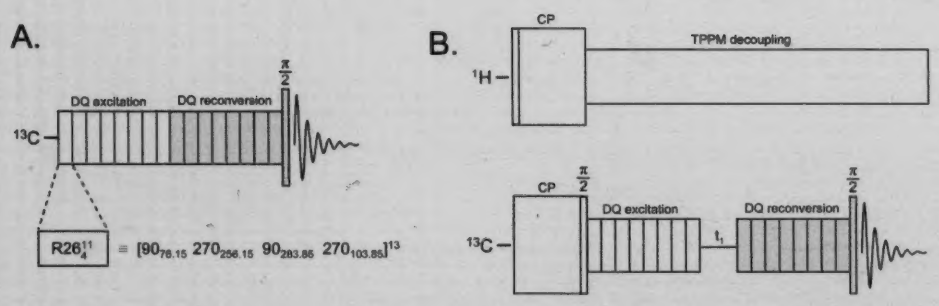

Figure 3.7: A. Symbolic display of a one-dimensional, single-channel ^{13}C $SR26_4^{11}$ homonuclear dipolar recoupling pulse sequence; pulses in one $R26_4^{11}$ block are shown using the $(\text{Pulse Angle})_{\text{Phase}}$ convention. B. Two dimensional, two-channel version of the $SR26_4^{11}$ sequence, with signal enhancement via $^{1}H \rightarrow {}^{13}C$ CP followed by a flip-back pulse, and heteronuclear decoupling during both homonuclear recoupling and acquisition.

sequence (depicted as shading in Figure 3.7). Also, if there are heteronuclear spins present in the sample, CP pulses can be added prior to the recoupling sequence, and decoupling may need to be applied during acquisition; note that decoupling may not be necessary during the $SR26_4^{11}$ pulses, as the sequence itself leads to some heteronuclear decoupling.[48]

In addition to functioning as a filter for homonuclear spin pairs, the intensity of the DQ-filtered peaks encode the strength of the dipolar couplings involved. Assuming the same length of time, τ, is used for both excitation and reconversion blocks in the $SR26_4^{11}$ sequence, the signal intensity from one homonuclear spin pair is described by the function[47]

$$I(\tau) = \frac{1}{2} - \frac{\sqrt{2}\pi}{8} J_{+1/4}(-1.6\, R_{\text{eff}}\, \tau) J_{-1/4}(-1.6\, R_{\text{eff}}\, \tau)\,, \qquad (3.42)$$

where $J_{\pm 1/4}$ are the quarter-integer Bessel functions. The theoretical behaviour described by Equation 3.42 is shown in Figure 3.8, where the example of a ^{13}C-^{13}C homonuclear spin pair is used. It should be noted that the value of τ cannot be

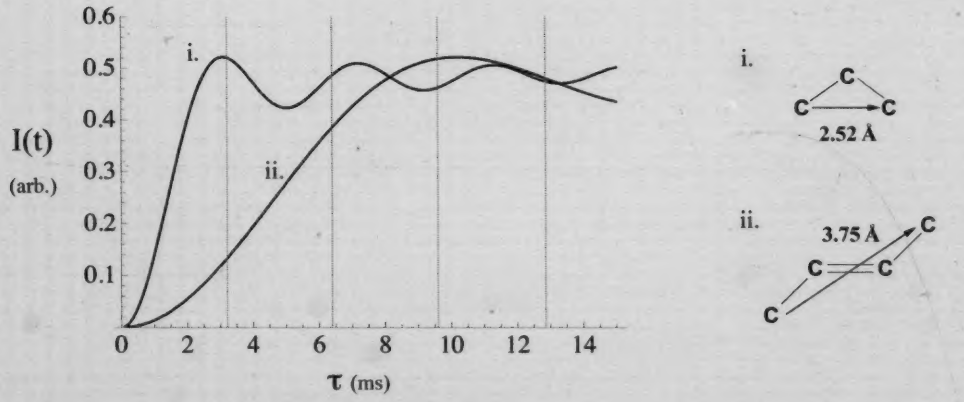

Figure 3.8: Theoretical behaviour of intensity versus time for the DQ signal intensity from an $SR26_4^{11}$ experiment, see Equation 3.42. Curves for two example distances, *i.* and *ii.*, from idealized propane and *trans*-2-butene are shown. Vertical gray lines in the graph indicate the allowed values of $\tau = n \cdot 3.2$ ms at a rotor spinning frequency of 5 kHz.

varied completely arbitrarily, as the total time for one $SR26_4^{11}$ block must equal 16 rotor periods. This "quantization" of allowed τ values is displayed in Figure 3.8, where the vertical lines show the possible values at a rotor spinning frequency of 5 kHz; these longer values of τ can be accessed by using an integer number of $SR26_4^{11}$ blocks. Although other values of τ can be applied by changing the spinning frequency, this would necessitate the redetermination of rf power levels. The form of Figure 3.8 shows it is possible to differentiate spin pairs with differing magnitudes of R_{eff} coupling constants, through examination of the peak heights. Alternatively, internuclear distances may be determined quantitatively by acquiring multiple experiments with different τ values, and then fitting Equation 3.42 to the experimental intensities. There may be further modulation of the signal intensity in Equation 3.42 from experimental errors or relaxation effects, but there are published strategies for minimizing the effect of such deviations.[47]

It is also possible to use the $SR26_4^{11}$ pulse sequence as a two dimensional DQ

correlation experiment, i.e., an experiment in which it is possible to determine which NMR peaks from the one dimensional experiment are dipolar coupled to each other. The pulse sequence is nearly the same as the 1D version, except that the DQC created by the excitation block is allowed to evolve during a t_1 period before being reconverted to longitudinal magnetization, see Figure 3.7B. Therefore, evolution during t_1 encodes the evolution frequency of the DQC, which is equal to the sum of the chemical shifts of the nuclei forming the dipolar-coupled spin pair. It is important to note that, just as in 1D NMR spectra, the DQ frequency is measured with respect to the transmitter frequency. Also, further phase cycling must be be applied in order to generate pure absorption peaks in the second dimension, e.g., by the States method or through time-proportional phase increments.[8] The 2D peak intensities depend on R_{eff} through Equation 3.42, matching the behaviour of the 1D spectra. The power of this technique is shown in the example spectrum in Figure 3.9, where *intermolecular* dipolar coupling between ^{13}C nuclei in neighbouring molecules is enough to produce the DQ correlation. Given that it can be used to probe intermolecular distance scales, the $SR26_4^{11}$ experiment is obviously an extremely sensitive technique. In fact, in a study of zeolite crystals, ^{29}Si-^{29}Si distances of up to 8 Å (10 Hz dipolar couplings) were found to affect the spectra.[49,50]

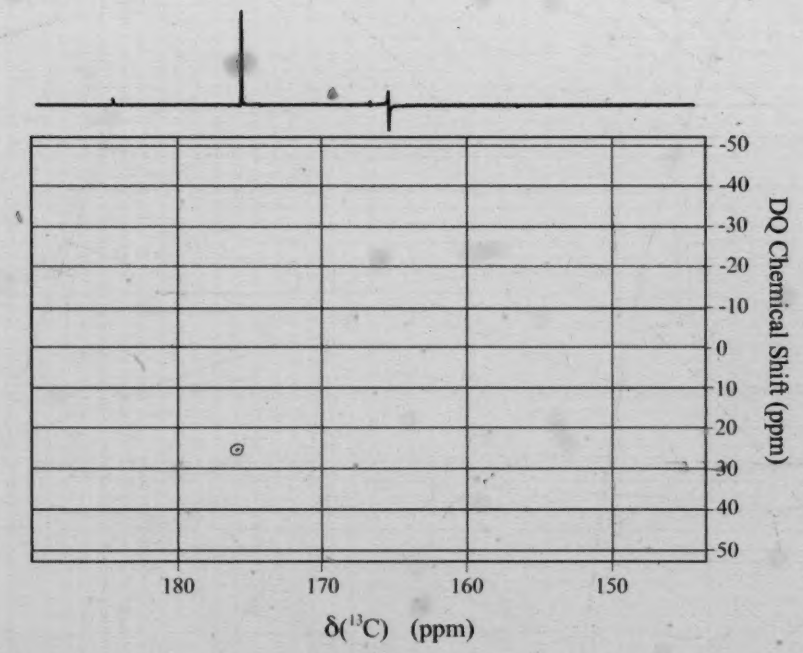

Figure 3.9: 2D carbon-13 CP-SR26$_4^{11}$ spectrum of 1-^{13}C-glycine probing intermolecular dipolar couplings ($|\boldsymbol{r}_{CC}| = 3.104$ Å, and $R_{\text{eff}} = 254$ Hz); spectrum collected using a 75.1 MHz transmitter frequency, with $\nu_{rot} = 8.097$ kHz, and $\tau = 3.95$ ms; high power TPPM decoupling was applied during signal acquisition. The spectrum from the analogous 1D CP-SR26$_4^{11}$ sequence is shown above the 2D spectrum. Note that because the 1D peak occurs at +12.5 ppm from the transmitter frequency, the self-correlation peak (correlating two nuclei at the same chemical shift) occurs at +25 ppm in the indirect dimension.

Chapter 4

A ^{15}N and ^{13}C NMR Investigation of Cyanoaurate Salts

4.1 Introduction

Molecules containing gold have been recognized for some time as having the potential to form an "extra" bond between closed-shell gold cations, despite the expected Coulombic repulsion.[51–55] While this interaction between heavy, closed-shell atoms has been assigned a variety of labels, for convenience we here apply the terms aurophilic to describe gold-gold interactions, and metallophilic to describe the analogous heteronuclear bonds. Metallophilic bond energies are similar in magnitude to those of hydrogen bonds, but are somewhat stronger, reaching a maximum between that of the strongest hydrogen bond and the weakest covalent bond.[56] Theoretical studies have shown that metallophilic bonds result from electron correlation ef-

A version of this chapter has been published. Harris, K.J.; Wasylishen R. E. *Inorg. Chem.* **2009,** *48,* 2316-2332

fects.[56–60] Furthermore, it has been shown that relativistic effects further strengthen the effect, providing an approximately 30% increase in the case of aurophilic interactions.[56,57] Much of the current research on gold compounds focuses on using aurophilic bonds for controlling supramolecular structures,[55,61–63] or studying the unusual photophysics often associated with the presence of aurophilic bonds.[56,64–67] For example, recent studies have found that the photoluminesence of gold-containing materials are influenced by factors such as temperature,[68] freezing of a solution containing a gold(I) complex,[69] or introduction of an organic solvent to a solid gold(I) material, either as a vapor,[70–74] or as a liquid.[75] Rational design of functional materials based on these properties is already underway in several labs: detection of alkali metal cations has been shown possible through design of a suitable gold(I) compound with crown ether pendants,[76,77] and a sensor for volatile organic compounds based on the vapochromism of a gold(I) material has already been built.[70]

The cyano complexes of gold are of great commercial importance, through their useage in gold extraction,[78] and are also of medicinal interest.[79] Aurophilic interactions between gold atoms in approximately linear dicyanoaurate anions, $[NCAuCN]^-$, are strong enough that the anions associate into oligomers in solution,[80,81] and also affect the structure of materials containing this anion.[55,61–63] Combining the abilities of both cyanide ligands and gold atoms to bridge metals, through bidentate or metallophilic bonding, has lead to the development of new heterometallic network materials, with a plethora of novel features. Research into coordination polymers composed of cyanide and gold has been recently reviewed,[62,63] and continues to be an area of active research.[68,82–94] Coordination polymers of this type have demonstrated unusually high optical birefringence,[95,96] tunable electron lone-pair stereochemistry in Pb(II),[92] and the ability to reversibly absorb water,[97,98] organic vapors,[73] or ammonia,[74] the latter two causing an observable difference in the photophysics. The heterometallic nature of these polymers has also allowed

the incorporation of metals with accessible high-spin electronic states, providing a means to study magnetic properties.[73,83,84,86,87,89–91,93,97–116] Magnetic exchange between electron spins on adjacent metal centres has been shown to occur along diamagnetic gold(I) or gold(III) cyanide chains.[73,90,93,97,100,102,111,114,115] Furthermore, materials containing dicyanoaurate bridges and aurophilic bonds have been investigated in regards to promising behaviours with respect to transitions between high- and low-spin states of neighbouring metals.[104,110]

Presented below is a ^{13}C and ^{15}N solid-state NMR study of some prototype gold cyano complexes, in an effort to investigate the interesting fundamental physics of these systems, as well as provide benchmark data and techniques useful for investigation of the cyanoaurate coordination polymers discussed above. SSNMR studies of cyano ^{13}C and ^{15}N nuclei are well known to provide useful information on cyanide containing materials.[117–131] To date, ^{13}C and ^{15}N NMR parameters have only been reported for one cyano gold complex, $Pb[Au(CN)_2](H_2O)_x$ (x=0,1),[95] in the solid state. One aim of the present research is to determine the effect of structural changes, including changes in metallophilic bonding, on the NMR properties of the cyanide ligand. Samples investigated include the dicyanoaurate anion complexed with a series of counterions, $M^+[Au(CN)_2]^-$, where M^+ = n-butylammonium (no aurophilic interactions between anions),[132] potassium (anions associated via aurophilic bonds),[133] and thallium (both Au-Au and Au-Tl metallophilic bonding present).[134] In addition to investigating these gold(I) dicyanides, we also present data for potassium tetracyanoaurate(III), in an effort to determine the effect of gold's formal oxidation state on the cyano NMR properties. NMR spectra of samples undergoing magic angle spinning as well as stationary samples (where possible), were recorded to determine the ^{13}C and ^{15}N chemical shift tensors and ^{13}C,^{15}N dipolar coupling constants in these systems.

4.2 NMR Terminology and Theory

The samples investigated herein are composed of cyanide ligands dilabelled with the spin-$\frac{1}{2}$ ^{13}C and ^{15}N nuclei; therefore, the samples involve AX spin pairs and may be analyzed using the methods described in Chapter 3. Where possible, spectra from stationary samples were recorded in order to determine the principal components of each chemical shift tensor and its orientation with respect to the dipolar vector, i.e., the C,N bond. In samples where the signal-to-noise ratio did not allow acquisition of spectra from stationary samples, slow MAS samples were instead used. The intensity pattern of the array of spinning sidebands, ssbs, from these slow MAS samples encodes the NMR observables. In these systems, the ssb intensities are modulated both by the chemical shift tensor and the dipolar coupling to the neighbouring spin-$\frac{1}{2}$ nucleus.[42] Spectral simulations therefore require inclusion of both interactions, and we applied the program SPINEVOLUTION to determine CS tensor elements.[135] It should also be noted that the procedure of fitting sideband intensities from isolated spins has difficulty in differentiating axially symmetric CS tensors from those that deviate slightly from axial symmetry.[42, 136]

As noted in Chapter 3, NMR experiments are not directly sensitive to the dipolar coupling constant, R_{DD}, but rather to a combination the dipolar coupling and a portion of the J coupling, as represented by the effective dipolar coupling constant, R_{eff}. However, in a cyanide the value of $J_{\text{iso}}(^{15}\text{N},^{13}\text{C})$ is generally less than 20 Hz and is therefore too small to affect these spectra;[137–140] accordingly, we have assumed $R_{DD} = R_{\text{eff}}$. The distance measured via R_{eff} is typically a few percent different from the corresponding X-ray diffraction derived value, because of a slightly different dependence on vibrational averaging, and is known to yield a 1-4% longer bond distance for C-C distances measured via NMR as compared to X-ray distance determinations.[26–28] In an SSNMR study of AgCN, it was argued that a value for the C,N bond length more amenable to direct comparison with diffraction data

could be produced through shortening the NMR-measured length by 2.5±1.5%.[140] All distance measurements reported here include this vibrational correction of shortening the NMR-derived bond lengths and applying the concommitant increase in error range.

In each compound the carbon, and in AuCN the nitrogen, atoms are directly bonded to gold, internuclear coupling with which can affect the spin-$\frac{1}{2}$ NMR spectra. Gold-197 is a 100% abundant spin-$\frac{3}{2}$ quadrupolar nucleus with a small magnetic moment (<1/50$^{\text{th}}$ that of ^{1}H), and a large nuclear quadrupole moment (Q = 54.7 fm^2).[141] The ^{197}Au nucleus may perturb the energy levels of neighbouring ^{13}C or ^{15}N nuclei through both of the two spin-spin coupling mechanisms described above: J coupling and direct dipolar coupling. As mentioned in Chapter 3, the direct dipolar coupling between two spin-$\frac{1}{2}$ nuclei is averaged to zero when the sample is spun rapidly at the magic angle. For a spin-$\frac{1}{2}$ nucleus coupled to a nucleus with a large quadrupolar coupling constant however, the direct dipolar coupling between the two cannot be averaged to zero by magic-angle spinning, and a *residual* dipolar coupling remains. For many systems studied at room temperature, ^{197}Au relaxes so rapidly that no effects on the spin-$\frac{1}{2}$ NMR spectra are observed; however, there have been examples in which spin-spin coupling to ^{197}Au has been observed in ^{31}P NMR spectra.[142–148]

As an example of the effects expected from residual dipolar coupling to ^{197}Au, we here estimate the ^{13}C lineshape of K[Au(CN)$_2$] expected under MAS from such an interaction. In this approximately linear molecule, the ^{197}Au EFG tensor is likely axially symmetric with V_{zz} along the Au-C bond. An approximate value of C_Q(^{197}Au), 1.27 GHz, has been obtained from Mössbauer data for K[Au(CN)$_2$];[149] however, due to the low Larmor frequency of ^{197}Au, the simulated spectra are nearly invariant to the magnitude of C_Q as long as it is greater than ~300 MHz. With the orientation and principal components of the EFG tensor so defined, spectral

simulations of the lineshape need include only two variables: R_{eff} and J_{iso}.[150] The published crystal structure allows an initial estimate of 69 Hz for R_{eff} to be set from the Au,C bond length. An estimate of the expected $J_{\text{iso}}(^{197}\text{Au},^{13}\text{C})$ can be determined through comparison to an analogous system, using the reduced coupling constant,[29,151] $K(I,S) = 4\pi^2 h^{-1} \frac{J(I,S)}{\gamma_I \gamma_S}$. Analogous molecules where one nucleus is replaced by a heavier congener are typified by a larger K because of increased electron density at the nucleus. For example, in the analogous series of molecules $ClM(PR_3)$ (where M = Cu, Ag, Au), $^1K_{\text{iso}}$(M,P) approximately doubles for each step down the periodic table.[145] Also, the value of $^1K_{\text{iso}}$(M,C) in AgCN is approximately double that of CuCN. This same numerical relationship between J couplings in analogous molecules does not hold across the entire periodic table, but seems to be useful within the group 11 metals. The value of $^1K_{\text{iso}}$(Au,C) in $[Au(CN)_2]^-$ anions are therefore likely close to double the known[140] value of $^1K_{\text{iso}}$(Ag,C) in $\cdots$CNAgCNAgCN$\cdots$, and a value of $J_{\text{iso}}(^{197}\text{Au},^{13}\text{C}) \simeq 180$ Hz is predicted. Lineshape simulations, using WSOLIDS,[24] show that the expected spectrum is composed of four peaks separated by 60 to 160 Hz, covering a total range of ~400 Hz. Even if the J coupling is 0, R_{eff} alone is enough to cause the four peaks of the simulated spectrum to cover a range of ~250 Hz. We therefore expect that residual dipolar coupling to ^{197}Au will have a noticeable effect on the ^{13}C spectra, unless the gold nucleus is self-decoupled by rapid relaxation.

4.3 Experimental

4.3.1 Sample Preparation

A sample of AuCN used as a starting material was prepared from commercial $K[Au(CN)_2]$ through treatment with HCl according to literature methods.[152] The sample of ^{13}C,^{15}N-labelled $K[Au(CN)_2]$ was prepared via dissolution of AuCN in

a hot aqueous solution of 99% ^{13}C,^{15}N-labelled KCN, followed by recrystallization from hot water.[152] The sample of ^{13}C,^{15}N-labelled $[(n\text{-}C_4H_9)_4N][Au(CN)_2]\cdot H_2O$ was prepared by dissolution of AuCN in a hot aqueous solution of 60% ^{13}C,^{15}N-labelled KCN, followed by precipitation with an aqueous solution of tetra-n-butylammonium chloride, and then recrystallization from hot water.[132] Note that while originally reported as an anhydrous salt, and discussed as such in the journal article corresponding to this thesis chapter,[2] this synthetic route has since been determined to produce a stable monohydrate.[153] We found it necessary to spin the sample at less than ~6 kHz during MAS experiments to prevent frictional heating from introducing enough motion in the cation to interfere unfavourably with $^1H \rightarrow {}^{13}C$ CP. The sample of ^{13}C,^{15}N-labelled $Tl[Au(CN)_2]$ was prepared by dissolution of AuCN in a hot aqueous solution of 60% ^{13}C,^{15}N-labelled KCN, followed by precipitation with an aqueous solution of Tl_2SO_4 and recrystallization from hot water.[134] A sample of $K[AuBr_2(CN)_2]$ for use as a starting material was prepared by oxidation of commercial $K[Au(CN)_2]$ with a solution of Br_2 in MeOH followed by recrystallization from hot water;[154] this material was then added to a methanol solution of 99% ^{13}C,^{15}N-labelled KCN, and the result recrystallized from hot water to yield $K[Au(CN)_4]$ which was then dehydrated under high vacuum at RT.[154] The identity of $K[Au(CN)_2]$, $Tl[Au(CN)_2]$ and $[(n\text{-}C_4H_9)_4N][Au(CN)_2]\cdot H_2O$ was confirmed by matching the experimental and theoretical X-ray powder diffraction patterns.[132–134] Only the hydrate of $K[Au(CN)_4]$ has a known crystal structure, but this material was found to dehydrate too quickly for identification by powder XRD. Therefore, the identity of $K[Au(CN)_4]$ was confirmed by matching the 2189.5 cm^{-1} CN stretch to the published 2189 cm^{-1} value,[154] and the fact that only a single ^{13}C NMR peak is observed in the solid state. A small IR absorption at 2145 cm^{-1} is assigned to the ^{13}C,^{14}N moieties following Jones and Smith,[154] and the remaining intense stretch at 2115 cm^{-1} is therefore assigned to ^{13}C,^{15}N moieties. Powder XRD measurements

used an Inel powder diffractometer with copper $K\alpha_1$ radiation, while IR spectra were collected on a Nic-Plan FTIR Microscope.

4.3.2 SSNMR

Carbon-13 NMR spectra were acquired at 50.3 MHz (4.70 T) using a Chemagnetics CMX Infinity 200, at 75.5 MHz (7.05 T) using a Bruker Avance 300, or at 125.8 MHz (11.75 T) with a Bruker Avance 500. All ^{13}C experiments used powdered samples packed in 4 mm outer diameter rotors, were recorded using 4 μs $\pi/2$ pulses, and were referenced to TMS by setting the high-frequency peak of an external adamantane sample to 38.56 ppm.[155] For all samples except $[(n\text{-}C_4H_9)_4N][Au(CN)_2]\cdot H_2O$, Bloch-decay experiments were used for MAS spectra, while Hahn-echo experiments were used for spectra of stationary samples. Experiments used pulse delays of 25 min. for $K[Au(CN)_2]$, 30 min. for $Tl[Au(CN)_2]$, and 30 min. (but using a 45° pulse) for $K[Au(CN)_4]$. Variable-amplitude[156] cross polarization[157–159] from the protons in the tetra-n-butylammonium cation was used to collect ^{13}C NMR spectra of $[(n\text{-}C_4H_9)_4N][Au(CN)_2]\cdot H_2O$, under the Hartmann-Hahn match condition,[157,159,160] and TPPM decoupling[161] at a power level of ~60 kHz was applied during acquisition. Under these conditions, a 10 s pulse delay was utilized for both the CPMAS and static CP Hahn-echo experiments.

Nitrogen-15 NMR spectra were collected at 20.3 MHz (4.70 T) using a Chemagnetics CMX Infinity 200, at 30.5 MHz (7.05 T) with a Bruker Avance 300, or at 50.7 MHz (11.75 T) using a Bruker Avance 500. All experiments used 4 mm rotors, and peaks were referenced by setting the low-frequency peak of an external sample of ammonium nitrate to 23.8 ppm (with respect to neat liquid ammonia at 0 ppm).[162] The MAS spectra, except those of $[(n\text{-}C_4H_9)_4N][Au(CN)_2]\cdot H_2O$, used Bloch-decay experiments. A B^1 field sufficient to generate a 5 μs $\pi/2$ pulse was used for all experiments. Spectra of $K[Au(CN)_2]$ used a 30° excitation pulse and

Table 4.1: Local Structural Parameters for Gold(I) Cyanides

Salt	Au site	C-N bond (Å)	Au-C bond (Å)	C-Au-C angle (deg.)	Au-C-N angle (deg.)	Au-Au (Å)	Au-Tl (Å)
$K[Au(CN)_2]$[a]		1.17(20)	2.12(14)	180	173(7.5)	4@3.64	
$[(n\text{-}C_4H_9)_4N][Au(CN)_2]\cdot H_2O$[b]		1.03(4)	1.96(4)	180	174(3)	4@8.05	
$Tl[Au(CN)_2]$[c]	1	1.148(2)	1.970(2)	180	180	2@3.560	
		1.148(2)	1.971(2)	180	180		
	2	1.145(2)	1.971(2)	180	180	2@3.560	
		1.146(2)	1.970(2)	180	180	2@3.037	
	3	1.145(2)	1.972(2)	180	176.6(4)	2@3.037	3.463
		1.148(2)	1.971(2)	177.1(2)	175.8(4)	2@3.068	3.446

[a]Data from the X-ray diffraction study of Rosenzweig and Cromer.[133]
[b]Data from an X-ray diffraction study of Schubert and Range.[132]
[c]Neutron diffraction study by Blom et al.[134]

40 min. recycle delay, $Tl[Au(CN)_2]$ required a 10 min. pulse delay when applying a 30° pulse, and $K[Au(CN)_4]$ required a 30 min. delay when using a 20° pulse. Variable-amplitude[156] cross polarization[157,159,160] followed by TPPM decoupling[161] at a power level of ~60 kHz during acquisition was used for the ^{15}N MAS spectra of $[(n\text{-}C_4H_9)_4N][Au(CN)_2]\cdot H_2O$ and CP followed by a 180° refocussing pulse was used for static spectra. Recycle delays of 10 s were used for all CP spectra of $[(n\text{-}C_4H_9)_4N][Au(CN)_2]$.

Carbon-13 and nitrogen-15 NMR spectra from stationary samples were simulated using WSOLIDS,[24] while nitrogen-15 spectra from slow-spinning samples were simulated using SPINEVOLUTION.[135] Simulated ^{13}C spectra from MAS samples including residual dipolar coupling to ^{197}Au were calculated using WSOLIDS.[24]

4.4 Results and Discussion

4.4.1 ^{13}C NMR of Gold(I) Dicyanides

A sample of $K[Au(CN)_2]$ was prepared and investigated by ^{13}C SSNMR. The structure, reported in 1959 by Rosenzweig and Cromer,[133] contains alternating sheets of potassium and gold atoms with cyanide ligands above and below the gold plane.

The local structure around the single unique CN moiety, reported in Table 4.1, has the unique Au atom surrounded by four Au neighbours at 3.64 Å, at the upper limit of what may be considered an aurophilic bond.[163,164] Presented in Figure 4.1 is the ^{13}C NMR spectrum of a stationary sample of 50% ^{13}C,^{15}N-labelled K[Au(CN)$_2$], the shape of which evinces the axial symmetry of the CS tensor. Also shown in Figure 4.1 are the specific effects of $R_{eff}(^{15}N,^{13}C)$, $\delta_{11} = \delta_{22}$, and δ_{33} on the spectrum. The axial symmetry and principal component values of the CS tensor allows its orientation to be assigned as δ_{33} along the C,N bond, and the equivalent δ_{11}, δ_{22} components perpendicular to the bond (*vide infra*). Parameters obtained from lineshape simulations of the ^{13}C NMR spectrum from K[Au(CN)$_2$] are presented in Table 4.2. After applying the vibrational corrections for $R_{eff}(^{15}N,^{13}C)$ described in Section 4.2, a C,N distance of 1.15(4) Å is derived. This bond length is consistent with the X-ray diffraction-derived value of 1.17(20) Å. The anomalously long Au-C bond length and large error parameters of the x-ray diffraction study, see Table 4.1, suggest that it is particularly worthwhile to corroborate the C,N bond length in this system. The NMR-derived bond length is of higher precision than the X-ray value, whose lower than typical precision is probably due to the large electron density of the neighbouring gold atom. This example shows how an SSNMR experiment can supplement an X-ray diffraction study where it may be difficult to pick out light atoms against a background of very heavy atoms.

The CS tensor for a carbon-13 nucleus in a linear molecule (i.e., one with a C_∞ symmetry axis) is defined by two components: $\delta_\perp$ measured perpendicular to the long axis of the molecule and $\delta_\parallel$ along it; furthermore, it is well known that $\delta_\parallel$ will be approximately -90 ppm.[165,166] In brief, the reason for this is that $\sigma^{paramagnetic}$, the term responsible for most of the change in shielding between nuclei in differing environments, is identically zero along a C_∞ axis.[167] K[Au(CN)$_2$] has CS tensor components $\delta_{11} = \delta_{22} = 279$ ppm, and $\delta_{33} = -81$ ppm, but the orientation of the PAS

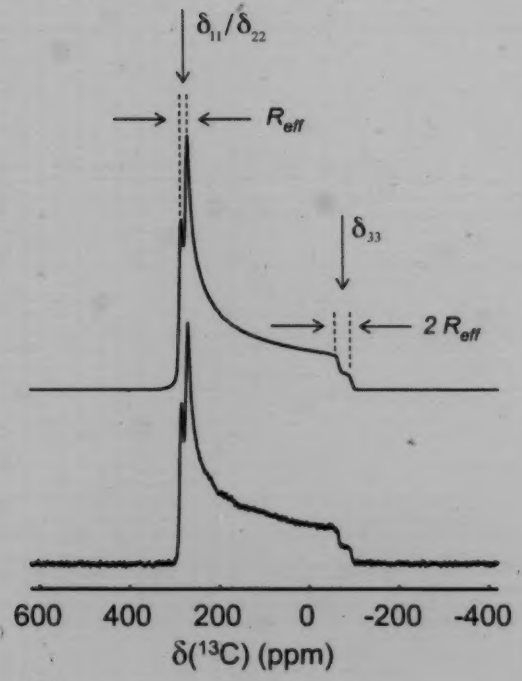

Figure 4.1: Simulated (upper trace) and experimental (lower trace) ^{13}C NMR spectra of a stationary sample of K[Au(CN)$_2$] at 11.75 T.

cannot be determined from symmetry arguments because the molecule is not quite linear, see Table 4.1; however, the value of δ_{33} is similar enough to that expected for $\delta_{\|}$ in a linear molecule to imply that it is oriented along the CN bond. The two remaining components, δ_{11} and δ_{22}, must therefore be perpendicular to the CN bond.

A relaxation study was also performed on K[Au(CN)$_2$], at 4.70 T, in order to investigate the origins of the ^{13}C NMR peaks linewidth. The ^{13}C longitudinal relaxation time constant, $T_1 \simeq 5$ min., was measured using an inversion-recovery experiment in which ten data points with delays of 121 μs to 1200 s were measured; see Figure 4.2. The value of the transverse relaxation time constant, $T_2 \simeq 4.3$ ms, was measured using a 90°-τ-180°-τ-ACQ Hahn-echo pulse sequence, in which τ

Table 4.2: Parameters Derived from Simulations of Carbon-13 SSNMR Spectra

Salt	Au site site	δ_{iso} (ppm)	LWHH[a] (Hz)	Ω (ppm)	κ	$R_{eff}(^{15}N,^{13}C)$[b] (Hz)	C-N bond[c] NMR (Å)	C-N bond X-ray (Å)
$K[Au(CN)_2]$		158.7(1)	85	360(2)	1	1850(100)	1.15(4)	1.17(20)
$[R_4N][Au(CN)_2]\cdot H_2O$[d]		151.90(5)	25	341(2)	1	1800(150)	1.16(5)	1.03(4)
$Tl[Au(CN)_2]$	1 or 2	167.5(4)	255	361(50)	1			
$Tl[Au(CN)_2]$	1 or 2	161.3(4)	315	352(50)	1			
$Tl[Au(CN)_2]$	3	151.7(2)	250	338(50)	1			
$Pb[Au(CN)_2]_2(H_2O)$[e]		167(1)		346	> 0.95			
$Pb[Au(CN)_2]_2$[e]		173(1)		353	> 0.95			
$K[Au(CN)_4]$		107.8(1)	110	337(3)	0.485(10)	1925(200)	1.14(6)	

[a]LWHH measured at 7.05 T.
[b]From best-fit simulated spectra.
[c]Corrected for vibrational effects (see text).
[d]R = n-butyl.
[e]SSNMR study from Katz et al.[95]

was increased from 0.2545 ms to 10.9025 ms in seven steps; see Figure 4.2. For a Lorentzian lineshape, the line width at half height, LWHH, caused by T_2 is given by $(\pi * T_2)^{-1}$. The LWHH of the potassium salt expected from T_2 relaxation alone is therefore ~75 Hz, which is quite close to the experimentally measured value of 85 Hz. It can therefore be concluded that residual dipolar coupling with ^{197}Au does not affect the ^{13}C spectrum, and ^{197}Au is probably self-decoupled because of efficient ^{197}Au quadrupolar relaxation at room temperature.

The structure of $[(n\text{-}C_4H_9)_4N][Au(CN)_2]\cdot H_2O$ differs from that of $K[Au(CN)_2]$ in that the $[Au(CN)_2]^-$ units are separated by large tetra-n-butylammonium cations,[132] with the closest Au-Au contact well beyond the reach of aurophilic bonding at 8.05 Å.[163,164] Local structural parameters for the single crystallographically independent site are provided in Table 4.1. The linewidth obtained for samples under MAS, 25 Hz, is much less than the value expected from residual dipolar coupling with ^{197}Au, see Section 4.2; therefore, the quadrupolar nucleus is clearly self-decoupled at room temperature. Carbon-13 NMR parameters derived from theoretical simulation of experimental spectra from the 30% ^{13}C,^{15}N-labelled material are given in Table 4.2. These spectral simulations show an axially-symmetric CS tensor and a value

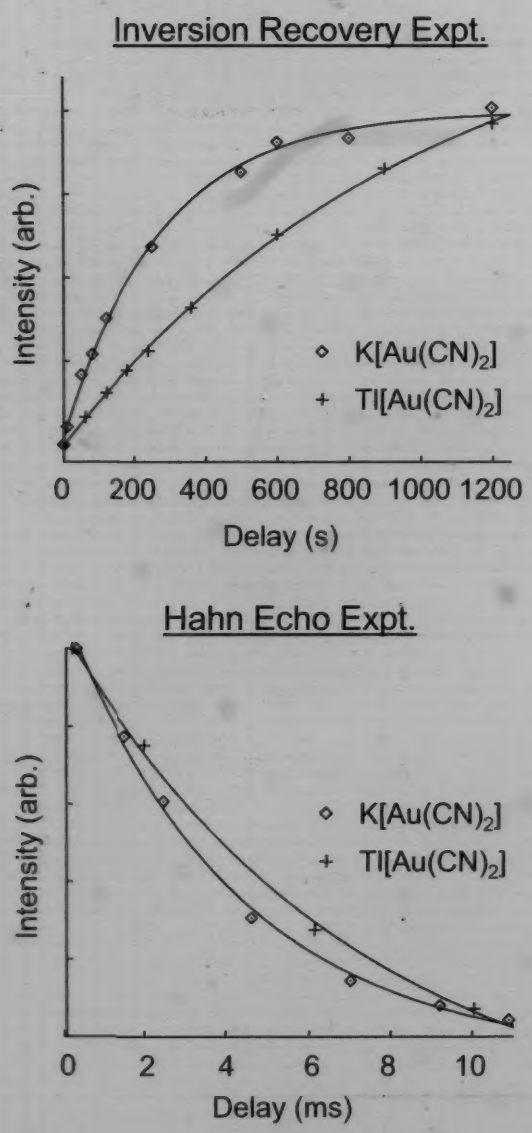

Figure 4.2: Carbon-13 T1 and T2 relaxation data and theoretical fits from $K[Au(CN)_2]$ and the low-frequency site of $Tl[Au(CN)_2]$. See text for details of experiments.

of -75 ppm for δ_{33}. Following the reasoning from above, we assign an analogous CS tensor orientation, i.e., δ_{33} along the C,N bond. The published value for the C,N bond length, 1.03(4) Å,[132] appears anomalously short when compared to typical values. Deriving a C,N bond directly from R_{eff} yields 1.194(33) Å, and after applying the vibrational corrections discussed above a final bond length of 1.16(5) Å is found. Whether correcting for vibrational effects or not, the NMR-derived values are more consistent with a typical C,N bond length than the 1.03(4) Å X-ray value. One possible explanation for the discrepancy is the inherent difficulty of fitting the small C,N electron densities against the background of the large Au atom when analyzing the X-ray experiment. Also, as it is now known that the material is a hydrate, the original structural solution not incorporate the water molecule would be prone to errors. Further discussion of this C,N bond length is presented below.

There have been several diffraction studies performed on the complicated structure of $Tl[Au(CN)_2]$,[134,168,169] in which there are gold-gold as well as gold-thallium metallophilic bonds. The unit cell is composed of alternating layers of Tl atoms and $Au(CN)_2$ groups; a small section of the unit cell is reproduced in Figure 4.3. There are three crystallographically distinct Au atoms, and these are linked together into two perpendicular chains of Au atoms with bond lengths as noted in Figure 4.3 and Table 4.1. There is an interesting range of Au coordination environments displayed in the structure: Au(1) shares bonds to four gold atoms, Au(2) is bound to two gold atoms, and Au(3) is coordinated to two gold and two thallium atoms. The two CN ligands bound to each Au atom are not related by any symmetry element, so that there are a total of six distinct carbon atoms in the structure. In the following discussion, we label the two carbons bonded to Au(1) as C1 and C2, those bonded to Au(2) as C3 and C4, and those bound to Au(3) as C5 and C6; the nitrogen atoms will be labelled analogously. The occurrences of Au(1) to Au(2) and Au(3) in the unit cell are in the ratio 1:1:2, and there are therefore the same total number of C5

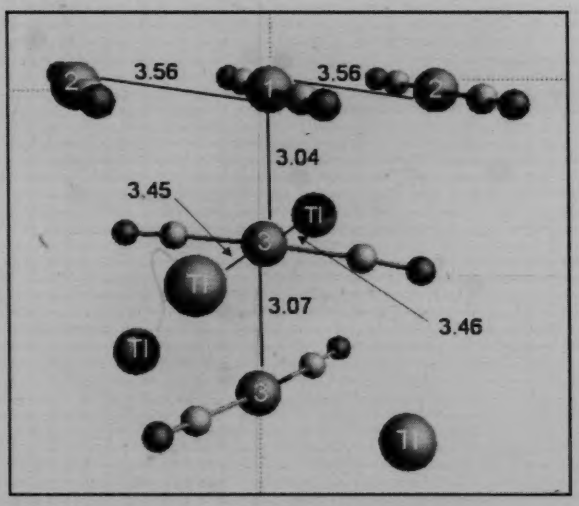

Figure 4.3: Local structure of $Tl[Au(CN)_2]$ depicting the intersection of the two Au chains, where Au atoms 1, 2, and 3 are numbered; and metallophilic bond lengths are given in Angstroms. Cyanide ligands are oriented with carbon bonded to the gold atoms.

and C6 atoms as there are C1 through C4 atoms.

Spectra from 30% ^{13}C,^{15}N-labelled samples of $Tl[Au(CN)_2]$ undergoing MAS are shown in Figure 4.4 where the 1:1:2 ratio of peak heights is apparent; it is interesting that the six symmetry-unique carbon atoms in $Tl[Au(CN)_2]$ produce only three ^{13}C peaks in the MAS NMR spectrum at 7.05 T. In the analogous spectrum at 11.75 T the two high-frequency peaks are asymmetric, which demonstrates that these two peaks arise from at least two carbon sites each. Given that at least four of the total six carbon sites are associated with the two high-frequency peaks, and that there must be twice the intensity produced from C5 and C6 as from C1-C4 sites, the only possible assignment is that the low-frequency peak is the sum of peaks from carbon atoms C5 and C6. It follows that the two high-frequency peaks are each composed of signals from one pair of the C1 through C4 atoms.

The structure of $Tl[Au(CN)_2]$ provides valuable insight into the isotropic chemical shifts observed. The authors of the original neutron diffraction study noted that

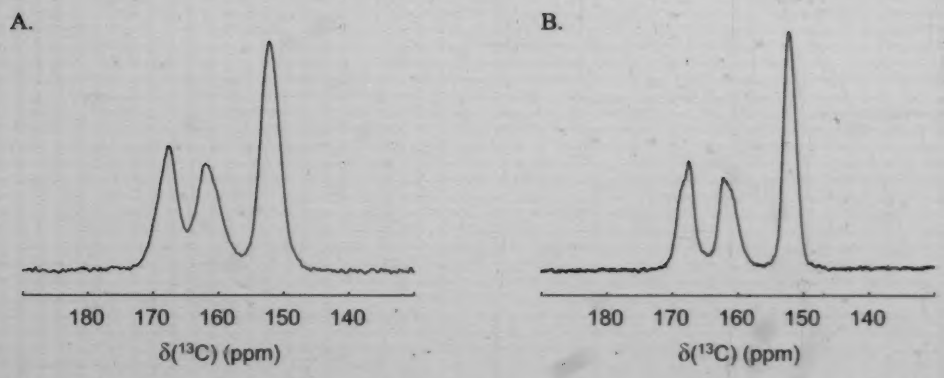

Figure 4.4: A. ^{13}C NMR spectrum of Tl[Au(CN)$_2$] under MAS, ν_{rot} = 10 kHz, acquired at 7.05 T. B. ^{13}C NMR spectrum of Tl[Au(CN)$_2$] under MAS, ν_{rot} = 12 kHz, acquired at 11.75 T.

the observed *Pbcn* structure of Tl[Au(CN)$_2$] displays pseudosymmetry: all positions in the crystal deviate by at most 0.3 Å from a higher-symmetry *Imcb* structure.[134] In the higher-symmetry space group, C1 to C4 are all equivalent, and C5 is equivalent to C6. One point of note is that within the *Pbcn* structure, Au(1) and Au(2) are differentiated by the fact that Au(1) is involved in an extra aurophilic bond, being at the intersection point of the two perpendicular Au chains shown in Figure 4.3. In the theoretical *Imcb* structure, Au(1) and Au(2) of the *Pbcn* structure converge to a single site, but only every second occurrence of the site equivalent to Au(3) from the *Pbcn* structure is occupied. This alternating occupation of Au(3) splits into two the otherwise equivalent C1 through C4 atoms in the *Imcb* structure. The pseudosymmetry reported by Blom et al.[134] demonstrates that the six nonequivalent carbon sites in the *Pbcn* structure are geometrically very close to being only three sites. It is also apparent from this argument that C1 through C4, shown above to be split into two NMR peaks 6.2 ppm apart, are different from each other in two ways: small geometrical differences and different aurophilic bonding of the directly bonded gold atom.

The pseudosymmetry present in $Tl[Au(CN)_2]$ provides a hint that the presence of two distinct chemical shifts from carbons C1-C4 is due to the presence of the different arrangements of aurophilic bonds. However, the experimental structure contains deviations of up to 0.3 Å from the higher-symmetry *Imcb* structure so it is necessary to explicitly compare the local structure around each carbon atom. The geometry of the two $Au(CN)_2$ anions containing C1-C4 are strikingly similar: all bond lengths are equal within 0.003 Å, and all bond angles are exactly equivalent (see Table 4.1). Therefore, it seems unlikely that the local structure of each anion is responsible for producing the two different chemical shifts observed for C1-C4. The first coordination sphere around the $Au(CN)_2$ anions containing C1 to C4 includes thallium cations and neighbouring $Au(CN)_2$ anions. It is important to evaluate the thallium contacts because this heavy atom can have a large effect on the chemical shift of nearby nuclei, an effect known as the relativistic heavy-atom light-atom (HALA) effect.[170,171] The HALA effect involves a relativistic induction of electron spin density on the heavy atom whose outcome is an altered chemical shift at nearby nuclei. The $Au(CN)_2$ anions containing C1-C4 are coordinated at each end by two Tl atoms, the average N-Tl bond length being 2.871 Å. While the N-Tl bond length is different for each nitrogen atom, the maximum deviation from this average is only 0.055 Å. It therefore seems unlikely that the very small changes in anion geometry and cation coordination are responsible for splitting the chemical shifts of C1-C4. We can then ascribe one of the two high-frequency peaks to C1 and C2, and the other peak to C3 and C4. The 6.2 ppm difference in chemical shifts between the two peaks provides a measure of the effect of the two 3.04 Å aurophilic bonds formed by the gold atoms bonded to C1 and C2, but not the gold atoms bonded to C3 and C4.

The low-frequency NMR peak of $Tl[Au(CN)_2]$ is assigned to carbons C5 and C6 as a corollary to the above arguments, and is shielded by 15.8 and 9.6 ppm with respect to the two peaks from carbons C1 through C4. Insight into why the

chemical shift for C5 and C6 differs from the two chemical shifts for C1,C2 and C3,C4 is again provided by consideration of the structure. This final $Au(CN)_2$ anion is also coordinated at the nitrogen atom by two thallium cations: N5 at 2.856 and 3.039 Å, and N6 at 2.861 and 3.091 Å. There is also a third, more distant, N-Tl contact at 3.414 Å for N5 and 3.178 Å for N6. Given that these more distant thallium contacts are significantly different, but C5 and C6 have the same chemical shift, these longer N-Tl bonds are probably not too influential on the shift. The remaining distances are similar to the range of 2.816 to 2.904 Å N-Tl bond lengths of N1 through N4, but the deviations from average are slightly larger. Comparison of the $Au(CN)_2$ anion containing Au(3) to the anions containing Au(1) and Au(2) shows that the anion geometry is nearly identical and the thallium coordination to the nitrogen atoms is also similar; however, there is a significant difference in the metallophilic bonding environment at Au(3), where two Au-Au and two Au-Tl bonds are present (see Figure 4.3). This difference in metallophilic bonding is therefore assigned as the cause of the difference observed for the chemical shifts of carbon atoms C5 and C6 as compared to C1 through C4. There are somewhat larger variations in local structure around C5 and C6 as compared to C1 through C4, viz. bond angles in the anion and N-Tl contacts, so assignment of the chemical shift change to solely alteration of the metallophilic bonding near C5 and C6 is less certain than the case of C1 and C2 versus C3 and C4. However, the difference in metallophilic bonding in the anion is likely the dominant effect causing the different chemical shifts found for C5 and C6 versus those of C1 through C4. In summary, a variation in isotropic ^{13}C chemical shifts of 6.2 ppm from differences in aurophilic bonding has been observed, while differences in metallophilic gold-thallium bonding has been found to cause a variation of 15.8 ppm.

The ^{13}C NMR spectrum of a stationary sample of $Tl[Au(CN)_2]$ was also acquired, unfortunately, multiple sites and broad linewidths make full analysis of the

lineshape difficult. An axially symmetric CS tensor is expected from the investigation of $K[Au(CN)_2]$ and $[(n\text{-}C_4H_9)_4N][Au(CN)_2]\cdot H_2O$, and the lineshape of this static spectrum is consistent with that symmetry, so a value of $\kappa = 1$ was fixed in the simulations. Spectral overlap prevented determination of the three R_{eff} values; therefore, the simulations instead used the average value of R_{eff}, 1815 Hz, from $K[Au(CN)_2]$ and $[(n\text{-}C_4H_9)_4N][Au(CN)_2]\cdot H_2O$. With the geometry, R_{eff}, δ_{iso}, and κ fixed, the only remaining parameter is the span,Ω . An initial estimate of Ωcan be obtained from the fact that δ_{33} is not expected to change very much from -80 ppm (*vide supra*). For an axially symmetric CS tensor, $\Omega = 1.5(\delta_{iso} - \delta_{33})$, making initial estimates of the respective spans for the δ_{iso} = 151.7, 161.3, and 167.5 ppm sites equal to 348, 362, and 371 ppm. A simulated spectrum using these parameters closely matches the shape of the experimental one, but is slightly too broad. Reduction of each span by 10 ppm produced a theoretical spectrum matching well with the experimental one, see Figure 4.5, and the chemical shift parameters are shown in Table 4.2. Because the three sites are not resolved, the entire width of the region containing the high-frequency discontinuites, ~50 ppm, is reported as an error range. However, given the above arguments used to set the initial estimate ofΩ , this large error range can be viewed as rather generous. A stationary experiment was chosen over a slow MAS experiment in order to limit the total MAS experimental time used for this thallium salt given its expected toxicity.

The ^{13}C MAS NMR spectrum of $Tl[Au(CN)_2]$ differs from those of the potassium and tetra-n-butylammonium aurocyanides in that a larger linewidth is observed, see Table 4.2. The observed linewidths match well with the values predicted from coupling to the neighbouring ^{197}Au nucleus, *vide supra*, but this is not the only possible source of line broadening. Other sources include chemical shift broadening, spin-spin coupling to $^{205/203}Tl$, or rapid relaxation. Comparing the lineshapes of the two high-frequency peaks at 4.70 and 11.75 T, see Figure 4.4, shows that the two

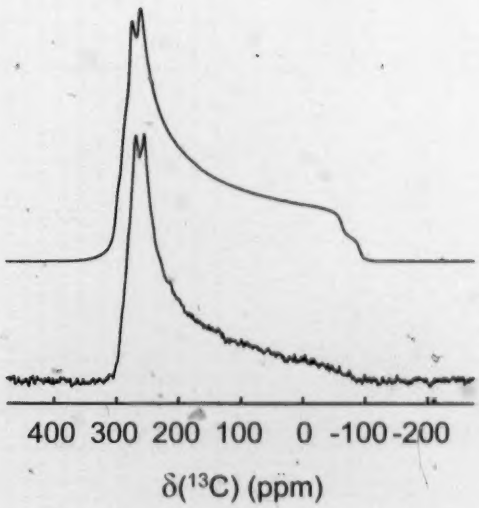

Figure 4.5: Experimental (lower trace) and simulated (upper trace) ^{13}C NMR spectra of a stationary sample of Tl[Au(CN)$_2$] at 11.75 T.

underlying sites are beginning to separate. In contrast, the lineshape of the 151.7 ppm peak is nearly exactly superimposable despite the magnetic field strength more than doubling. Such a field-independent linewidth shows that the cause is not a distribution of chemical shifts, which would lead to superimposable peaks plotted on a ppm rather than a frequency scale. We also performed relaxation measurements on Tl[Au(CN)$_2$] to measure the ^{13}C T_1 and T_2 relaxation time constants of the 151.7 ppm sites using the same methods applied to K[Au(CN)$_2$]; however, the measurements on Tl[Au(CN)$_2$] were performed at 11.75 T. The value of T_1 was determined as $\sim$17 min., using 9 data points spanning 1 s to 1200 s. Hahn-echo experiments yielded T_2 as $\sim$7.3 ms, where the long T_1 limited acquisition to only four data points, spanning 0.15 ms to 10.05 ms (at which point the signal had decayed to $< 10\%$ of its original value). The data from these relaxation experiments is reported in Figure 4.2. In Tl[Au(CN)$_2$], the contribution from T_2 to the LWHH is only $\sim$45 Hz, whereas the experimental value of the LWHH is much larger at 250 Hz. Coupling with other

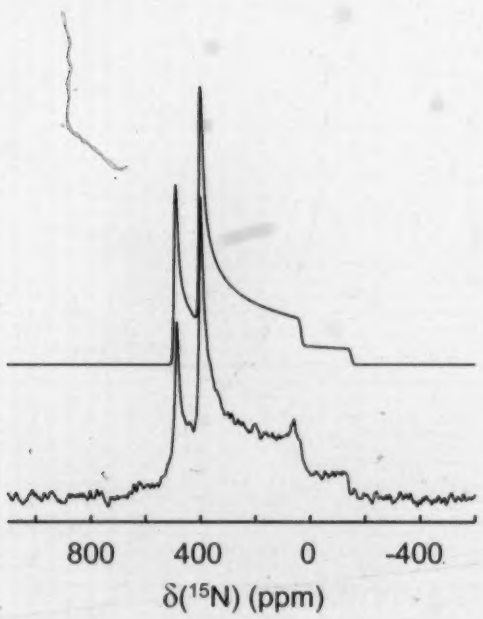

Figure 4.6: Simulated (upper trace) and experimental (lower trace) ^{15}N cross-polarized NMR spectra acquired from a stationary sample of [(n-C_4H_9)$_4$N][Au(CN)$_2$]·H$_2$O at 4.70 T.

nuclei in the sample is the only remaining explanation of the broad ^{13}C linewidth in Tl[Au(CN)$_2$]. However, it is not possible at this time to differentiate between coupling to the directly bonded ^{197}Au, or the $^{205/203}$Tl nuclei. This ambiguity arises because while one would expect $^{205/203}$Tl,^{13}C dipolar interactions to be removed by MAS, $J(^{205/203}\text{Tl},^{13}\text{C})$ would not be.

4.4.2 ^{15}N NMR of Gold(I) Dicyanides

The sample of 30% ^{13}C,^{15}N-labelled [(n-C_4H_9)$_4$N][Au(CN)$_2$]·H$_2$O discussed above was also investigated using ^{15}N SSNMR. A CP Hahn-echo spectrum from a stationary powder of this sample together with the best-fit simulation is displayed in Figure 4.6, while data determined from spectral simulations are given in Table 4.3. Just as in the ^{13}C data, an axially symmetric ^{15}N CS tensor is found, so the orientation of δ_{33} is assigned as coincident with the C,N bond. The derived value of

Table 4.3: Parameters Derived from Simulations of Nitrogen-15 SSNMR Spectra

Salt	δ_{iso} (ppm)	LWHH[a] (Hz)	Ω (ppm)	κ	$R_{eff}(^{15}N,^{13}C)$[b] (Hz)	C-N bond[c] NMR (Å)	C-N bond X-ray (Å)
$K[Au(CN)_2]$	266.0(1)	25	475(20)	0.993(4)			
$[R_4N][Au(CN)_2]\cdot H_2O$[d]	275.33(5)	9	505(5)	1	1790(75)	1.17(3)	1.03(4)
$Tl[Au(CN)_2]$	291.3(5)	325					
$Tl[Au(CN)_2]$	284(2)	325					
$Pb[Au(CN)_2]_2(H_2O)$[e]	266(1)		480	> 0.8			
$Pb[Au(CN)_2]_2(H_2O)$[e]	259(1)		450	> 0.7			
$Pb[Au(CN)_2]_2$	276(1)						
$K[Au(CN)_4]$	285.31(5)	25	495(25)	1.000(1)			
$K[Au(CN)_4]$	282.38(5)	25	495(30)	0.989(1)			

[a]LWHH measured at 11.75 T.
[b]From best-fit simulated spectra.
[c]Corrected for vibrational effects (see text).
[d]R = *n*-butyl.
[e]SSNMR study from Katz et al.[95]

R_{eff}, 1790(75) Hz, agrees with the value determined from the ^{13}C spectrum within experimental uncertainty. Correcting for vibrational effects leads to a final bond length of 1.17(3)Å. Both NMR measurements of R_{eff}, by observing ^{13}C or ^{15}N, support the value of a typical C,N bond length in opposition to the X-ray study where an anomalously short distance was reported.

The sample of 50% ^{13}C,^{15}N-labelled $K[Au(CN)_2]$ was also studied using ^{15}N SSNMR; however, the long T_1 values and lack of protons for CP enhancement prevented acquisition of spectra from stationary samples. Values for the CS parameters were therefore obtained from a slow-spinning MAS experiment. As mentioned above, the spinning-sideband intensities depend on the CS tensor span and skew, as well as the dipolar coupling to the neighbouring ^{13}C nucleus. The spinning sideband intensities were analyzed as an AX spin pair using the nonlinear least-squares fitting mode of the SPINEVOLUTION software package.[135] The value of $R_{eff}(^{15}N,^{13}C)$ used in this analysis was fixed to that found from analysis of the ^{13}C NMR spectrum, and the orientation of δ_{33} was not varied, but affixed along the C,N bond axis. Presented in Figure 4.7 are the experimental spectrum and best-fit simulation, while

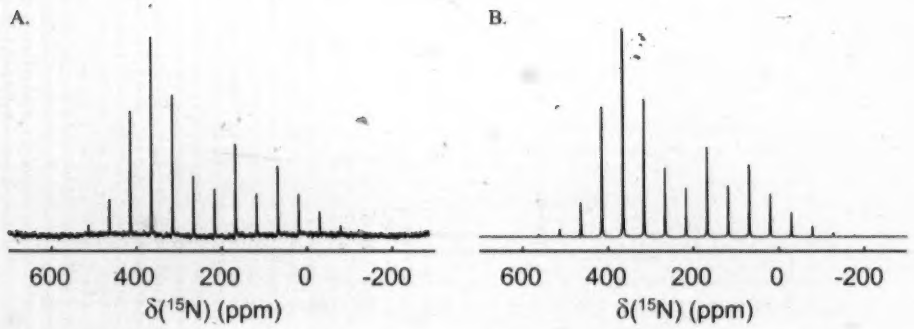

Figure 4.7: Experimental (A.) and simulated (B.) slow-spinning ^{15}N NMR spectra of K[Au(CN)$_2$] at 11.75 T ($\nu_{rot} = 2.5$ kHz).

the parameters used in the simulation are given in Table 4.3. Error values shown in Table 4.3 are 99% confidence intervals determined in the fitting procedure; however, the procedure does not incorporate error ranges in the experimental peak heights, so the reported error values should be considered conservative. Also, for isolated spins, the difficulty in obtaining accurate values of κ from slow MAS data in systems where this parameter is near 1 have been well documented,[42,136] and this difficulty probably persists in the present AX spin system. The fact that the fitting procedure determines a value of approximately 1 for κ, and reports a small error range, should therefore not be over-interpreted in terms of being an absolute determination of axial symmetry.

Nitrogen-15 NMR spectra of Tl[Au(CN)$_2$] were also acquired. The isotropic peak of the MAS spectrum is displayed in Figure 4.8, where it may be observed that none of the six unique cyanides are clearly resolved. Unfortunately, the low receptivity of ^{15}N combined with the broad lines and site multiplicity prevented determination of the CS tensors from slow MAS experiments. If the hypothesis that ^{13}C chemical shifts of Tl[Au(CN)$_2$] are insensitive to small changes in local geometry but dependent mainly on bonding around the Au atom is correct, the further-displaced ^{15}N nuclei would be expected to show less sensitivity in their chemical shifts. Conversely,

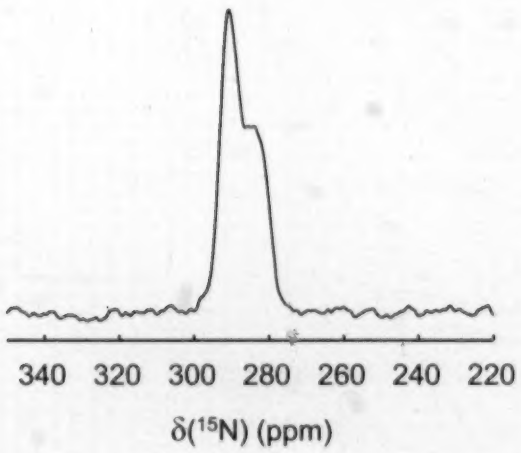

Figure 4.8: Experimentally observed ^{15}N NMR spectrum of Tl[Au(CN)$_2$] at 11.75 T under MAS ($\nu_{\mathrm{rot}} = 10$ kHz).

if it were the thallium contacts that instead controlled the ^{13}C chemical shifts, the ^{15}N nuclei would be expected to display a larger spread in chemical shifts as they are all closer to the Tl atoms. The above assignment of metallophilic bonding controlling ^{13}C chemical shifts is thus borne out in the observation of clearly separated ^{13}C peaks, while nonequivalent ^{15}N sites remain unresolved.

4.4.3 ^{13}C and ^{15}N NMR of a Gold(III) Tetracyanide

A sample of 50% ^{13}C,^{15}N-labelled potassium tetracyanoaurate(III), K[Au(CN)$_4$], was prepared in order to investigate how the formal oxidation number of Au affects the cyanide NMR parameters. A structure for the hydrate has been published,[172] but we found the dehydrate more amenable to NMR study as the hydrate is not stable to dehydration,[154] and also yielded fewer NMR resonances than expected for the low-symmetry hydrate. Neutron diffraction data for the hydrate evidences an approximately square-planar [Au(CN)$_4$] anion, no Au-Au contacts < 4.8 Å, and bond lengths similar to those of the gold(I) cyanides.[172] For an ideal D_{4h} [Au(CN)$_4$]

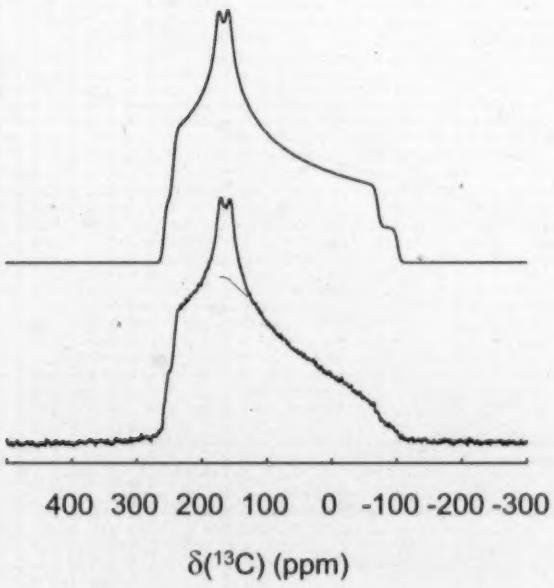

Figure 4.9: Experimental (lower trace) and simulated (upper trace) ^{13}C NMR spectra of a stationary sample of K[Au(CN)$_4$] at 11.75 T.

anion, two of the mirror planes would restrict the principal axis systems of both ^{13}C and ^{15}N CS tensors: one component would be along the CN bond, one perpendicular to the plane of the molecule, and the third perpendicular to the first two components.

Only one ^{13}C isotropic peak is observed in the MAS NMR spectrum for the unknown dehydrate structure, evidencing a close similarity to D_{4h} symmetry. We therefore expect the CS tensor to have an orientation similar to that described for a D_{4h} tetracyanoaurate anion. Observing the spectrum of a stationary sample, Figure 4.9, it is clear that the value of δ_{33} is very similar to that observed for the gold(I) dicyanides. This similarity provides further evidence that one CS tensor component is aligned along the C,N bond, and allows assignment of that component as δ_{33}. Therefore the value of β (see Section 3.6.1) was assigned as 0°, which allowed the best-fit simulated spectrum displayed in Figure 4.9 to be generated, using the parameters reported in Table 4.2. The remaining task is to assign which of the prin-

cipal CS tensor components is perpendicular to the (approximate) molecular plane. Comparing δ_{11} and δ_{22}, it may be seen that the value of δ_{11}, 246 ppm, is similar to the ~270 ppm found for δ_{11},δ_{22} values in the dicyanoaurate(I) salts, while the value of δ_{22}, 162 ppm, is quite different. This comparison to the gold(I) dicyanides shows that δ_{22} is the component out of the molecular plane, as CS tensor components are sensitive to changes in the planes perpendicular to their direction. The $[Au(CN)_4]$ anion may not be of D_{4h} symmetry, so the described tensor orientation should be taken as approximate. However, given the similarity of δ_{33} = -88 ppm to the value of ~ -80 ppm observed for the gold(I) dicyanides, it seems unlikely that δ_{33} deviates much from the C,N bond vector.

Nitrogen-15 NMR data for the 50% ^{13}C,^{15}N-labelled sample of $K[Au(CN)_4]$ is summarized in Table 4.3. The CS tensors for each of the two sites were determined using the same method applied for analysis of $K[Au(CN)_2]$: nine peaks from a slow MAS spectrum obtained at 11.75 T were modelled as an AX spin system using a least-squares fitting method.[135] Again, the value of R_{eff} was fixed to the value determined from the ^{13}C NMR spectrum, and δ_{33} was affixed along the C,N bond vector. There are two isotropic ^{15}N shifts observed, showing that the dehydrate crystal structure may deviate at least somewhat from anions of D_{4h} symmetry. It is perhaps worthwhile pointing out that the presence of two ^{15}N peaks does not prove a break from D_{4h} symmetry since there may simply be two molecules in the asymmetric unit cell of this unknown structure. However, the small 2.9 ppm difference in isotropic shifts would not require much deviation from D_{4h} symmetry. While the ^{13}C isotropic shift for this gold(III) cyanide lies some distance from the observed range of values for gold(I) cyanides, the ^{15}N isotropic shift of $K[Au(CN)_4]$ lies within the range seen for gold(I) complexes. The carbon atom is directly bound to the gold atom and hence its chemical shift is affected greatly by a change in oxidation state of the metal. Conversely, the chemical shift of the more distant

nitrogen atom is less affected by the oxidation state of the metal, less in fact than the differences in bonding and geometry between dicyanoaurate(I) anions in different salts.

4.5 Conclusions

Carbon-13 and nitrogen-15 NMR spectra of several gold(I) dicyanides and one gold(III) tetracyanide have been acquired and are useful in providing survey data for the interpretation of future NMR experiments on cyano gold coordination polymers. Chemical shift tensors for the cyano ^{13}C and ^{15}N nuclei are reported, and a range of isotropic shifts for the various environments were determined. Static ^{13}C, and in some cases ^{15}N, NMR spectra were used to provide several r(C,N) distance measurements; in one case, the value of 1.17(3) Å for the CN bond in [(n-$C_4H_9)_4N$][$Au(CN)_2$]·H_2O, a measurement more accurate than the existing X-ray bond length was determined. The impact of metallophilic bonding on ^{13}C chemical shifts was isolated, and this bonding was found to cause a range of approximately 16 ppm in $\delta_{iso}(^{13}C)$. Also, the effect of gold's formal oxidation state on ^{13}C and ^{15}N chemical shifts were determined; specifically, a change from gold(I) to gold(III) was found to decrease the cyanide ^{13}C chemical shift by approximately 50 ppm, whereas only minor changes were observed for the ^{15}N chemical shift of the the more distant nitrogen nucleus.

Chapter 5

A ^{15}N and ^{13}C NMR Study of Disorder in Polymeric Gold Monocyanide

5.1 Introduction

As discussed in Chapter 4, cyanoaurate coordination polymers have been shown to possess novel structures and desirable properties.[62,63,68,82–92] The simplest member of this class of materials is gold monocyanide, and an SSNMR study of this disordered polymeric material is presented below. Benchmark NMR data presented in Chapter 4 is shown to allow the interpretation of NMR spectra from AuCN; furthermore, the methods applied here for elucidation of structural disorder in AuCN should prove generally applicable to studies of other cyanoaurate coordination polymers.

Monocyanides formed by the group 11 transition metals, of which AuCN is the

A version of this chapter has been published. Harris, K.J.; Wasylishen R. E. *Inorg. Chem.* **2009,** *48,* 2316-2332

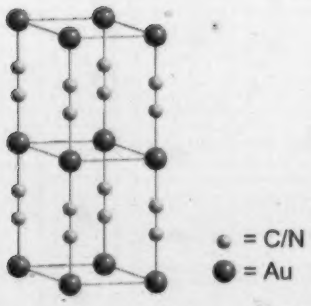

Figure 5.1: Two unit cells of AuCN; carbon and nitrogen atoms are not distinguished by the neutron diffraction experiment and are therefore represented using the same shade. See text for further discussion of the structure.

heaviest, resisted structural characterization for a long time, mainly due to disorder and poor sample crystallinity. A series of powder X-ray and neutron diffraction studies have, at long last, determined accurate structures for these materials.[173–180] Two polymorphs of CuCN are known, and structures of both the high temperature, HT-CuCN, and low temperature, LT-CuCN, polymorphs of CuCN have been determined.[174,175,178–180] In HT-CuCN, AgCN and AuCN, the materials are composed of infinite, linear $[\text{-M-CN-}]_{(\infty)}$ chains,[174,176,177] with neighbouring chains aligned at the metal for AuCN, but staggered for HT-CuCN and AgCN. Chain alignment in AuCN presumably[173] arises from the favorable energetics of forming aurophilic bonds.[51–55] LT-CuCN is also comprised of infinite MCN chains, but these are packed together in a more complicated way, with bond angles along the chain deviating slightly from 180°, ranging from 174.0 to 179.3°.[175] Neighbouring MCN chains in LT-CuCN are also lined up at the metal, e.g., in two neighbouring chains, d(Cu3-Cu3) = 2.997 Å.[175] The remaining group 11 monocyanide, AuCN, resisted structural characterization for a long time due to the unavailability of crystals suitable for single-crystal diffraction measurements. A combined total neutron diffraction and X-ray diffrac-

tion study of the powdered material determined the structure, but showed evidence of disorder.[177] The structure is depicted in Figure 5.1, where it can be seen that the infinite $\cdots$CN-Au-CN$\cdots$ chains are aligned to form sheets of aurophilically bonded Au atoms (Au-Au distance = 3.39 Å). Interestingly, one phase of AuCN monolayers adsorbed onto an Au(111) surface has been shown, through scanning tunneling microscopy and low-energy electron diffraction, to have the same structure as a 2D slice of the structure displayed in Figure 5.1.[181,182]

Despite the excellent progress represented by the diffraction studies, a complete picture of the structure is not obtainable from diffraction experiments alone. For example, it is not possible to differentiate the carbon from the nitrogen atoms in these systems using diffraction experiments, making the orientation of the cyanide ligands in these chains unknown.[173–180] Therefore, some other form of spectroscopy is required to determine the disorder superimposed on the known average structures. Even before a reliable structure of CuCN was determined using diffraction, a combined SSNMR and NQR investigation indicated a linear structure incorporating "head-tail" disorder of the cyanide ligands.[183] The EFG at copper was found to depend critically on the orientation of the two neighbouring cyanides, and $^{65/63}$Cu NQR spectroscopy was the deciding factor in determining the cyanide orientations. It was found that 30±10% of the metal sites have the two coordinating cyanides in opposing orientations, [-NC-Cu-CN-], while 70±10% have the two cyanides in the same orientation, [-CN-Cu-CN-].[183] The relative orientation of cyanide ligands in AgCN has also been investigated using SSNMR.[140] Here, J coupling between ^{13}C and $^{109/107}$Ag was observed in the ^{13}C NMR spectra, and proved to be the key factor in determining cyanide head-tail disorder in AgCN. Interestingly, the same ratio of metal sites with neighbouring cyanides opposed vs. aligned was found in both CuCN and AgCN. Head-tail disorder of the cyanides is not the only possible mode of disorder that may be uncovered using SSNMR. At least two polymorphs

are formed by CuCN,[174,175,178–180] and theoreticians have proposed a second polymorph of AuCN;[184,185] therefore, it seems prudent to consider polymorphism when interpreting the NMR spectra. Static disorder of the long chains with respect to each other has also been proposed.[174,176,177] Of course, there are other forms of disorder, e.g. vacancies, that can occur in such systems, but cyanide head-tail disorder, chain slipping, and polymorphism are the most likely types.

Presented below is a ^{13}C and ^{15}N SSNMR study investigating the form of disorder superimposed on the known average structure of AuCN. Several synthetic routes were examined to determine the effects of preparation conditions on sample composition. Samples of AuCN, in which 50% of the cyanide ligands are ^{13}C,^{15}N dilabelled, have been analyzed using NMR spectroscopic methods similar to those utilized in Chapter 4. Additionally, we applied ^{13}C,^{13}C homonuclear dipolar recoupling experiments for assistance in assigning sites in the 1D spectra.

5.2 Experimental

5.2.1 Sample Preparation

Gold monocyanide was prepared via several synthetic routes. The first sample, Intermediate(A), was synthesized using the method of U.S Patent #4,222,996.[186] 0.5 g of metallic gold was dissolved in 2.5 mL aqua regia (3:1 HCl/HNO_3), and then diluted to an orange/yellow solution with 50 mL of distilled water. This solution was then filtered through a sintered glass frit and treated with 21 mL of 1M KOH solution (added dropwise) until a pH of 12 was reached, at which point the solution was a pale yellow. The solution appeared to be slowly turning green, and was quickly treated with 0.241 g (0.75 equivalents) of Na_2SO_3, yielding a dark violet solution, to which 0.1797 g of 50% ^{13}C,^{15}N-labelled KCN was added. This solution was then acidified dropwise with 1M HCl solution to a pH of ~2. When neutral pH

was reached, the solution appeared to contain a milky white solid, which quickly turned yellow with lowering pH. The solid collected by vacuum filtration, followed by washing with distilled water and methanol is labelled Intermediate(A). AuCN(A) was synthesized by soaking Intermediate(A) in distilled water for 1 week at room temperature, filtering, and washing with several volumes of water, and then with MeOH. Intermediate(A′) was prepared analogously to Intermediate(A), except that a 10% excess of the reducing agent, Na_2SO_3 was applied. The only observable difference being the presence of some small amount of dark precipitate yielded by the addition of the reducing agent (likely some small particles of metallic Au). This precipitate appeared to colour the milky white precipitate (produced by neutralizing the Au(I) basic solution) an iridescent milky blue, and produced a final product that was tinted green instead of the expected lemon yellow. A similar soaking and washing procedure provided AuCN(A′) from Intermediate(A′). Hydrothermal treatment of AuCN(A) was performed in a teflon-lined sealed bomb in an oven at 160 °C for two weeks using a few mole % of KCN and ~10 mL of distilled water. The final synthetic method produced yellow-coloured AuCN(B) from 50% ^{13}C,^{15}N-labelled $K[Au(CN)_2]$, prepared as described in Chapter 4, by treatment with HCl at 60-70 °C.[152]

Samples of 99% ^{13}C,^{15}N dilabelled KCN and 90% ^{13}C monolabelled NaCN were available commercially and were investigated using SSNMR without further purification. $Na[Au(CN)_2]$ was prepared by treating a sample of AuCN, synthesized analogously to AuCN(B), with a hot solution of the 90% ^{13}C labelled NaCN; a near stoichiometric amount of NaCN was added until only a very small amount of the insoluble AuCN remained, and this starting material was then filtered off. The sample of $K[Au(CN)_2]$ investigated further here is the sample discussed in Chapter 4. All samples labelled "amorphous" were dissolved in water, which was subsequently removed under high vacuum with vigorous stirring.

Powder XRD measurements used an Inel powder diffractometer with copper $K\alpha_1$ radiation. IR spectra were collected on a Nic-Plan FTIR Microscope, including a reinvestigation of AgCN samples discussed in a previous publication.[140,187]

5.2.2 SSNMR

Carbon-13 NMR spectra were acquired at 50.3 MHz (4.70 T) using a Chemagnetics CMX Infinity 200, at 75.5 MHz (7.05 T) using a Bruker Avance 300, or at 125.8 MHz (11.75 T) with a Bruker Avance 500. All ^{13}C experiments performed on AuCN used powdered samples packed in 4 mm outer diameter rotors, were recorded using 4 μs $\pi/2$ pulses, and a 20 min. recycle delay. NMR spectra of all samples other than AuCN were acquired at 11.75 T, and used samples packed in 2.5 mm outer diameter rotors. Experiments on KCN and NaCN used 1 μs $\pi/4$ pulses and 10 min. recycle delays, while spectra of $Na[Au(CN)_2]$, $K[Au(CN)_2]$, and residue from the Intermediate(A) $\rightarrow$ AuCN(A) reaction water used 2 μs $\pi/2$ pulses and 25 min. recycle delays. Carbon-13 NMR peaks were referenced to TMS by setting the high-frequency peak of an external adamantane sample to 38.56 ppm.[155] Bloch-decay experiments were used for MAS spectra, while Hahn-echo experiments were used for spectra of stationary samples.

Two-dimensional ^{13}C homonuclear dipolar-correlation experiments made use of the $SR26_4^{11}$ pulse sequence.[46,47,49,50] Phase cycling and pulse timings were those of the published sequence,[50] pure absorption spectra were obtained using the States method, and recoupling-field power levels were optimized using arrays of experiments with power levels near the theoretical value (typically, steps of 0.1 to 0.3 dB). The pulse sequence was benchmarked using 60% 1-^{13}C-labelled glycine, Raylo Chemicals, in which intermolecular distances are short enough to allow ^{13}C,^{13}C recoupling.[47] Setup spectra of 60% 1-^{13}C-labelled glycine were obtained at an MAS rate of 8.097 kHz using two excitation blocks totaling 3.95 ms; DQ recoupling effi-

ciencies similar to reported values were obtained.[46,47] Recoupling experiments performed on AuCN used an MAS rate of 9.615 kHz and three $SR26_4^{11}$ DQ-excitation blocks totaling 4.992 ms.

Nitrogen-15 NMR spectra were collected at 50.7 MHz (11.75 T) using a Bruker Avance 500 or at 91.2 MHz (21.14 T) using a Bruker Avance II 900. All experiments used 4 mm rotors, and peaks were referenced by setting the low-frequency peak of an external sample of ammonium nitrate to 23.8 ppm (with respect to neat liquid ammonia at 0 ppm).[162] Experiments on AuCN used a B^1 field sufficient to generate a 5 μs $\pi/2$ pulse for experiments recorded at 4.70, 7.05, and 11.75 T, while a 9 μs $\pi/2$ pulse strength was applied for experiments at 21.14 T. All spectra were acquired as Bloch-decay experiments, using 20° excitation pulses and 10 min. recycle delays.

Carbon-13 and nitrogen-15 NMR spectra of stationary samples were simulated using WSOLIDS,[24] while nitrogen-15 spectra from slow-spinning samples were simulated using SPINEVOLUTION.[135] Simulated ^{13}C spectra from MAS samples including residual dipolar coupling to ^{197}Au were calculated using WSOLIDS.[24] We found the programs SIMPSON[188] and SPINEVOLUTION[135] invaluable for theoretically comparing various recoupling conditions used in the $SR26_4^{11}$ pulse sequence.

5.3 Results and Discussion

5.3.1 ^{13}C NMR of Gold(I) Monocyanide

Figure 5.2 displays the MAS spectrum of AuCN(A), and the isotropic shifts, linewidths and peak areas are summarized in Table 5.1. There are two isotropic shifts visible despite the fact that the crystal structure contains only one unique site in the absence of disorder. A 2D homonuclear dipolar-correlation experiment, $SR26_4^{11}$, was performed in order to determine if there was an impurity or if there is indeed two different sites in the material. The ~5 ms excitation period used yields spectra

Table 5.1: Carbon-13 NMR Parameters of AuCN

AuCN Sample	δ_{iso} (ppm)	LWHH[a] (Hz)	Area (%)
AuCN(A)	154.1(5)	590	76(5)
	164.1(5)	450	24(5)
AuCN(B)	154.6(5)	550	84(5)
	164.0(5)	450	6.5(2)
	136(2)	540	6.5(5)
	145(2)	650	3(3)

[a]LWHH measured at 11.75 T.

sensitive to ^{13}C,^{13}C dipolar couplings corresponding to C-C distances of ~5 Å, the exact distance depending on complicated experimental and site parameters. This distance is large enough that even under the presence of chain slipping and CN head-tail disorder, inter-site correlation can be probed. In the $SR26_4^{11}$ experiment, peaks occur only for dipolar-coupled nuclei, and are observed in the indirect dimension at the sum of the chemical shifts for the two sites. The format of the experimental spectrum shown in Figure 5.3 is such that the self-correlation peaks expected from the network structure of AuCN occur on the diagonal, and are observed for both peaks. Because the two sites are at +10 and +20 ppm from the transmitter in the direct dimension, the two +30 ppm peaks in the DQ dimension demonstrate intersite connectivity. Experimental artifacts have no frequency dependence in the second dimension and create the small features at 0 ppm. Unfortunately, the similarity of model C-C distances produced by head-tail disorder or chain slipping precluded us from attempting to distinguish between them with the resolution available using this experiment.

Two separate ^{13}C isotropic shifts are observed within the same material, therefore the chemical shift of the carbon nucleus must be sensitive to some disorder in the material. Assignment of the multiplicity as due to head-tail cyanide disorder or

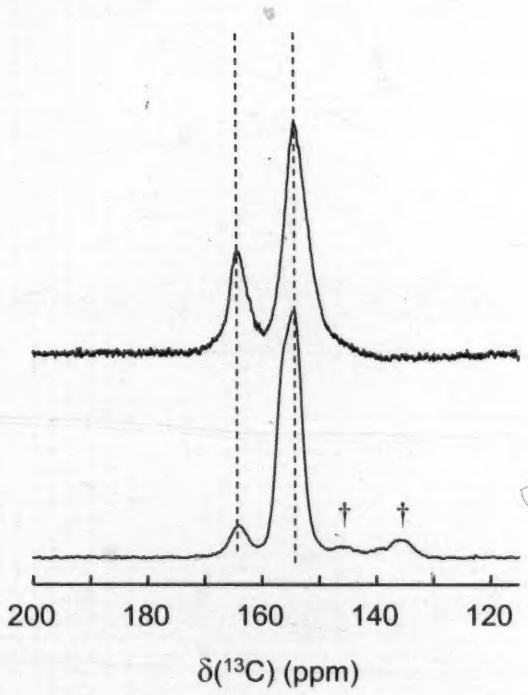

Figure 5.2: Upper spectrum: ^{13}C NMR spectrum of AuCN(A) under MAS, $\nu_{\mathrm{rot}} = 13$ kHz, acquired at 11.75 T. Lower spectrum: ^{13}C NMR spectrum of AuCN(B) under MAS, $\nu_{\mathrm{rot}} = 10$ kHz, also acquired at 11.75 T. Peaks marked with a † in the spectrum of AuCN(B) have been assigned as impurities (see text).

chain slipping can be performed by comparison to the expected chemical shift effect of each. In an SSNMR study of CuCN, an upper limit of ~2 ppm for the difference in $\delta_{iso}(^{13}\mathrm{C})$ from a change in neighbouring CN orientation was found, i.e., the difference in δ_{iso} for ^{13}C-Cu-NC versus ^{13}C-Cu-CN is < 2 ppm.[183] The analogous effect of cyanide orientation on ^{13}C chemical shift in the material AgCN was placed as approximately 0.8 ppm.[140] The carbon-metal bond distance in AuCN is midway between that of AgCN and CuCN, so the effect of neighbouring CN orientation on ^{13}C chemical shift is likely midway between 0.8 and < 2 ppm, or at least much less than 10 ppm. Because chain slipping would be accompanied by breaking of aurophilic bonds, the effect of chain slipping on $\delta_{iso}(^{13}\mathrm{C})$ can be estimated from

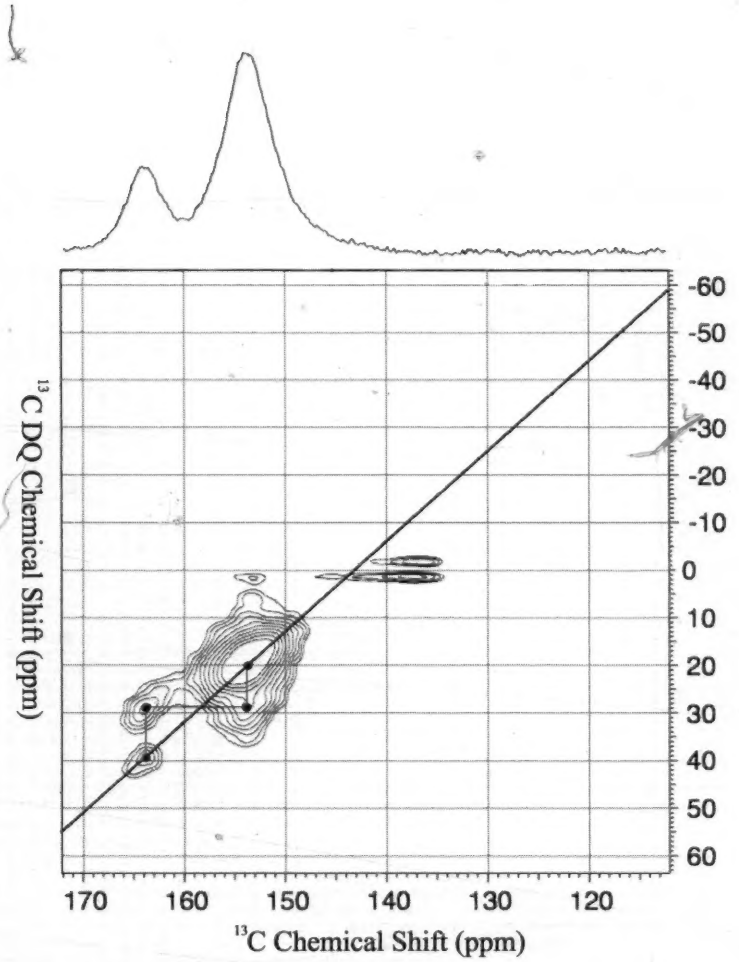

Figure 5.3: Carbon-13 $SR26_4^{11}$ homonuclear dipolar correlation spectrum of AuCN(A) acquired under MAS, $\nu_{\text{rot}} = 9.615$ kHz, at 7.05 T; spectrum resulted from 6 days of experimental time. The corresponding 1D Bloch-decay experiment is placed at the top of the spectrum. In the presented expansion, self-correlation appears on the diagonal, while inter-site correlations occur as pairs of peaks offthe diagonal. Spectral artifacts have no frequency dependence in t_1, and occur at 0 ppm in the indirect dimension.

the data presented in Chapter 4 for $Tl[Au(CN)_2]$. For $[Au(CN)_2]^-$ moieties with nearly identical geometries, changes are seen in the ^{13}C isotropic shifts of up to 15.7 ppm from differences in the metal identity and length of metal-metal bonds, while a change of 5.9 ppm was observed for differences in the number and length of Au-Au contacts for aurophilic bonding. The observed 10 ppm difference between the two AuCN(A) sites is consistent with this range while being noticeably larger than the small range expected from CN head-tail disorder. This argument does not rule out the presence of head-tail disorder, it simply shows that any effect of that type of disorder on $\delta_{iso}(^{13}C)$ is likely hidden in the large (5 ppm) linewidth.

Infrared spectroscopy is also useful, and serves to confirm the interpretation of the ^{13}C NMR spectra from this material. The infrared spectrum of AuCN(A), represented in Figure 5.4, shows two $^{12}C,^{14}N$ peaks at 2230.2 and 2167.4 cm^{-1}, which have a similar intensity ratio to those in the ^{13}C NMR spectrum. Two peaks from the $^{13}C,^{15}N$-labelled cyanides in the sample are also visible at 2147.8 and 2087.1 cm^{-1}, positions matching well with those predicted by the simple harmonic oscillator model. Sensitivity of the IR spectrum to head-tail cyanide disorder versus chain slipping may be found by investigating the analogous material AgCN. NMR spectroscopy has shown that there is head-tail cyanide disorder in AgCN, while there is only one stretching mode present in the IR spectrum.[140,187] It seems that vibrational spectroscopy is not sensitive to head-tail disorder, perhaps because the M-C versus M-N force constants mimic the indistinguishability of the bond lengths. In the silver-based material, without aurophilic bonding, the chains are farther apart than those in AuCN at 5.9 versus 3.4 Å, and are not aligned at the metal position. Since the chains of AuCN interact more strongly than those of AgCN, it is quite plausible that IR spectroscopy is sensitive to chain slipping in AuCN while no change is observed in AgCN. Vibrational spectroscopy therefore supports the ^{13}C NMR argument for the presence of chain slipping in AuCN.

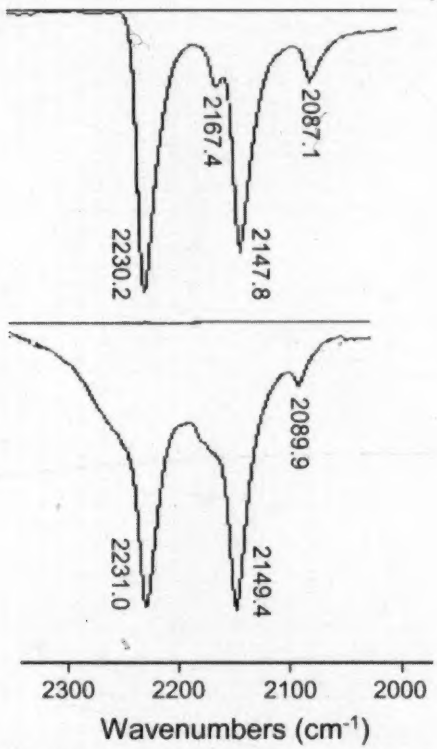

Figure 5.4: IR spectra of the CN stretching region, upper spectrum from AuCN(A), and lower spectrum from AuCN(B).

An alternate synthetic method, *vide supra*, yielded AuCN(B), whose ^{13}C NMR (Figure 5.2), powder XRD pattern (Figure 5.5), and IR spectrum (Figure 5.4) provides further insight into the AuCN system. Two samples were synthesized using this method, and the two samples were found to produce nearly exactly superimposable ^{13}C lineshapes at 11.75 T. The ^{13}C NMR spectrum of AuCN(B) undergoing MAS is shown in Figure 5.2, with the corresponding lineshape information in Table 5.1. This second sample has two additional peaks beyond the pair of resonances it has in common with AuCN(A). Comparing ^{13}C SSNMR spectra for the two samples, it may be seen that the ratio of the pair of resonances the two samples have

in common differs: there is more of the high-frequency site in AuCN(A). A sample with more chain slipping would be expected to yield a broader XRD pattern whereas a sample with a differing amount of head-tail disorder would yield the same XRD peak breadths due to the similar scattering power of C and N atoms. Linewidths in the XRD pattern of AuCN(B) are narrower than those from AuCN(A), consistent with an assignment of the 154 ppm site as an ordered site and the 164 ppm peak as a chain slipped site.

Unfortunately, lower intensity and resolution prevented the use of an $SR26_4^{11}$ experiment to identify the extra two peaks in the ^{13}C NMR spectrum of AuCN(B). The nature of the sites producing these two NMR resonances is, however, hinted at by the XRD pattern of AuCN(B): if the extra peaks represented new types of disorder superimposed on the AuCN structure, an XRD pattern broader than that observed for AuCN(A) would be expected, whereas a narrower pattern is observed. On the other hand, amorphous impurities could very easily cause only a broad, diffuse X-ray pattern and not provide any noticeable change in the overall XRD pattern. We therefore assign the two low-frequency ^{13}C NMR peaks of AuCN(B) as amorphous impurities rather than components in a disordered AuCN structure. The IR spectrum of AuCN(B), represented in Figure 5.4, contains the same peaks as the spectrum from AuCN(A), but the CN region is broader. Such an increased breadth of IR resonances from AuCN(B) is also consistent with the presence of amorphous impurities in that sample. Identification of the low-frequency peaks as impurities also seems logical as it is unlikely that AuCN(B), which has less chain slipping, would be the material that displays an increase in the types of disorder. In summary, investigation of a second sample, AuCN(B), with a slightly different composition yielded observations entirely consistent with the above assertion of measurable chain slipping in AuCN. Interestingly, the 7±2% fraction of cyanides in slipped chains observed for AuCN(B) is lower than the 24±5% found for AuCN(A).

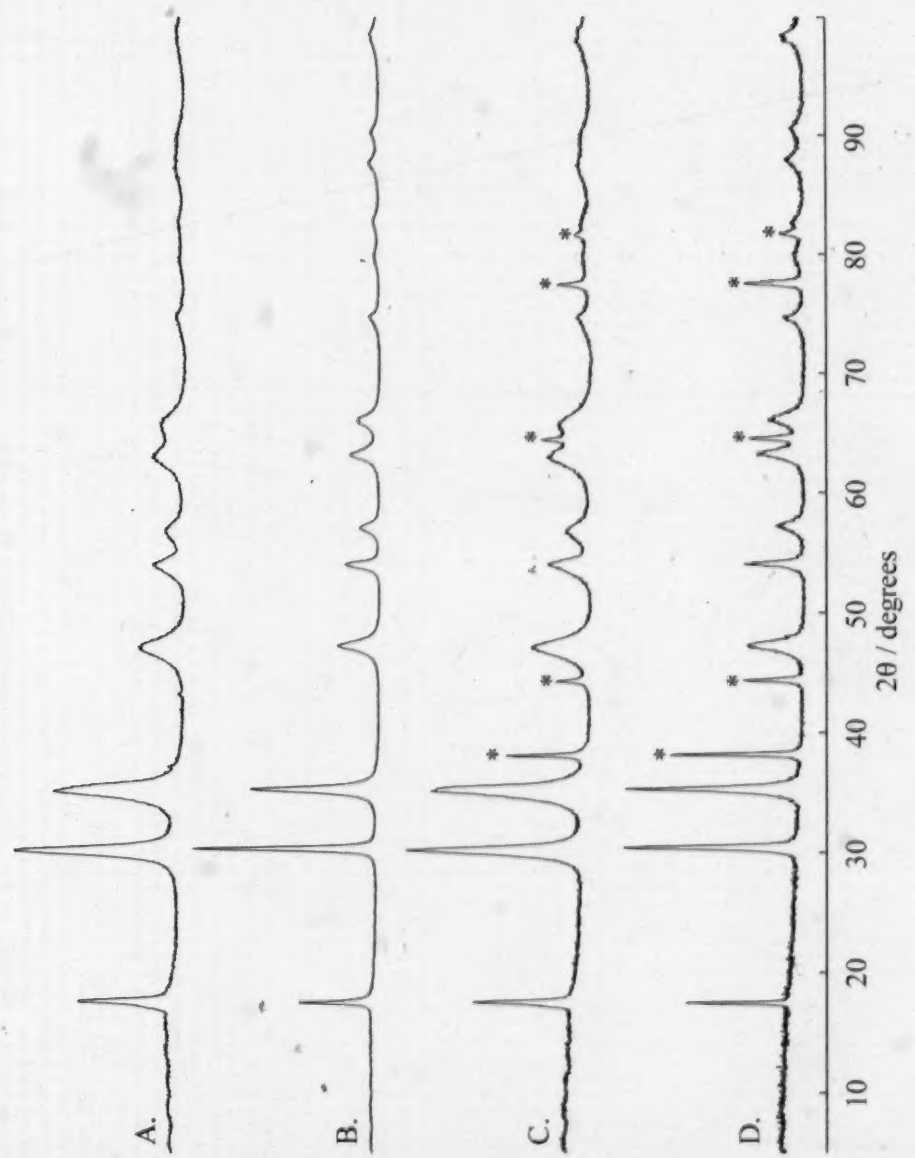

Figure 5.5: Powder X-ray diffraction spectra of different AuCN samples. The spectrum from AuCN(A) is shown as trace A. and that of AuCN(B) is shown as B., while powder patterns from AuCN(A′) are shown both before, in C., and after, in D., mineralization at high temperature with an aqueous solution of KCN. Peaks marked with a * in C. and D. are assigned to metallic Au. See text for preparation details of each sample.

A third sample of gold monocyanide, AuCN(A′), was prepared using a slight modification of the procedure applied for AuCN(A) - the difference being a deficiency of the reducing agent (75%) used in the AuCN(A) preparation, but a slight excess (10%) for AuCN(A′). In the ^{13}C MAS NMR spectrum of AuCN(A), a very broad resonance centered at ~50 ppm to low frequency of the main peaks was observed. This broad peak was assigned to cyanides bound to Au(III) based on the isotropic shift observed for K[Au(CN)$_4$], see Chapter 4. The approximately 30 ppm broad (at 11.75 T) peak was found to remain even after repeated attempts at sample washes, which only reduced the peak intensity slightly. Investigation of AuCN(A′) showed that some of the Au(III) ions from solution were reduced further than to the intended target of Au(I) by the excess reducing agent. Comparison of the XRD pattern for AuCN(A′), Figure 5.5, to that of an Au(s) powder showed that there was indeed some metallic gold present. The presence of Au(s) also affected the colour of the material: the expected lemon yellow colour was found to be tinted green. Clearly, batches of AuCN made via the process in patent #4,222,996[186] without careful control of the amount of reducing agent will contain either Au(III) or Au(0) as an impurity. While there is a difference between impurities present in AuCN(A) and AuCN(A′), all other results for the two samples are comparable. In particular, the same ratio of chain-slipped versus aligned sites was recorded.

The ^{13}C NMR spectrum from a stationary sample of AuCN(B), see Figure 5.6, has the appearance of that from a single-site material. Most likely, the powder pattern is representative of the 85% dominant site, see Table 5.1, with the other minor sites contributing to broadening only. Simulation of this powder pattern therefore provides the CS tensor and $R_{\text{eff}}(^{15}\text{N},^{13}\text{C})$ coupling constant from the main, aligned-chain, site. If we ignore cyanide head-tail disorder in neighbouring chains, a factor unlikely to affect the CS tensor, the CN bond lies along a C_6 symmetry axis;[177] therefore, the CS tensor is axially symmetric and the PAS is oriented with

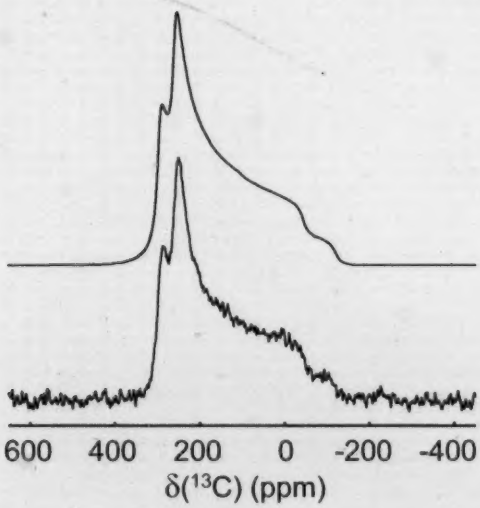

Figure 5.6: Experimental (lower trace) and simulated (upper trace) ^{13}C NMR spectra of a stationary sample of AuCN(B) at 4.70 T.

δ_{33} along the C,N bond.[19,20,189] From the best-fit simulation, the CS tensor span is 357(5) ppm and the value of $R_{\text{eff}}(^{15}\text{N},^{13}\text{C})$ is 1925(100) Hz. This dipolar coupling constant translates into a value of 1.14(4) Å for the C,N bond length, which is in excellent agreement with the neutron-diffraction value of 1.150(28) Å.[177]

5.3.2 ^{13}C NMR Linewidths in Gold(I) Monocyanide

Based on the above analysis of spectra from MAS samples, we feel the two isotropic shifts displayed by AuCN(A) are well understood; however, the large ^{13}C linewidths are complicated and require further experiments to fully understand. Several overlays of ^{13}C NMR spectra from samples of AuCN(A) and AuCN(B) undergoing MAS are presented in in Figure 5.7, as they provide some insight into the sources of line broadening. The LWHH observed for the 154 ppm peak of AuCN(A) is ~450 Hz at 7.05 T, while at 11.75 T it is ~590 Hz. The pair of isotropic shifts displayed in the spectra of AuCN(A) result from chain-aligned and chain-slipped sites, but

each peak probably has contributions from varying numbers of aurophilic bonding partners, as well as from head-tail cyanide disorder; accordingly, it is sensible for the linewidths to increase with the applied field. In contrast to the behaviour observed in AuCN(A), the linewidth for the 154 ppm peak of AuCN(B) changes very little: ~530 Hz at 7.05 T and ~550 Hz at 11.75 T. Interestingly, the 154 ppm peaks obtained for AuCN(B) at 7.05 and 11.75 T are nearly exactly superimposable when plotted on a frequency scale. The 154 ppm peaks of the two samples have nearly the same linewidth at 11.75 T, but slightly different lineshapes; in particular, a slightly narrower base is found for the AuCN(B) peak. Because of the difference in field-dependent behaviour of the two samples however, the linewidths are quite different at 7.05 T. In an attempt to better understand the linewidth of AuCN(B), a ^{13}C MAS NMR spectrum was acquired at 21.1 T (226.4 MHz), where a marginally increased linewidth of ~590 Hz was observed.

The near field-independent linewidth in AuCN(B) suggests the presence of significant broadening due to either spin-spin coupling or a short T_2 relaxation time constant, as discussed in Chapter 5, but it seems extremely unusual for this mechanism to be different in AuCN(B) and AuCN(A). The broadening factor that is most easily separable is the relaxation parameters, and we measured these using methods similar to those discussed for $K[Au(CN)_2]$ and $Tl[Au(CN)_2]$ in Chapter 4. Using an inversion-recovery experiment, a value for T_1 in AuCN(A) of ~170 s was obtained, and T_2 was determined as ~2.0 ms using 5 Hahn-echo experiments with delays spanning from 52.6 μs to 4208 μs. The predicted value for the LWHH of the 154 ppm peak in AuCN(A) from relaxation alone, assuming a Lorentzian lineshape, is 160 Hz. A more approximate value for the T_2 relaxation time constant in AuCN(B) was determined using a Carr-Purcell-Meiboom-Gill pulse sequence (phase-cycled train of Hahn echoes), yielding a value of ~3.2 ms; the corresponding relaxation-only LWHH is 100 Hz. These values are imprecise, but still allow one to conclude that

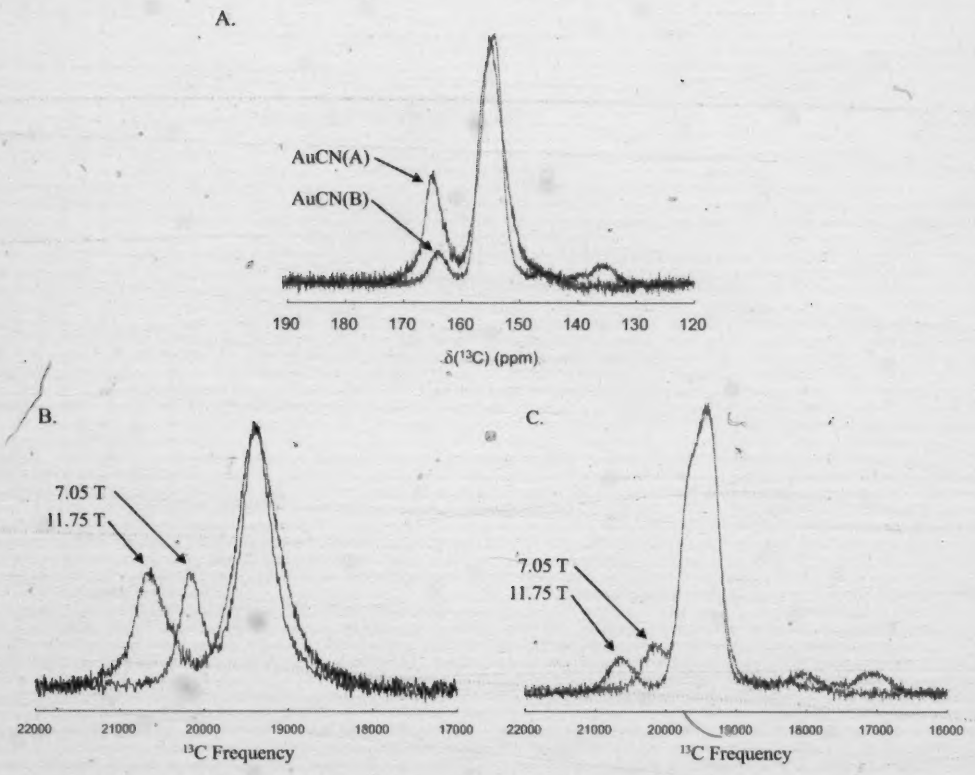

Figure 5.7: Comparison ^{13}C MAS NMR spectra obtained for AuCN(A) and AuCN(B). A. Spectra from both samples acquired at 11.75 T, plotted on a chemical shift scale. B. Spectra from AuCN(A) acquired at 7.05 and 11.75 T, plotted on a frequency scale. C. Spectra from AuCN(B) acquired at 7.05 and 11.75 T, plotted on a frequency scale.

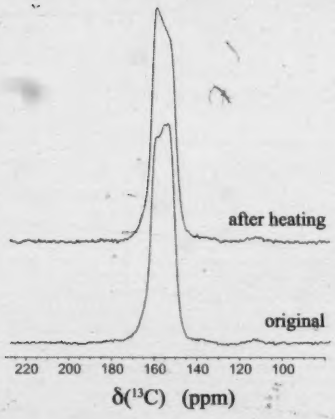

Figure 5.8: Carbon-13 MAS NMR spectra obtained at 4.70 T for AuCN,[190] before and after heating to 180 °C.

relaxation is important to the LWHH, but is not the sole determining factor.

As discussed in Chapter 4, a linewidth of ~250 Hz from residual dipolar coupling with ^{197}Au is expected unless this interaction is decoupled by rapid relaxation of the ^{197}Au nucleus; furthermore, this linewidth is expected to be independent of the applied field strength (with currently available spectrometers), because the quadrupolar interaction of ^{197}Au greatly dwarfs its interaction with the external magnetic field. Given that the experimentally observed linewidth encompasses the predicted value, it is possible that residual dipolar coupling with ^{197}Au is present. Because the ^{197}Au nucleus is expected to relax much more quickly at high temperature, we attempted to induce line narrowing by observing the ^{13}C MAS NMR spectrum at high temperature (at both 4.70 and 11.75 T).[190] Unfortunately, no significant line narrowing was observed at the temperatures accessible with our equipment ($\leq$ 180 °C). A slight alteration of the peak shape was observed at high temperature, and was found to remain after the sample was cooled; see Figure 5.8. Because of the permanent nature of the lineshape modification, some minor structural change in the sample was likely induced.

As a side note, the possibility of coupling to the ^{197}Au nucleus caused us to consider whether the lifetime of the quadrupolar nucleus at RT would be long enough to allow observation of ^{197}Au NQR spectra. Therefore, we attempted to observe an NQR signal using a standard NMR probe well removed from the superconducting magnet. Using $C_Q(^{197}\text{Au}) = 1005(7)$ MHz, data available from published Mössbauer spectra of AuCN,[149] the expected NQR resonance frequency can be predicted as ~500 MHz, which fortuitously matches with the proton channel of an available Bruker Avance 11.75 T NMR system. We applied the same pulse sequence found useful in a previous $^{65/63}$Cu NQR study of CuCN,[183] but unfortunately no signal was observed.[190] However, the lack of signal is not entirely unexpected given the small bandwidth of the spectrometer channel and the large range over which this possibly temperature-dependent frequency might be found. Because of the noted fortuitous match between the proton channel of an available system and the predicted ^{197}Au transition frequencies, we also attempted to probe for residual dipolar coupling by observing the ^{13}C MAS NMR spectrum while perturbing the ^{197}Au energy levels with CW rf irradiation. Unfortunately, stepping through the available bandwidth on the high-frequency (^{197}Au) channel produced no visible change in the ^{13}C MAS NMR spectrum.

Reducing the amount of disorder might allow the effects of spin-spin coupling to be observed directly. It is possible that annealing techniques, shown useful in diffraction studies of CuCN,[175] could remove significant amounts of chemical shift broadening. Initial attempts at annealing the sample of AuCN(A), *vide infra*, resulted in some narrowing of the peak; however, it would likely take several repeated rounds of annealing, for which there was not enough sample, to cause enough line narrowing to prove the presence of residual dipolar coupling with ^{197}Au. So far, a full explanation for the broad ^{13}C linewidths remains elusive.

5.3.3 ^{15}N NMR of Gold(I) Monocyanide

Nitrogen-15 NMR of AuCN was also investigated. The MAS spectrum of AuCN(A), shown in Figure 5.9, is composed nearly ninety percent of one peak, with an additional small peak to low frequency and a broad absorbance to high frequency, see Table 5.2. Nitrogen-15 chemical shifts are typically more sensitive to environmental changes than are carbon-13 shifts,[191] which hints at one possible explanation for the spectrum seen in Figure 5.9. While only two distinct values are observed for $\delta_{iso}(^{13}C)$, for aligned and shifted chains, the typically more sensitive nitrogen-15 nucleus may allow resolution of more sites, e.g., differences in the number of nearest neighbours. If the argument about increased sensitivity for ^{15}N over ^{13}C is the true cause of an increased number of sites, it may be that increased chemical shift broadening is responsible for the lower relative integrated intensity of the secondary peaks in the ^{15}N spectrum (see data for AuCN(A) in Table 5.1 versus that in Table 5.2). Also shown in Figure 5.9 is the nitrogen-15 spectrum of AuCN(B) under MAS, an interesting spectrum in that only one peak is visible despite the multiplicity seen in the carbon-13 spectra. AuCN(B) has less than one third the amount of slipped chains present in AuCN(A), which may be the reason that secondary resonances are only observed in nitrogen-15 spectra of the latter, particularly given that the ^{15}N NMR spectra of AuCN(A) display secondary resonances at only approximately half the integrated intensity seen in the ^{13}C NMR spectra of this material. The larger amount of disorder in AuCN(A) as compared to AuCN(B) is likely responsible for the nearly doubled ^{15}N MAS NMR linewidth of the former material. We did attempt to observe secondary peaks in a ^{15}N spectrum of AuCN(B) by increasing the applied field to 21.14 T (a 91.2 MHz Larmor frequency), but only a single peak with LWHH = 190 Hz was obtained.

There is some uncertainty in a full assignment of the ^{15}N data, but there is little doubt that the main ~224 ppm resonance is that of the neutron-diffraction

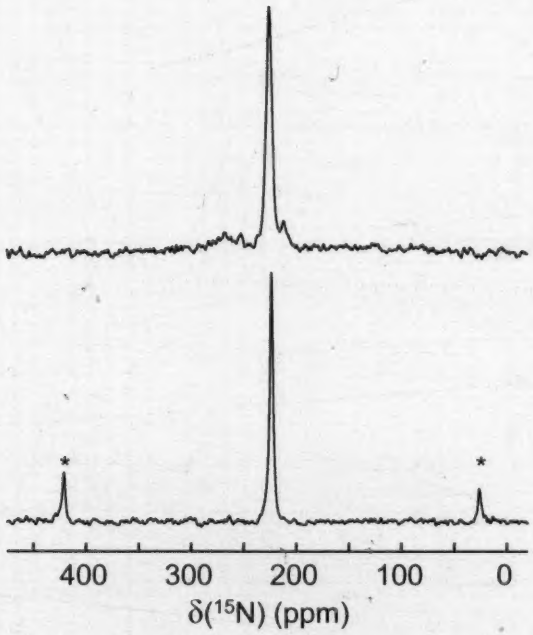

Figure 5.9: Upper spectrum: ^{15}N NMR spectrum of AuCN(A) under MAS, $\nu_{\text{rot}} = 13$ kHz, acquired at 11.75 T. Lower spectrum: ^{15}N NMR spectrum of AuCN(B) under MAS, $\nu_{\text{rot}} = 10$ kHz, also acquired at 11.75 T - spinning sidebands marked with a *.

structure (i.e., aligned gold cyanide chains). This peak is the same in all the samples, so we used the highest-quality slow MAS spectrum, that of AuCN(B) at 11.75 T, to determine the ^{15}N CS tensor. Eight peaks from the experimental spectrum were used in the least-squares fit,[135] and R_{eff} was set to the value determined from the ^{13}C NMR spectrum. Due to the C_6 symmetry axis at the nitrogen,[177] the model used for analyzing the spectrum had κ fixed to 1 and δ_{33} fixed along the C,N bond. A final value for the CS tensor span of 425(25) ppm is determined from the best-fit simulation. Interestingly, the ^{15}N chemical shift of AuCN lies outside the range found for those of the other gold(I) and gold(III) cyanides presented in Chapter 4. As might be expected, $\delta_{iso}(^{15}\text{N})$ appears more sensitive to bond formation at the

Table 5.2: Nitrogen-15 NMR Parameters of AuCN

AuCN Sample	δ_{iso} (ppm)	LWHH[a] (Hz)	Area (%)
AuCN(A)	224.1(5)	270	87
	211.5(10)	300	6
	270(10)	1500	7
AuCN(B)	223.40(25)	140	100

[a]LWHH measured at 11.75 T.

nitrogen in this bridging CN ligand than to small geometry changes between the gold(I) dicyanides investigated in Chapter 4. In fact, coordination at the nitrogen causes an even larger change in $\delta_{iso}(^{15}N)$ than does a change in oxidation state of the gold atom (see data for $K[Au(CN)_4]$ in Chapter 4). Previously reported nitrogen-15 data from a dicyanoaurate in which the cyanide forms a bridging bond to lead in $Pb(H_2O)[Au(CN)_2]_2$ (and its dehydrate),[95] see Table 4.3, exhibits ^{15}N chemical shifts that match better with the range observed here for non-bridging cyanide groups than that observed for the bridging cyanide of AuCN. The reason for the $\delta_{iso}(^{15}N)$ of $Pb[Au(CN)_2]_2(H_2O)_x$ agreeing better with the non-bridging nitrogen environments may be that the Pb-N bond is much longer (2.595 - 2.8 Å) than the Au-N bond in AuCN (1.9703 Å).

5.3.4 Hydrothermal treatment of AuCN(A)

In a diffraction study of CuCN, it was found that crystals of material, hitherto available only as a highly disordered powder, could be grown at elevated temperature using KCN as a mineralizer.[175] We were interested in any changes that may occur in AuCN were it submitted to these conditions. We therefore heated AuCN(A) for two weeks at 160 °C in a teflon-lined bomb in the presence of a few mole % of KCN in distilled water. The ^{13}C NMR spectra showed that the same two peaks were

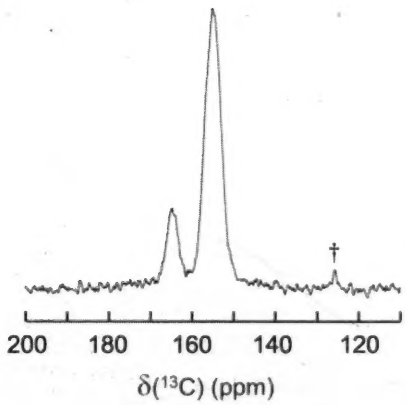

Figure 5.10: Carbon-13 NMR spectrum of annealed AuCN(A) under MAS, $\nu_{\text{rot}} = 19$ kHz, acquired at 11.75 T; a small spectral artifact (quadrature image) is marked with a †.

present, but somewhat narrowed; see Figure 5.10 and Table 5.3. Also, the amount of carbon atoms in the chain-slipped sites is reduced in the annealed sample to ~17%, down from ~24% in the pre-treatment AuCN(A). The powder XRD spectrum is also consistent with a reduction in disorder as the diffraction peaks are found to be narrowed after the heating procedure. We did not have enough sample to investigate further rounds of the hydrothermal treatment, because some AuCN is lost as $K[Au(CN)_2]$ during the treatment. However, these initial results are still quite interesting, because removal of some chemical-shift broadening through control over the amount of disorder may provide a route to further understanding contributions to the line width of the ^{13}C peak from the principal (chain-aligned) site.

5.3.5 Analysis of the Intermediates

The powder XRD patterns of samples produced using the synthetic method of patent #4,222,996 clearly showed the presence of some unknown material in addition to AuCN. Because these samples are not pure, we use the labels Intermediate(A) and

Table 5.3: Carbon-13 NMR Parameters for Annealed AuCN

AuCN Sample	δ_{iso} (ppm)	LWHH[a] (Hz)	Area (%)
Annealed AuCN(A)	154.4(5)	550	83(5)
	164.5(5)	400	17(5)

[a]LWHH measured at 11.75 T.

Intermediate(A′); while different names are used for these two samples, note that their preparation differed only in the amount of reducing agent used, and nearly all of the results discussed here are the same for both. Soaking of the intermediates in distilled water (1 week) followed by thorough washing yielded samples whose powder XRD patterns matched well with the theoretical pattern expected for AuCN. A similar washing procedure was attempted on AuCN(B), but the two small unassigned peaks in its ^{13}C MAS NMR spectrum remained unchanged. Polymorphism is known in the lighter congener CuCN, and an alternate structure of AuCN has been proposed in a DFT study;[184,185] therefore, we were interested in whether these intermediates contained a polymorph of AuCN. Additionally, there is a possibility that the intermediates could show evidence of a more highly disordered form of AuCN.

Residue collected after evaporation of the soaking water was analyzed in order to investigate the purification process, and it was determined that the water-soluble residue formed ~6% w/w of Intermediate(A). Solution NMR spectra of the residue, both ^{15}N and ^{13}C, contained peaks from the dicyanoaurate anion, as determined through comparison to solutions of $K[Au(CN)_2]$, but no other resonances. Intermediates A and A′ therefore contained a mixture of AuCN and one or more dicyanoaurate salts, i.e., compounds of the form $M^+[Au(CN)_2]$.

Because of the small sample size, this value is approximate.

Elemental analysis of the wash residue from Intermediate(A) yielded 9.62% C and 9.33% N, close to the theoretical value for $K[Au(CN)_2]$ of 8.62% C and 10.00% N. Note that elemental analyses of the related compound CuCN are known to report a slightly high value of atom % C, and a slightly low value for N, so the present data can be viewed as a good match.[179] The solution used in the synthesis contained not only K^+, but also Na^+ and H^+ ions; however, results of the elemental analysis would not change appreciably if a mixture of dicyanoaurate anions with differing cations were present. It is clear though, that the residue is composed nearly entirely of $M[Au(CN)_2]$ materials. This is interesting, because it appears that most of the byproducts (i.e., nitrates, sulfates, and chlorides of sodium and potassium) were washed out effectively, while cyanide-containing materials were not. Perhaps the rapidity of the reaction caused the $M[Au(CN)_2]$ and MCN starting materials to be trapped in the AuCN matrix.[192] Unfortunately, the expense involved in preparing multiple samples prevented us from investigating the length of time required for the conversion of Intermediate(A) $\rightarrow$ AuCN(A). The presence of dicyanoaurate anions in the residue brings up an interesting question: were all impurities simply washed out during purification, or could the anions have acted as a catalyst? Specifically, the presence of CN^- or $[Au(CN)_2]^-$ could have catalyzed the conversion of an unknown polymorph into the known AuCN form, or reduction of disorder in AuCN. Both of these catalytic activities have been observed in the group 10 monocyanides: KBr(aq) can be used to convert between the high- and low-temperature polymorphs of CuCN,[175] while annealing with $KCN(aq)/K[Cu(CN)_2]$ greatly increases the crystallinity of CuCN.[175]

A ^{13}C solid-state NMR study of Intermediates A and A′ was performed in order to further investigate these materials. Carbon-13 MAS NMR spectra from Intermediates(A) and (A′), along with the corresponding washed materials, AuCN(A) and (A′), are shown in Figure 5.11, and the chemical shifts are shown in Table 5.4. To

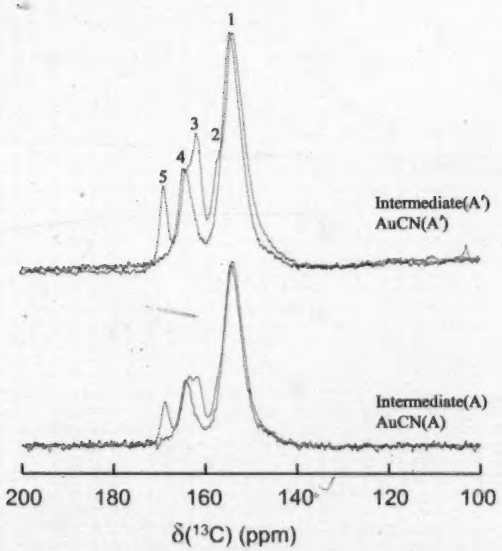

Figure 5.11: Carbon-13 NMR spectra acquired at 11.75 T under MAS, $\nu_{rot} = 13 - 19$ kHz; spectra of Intermediate(A) and (A′) are superimposed on those of the corresponding washed samples. Peaks are labelled 1 to 5 for simplicity (see text).

facilitate the following discussion, the peaks in Figure 5.11 have been labelled 1 - 5, but note that peaks 1 and 4 are assigned in the spectra of AuCN, and are thus the "expected" spectrum of pure AuCN (*vide infra*). It is clear that there are at least three extra sites in Intermediate(A) which do not arise from the known AuCN structure. While the spectra for the two intermediates are similar, the unassigned peaks appear to be slightly more intense for Intermediate(A′). Because the three sites do not match known shifts for $M^+[Au(CN)_2]$ salts, and have large linewidths similar to that observed for AuCN(A), it is possible that they may in part be due to a second polymorph of AuCN, or to some extra mode of disorder in the AuCN present.

In order to better explain the ^{13}C NMR spectra of the intermediates, a variety of expected impurities were investigated using SSNMR. An overlay of ^{13}C MAS NMR spectra from all these materials is shown in Figure 5.12, and the isotropic

Table 5.4: Carbon-13 NMR parameters for Intermediate (A) and (A′)

	Peak	5	4	3	2	1
	δ_{iso} (ppm)	168.8(3)	163.5(10)	161.5(5)	157(1)	153.5(5)
Intermediate(A)	% Area[a]	8	17	13	< 1	100
Intermediate(A′)	% Area[a]	12	22	19	5	100

[a]Normalized to intensity of peak 1, errors are ~20% of the listed area.

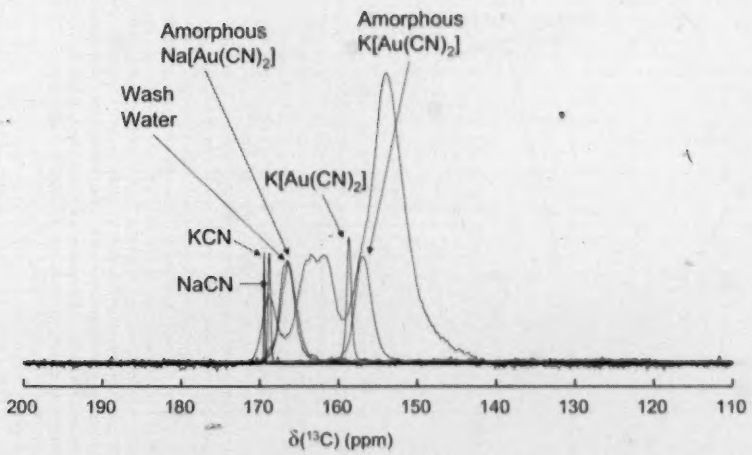

Figure 5.12: Carbon-13 NMR spectra, acquired at 11.75 T under MAS, of a variety of materials expected as possible impurities in the AuCN(A) and (A′) synthesis superimposed on the spectrum obtained from AuCN(A) at the same field. See Table 5.5 for isotropic chemical shifts.

chemical shifts are given in Table 5.5. It is of note that there is a nearly 2 ppm difference between the isotropic shifts of crystalline and amorphous $K[Au(CN)_2]$. It is possible that the effect of aurophilic bonding on the cyanide ^{13}C chemical shifts noted above serves to magnify the sensitivity of δ_{iso} to preparation method. The chemical shift of amorphous $K[Au(CN)_2]$ appears to be a close match with that of peak 2 in Intermediate(A). We also prepared amorphous $Na[Au(CN)_2]$, and found a chemical shift significantly different than that of $K[Au(CN)_2]$. There is a reasonable agreement between the ^{13}C chemical shifts of KCN (and NaCN) with the high frequency peak of Intermediate(A). Note that the linewidth observed for NaCN, see Table 5.5, could be slightly broadened with respect to the potassium salt by residual dipolar coupling with the neighbouring quadrupolar ($I = \frac{3}{2}$, N.A. = 100%) ^{23}Na nucleus. While no KCN or NaCN was observed in ^{15}N or ^{13}C NMR spectra acquired from solutions of the residue, these two compounds may have been present in the intermediate because the week-long soaking process represents overwhelmingly sufficient time for them to have reacted with AuCN (to form the respective dicyanoaurate). The ^{13}C chemical shift of the solid residue collected by evaporation of the soaking water is also shown in Figure 5.12, where the close match with the signal observed from amorphous $Na[Au(CN)_2]$ is apparent. From the above information, it is not possible to definitively assign the unknown peaks in the ^{13}C MAS NMR spectrum of Intermediate(A), a situation complicated by the apparent extreme sensitivity of ^{13}C chemical shifts from dicyanoaurate anions to their environment.

A 2D homonuclear dipolar-recoupling SSNMR experiment, using the $SR26_4^{11}$ pulse sequence, was performed in order to further investigate the origins of the three extra ^{13}C NMR peaks in Intermediate(A). The spectrum is shown in Figure 5.13, where a ~5 ms excitation period was used, yielding spectra sensitive to ^{13}C,^{13}C dipolar couplings corresponding to C-C distances of ~5 Å. This distance is large

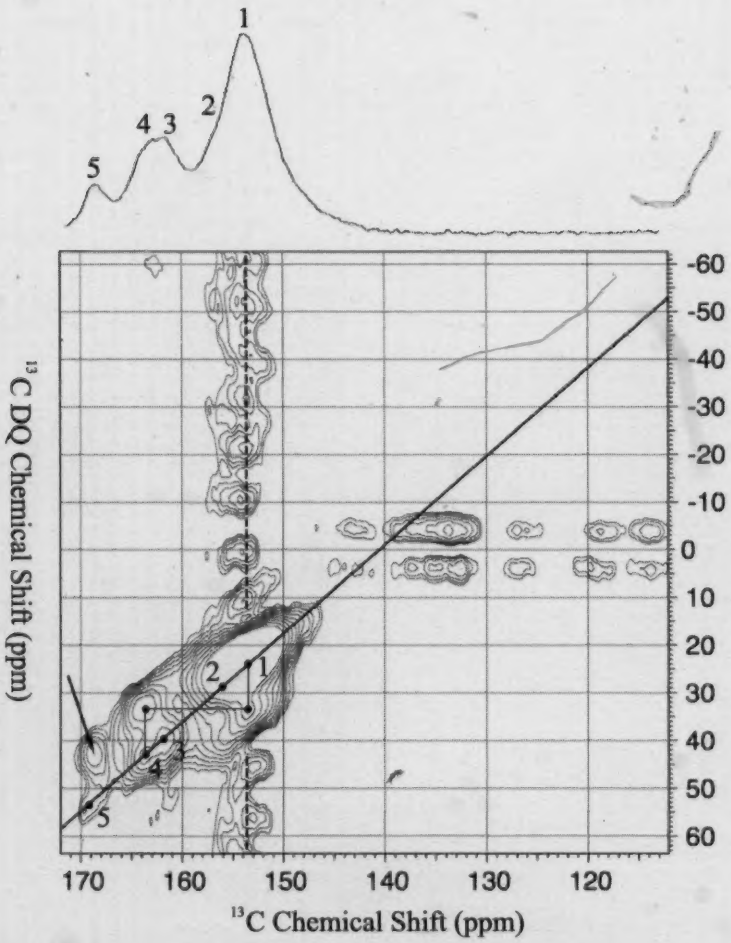

Figure 5.13: Carbon-13 $SR26_4^{11}$ homonuclear dipolar-recoupling spectrum of Intermediate(A) acquired over 6 days under MAS, $\nu_{\text{rot}} = 9.615$ kHz, at 7.05 T. Peaks on either side of the 0 ppm line in the indirect dimension are small dispersion-shaped spectral artifacts. Short acquisition time in t_1 causes peaks to have the typical $\sin(x)/x$ shape in the indirect dimension, where the "feet" are a few percent of the main peak height. These features can be seen for the very intense peak from site 1, and have been marked with a dashed vertical line. Self-correlation peaks occur along the solid diagonal line, while inter-site correlation peaks occur in pairs offof the line. Peaks from self correlations for each of the sites numbered 1 - 5 are marked (expected location for site 2), and the correlations between sites 1 and 4 assigned to AuCN are indicated. An arrow highlights the inter-site correlation involving site 5.

Table 5.5: Carbon-13 Isotropic Chemical Shifts for Amorphous Cyanide Materials from SSNMR Spectra

Compound[a]	KCN	NaCN	$Na[Au(CN)_2]$	Wash Residue	$K[Au(CN)_2]$[b]	$K[Au(CN)_2]$
δ_{iso} (ppm)	169.4	168.8	166.5	166.4	158.7	156.9
LWHH[c] (Hz)	20	45	300	250	85	300

[a]All samples except NaCN used dilabelled ^{13}C,^{15}N cyanide ligands, NaCN used monolabelled ^{13}C cyanide. All samples are amorphous unless otherwise noted.
[b]Crystalline sample from Chapter 4.
[c]Measured at 11.75 T.

enough that even under the presence of extensive disorder, inter-site correlations can still be probed. All of the sites appear to be self-correlated, and there is also clear evidence of some inter-site correlations. The correlations shown in Section 5.3.1 to be from AuCN, i.e., self correlations of sites 1 and 4, and the site-1/site-4 correlation, are marked on the 2D spectrum in Figure 5.13. Spectral crowding around peak 2 prevents any possible correlations from being seen, and there are no visible correlations other than the self-correlations for site 3. Unfortunately, because linewidths in the indirect dimension are several ppm, about the same order as the site separations, the presence of a correlation can be determined with confidence, but the absence of one is not definitive evidence. In contrast to the first two unassigned peaks (2 and 3), site 5 is undoubtedly correlated to at least one other site. The inter-site correlation peak involving site 5 appears to be a correlation with site 2, but the large linewidth means that it may instead be a correlation of site 5 with either site 3 or site 1. In particular, site 1, which has been assigned to AuCN, yields a broad line whose tail undoubtedly extends under the peak for site 2. It would be tempting to assign the peak from site 5 to leftover KCN/NaCN starting material based on the results of the 1D NMR spectra, but the 2D recoupling experiment shows that some more complicated material is present.

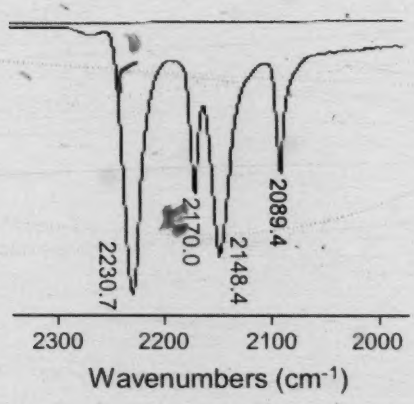

Figure 5.14: IR spectra of the CN stretching region, from Intermediate(A).

As IR spectroscopy turned out to be useful in the above investigation of AuCN, and should prove useful for speciation of various cyanoaurates, we recorded the IR spectrum of Intermediate(A) shown in Figure 5.14. However, comparison to the IR spectra of AuCN(A) and AuCN(B), see Figure 5.4, shows very little difference. Only peaks assigned to the ordered and chain-slipped sites of AuCN (and their isotopic counterparts) are seen in the spectrum. Results for the solution NMR spectra show that compounds of the form MCN or $M[Au(CN)_2]$ are present in the the intermediate, and one would expect that cyanide stretches from these would be readily apparent - perhaps disorder plays some role in masking their signature through peak broadening. The IR peak associated with the chain-slipped site is much more intense in the IR spectrum of Intermediate(A) versus AuCN(A), despite the ratio of ^{13}C NMR peaks 1 and 4 agreeing within error for these two materials.

An investigation of the ^{15}N SSNMR spectra of Intermediate(A) and Intermediate(A′) was also pursued in hopes of determining more information about their composition. The NMR spectra of the two samples were found to be virtually identical, and that of Intermediate(A) is shown in Figure 5.15. The only difference from the ^{15}N NMR spectrum of AuCN(A) is the presence of two lines at 250.9(5)

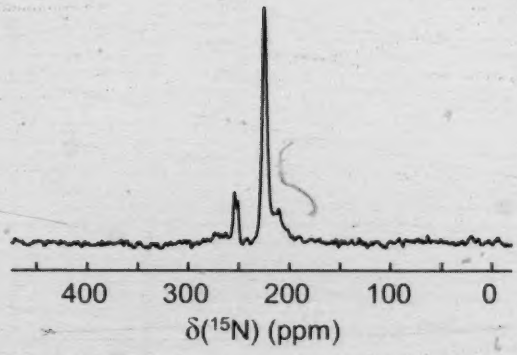

Figure 5.15: Nitrogen-15 NMR spectrum of Intermediate(A) under MAS, $\nu_{\text{rot}} = 13$ kHz, acquired at 11.75 T.

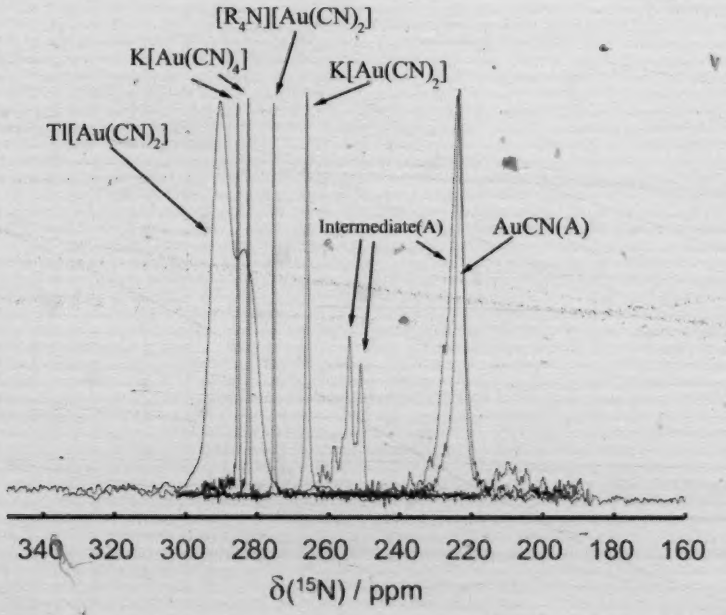

Figure 5.16: Nitrogen-15 NMR spectrum of Intermediate(A) under MAS, $\nu_{\text{rot}} = 13$ kHz, acquired at 11.75 T.

ppm (125 Hz at half height) and 254.0(5) ppm (150 Hz at half height), contributing 4 and 8% of the total peak area, respectively. As was noted above, the ^{15}N isotropic chemical shift for AuCN, where the nitrogen is bonded to gold in the bridging cyanide, was found to be shielded by at least 40 ppm with respect to the range observed for the cyanoaurates where the nitrogen is not involved in a second covalent bond. It is interesting that the two ^{15}N NMR peaks of Intermediate(A) not found in AuCN(A) have chemical shifts intermediate between those observed for the bridging versus non-bridging cyanides, as shown in Figure 5.16. The ^{15}N NMR spectra therefore provide further evidence that the composition of the intermediates is not as simple as might first be expected.

5.4 Conclusions

Disorder in AuCN was investigated by studying several samples using ^{13}C and ^{15}N SSNMR, powder X-ray diffraction, and IR spectroscopy. Homonuclear carbon-13 dipolar recoupling experiments are found to be invaluable in characterizing the disordered materials. Furthermore, the ^{13}C isotropic chemical shift is found to be sensitive to alignment of the one-dimensional chains with respect to their neighbouring chains, i.e., breaking of the aurophilic bonds. The fraction of chains which are slipped is found to vary with sample preparation, with a range of 7±2% to 25±5% observed here; furthermore, the amount of slipped chains can be reduced through hydrothermal treatment with KCN. Results from the method of Patent #4,222,996[186] for synthesizing AuCN was also investigated, where it was found that more extensive than typical washing was necessary to ensure impurities were effectively removed. These impurities were not able to be assigned definitively, and appear to have some complicated structure with multiple sites.

Carbon-13 and nitrogen-15 NMR experiments have provided a clearer picture of the disorder superimposed on the average structures of the coinage metal mono-

cyanides. These materials are all composed of one-dimensional $\cdots$NC-M-CN$\cdots$ chains,[173–180] and $^{65/63}$Cu NQR studies in combination with ^{13}C and ^{15}N NMR spectroscopy of CuCN and AgCN has shown that the orientation of the cyanide ligands varies: 30±10% of the metal sites were disordered (C-M-C or N-M-N), while 70±10% were ordered (C-M-N).[140,183] Disorder of the cyanide orientations is likely also present in AuCN, but simply not visible given the expected effect on the chemical shifts is smaller than the observed linewidths. The major difference between the structures of AuCN and CuCN/AgCN is that with the presence of gold, there is an increased interaction between the metal atoms. Because only very weak interactions between the chains in CuCN and AgCN exist, any misalignment of the chains creates no visible effect on the NMR parameters. It follows logically that the stronger interchain forces in AuCN allow the possibility of chain slipping to be investigated. It is likely that the lowered strength of interchain interactions in AgCN/CuCN versus AuCN is responsible for an increased amount of chain slipping in the two lighter systems. This increased slipping is consistent with the broader XRD patterns observed for AgCN/CuCN as compared to AuCN.[173] The body of research on the group 11 monocyanides all converges to describe a picture of these materials as infinite one-dimensional chains, with a significant fraction of the cyanide ligands disordered and also with a large percentage of the chains slipped with respect to their neighbours.

Chapter 6

Acetylenic Carbon-13 Chemical Shift Tensors for Diphenylacetylene and (η^2-Diphenylacetylene)$Pt(PPh_3)_2$: A Solid-State NMR and Theoretical Study

6.1 Introduction

The field of unsaturated-ligand organometallic complexes continues to be an area of extensive research, mainly because of their unusual structures and useful catalytic properties.[193] Molecular complexes of platinum(0) and platinum(II) are important

A version of this chapter has been published. Harris, K.J.; Bernard, G. M.; McDonald, C.; McDonald, R.; Ferguson, M. J.; Wasylishen, R. E. *Inorg. Chem.* **2006,** *45,* 2461-2473

prototypes for the bonding of unsaturated carbon atoms to late transition metals.[194,195] A useful technique used for characterizing these compounds has been their ^{13}C NMR spectra obtained in suitable solvents.[196] These studies have shown that, in general, coordination to platinum(II) results in an increased magnetic shielding for both alkenyl- and alkynyl-carbon nuclei.[196,197] Coordination to platinum(0) causes an increase in shielding for alkenyl carbons,[196,198] but a decrease in shielding for alkynyl carbons.[196,199] An NMR investigation of solid copper(I)-acetylene complexes spinning rapidly at the magic angle has also been performed by Walraff, who found that only small changes in the isotropic shielding occur upon bonding to copper.[200,201]

While the solution ^{13}C NMR studies mentioned above provide classificatory data, only the isotropic portion of the chemical shifts are determined. Examining solid samples offers the opportunity to elucidate the orientation-dependent chemical shift tensor. Solid-state NMR studies of slow-spinning samples have been used to elucidate the CS tensor principal components for the alkenyl carbons in a large series of platinum-alkene compounds.[202–206] In addition to principal-component magnitudes, the orientations of the alkenyl-carbon CS tensors have been measured experimentally (with respect to the $^{13}C,^{13}C$ internuclear vector) for Zeise's salt,[207] a Pt(II) complex, as well as $(\eta^2\text{-}H_2C{=}CH_2)Pt(PPh_3)_2$,[207] and $(\eta^2\text{-}trans\text{-}Ph(H)C{=}C(H)Ph)Pt(PPh_3)_2$,[208] both Pt(0) complexes. Also, alkenyl-carbon CS tensor orientations for selected cyclooctadiene and ethylene ligands in platinum, silver, rhodium and copper organometallic complexes were calculated by Havlin et al.[204] A review of ^{13}C SSNMR investigations on the wealth of organometallic environments including assorted metal-olefin complexes, metallocenes, cyclopentadiene compounds, metal carbides and fullerides, as well as surface-adsorbed olefins and

For ease of discussion, the terms alkenyl and alkynyl carbon will be used to describe nuclei of the uncoordinated ligand and the corresponding nuclei in the complex, although in the latter case this does not correspond to a strict definition of the term.

acetylenes has been compiled by Bernard and Wasylishen.[201]

To our knowledge, the principal components and orientation of a CS tensor for an alkynyl carbon η^2-bonded to a transition metal have never been reported. Determination of such data should provide insight into why the effect of η^2-bonding on the isotropic chemical shift is different for alkenyl and alkynyl carbons. In this Chapter we report the characterization of alkynyl-carbon CS tensors for the representative compound (η^2-diphenylacetylene)$Pt(PPh_3)_2$ (herein labelled PtDPA). Introduction of double ^{13}C-labelling at the alkynyl-carbon position allows analysis of the NMR spectra from stationary samples as AB spin pairs using the methods discussed in Section 3.6.2. This analysis determines the principal components of the carbon CS tensors and the orientation of each PAS relative to the $^{13}C,^{13}C$ internuclear vector (i.e., the alkynyl bond).

A complete structure for PtDPA has not previously been determined, although a preliminary X-ray study reported the space group and unit-cell parameters, but only a few bond lengths and angles.[209] In order to complete the structural information, we undertook a single-crystal X-ray diffraction study of PtDPA. Crystals of PtDPA as benzene and dichloromethane solvates, as well as without co-crystallized solvent, are found to be readily isolable and we report structural details for each form. Due to favorable symmetry properties, the SSNMR data presented here was obtained from a powdered, microcrystalline sample of the benzene solvate.

Alkynyl-carbon CS tensors of unbound diphenylacetylene (DPA) are also determined by analyzing the stationary-sample NMR spectrum of a doubly ^{13}C-labelled sample. The current investigation of DPA, in conjunction with data from PtDPA, allows a complete picture of the changes that η^2-bonding to platinum causes in the CS tensor of an alkynyl carbon. An assortment of alkynyl-carbon CS tensors have previously been reported for compounds with a variety of substituents on the acetylenic carbons.[160,165,210–214] The alkynyl-carbon CS tensor of DPA was reported

during a preliminary investigation of DPA and PtDPA;[201] however, the presence of multiple solvate forms of PtDPA hindered completion of the study.

A theoretical investigation of the alkynyl-carbon CS tensors of PtDPA and DPA is also presented. Numerous computational studies of transition metal complexes have been performed and the area has been the subject of recent reviews by Dedieu[215] as well as by Frenking and Fröhlich.[216] For both DPA and PtDPA, ambiguities in the CS tensor orientation arising from the cylindrical symmetry of the dipolar interaction are resolved using DFT calculations. In addition, DFT calculations are used to investigate the nature of relativistic effects on carbon CS tensors in the platinum complex.[217] Intuitive insight can be gained from theoretical investigations of CS tensors using e.g., the Cornwell approximation,[218–220] the DFT implementation of Schreckenbach and Ziegler,[221–223] or the individual gauges for atoms in molecules (IGAIM) method.[213,224,225] The DFT method of Schreckenbach and Ziegler is here applied to the CS tensor in the model compound (η^2-acetylene)$Pt(PMe_3)_2$ in order to clarify the effects of bonding on the CS tensor of an alkynyl carbon.

6.2 Experimental

6.2.1 Sample Preparation

A sample of DPA at natural isotopic abundance was acquired from a commercial source (Aldrich) and used without further purification. Diphenylacetylene-α,β-$^{13}C_2$ was prepared from *trans*-stilbene-α,β-$^{13}C_2$ (MSD Isotopes, 99% ^{13}C) according to standard techniques (see, for example, reference 50). The labelled diphenylacetylene so produced was characterized by its melting point (59 - 60 °C) and solution ^{13}C NMR spectroscopy. Both (η^2-diphenylacetylene-α,β-$^{13}C_2$)$Pt(PPh_3)_2$ and its counterpart of natural isotopic abundance were prepared under a nitrogen at-

mosphere from the corresponding diphenylacetylene according to literature procedures.[226] Both natural isotopic abundance and $^{13}C_2$-labelled PtDPA were characterized by solution ^{13}C and ^{31}P NMR spectra (*vide infra*). Crystals of PtDPA suitable for X-ray analysis were grown by slow cooling from acetone while benzene and dichloromethane solvates were grown by slow cooling from the respective pure solvents. The polycrystalline powder samples of PtDPA·C_6H_6 used for the SSNMR experiments were prepared by recrystallization from a 7:3 acetone/benzene mixture.

6.2.2 X-ray Crystallography

Complete structures of PtDPA, PtDPA·C_6H_6 and PtDPA·CH_2Cl_2 were determined from studies of single crystals. The crystallographic data presented herein were recorded on a Bruker PLATFORM/SMART 1000 CCD diffractometer which was used to measure > 7000 reflections of graphite-monochromated Mo Kα radiation ($\lambda = 0.71073$ Å) at -80 °C. Structural models were refined to the data with a full-matrix least-squares method on F^2 using the SHELXL-93 computer program.[227] Before analysis, an absorption correction was applied to the data using software packaged with the diffractometer.

6.2.3 NMR Spectroscopy

Proton-decoupled ^{13}C and ^{31}P NMR spectra of natural isotopic abundance and ^{13}C-labelled PtDPA dissolved in CD_2Cl_2 (approximately 0.1 M) were acquired on a Varian Unity 500 NMR spectrometer. Peaks in the ^{13}C NMR spectra were referenced to neat, liquid TMS at 0.0 ppm by setting the solvent ^{13}C peak to 53.8 ppm; those for the ^{31}P NMR spectra were referenced to an external 85% H_3PO_4(aq) sample at 0.0 ppm. The presence of ^{13}C NMR peaks from the 48 phenyl carbons in ^{13}C spectra of PtDPA overlapping with the alkynyl-carbon peaks makes direct analysis intractable. As a simplifying treatment, contributions to spectra of the $^{13}C_2$-labelled samples

from isochronous aromatic ^{13}C nuclei were removed by subtracting the spectra of a sample at natural isotopic abundance. Carbon-13 and phosphorus-31 NMR spectra of the $^{13}C_2$-labelled samples were simulated using the SIMPSON program.[228]

SSNMR spectra were acquired using variable-amplitude cross polarization,[156] under the Hartmann-Hahn matching condition,[157–159] and high-power (50-100 kHz) ^1H decoupling during acquisition. Carbon-13 SSNMR spectra of solid DPA samples were obtained on Chemagnetics CMX Infinity 200 and Bruker AMX-400 NMR spectrometers using contact times of 2 ms and ^1H $\frac{\pi}{2}$ pulses of 3.0 to 4.0 μs combined with 10-20 s recycle delays. SSNMR spectra of ^{13}C and ^{31}P nuclei in PtDPA were obtained on Bruker Avance 300 and 500 MHz NMR systems using TPPM ^1H decoupling during acquisition.[161] Proton $\frac{\pi}{2}$ pulses of 4.0 μs were used while 6 ms contact times and recycle delays of 30-60 s were implemented. The ^{13}C NMR spectra were referenced to TMS using an MAS experiment through assignment of the high-frequency peak of an adamantane spectrum to 38.56 ppm.[155] The ^{31}P NMR spectra were referenced to 85% H_3PO_4(aq) by setting the lone peak (under MAS conditions) of solid $NH_4H_2PO_4$ to +0.81 ppm.[162] Contributions to ^{13}C NMR spectra of stationary samples from the aromatic ^{13}C nuclei at natural abundance were subtracted as described above for solution NMR experiments, yielding spectra from only alkynyl carbons. The amount of correction necessary for MAS experiments was reduced through use of the dipolar-dephasing experiment which depresses the signal from carbon nuclei in methine or methylene environments.[229] Spectra of the $^{13}C_2$-labelled samples were simulated with the WSOLIDS package (stationary samples),[24] or the SIMPSON program (samples undergoing MAS).[228]

6.2.4 DFT Calculations

Calculations of the alkynyl-carbon magnetic shielding tensors for DPA used a structural model based on data obtained from an X-ray study at 293 K.[230] We applied the

Amsterdam Density Functional suite of programs (ADF 2004.01),[231–233] including the effects of an applied magnetic field with the NMR module,[221–223,234,235] which makes use of gauge-including atomic orbitals (GIAOs).[236,237] The functional employed contains the local-density approximation of Vosko, Wilk and Nusair,[238] as well as the nonlocal exchange correction of Becke,[239] and the nonlocal correlation correction of Perdew.[240,241] Calculations used the vendor-supplied TZP basis set consisting of Slater-type orbitals which are of triple-zeta, single-polarization flexibility in the valence (double-zeta core). The calculated magnetic shielding data were converted to chemical shifts (referenced to TMS using Equation 3.14 and the value of 184.1 ppm[23] for σ_{iso}^{TMS}) according to equation 3.14. We also calculated the alkenyl-carbon shielding tensors for ethylene using the geometry of Duncan,[242] and for *trans*-stilbene using the structure of the non-disordered site from the study of Harada and Ogawa.[243]

DFT calculations used for analyzing the alkynyl-carbon shielding tensors for PtDPA used the same method applied to DPA, but relativistic effects[217] were included through two different theoretical methods. All-electron calculations used the relativistic version of the TZP basis set and the zeroth-order regular approximate Hamiltonian,[244,245] including both spin-orbit coupling and scalar relativistic effects (ZORA-DFT). Calculations of PtDPA without a relativistic Hamiltonian used the nonrelativistic version of the TZP basis set, but with a frozen core on platinum (frozen at the $4f$ level and below). The structural model used in all calculations of PtDPA was obtained from the X-ray structure of the benzene solvate, where for reasons of efficiency, PPh_3 moieties were replaced with PMe_3 ligands. Methyl-carbons for PMe_3 were fixed at the position of the phenyl-ring *ipso* carbons and proton positions were set with idealized bond lengths of 1.089 Å and tetrahedral angles.

The alkynyl-carbon shielding tensors of the model compound (η^2-acetylene)-$Pt(PMe_3)_2$ were also calculated with the frozen-core method described above for

PtDPA. In this case the EPR/NMR module was applied to analyze the magnetic shielding tensor in terms of individual molecular-orbital contributions.[221–223] The structure of (η^2-acetylene)Pt(PMe_3)$_2$ was first optimized, under the constraint of C_{2v} symmetry, using the same nonrelativistic Hamiltonian and frozen-core basis set as the shielding calculations.

6.3 Results and Discussion

6.3.1 Diphenylacetylene-α,β-$^{13}C_2$

Crystal Structure and Solid-State ^{13}C NMR Spectra

Before discussing the results of ^{13}C NMR studies on DPA, it is worthwhile to first consider its solid-state structure as its symmetry is reflected in the NMR observables. The most recent structural examination found two symmetry-unique molecules per unit cell, but our SSNMR data does not distinguish the pair.[230] The source of this may be that while the two molecules are formally different, all chemically equivalent C,C bonds in the two were found to be of equal length when atomic motions were taken into account.[230] Also, the large angle librations about the long axis of the molecule may serve to further negate site differences.[230] As the two molecules of DPA each provide the same ^{13}C NMR frequency response within the resolution, the spectra will be discussed as if a single site is present. The inversion centre relating the alkynyl-carbon nuclei requires that the two exhibit identical chemical shift tensors and thus form an A_2 spin system at every orientation in the magnetic field. While the only requirement of the space group on the molecular symmetry is this inversion centre, there is very little deviation from D_{2h} symmetry.[230] Assuming an effective D_{2h} symmetry, the PAS of the CS tensor must be oriented such that one principal component is perpendicular to the plane of the molecule, another along the alkynyl bond, and the final component in the plane of the molecule but perpendicular to

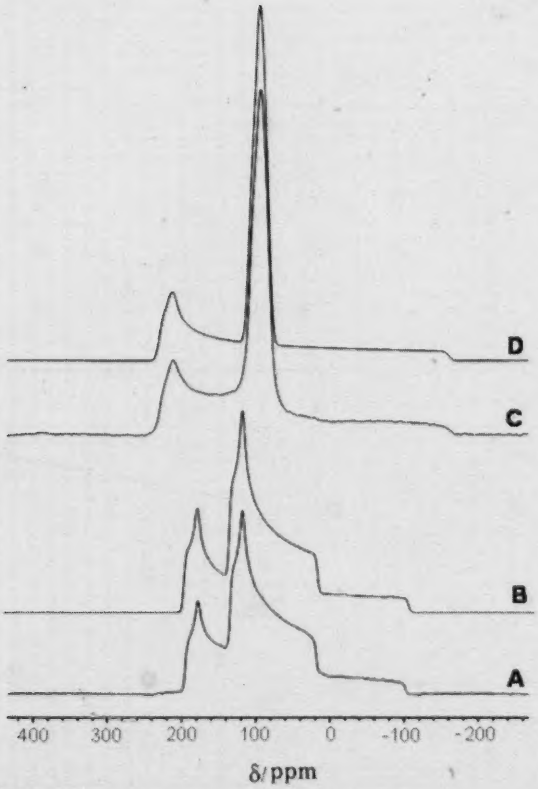

Figure 6.1: Simulated and experimental ^{13}C NMR spectra of the alkynyl carbons from stationary samples of DPA. Experimental spectra were recorded at applied field strengths of 9.4 (A) and 4.7 (C) T. The corresponding simulations are presented as traces B and D.

the alkynyl bond.

The ^{13}C NMR spectra from a stationary powder sample of diphenylacetylene-α,β-$^{13}C_2$ obtained at 4.7 and 9.4 T are shown in Figure 6.1; Table 6.1 summarizes data derived from the ^{13}C spectral simulations. While the line shape seen in Figure 6.1C appears unusual at first glance, this pattern has been observed before and arises from a cancellation effect in the orientation dependence of the shielding and dipolar coupling interactions for one of the transitions.[212,29] The best-fit simulated spectra yield a value of $R_{\text{eff}} = 4025 \pm 50$ Hz corresponding to a length of 1.236(5)

Table 6.1: Experimental and Calculated Alkynyl-Carbon Chemical Shift Tensors for Diphenylacetylene and (η^2-Diphenylacetylene)Pt(PPh_3)$_2$

	δ_{11}	δ_{22}	δ_{33}	δ_{iso}[a]	Ω[a]	α[b]	β	γ
DPA								
Exp[c]	165	147	−42	89.8	207	0	0	0
Calc	181	160	−39	101	220	0	0	0
PtDPA								
Exp[d]	226.5	142	23.5	130.6	203	0	85	78
	221	140	21.5	127.6	200	0	94	104
Calc	223	158	45	142	178	0	83	82
	222	154	44	140	178	2	80	101

[a]Chemical shift, δ_{iso}, and span,Ω , values are in ppm.

[b]The angles α, β, and γ are in degrees; see text for Euler angle conventions.

[c]Uncertainties are estimated to be: ± 0.2 ppm for δ_{iso}; ± 2 ppm for the principal components of the CS tensors and ± 3° for the angles.

[d]Uncertainties are estimated to be: ± 0.2 ppm for δ_{iso}, ± 3 ppm for the principal components of the CS tensors, ± 5° for β and γ, but ± 10° for α.

Å for the alkynyl bond. This NMR-derived bond length is ~4% greater than the 1.192(4) Å measured via X-ray crystallography by Zanin et al.[230] Such an apparent lengthening is not unexpected as NMR-determined bond lengths are generally 1-4% larger than those measured by diffraction studies because of averaging from vibrational/librational motion.[26–28] The isotropic chemical shift measured from the spectrum of the sample under MAS conditions, δ_{iso} = 89.8 ppm, is consistent with the previously reported solvated-sample value of 89.6 ppm.[246] Fits of simulated spectra to the data show that δ_{33} (-42 ppm) is along the alkynyl bond, but does not distinguish which of δ_{11} (165 ppm) and δ_{22} (147 ppm) is perpendicular to the molecular plane and which within it. DFT calculations (*vide infra*) suggest that δ_{11} is the component perpendicular to the molecular plane, as shown in Figure 6.2.

Alkynyl-carbon CS tensors have previously been published for acetylene,[210] propyne,[165] 2-butyne,[160,165] diacetylene,[211] 2-butyne-1,4-diol,[212] methoxyacety-

lene,[213] propiolaldehyde,[213] trimethylsilylacetylene[213] and phenylacetylene[214] (relaxation study). The CS tensor of DPA resembles that of the structurally similar phenylacetylene, whose terminal carbon has CS tensor components: δ_{33} = -27.8 ppm and $\delta_{11} = \delta_{22}$ = 131.8 ppm (values determined under the assumption $\delta_{11} = \delta_{22}$).[214] The common characteristic of alkynyl-carbon CS tensors is axial or near axial symmetry, with the direction of greatest shielding along the alkynyl bond. The other two components, which are identical or similar, are in the plane perpendicular to the alkynyl bond and exhibits a much less effective shielding. The CS tensor of DPA conforms to the above pattern closely.

Several theoretical investigations into the origins of chemical shifts in alkynyl carbons have been published using either the Cornwell approximation,[218–220] or the more sophisticated IGAIM method.[213,225] Examination of these analyses demonstrates that any substituents which do not affect the π-system of an acetylenic moiety will produce CS tensors very similar to those of the parent molecule, acetylene. Observe, for example, that the CS-tensor components of propyne and 2-butyne,[165] where the methyl substituents would not be expected to significantly affect the π-system, differ by a maximum of 15 ppm from those of acetylene.[210] Any more complicated π-system requires individual analysis due to the dependence of shielding on the structure and symmetry of the wave function. Even without such an analysis, it is the chemical shift along the alkynyl bond which will be most affected by the loss of a C_∞ axis. This is because it is only in the direction of a C_∞ axis that there is an identical lack of paramagnetic shielding terms.[167] For a detailed analysis of the effects of both substituents and an extended π-system, see the recent articles by Wiberg et al.[213,225] Theoretical studies of alkynyl-carbon chemical shifts have also been undertaken by Moss and Goroff, who investigated complexation of iodoalkynes.[247] There has also been some discussion on the effects of phenyl-ring substituents on diphenylacetylene.[248]

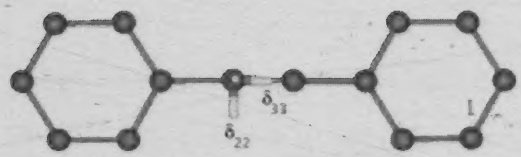

Figure 6.2: Principal axis system of the alkynyl-carbon CS tensor of DPA. The unlabelled principal component directed out of the page is δ_{11}.

DFT Chemical Shift Calculations

Given that the two symmetry non-equivalent DPA molecules are not distinguished by SSNMR, we chose only one for computational study. We selected the site for which all hydrogen atoms are recorded in the 293 K X-ray structure of Zanin et al.,[230] but we do not expect this selection to be pivotal considering the close structural similarities of the sites. The alkynyl-carbon CS tensors (see Table 6.1) were calculated and these reproduce δ_{33} to within 3 ppm, while δ_{11} and δ_{22} are slightly less accurate, being 16 and 13 ppm too large. The calculated CS tensor places δ_{33} along the alkynyl bond in agreement with experiment and the calculated orientations of δ_{11} and δ_{22} are as shown in Figure 6.2.

6.3.2 (η^2-Diphenylacetylene-α,β-$^{13}C_2$)Pt(PPh_3)$_2$

Crystal Structure

In 1967 a preliminary report on the structure of PtDPA was issued, in which unit-cell parameters as well as bond lengths and angles around the phosphorus, platinum, alkynyl-carbon and *ipso* phenyl carbon atoms were reported.[209] Apparently the investigation was hindered by the existence of both monoclinic and triclinic forms,[199] which, in light of the present results was likely due to inclusion of solvent molecules in the crystals (*vide infra*). The 1967 study reported that the compound crystallizes

in the triclinic space group $P\bar{1}$ with unit-cell parameters: a = 11.32(5) Å, b = 15.83(5) Å, c = 13.34(5) Å, α = 112.9(3)°, β = 113.4(3)°, γ = 83.7(3)°. While the authors do not state the solvent of crystallization, we find this to be an important factor for PtDPA. From acetone, we also found that the crystallites exhibited the symmetry of space group $P\bar{1}$, but with differing unit-cell parameters (see Table 6.2). While the values are significantly different, given the preliminary nature of the 1967 report as well as the lack of preparatory information, a direct comparison may not be valid. When using benzene as a mother liquor, we found that a 1:1 solvate was formed, crystals of which have the symmetry properties of monoclinic space group $P2_1/n$ (alternate setting of $P2_1/c$). Crystals could also be grown as solvates from dichloromethane, and these too were members of $P2_1/n$. Important structural features of the three forms we have observed are summarized in Table 6.2. Full details of the $P\bar{1}$ structure as well as the benzene and dichloromethane solvates can be found in Reference 3.

Because the SSNMR results are for the benzene solvate complex, and there are only minor differences in bond lengths and angles in the different forms, we limit further discussion and data to PtDPA·C_6H_6 only. The structure displayed in Figure 6.3 shows that the immediate coordination sphere of platinum displays a highly distorted square-planar geometry. The alkynyl carbons, which were related by an inversion centre in DPA, are crystallographically independent. The two phosphorus nuclei are also unrelated by any symmetry operation. Upon coordination to the metal, the alkynyl bond of diphenylacetylene is elongated from 1.197 (and 1.198) Å to 1.280(5) Å. The linear geometry along the triple bond is also lost, with the *ipso* carbons of the phenyl rings bent back from the unsaturated C,C bond vector by 37.4(3) and 37.7(3)°. The phenyl rings of the diphenylacetylene ligand are also twisted out of the plane (in opposite directions). The Pt,C bonds are 2.047(3) and 2.048(3) Å, and the C-Pt-C angle is 36.4(1)°. All structural parameters are similar

Table 6.2: Crystallographic Data for (η^2-Diphenylacetylene)Pt(PPh_3)$_2$ and Solvates

	PtDPA	PtDPA·C_6H_6	PtDPA·CH_2Cl_2
Formula	$C_{50}H_{40}P_2Pt$	$C_{56}H_{46}P_2Pt$	$C_{51}H_{42}Cl_2P_2Pt$
Cryst Syst	triclinic	monoclinic	monoclinic
Space Group	$P\bar{1}$	$P2_1/n$	$P2_1/n$
a (Å)	13.3195(8)	13.2507(7)	11.7140(8)
b (Å)	16.6524(9)	16.5061(9)	15.250(1)
c (Å)	18.304(1)	20.496(1)	23.707(2)
α (deg)	81.101(1)	90	90
β (deg)	87.024(1)	101.891(1)	91.847(2)
γ (deg)	77.930(1)	90	90
Z	4	4	4
Unique Molecules	2	1	1
S[a]	1.018	0.999	1.028
D map $\leq$ [b]	1.067	1.192	1.349
D map $\geq$ [c]	-0.450	-0.628	-0.571

[a]Goodness-of-fit: $S = [\sum w(F_o^2 - F_c^2)^2/(n-p)]^{\frac{1}{2}}$; n =number of data, p =number of parameters varied, $w = [\sigma^2(F_o^2) + (0.0278P)^2 + 1.0983P]^{-1}$, where $P = [\frac{1}{3}\mathrm{Max}(F_o^2, 0) + 2F_c^2]$.

[b]All peaks in final difference map less than the reported number in units of electrons per Å^3.

[c]All peaks in final difference map greater than the reported number in units of electrons per Å^3.

to those previously reported for (η^2-PhC≡CMe)Pt(PPh_3)$_2$.[249]

Solution ^{13}C NMR Spectra

The ^{13}C NMR spectrum of PtDPA dissolved in CD_2Cl_2, see Figure 6.4, was analyzed to produce the data shown in Table 6.3, where the information previously reported by Boag et al. is also reproduced for convenience.[199] The present use of doubly ^{13}C-labelled PtDPA provides information beyond that available in the earlier study. All parameters found from the solution ^{13}C NMR spectra are in good agreement with prior data. We note that the DPA ligand slowly dissociates in CD_2Cl_2, as peaks from PtDPA (centered at 127 ppm) lost intensity over time such that no signal from the complex was detectable in the ^{13}C NMR spectrum after 24 hours. Furthermore,

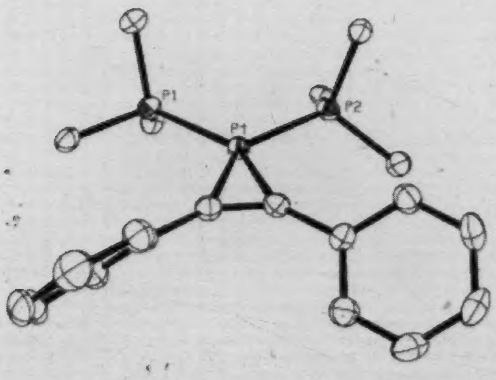

Figure 6.3: ORTEP[250] plot of PtDPA·C_6H_6 (50% probability ellipsoids) with hydrogen atoms and all but *ipso* carbons of the PPh_3 phenyl rings removed for clarity.

a signal of increasing intensity from unbound DPA at 89.581(5) ppm was observed. These effects in the spectra are not indicative of fast exchange however, as both $^1J(^{195}Pt,^{13}C)$ and $^2J(^{31}P,^{13}C)$ are observed. The compound appears stable in the solid form however, as samples of the benzene solvate packed into standard rotors exhibited no changes in the ^{13}C or ^{31}P NMR spectra over the course of several months.

NMR peaks from the ^{195}Pt-containing isotopomers (33.8%) are conveniently separated by the large magnitude of $^1J_{iso}(^{195}Pt,^{13}C)$ thus yielding this parameter, 301.1 Hz, separately. This value is typical for $^1J_{iso}(^{195}Pt,^{13}C)$ in Pt(0) complexes; further values including those for Pt(II) complexes can be found in references 196 and 197, but take note of Boag et al.'s word of caution[199] about errors in previous reports for the compounds (η^2-MeC≡CMe)Pt(PPh_3)$_2$ and *trans*-[PtMe(MeC≡CMe)-(PMe_2Ph)$_2$][PF_6].

Carbon-13 NMR signals arising from the alkynyl carbons allow J-couplings with phosphorus-31 to be elucidated. The isotopomers that do not contain ^{195}Pt constitute an AA′XX′ spin system,[251,252] spectral analysis of which shows that the *cis* and

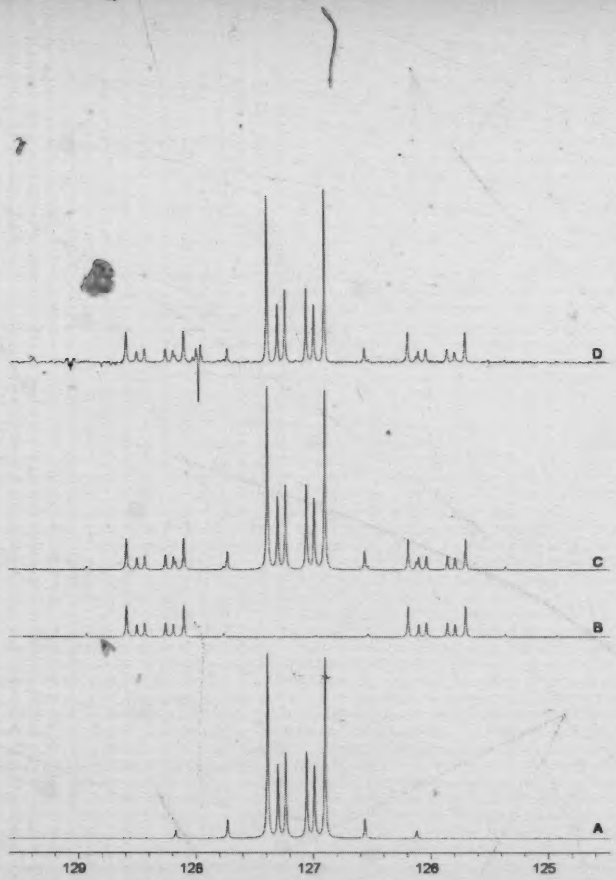

Figure 6.4: Simulated and experimental ^{13}C NMR spectra acquired from a sample of (η^2-diphenylacetylene)$Pt(PPh_3)_2$ dissolved in CD_2Cl_2. Simulated spectra are shown without (A) and with (B) ^{195}Pt ($I = \frac{1}{2}$, N.A. = 33.8 %). The sum of the subspectra is also shown (C) for comparison with the experimental spectrum (D), which has been corrected to show only alkynyl-carbons through subtraction of the spectrum from a non ^{13}C-labelled sample. The small distortions and negative peaks in the experimental spectrum arise from imperfections in the subtraction.

trans $^2J_{iso}(^{31}P,^{13}C)$ couplings are of opposite sign and have magnitudes of 68.7 and 7.1 Hz. The opposing signs of these terms makes their sum ±61.6 Hz, in close agreement with the value of ±61 Hz reported by Boag et al.[199] The larger of these values is assigned to the *trans* coupling as is usually done for the analogous alkene complexes of platinum.[253] Also, Wrackmeyer has shown that the sum $^2J_{iso}(^{31}P_{cis},^{13}C)$ + $^2J_{iso}(^{31}P_{trans},^{13}C)$ is positive for (η^2-C_2H_4)$Pt(PPh_3)_2$,[253] so it follows that for Pt-DPA the larger (*trans*) value of 68.7 Hz is positive and the smaller (*cis*) coupling of 7.1 Hz is negative. Analysis of the AA′XX′ spectrum also shows that $^1J_{iso}(^{13}C,^{13}C)$

has the value of either 85.7 or 31.8 Hz and $^2J_{iso}(^{31}P,^{31}P)$ has the other, but does not yield the relative signs of these two couplings.[251,252] The value of ±31.8 Hz has been assigned to $^2J_{iso}(^{31}P,^{31}P)$ given the similar magnitude to the 27 Hz reported for (η^2-PhC≡CPh)Pt(PMe_3)$_2$,[199] and the range of 35-56 Hz reported by Chaloner et al. for $^2J_{iso}(^{31}P,^{31}P)$ in a series of asymmetrical (η^2-alkene)Pt(PPh_3)$_2$ complexes.[198] Thus, the value of $^1J_{iso}(^{13}C,^{13}C)$ for PtDPA in solution is ±85.7 Hz, significantly less than that expected for an alkyne. For comparison, in acetylene $^1J_{iso}(^{13}C,^{13}C)$ is 171.5 Hz, in ethylene it is 67.6 Hz, and in ethane the coupling is 34.6 Hz.[254]

Solution and Solid-State ^{31}P MAS NMR Spectra

Analysis of the solution ^{31}P NMR spectrum (not shown) of doubly ^{13}C-labelled PtDPA is analogous to the ^{13}C case, and yields $\delta_{iso}(^{31}P)$ and ^{195}Pt coupling to ^{31}P. The data determined from this spectrum are also reported in Table 6.3. The value of $^1J_{iso}(^{195}Pt,^{31}P)$ = 3454.2 Hz is expected to be positive, as has been found in a large series of platinum phosphine complexes.[255,256]

For SSNMR studies, samples in which crystal symmetry dictates that there is only one unique molecule yield NMR spectra that are much simpler to analyze than those with more sites. Our NMR investigations were therefore focussed on the solvate complexes, with the benzene solvate chosen for its expected lower volatility. However, given the similar bond lengths and angles in each form, we expect the results reported here to apply to each form without significant changes. Furthermore, preliminary spectra of what was likely the solvent-free form are consistent with only minor changes from the currently reported data.[201] With the lower intrinsic resolution of SSNMR, the smaller couplings observed in solution spectra, $^2J_{iso}(^{31}P,^{13}C)$ and $^2J_{iso}(^{31}P,^{31}P)$, are not resolved and each phosphorus site produces a signal at its isotropic shift as well as from the AX spin pair with ^{195}Pt. Parameters from the SSNMR spectrum are similar to the values observed in solution and are listed

Table 6.3: ^{13}C and ^{31}P NMR Parameters of (η^2-Diphenylacetylene)$Pt(PPh_3)_2$

Parameter[a]		Solvated[b]	Literature[c]	MAS[d]
$\delta_{iso}(^{13}C_A)$	/ppm	127.145(5)	127.9	127.6(2)
$\delta_{iso}(^{13}C_B)$	/ppm			130.6(2)
$^1J_{iso}(^{195}Pt,^{13}C_A)$	/Hz	301.1(4)	299	265(15)
$^1J_{iso}(^{195}Pt,^{13}C_B)$	/Hz			285(15)
$^2J_{iso}(^{31}P_{trans},^{13}C_A)$	/Hz	68.7(4)	[e]	60(10)
$^2J_{iso}(^{31}P_{trans},^{13}C_B)$	/Hz			60(10)
$^2J_{iso}(^{31}P_{cis},^{13}C)$	/Hz	7.1(4)	[e]	
$^1J_{iso}(^{13}C,^{13}C)$	/Hz	85.7(4)		87(10)
$\delta_{iso}(^{31}P_A)$	/ppm	28.090(5)	27.2	30.4(1)
$\delta_{iso}(^{31}P_B)$	/ppm			26.1(1)
$^2J_{iso}(^{31}P,^{31}P)$	/Hz	31.8(4)		
$^1J_{iso}(^{195}Pt,^{31}P_A)$	/Hz	3454.2(4)	3445	3510(30)
$^1J_{iso}(^{195}Pt,^{31}P_B)$	/Hz			3380(30)

[a] All ^{13}C parameters refer to the alkynyl carbons. See text for discussion of the signs of these parameters.
[b] Dissolved in CD_2Cl_2.
[c] Data from the study of Boag et al.[199]
[d] Solid sample is PtDPA·C_6H_6.
[e] See text.

in Table 6.3. The simplicity of the solid-state spectrum is indicative of a single symmetry-unique molecule and thereby confirms that the powder was composed of the benzene solvate. Phosphorus-31 SSNMR was therefore used before and after all ^{13}C SSNMR measurements as a confirmation of purity.

Solid-State ^{13}C NMR Spectra

The ^{13}C NMR spectrum from the alkynyl-carbons of PtDPA·C_6H_6 under MAS conditions is shown in Figure 6.5. Overlapping peaks from natural-abundance carbon nuclei were first removed (*vide supra*), and all spinning sidebands added into the isotropic peak in order to mimic an infinite spinning rate experiment. Best-fit parameters are shown in Table 6.3, and the simulated spectrum utilizing this data is presented in Figure 6.5, where subspectra from each contributing isotopomer is also

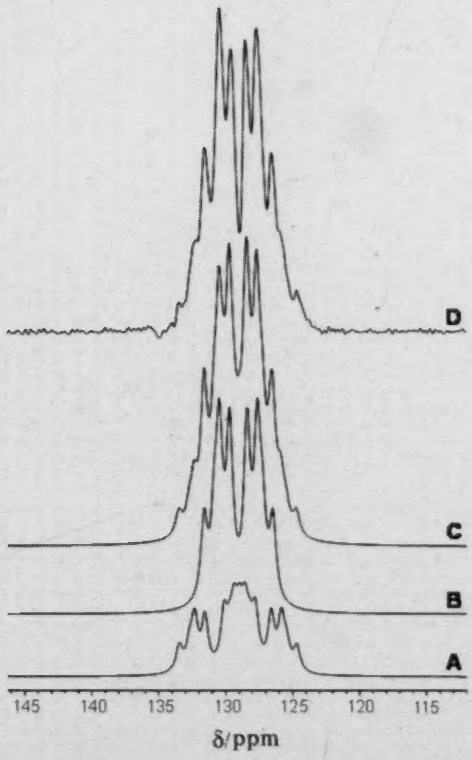

Figure 6.5: Simulated and experimental ^{13}C NMR spectra of the alkynyl carbons from PtDPA at 7.05 T, acquired with MAS (ν_{rot} = 8 kHz). Simulated spectra are shown with (A) and without (B) ^{195}Pt ($I = \frac{1}{2}$, N.A. = 33.8 %). The sum of the subspectra is also shown (C) for comparison with the experimental spectrum (D).

displayed. Non-quantitative matching of the simulation intensities to the central two peaks is attributed to the natural-abundance carbon correction which is largest in this region. These simulations were invariant to the value of $^2J(^{31}P_{cis},^{13}C)$ if this quantity is less than twice the value measured in solution. We also note that in this case, the relative signs of the J-couplings do not manifest themselves in the solid-state NMR spectrum. All parameters are found to be similar to those measured for PtDPA dissolved in CD_2Cl_2.

Both calculated and experimental ^{13}C NMR spectra of stationary $^{13}C_2$-labelled

PtDPA samples are shown in Figure 6.6. There remains some residual noise in the experimental line shapes from imperfect subtraction of natural-abundance ^{13}C signals. The 20 to 30 kHz broad powder patterns are not likely to be significantly affected by the less than 0.3 kHz couplings involving phosphorus-31 or the less than 0.8 kHz couplings involving platinum-195, particularly given the 33.8% natural abundance of ^{195}Pt. The system was therefore treated as an isolated AB spin pair of carbon-13 nuclei, and the chemical shift parameters derived from simulation are summarized in Table 6.1. Spectral simulations yield a value of 3250 $\pm$ 50 Hz for R_{eff} leading to an NMR-derived alkynyl C,C bond length of 1.327(7) Å, about 4% greater than that found by X-ray diffraction methods. As mentioned above, an apparent lengthening of this order is expected from vibrational/librational effects. We further note that simulations of the spectra from stationary samples are insensitive to $^1J(^{13}C,^{13}C)$ in the range determined from the MAS experiment.

The orientations for the alkynyl-carbon CS tensors of PtDPA are shown in Figure 6.7. As is seen there, the tensors are oriented such that δ_{22} is approximately along the alkynyl bond, δ_{33} is nearly perpendicular to the plane formed by platinum and the alkynyl carbons, while δ_{11} is approximately in the Pt-C_2 plane, orthogonal to the alkynyl bond. While this is one possible solution, the cylindrical symmetry of the dipolar interaction causes the spectral simulation to be invariant to simultaneous rotation of both tensors about the internuclear $^{13}C,^{13}C$ vector (in this case, the alkynyl bond).[32,33,207,208,210,257] All members of the solution set have δ_{22} approximately along the alkynyl bond while δ_{33} and δ_{11} are perpendicular to it, therefore these features are experimentally known. The absolute orientation of the tensors in the molecular framework can be determined if the dihedral angle between any one principal component and some other feature of the molecular geometry is found. Because the ZORA-DFT calculated CS tensors each have the δ_{11} principal component contained within the plane formed by the platinum and alkynyl-carbons atoms, this

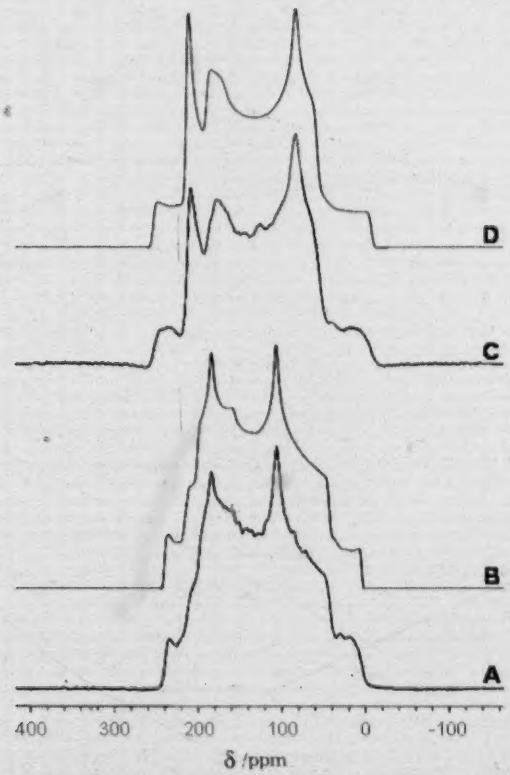

Figure 6.6: Simulated and experimental ^{13}C NMR spectra of the alkynyl carbons from stationary samples of PtDPA. Experimental spectra were recorded at applied field strengths of 11.75 (A) and 7.05 (C) T. The corresponding simulations are presented as traces B and D.

orientation parameter was fixed and all others seen in Figure 6.7 generated from the experimental Euler angles. In this instance, there is no ambiguity introduced from a need to pair specific calculated and experimental tensors, because the same relative orientation is shared by each experimental (where $\alpha_1 - \alpha_2 = 0$) and calculated (where $\alpha_1 - \alpha_2 = 2 \approx 0$) CS tensors.

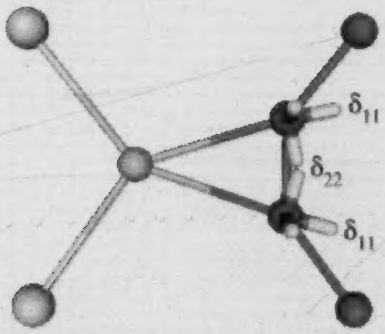

Figure 6.7: Principal axis systems for the alkynyl-carbon CS tensors of PtDPA. δ_{11} and δ_{22} are labelled, while δ_{33} is directed out of the page. For clarity, all phenyl rings are removed except the *ipso* carbons of the diphenylacetylene rings.

DFT Chemical Shift Calculations

The alkynyl-carbon CS tensors of PtDPA were calculated using the all-electron ZORA-DFT method described above. A similar theoretical method, equivalent other than the relativistic Pauli Hamiltonian and the frozen-core basis required, has been shown to yield excellent results in a series of $5d$ transition metal carbonyls.[235] Both the calculated shifts and available orientation information are in good agreement with experiment (see Table 6.1), which gives confidence in the angular information that was used to affix the CS tensors in the molecule.

Some previously published studies of alkenes η^2-bonded to platinum proposed absolute alkenyl-carbon CS tensor orientations based on $^{13}C,^{13}C$ dipolar chemical-shift solid-state NMR data together with Hartree-Fock or DFT (B3LYP) calculations employing an effective core potential (ECP) at platinum to account for relativistic effects.[207,208] Given the success of the relativistic all-electron calculations on the present system, an evaluation of the validity of the previous ECP calculations of carbon shielding is possible. Calculations using a nonrelativistic hamiltonian may fail to reproduce experimental observations for the following reasons: (*a*) absence

of the spin-orbit contribution to shielding which occurs only with a relativistic formalism,[217] or (*b*) lower quality of the zero-field wave function from the lack of a relativistic Hamiltonian. The spin-orbit contribution is < 6 ppm in any direction, therefore effect (*a*) does not seem to be significant here. Given that relativistic effects are greatest for core electrons and ECP methods replace these with relativistically derived pseudopotentials, it may be expected that ECP calculations will correct for most of effect (*b*). Using a frozen-core treatment (*vide supra*), which is analogous to an ECP calculation, the CS tensor is indeed reproduced with reasonable accuracy: $\delta_{11} = 226$ ppm, $\delta_{22} = 135$ ppm, $\delta_{33} = 68$ ppm. Furthermore, the orientations calculated with the two methods are qualitatively similar and when setting the final orientation of the experimental CS tensors as above, the two methods agree within 2 degrees. Based on this data, we find no reason to call into question the orientations proposed in earlier investigations through a combination of experiments and ECP calculations.[207,208]

6.3.3 Summary of the Effects of η^2-Bonding to Pt(0) on Unsaturated-Carbon CS Tensors

Effects of η^2-bonding to platinum on alkynyl-carbon chemical shifts have previously been probed with isotropic chemical shift data derived from spectra of solvated samples.[196] A consistent effect of decreased shielding has been observed; for example, Boag et al. reported a coordination-induced deshielding of 31.4 to 43.8 ppm for a large series of acetylenes in platinum(0) complexes.[199] For a solvated sample, the coordination-induced deshielding observed when DPA forms PtDPA has been reported as 38.3 ppm, similar to the 38 and 41 ppm observed here in the solid state.[199]

Determination of the orientation dependence of the alkynyl-carbon CS tensors for both DPA and PtDPA (see Figures 6.2, 6.7, and Table 6.1) provides a more

complete picture than the isotropic data previously investigated. The CS tensor of DPA is nearly axially symmetric and is aligned such that the direction of greatest shielding is along the triple bond, while two nearly equal principal components (avg. = 155 ppm) are found perpendicular to the bond. Upon coordination with platinum the chemical shift along the alkynyl bond, δ_{33} in DPA but δ_{22} in PtDPA, increases by nearly 200 ppm! Perpendicular to the C,C bond, bonding to platinum causes the chemical shift to increase by ~70 ppm in one direction (within the Pt-C_2 plane), but decrease by ~130 ppm in the other (perpendicular to the Pt-C_2 plane). It is particularly noteworthy that the chemical shift in directions perpendicular to the alkynyl bond is nearly the same in DPA (δ_{11} and δ_{22}), but varies by ~200 ppm in PtDPA (δ_{11} and δ_{33}). The net deshielding that has been observed upon coordination can now be seen to arise from a cancellation effect due to a deshielding in two directions, but an increased shielding in the third. Comparing just the principal components, δ_{22} is altered only slightly, while δ_{11} and δ_{33} are larger by approximately 60 ppm. However, consideration of the orientation information shows that δ_{22} of DPA is aligned perpendicular to the alkynyl bond, while it is nearly along the analogous bond in PtDPA. This reinforces the importance of analyzing chemical shift data utilizing not only the principal tensor components, but also geometrical information.

The effect of complexation with platinum(0) on an alkynyl-carbon CS tensor is different from what has been observed for alkenyl carbons. In PtDPA, there is a deshielding in two directions, and an increase in shielding along the third. In the closest alkene analogue, *trans*-stilbene forming (η^2-*trans*-stilbene)Pt(PPh_3)$_2$, coordination results in increased shielding in all directions.[208] A summary of the effects of bonding to platinum(0) on the CS tensors of alkynyl and alkenyl carbons is given in Figure 6.8.

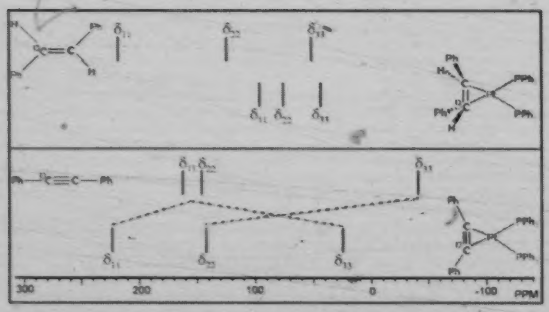

Figure 6.8: Summary of the effects on the CS tensors of alkenyl and alkynyl carbons caused by η^2-bonding with platinum(0). In the diagram for DPA forming PtDPA, dashed lines link orientationally similar principal components.

6.3.4 A Comparison of the Alkynyl-Carbon CS tensors for (η^2-Diphenylacetylene)Pt(PPh_3)$_2$ and *trans*-Stilbene

The bonding of unsaturated-carbon ligands to late transition metals is commonly discussed in terms of the Dewar-Chatt-Duncanson (DCD) model wherein donation of electron density to the π^*-type orbital of the ligand creates an effective double bond.[258–261] This model has provided effective arguments for the changes of such properties as bond lengths and vibrational frequencies of the ligand upon bonding to a transition metal. A key strength of the DCD model is that it is useful not only in property prediction, but also in providing intuitive insight into bonding which has proven helpful in modifying reactivity (e.g., reactivity umpolung).[262] As magnetic shielding is an electronic property, it is interesting to evaluate its relation to the DCD model. The obvious comparison for the alkynyl-carbon CS tensor in PtDPA is *cis*-stilbene since the DPA ligand in PtDPA has a similar structure to that of *cis*-stilbene. Although the alkenyl-carbon CS tensors for *cis*-stilbene are not known, they are not expected to be very different from those for *trans*-stilbene. This expectation is suggested by the fact that the principal components of the relevant carbon CS tensors for *cis*- and *trans*-2-butene do not differ by more than 15 ppm

and have the same orientation in their respective molecular frameworks.[263] The averaged values for the principal components of the alkynyl-carbon CS tensors of PtDPA, δ_{11} = 224 ppm, δ_{22} = 141 ppm and δ_{33} = 22 ppm, are similar to those measured for uncoordinated *trans*-stilbene: δ_{11} = 215 ppm, δ_{22} = 120 ppm and δ_{33} = 49 ppm.[208] This similarity is displayed visually in Figure 6.8. The orientation of the CS tensor of *trans*-stilbene is such that δ_{33} is approximately perpendicular to the molecular plane, δ_{22} is nearly parallel to the alkenyl C,C bond and δ_{11} is approximately in the molecular plane and orthogonal to the alkenyl bond; analogous to that of PtDPA (Figure 6.7). Not only are the CS tensors of the alkynyl-carbons of PtDPA similar to those of *trans*-stilbene, but the indirect coupling measured in solution, $^1J_{iso}(^{13}C,^{13}C)$ = 85.7 Hz, is also of similar magnitude to that of *trans*-stilbene, where $^1J_{iso}(^{13}C,^{13}C)$ = 72.9 Hz.[264]

Given the observed similarity for the CS tensors of PtDPA and *trans*-stilbene (TSB), the question becomes whether there is an equivalent response to the operators that describe magnetic shielding from TSB and the η^2-ligand in PtDPA. According to the DCD model, when analyzing the character (strength) of the alkynyl bond in PtDPA, the important features of the wavefunction are occupied molecular orbitals (MOs) containing fragment orbitals from the η^2-bonded portion of the organic ligand with σ, π_x, π_y, and π_y^* character. These fragment orbitals are interpreted to yield a net bond order of two between the carbons directly connected to platinum. However, since shielding depends on the entire MO (see appendix), the fact that these fragment orbitals exist in MOs that are linear combinations with *d*-orbitals on Pt becomes important. Since MO contributions from atomic orbitals at platinum need to be considered for shielding of the alkynyl carbon, there is likely some difference from the contributions to shielding of the alkenyl carbons in TSB.

Magnetic shielding can be calculated as a sum of contributions, whose exact form depends upon the theory applied. Here we discuss shielding in terms of the method

of Shreckenbach and Zeigler[221-223] (see also the appendix). Within this formalism, we examine the $\sigma^{p,oc-vir}$ term to probe for similarities or differences in the carbon shielding of TSB and PtDPA because of its similarity to the Cornwell approximation used in a body of literature analyzing shielding contributions.[218-220] There is a contribution to the magnetic shielding, σ, from the coupling of each pairing of an occupied, ψ_i^{occ}, with a virtual, ψ_j^{vir}, molecular orbital, and this contribution is labelled $\sigma_{ij}^{p,oc-vir}$. From the arguments presented in the appendix it is apparent that for PtDPA, the $\sigma_{ij}^{p,oc-vir}$ terms for the alkynyl carbons will include matrix elements of the $\hat{l}_z$ operator between atomic orbitals at platinum. We now turn to the question of whether these matrix elements have a significant effect on the shielding.

In order to address this question we investigate the alkynyl-carbon magnetic shielding tensor for the model system (η^2-acetylene)Pt(PMe_3)$_2$. DFT-GIAO calculation of magnetic shielding for the alkynyl carbons yield chemical shift tensor components: $\delta_{11} = 213$ ppm, $\delta_{22} = 56$ ppm, and $\delta_{33} = 55$ ppm, and a tensor orientation analogous to that of PtDPA (Figure 6.7). This is a fitting model as we here analyze the δ_{33} component which is only 10 (11) ppm different from the calculated results for the title complex. An energy level diagram of the complex is shown in Figure 6.9, which also displays two of the molecular orbitals relevant to magnetic shielding in this complex, designated HOMO-5 and LUMO+1. The coupling of HOMO-5 with LUMO+1 produces a $\sigma_{ij}^{p,oc-vir}$ term of +45 ppm in the shielding perpendicular to the Pt-C_2 plane. In the appendix, it is shown how a positive $\sigma_{ij}^{p,oc-vir}$ term is unusual, and furthermore how it originates in the structure of the occupied, ψ_i^{occ}, and virtual, ψ_j^{vir}, MOs away from the nucleus for which shielding is calculated. The two orbitals shown in Figure 6.9 have their largest contributions from atomic orbitals at Pt and this is the origin of the positive sign of $\sigma_{ij}^{p,oc-vir}$ for the alkynyl carbon arising from these two MOs. It is particularly interesting that contributions to the MOs from the atomic orbitals of platinum cause a large positive $\sigma_{ij}^{p,oc-vir}$ shielding

term for the alkynyl carbons, as this is the opposite sign to the usual case. In fact, DFT-GIAO calculations of the CS tensor for TSB (δ_{11} = 222 ppm, δ_{22} = 124 ppm, and δ_{33} = 30 ppm with orientation matching the experimental results noted above), and for the parent compound ethylene (δ_{11} = 267 ppm, δ_{22} = 113 ppm, and δ_{33} = 15 ppm with orientation analogous to TSB) show no positive contributions to $\sigma_{ij}^{p,oc-vir}$ perpendicular to the molecular plane greater than one quarter that shown above for (η^2-acetylene)Pt(PMe_3)$_2$. There are a large number of significant $\sigma_{ij}^{p,oc-vir}$ terms for (η^2-acetylene)Pt(PMe_3)$_2$, and many of these terms come from MOs that contain contributions from *d*-orbitals at Pt. While the effect on each of these terms is likely not as dramatic as the HOMO-5 and LUMO+1 coupling discussed above, according to the arguments in the appendix, each term between MOs containing contributions from atomic orbitals at Pt will be modulated by these contributions. Since the structure of the wavefunction at the metal is important for the alkynyl-carbon shielding, it appears that the metallic complex responds differently to the operators that describe magnetic shielding than does an organic alkene.

The DCD model provides invaluable insight into the nature of bonding in transition metal compounds. It is important however, to carefully consider the implications of this model. Typical applications of the DCD model are an explanation of the change in C,C bond length or IR frequency upon complexation. Effectively, these are both measures of the bond order which is dependent on the structure of the MOs local to the unsaturated carbon bond, while the magnetic shielding is an involved probe of the total structure of the occupied and virtual MOs. Describing an alkynyl ligand bound to platinum as an effective double bond is using terminology that refers to the electronic structure local to the ligand, while the shielding is shown here to not be local to the ligand. It then appears fitting to conclude that the CS tensors of the alkynyl carbons in PtDPA are similar to those of an alkene, but not *because* the alkynyl bond becomes an effective double bond in the complex.

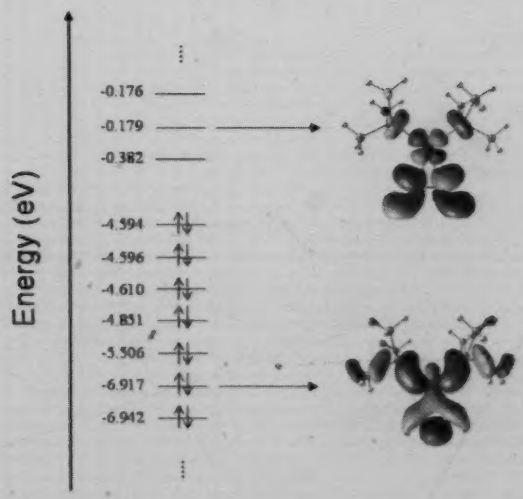

Figure 6.9: Abbreviated energy level diagram of the MOs of (η^2-acetylene)Pt(PMe_3)$_2$ on a nonlinear energy scale. We label the orbitals counting down from the HOMO, and counting up from the LUMO. The displayed molecular orbitals, HOMO-5 and LUMO+1, couple to produce a +45 ppm $\sigma_{ij}^{p,oc-vir}$ term directed out of the page for the alkynyl-carbon magnetic shielding (see text).

6.4 Conclusions

Previous studies of the orientation-dependent changes in alkenyl-carbon CS tensors upon coordination with Pt(0) and Pt(II) have provided prototypes for understanding isotropic chemical shift differences caused by bonding to late transition metals.[207,208] Because of the consistent effect of bonding on isotropic chemical shifts in a series of alkynes and their platinum(0) coordination complexes,[199] we believe study of a representative alkyne to be applicable to the CS tensor changes from coordination of alkynes with late transition metals. To this end, alkynyl-carbon chemical shift tensors of diphenylacetylene and (η^2-diphenylacetylene)Pt(PPh_3)$_2$ have been characterized by ^{13}C NMR spectroscopy of solid samples. Orientations for the carbon CS tensors have been proposed, based on a combined experimental and theoreti-

cal approach. This information provides a more complete picture of the effect of η^2-bonding to Pt(0) on the NMR parameters of alkynes. Upon coordination to platinum, the carbon chemical shift in two directions becomes larger (less effective magnetic shielding), but in the remaining one becomes smaller (increased magnetic shielding). These competing effects lead to a net larger value for the isotropic shift as has been observed in solution NMR studies for the coordination of alkynes in Pt(0) compounds.[199] This directional dependence is in contrast to the effects of coordination on alkenyl-carbon CS tensors, where formation of both Pt(0) and Pt(II) compounds causes the chemical shift to become smaller (more effective magnetic shielding) in all directions.[202–208] There exists a striking similarity between the orientation and principal component magnitudes of the alkenyl-carbon CS tensors in *trans*-stilbene and those of the alkynyl-carbons in PtDPA;[208] however, theoretical arguments demonstrate that the similarity is not due to the η^2-carbons forming an effective double bond. DFT calculations are found to be accurate enough for assigning final ^{13}C CS tensor orientations and valuable for providing theoretical insights.

6.5 Appendix

In order to contrast the origins of carbon magnetic shielding for alkenes versus η^2-bonded alkynyl carbons, we provide the following short theoretical discussion. The original formulation for the calculation of magnetic shielding is the perturbation-theory expression due to Ramsey which separates the shielding into diamagnetic and paramagnetic terms, $\sigma = \sigma^d + \sigma^p$.[167] The diamagnetic contribution contains terms only from the ground-state wavefunction and while large, varies little between compounds. Variations in the paramagnetic contribution are therefore responsible for nearly all of the difference in chemical shifts between compounds, and thus we focus on this term here.

We briefly discuss the DFT-GIAO formalism for the calculation of magnetic shielding due to Schreckenbach and Ziegler,[221,222] as it provides both accurate numerical results as well as the possiblity of deconvoluting the contributions to shielding. In this formulation, the paramagnetic term is further subdivided: $\sigma^{p} = \sigma^{p,oc-oc} + \sigma^{p,oc-vir} + \sigma^{p,rest}$, where $\sigma^{p,rest}$ is a "gauge invariance" term that is generally small, $\sigma^{p,oc-oc}$ arises from matrix elements between occupied MOs, and $\sigma^{p,oc-vir}$ are terms that involve matrix elements between occupied and virtual MOs. It is the $\sigma^{p,oc-vir}$ term that is informative in the present case, and its mechanism can be understood with relatively simple arguments in favorable cases. For a specific occupied, ψ_i^{occ}, and virtual, ψ_j^{vir}, molecular orbital (MO), the equation for this term is:

$$\sigma_{ij}^{p,oc-vir} = K u_{ji} h_{ji} \Delta E_{ji}^{-1}, \tag{6.1}$$

with K a collection of constants andΔ E_{ji}^{-1} the difference in energy between ψ_i^{occ} and ψ_j^{vir}.[221,222] All equations given below for the elements of u_{ji} and h_{ji} will be for the shielding observed when the magnetic field is along the z-axis. When expanding MOs in terms of atomic orbitals, AOs, we will use as notation: χ_μ^s for basis function μ centered at s, and $C_{\mu i}$ for the coefficient of this basis function in MO ψ_i. The operator for the z-component of angular momentum will be given as $\hat{l}_z^s$ which indicates that this operator is centered at the point s.

Several years ago, Schreckenbach and Ziegler pointed out that the leading contribution to u_{ji} is due to the sum (over all basis functions in ψ_i^{occ} and ψ_j^{vir}) of matrix elements with the form:[221,222]

$$T_{\nu\mu} = C_{\nu j} C_{\mu i} \langle \chi_\nu^t | \hat{l}_z^s | \chi_\mu^s \rangle . \tag{6.2}$$

To make the u_{ji} and h_{ji} terms of congruent form, one term from equation 3-22c of reference 222 is given, but with constants combined in K and the energy difference term given explicitly rather than absorbed in u_{ji}.

The second term, h_{ji}, is the sum of matrix elements:

$$U_{\nu\mu} = C_{\nu j} C_{\mu i} \langle \chi_\nu^t | \frac{\hat{l}_z^N}{r_N^3} | \chi_\mu^s \rangle \,, \tag{6.3}$$

again over all basis functions in both the occupied and virtual orbitals. In h_{ji}, the $\hat{l}_z$ operator is centered at the magnetic nucleus, N, and r_N^3 denotes the distance from the magnetic nucleus. We are interested in large changes in $\sigma_{ij}^{p,oc-vir}$, and therefore only need consider large terms. Since the $U_{\nu\mu}$ matrix elements fall off rapidly with distance from the magnetic nucleus, we exclude terms with atomic orbitals not from this nucleus (i.e., only terms with $t = s = N$ are kept for terms in h_{ji}). We also point out that as the $T_{\nu\mu}$ matrix elements in u_{ji} run over every atomic orbital that contributes to each of ψ_i^{occ} and ψ_j^{vir}, the magnitude of a given $\sigma_{ij}^{p,oc-vir}$ depends on the structure of the entire ψ_i^{occ} and ψ_j^{vir}, not just that at the magnetic nucleus.

Insight can be gained into the sign of $\sigma_{ij}^{p,oc-vir}$ from the form of these equations through consideration of the relative signs of u_{ji} and h_{ji}. An important point to note is that because $\frac{1}{r_N^3}$ is everywhere positive, the sign of $U_{\nu\mu}$ matrix elements are the same as those of $T_{\nu\mu}$ matrix elements between the same basis functions. For example, if the MOs ψ_i^{occ} and ψ_j^{vir} are both composed of a single AO at N, there is only one $T_{\nu\mu}$ and one $U_{\nu\mu}$ term, and these have the same sign and imaginary character. With these example MOs, the equation for $\sigma_{ij}^{p,oc-vir}$ is formed such that a negative contribution will result. If we now consider adding to both of the MOs ψ_i^{occ} and ψ_j^{vir} an AO with a larger coefficient at a second atom, the sign of h_{ji} is unaltered because it includes only the contribution at the magnetic nucleus. The u_{ji} term however, can have a different sign because it is dominated by the larger contribution from an AO at a second atom. This simple example shows how large positive contributions to $\sigma_{ij}^{p,oc-vir}$ can arise when the occupied and virtual orbitals involved are dominated by AOs at other atoms in the molecule. The effect on the

sign of σ^p contributions for a given nucleus by dominating MO contributions at other atoms was first described by Cornwell in explaining the "anomalous" ^{19}F shielding of ClF,[218] and Cornwell's argument was later shown to apply to the ^{19}F shielding in BrF and IF.[265] Positive paramagnetic shielding terms have also been the subject of IGAIM calculations.[224]

Chapter 7

NMR Line Shapes from AB Spin Systems in Solids: The Role of Antisymmetric Spin-Spin Coupling

7.1 Introduction

One of the most useful aspects of NMR spectroscopy for relating spectroscopic observables to molecular structure and dynamics is the inherent orientation dependence of the fundamental NMR interactions.[266] This orientation dependence is routinely measured in solid-state NMR spectroscopy, where, for example, internuclear coupling tensors, magnetic shielding tensors, and electric field gradient tensors are determined. Over the last decade, this orientation dependence has also been introduced in solution NMR spectroscopy by employing dilute liquid crystalline sol-

A version of this chapter has been accepted for publication. Harris, K.J.; Bryce, D. L.; Wasylishen, R. E. *Can. J. Chem.* **2009.**

vents which cause a small degree of molecular alignment, thereby preventing complete isotropic averaging of direct dipolar coupling tensors and magnetic shielding tensors.[267–272] By measuring the full orientation dependence of each interaction, a more complete description of the chemical environment can be built up. In this chapter, I will discuss one part of the indirect spin-spin coupling tensor, its antisymmetric component, that is usually ignored and has never been measured. In order to introduce the subject properly, I will discuss the various symmetry components of each interaction tensor, and describe why the antisymmetric component of $\underline{\mathbf{J}}$ is unique.

The most important fundamental NMR interactions in diamagnetic molecules include the electric field gradient ($\underline{\mathbf{V}}$), nuclear magnetic shielding ($\underline{\boldsymbol{\sigma}}$), direct dipolar coupling ($\underline{\mathbf{D}}$), and indirect coupling ($\underline{\mathbf{J}}$); each of which is represented by the noted second-rank tensor.[12] The $\underline{\mathbf{J}}$ tensor may be written in Cartesian form as follows, with up to nine elements:[151]

$$\underline{\mathbf{J}} = \begin{pmatrix} J_{xx} & J_{xy} & J_{xz} \\ J_{yx} & J_{yy} & J_{yz} \\ J_{zx} & J_{zy} & J_{zz} \end{pmatrix} . \tag{7.1}$$

In general, any second-rank tensor may be decomposed into three contributions. The rank-0 contribution is independent of orientation, and is given by (for $\underline{\mathbf{J}}$):

$$J_{\text{iso}} = \frac{1}{3} Tr(\underline{\mathbf{J}}) = \frac{1}{3}(J_{xx} + J_{yy} + J_{zz}) . \tag{7.2}$$

This term is also commonly known as the scalar coupling constant in the NMR spectroscopy literature of both solids and solutions. The isotropic portions of the $\underline{\mathbf{V}}$ and $\underline{\mathbf{D}}$ tensors are zero, while the isotropic part of $\underline{\boldsymbol{\sigma}}$ is the nuclear magnetic shielding constant, σ_{iso}. The shielding tensor and the isotropic shielding constant are

directly related to the experimentally observable chemical shift tensor $\underline{\boldsymbol{\delta}}$ and isotropic chemical shift δ_{iso}. Thus, the non-zero isotropic portions of NMR interaction tensors (J_{iso} and δ_{iso}) are routinely measured.

The rank-2 symmetric part of $\underline{\mathbf{J}}$ is given by:

$$\underline{\mathbf{J}}^{\text{sym}} = \frac{1}{2}\left(\underline{\mathbf{J}} + \underline{\mathbf{J}}^{\text{T}}\right) - J_{\text{iso}}\underline{\mathbf{1}} = \begin{pmatrix} J_{xx} - J_{\text{iso}} & \frac{1}{2}(J_{xy} + J_{yx}) & \frac{1}{2}(J_{xz} + J_{zx}) \\ \frac{1}{2}(J_{xy} + J_{yx}) & J_{yy} - J_{\text{iso}} & \frac{1}{2}(J_{yz} + J_{zy}) \\ \frac{1}{2}(J_{xz} + J_{zx}) & \frac{1}{2}(J_{yz} + J_{zy}) & J_{zz} - J_{\text{iso}} \end{pmatrix}$$

$$\underline{\mathbf{J}}^{\text{sym,PAS}} = \begin{pmatrix} J_{11} - J_{\text{iso}} & 0 & 0 \\ 0 & J_{22} - J_{\text{iso}} & 0 \\ 0 & 0 & J_{33} - J_{\text{iso}} \end{pmatrix}, \tag{7.3}$$

where $\underline{\mathbf{J}}^{\text{T}}$ is the transpose of $\underline{\mathbf{J}}$ and "symmetric" refers to the fact that $J_{ij}^{\text{sym}} = J_{ji}^{\text{sym}}$ in any axis system. As shown in Equation 7.3, when $\underline{\mathbf{J}}^{\text{sym}}$ is represented in its principal axis system, PAS, there are no off-diagonal elements and the diagonal elements are referred to as the principal components. Note that while there are three entries in $\underline{\mathbf{J}}^{\text{sym,PAS}}$, their sum is zero and $\underline{\mathbf{J}}^{\text{sym,PAS}}$ therefore contains only two independent elements (J_{iso} is an independent parameter, but it is part of the rank-0 component, and all elements of $\underline{\mathbf{J}}^{\text{sym,PAS}}$ can be expressed using J_{iso} and any two of J_{11}, J_{22}, and J_{33}). However, it should be noted that $\underline{\mathbf{J}}^{\text{sym}}$ is only fully described if its eigenvectors, i.e., the vectors that form its PAS, are known in addition to the two independent elements of $\underline{\mathbf{J}}^{\text{sym,PAS}}$. Because the PAS can be specified via three Euler angles that relate it to some reference frame in the molecule, $\underline{\mathbf{J}}^{\text{sym}}$ is generally described as containing five independent parameters. The principal components are defined as being ordered $|J_{33} - J_{\text{iso}}| \geq |J_{11} - J_{\text{iso}}| \geq |J_{22} - J_{\text{iso}}|$.[29,273] The $\underline{\mathbf{V}}$, $\underline{\mathbf{D}}$, and $\underline{\boldsymbol{\sigma}}$ tensors

can all have non-zero rank-2 symmetric contributions, but of course this depends on symmetry for $\underline{\mathbf{V}}$ and $\underline{\boldsymbol{\sigma}}$. For example, the nuclear quadrupolar coupling constant (C_Q) and asymmetry parameter (η_Q) are characteristic of $\underline{\mathbf{V}}^{\mathrm{sym}}$, the direct dipolar coupling constant used to extract internuclear distances from NMR measurements is characteristic of $\underline{\mathbf{D}}^{\mathrm{sym}}$, and the anisotropy and asymmetry parameters describing the nuclear magnetic shielding (or chemical shift) tensor are representations of $\underline{\boldsymbol{\sigma}}^{\mathrm{sym}}$. Thus, experimental measurements of the symmetric parts of $\underline{\mathbf{V}}$, $\underline{\mathbf{D}}$, and $\underline{\boldsymbol{\sigma}}$ (or $\underline{\boldsymbol{\delta}}$), are routinely made. Measurements of the principal components of $\underline{\mathbf{J}}^{\mathrm{sym}}$ are not nearly as straightforward;[25,29] nevertheless, much effort has been directed at making such measurements in the gas phase, in liquid crystal solutions, and in the solid state such that a body of reliable data now exists.[274,275] Quantum chemical calculation of J tensors is an important tool in the interpretation of experimental results,[171,276–285] and advances in this area are reviewed regularly.[274,286–288]

The rank-1 antisymmetric contribution to the NMR interaction tensors is zero for $\underline{\mathbf{V}}$ and $\underline{\mathbf{D}}$, but not for $\underline{\boldsymbol{\sigma}}$ or $\underline{\mathbf{J}}$. For the J tensor, this contribution is given by:[29,273]

$$\underline{\mathbf{J}}^{\mathrm{anti}} = \frac{1}{2}\left(\underline{\mathbf{J}} - \underline{\mathbf{J}}^{\mathrm{T}}\right) = \frac{1}{2}\begin{pmatrix} 0 & J_{xy} - J_{yx} & J_{xz} - J_{zx} \\ J_{yx} - J_{xy} & 0 & J_{yz} - J_{zy} \\ J_{zx} - J_{xz} & J_{zy} - J_{yz} & 0 \end{pmatrix}$$

$$= \begin{pmatrix} 0 & J_{yx}^{\mathrm{anti}} & J_{zx}^{\mathrm{anti}} \\ -J_{yx}^{\mathrm{anti}} & 0 & J_{zy}^{\mathrm{anti}} \\ -J_{zx}^{\mathrm{anti}} & -J_{zy}^{\mathrm{anti}} & 0 \end{pmatrix}. \qquad (7.4)$$

This component of $\underline{\mathbf{J}}$ is designated antisymmetric because of the obvious form of the matrix in Equation 7.4. An interesting geometrical argument rationalizing the function of $\underline{\mathbf{J}}^{\mathrm{anti}}$ has been presented by Robert and Wiesenfeld.[20] While $\underline{\mathbf{J}}^{\mathrm{sym}}$ can

be diagonalized through a change of basis, $\underline{\mathbf{J}}^{\text{anti}}$ remains in the form shown in Equation 7.4 under any choice of coordinate system. This means there is no obvious reference frame for $\underline{\mathbf{J}}^{\text{anti}}$, and therefore the simplest method is to report $\underline{\mathbf{J}}^{\text{anti}}$ in the PAS of $\underline{\mathbf{J}}^{\text{sym}}$; however, it should be noted that symmetry may require one or more elements of $\underline{\mathbf{J}}^{\text{anti}}$ to be zero in a particular coordinate system, in which case the tensor will still appear to have 6 entries (three unique) in other coordinate systems (compare with $\underline{\mathbf{J}}^{\text{sym}}$ versus $\underline{\mathbf{J}}^{\text{sym,PAS}}$). In summary, the rank-0 portion of $\underline{\mathbf{J}}$ contains one independent parameter, while the rank-2 symmetric portion contains five, and the rank-1 antisymmetric portion contains three. Any J tensor can therefore be represented in an arbitrary coordinate system using the six independent elements of $J_{\text{iso}} + \underline{\mathbf{J}}^{\text{sym}} + \underline{\mathbf{J}}^{\text{anti}}$, and three Euler angles relating the coordinate system to the PAS of $\underline{\mathbf{J}}^{\text{sym}}$.

It has been shown that the antisymmetric components of $\underline{\boldsymbol{\sigma}}$ affect the spectrum in second order only, causing small peak shifts and/or subtle pattern changes.[273,289,290] While direct effects on the spectra would generally be very small and thus difficult to detect, the components of $\underline{\boldsymbol{\sigma}}^{\text{anti}}$ can contribute to nuclear spin relaxation; however, only two reports of their influence on relaxation have been published.[291,292] Wi and Frydman have shown that cross-correlations with the quadrupolar Hamiltonian can make direct detection of $\underline{\boldsymbol{\sigma}}^{\text{anti}}$ more tenable, and have reported the antisymmetric components of the chemical shift tensor in cobalt (III) tris(acetylacetonate), referenced to 1M $K_3[Co(CN)_6](aq)$, as $\sigma_{zx}^{\text{anti}} = 1000 \pm 500$ ppm, $\sigma_{zy}^{\text{anti}} = -1000 \pm 500$ ppm, and $\sigma_{xy}^{\text{anti}} = 1000 \pm 1000$ ppm.[293] Nuclear spin relaxation measurements, similar to those used for $\underline{\boldsymbol{\sigma}}^{\text{anti}}$, could provide a method to detect the antisymmetric part of $\underline{\mathbf{J}}$,[191,294] while another experimental strategy may arise from the symmetry-based pulse-sequence design methodology developed by Levitt and co-workers.[45]

The rank-1 antisymmetric part of the J tensor remains as the only contribution to the four fundamental NMR interactions which has yet to be measured experi-

mentally. In 1968, Andrew and Farnell tackled this problem by considering a pair of spin-1/2 nuclei in the solid state, taking into account the full second-rank tensor nature of the chemical shift, the direct dipolar coupling tensor, and the indirect nuclear spin-spin coupling tensor.[4] Under rapid MAS, the chemical shift tensors are averaged to their isotropic values for each of the two nuclei involved; the direct dipolar coupling tensor is averaged to its isotropic value (zero); the isotropic J-coupling constant manifests itself in a fashion analogous to that in liquids, and the symmetric rank-2 part of the J tensor is averaged to zero. The most interesting aspect of their analysis, however, is with regards to the antisymmetric rank-1 part of $\underline{\mathbf{J}}$, which is averaged to zero in solution, but *not under MAS conditions.*[4,20] Here, the theory of Andrew and Farnell is extended to include averaging over the orientations of a micro-crystalline powdered sample, and methods for analyzing the resultant line shapes are presented. Additionally, the theory laid out by Andrew and Farnell alone does not provide much insight into what types of chemical systems may actually lead to an experimental observation of $\underline{\mathbf{J}}^{\text{anti}}$, and a discussion of such considerations is presented here. The discussion given below describes one strategy for the measurement of $\underline{\mathbf{J}}^{\text{anti}}$ and details some initial experimental attempts at its characterization.

7.2 Theory

The theory for describing NMR spectra from a pair of non-equivalent spin-1/2 nuclei in solution or in the solid state without effects from $\underline{\mathbf{J}}^{\text{anti}}$ is well established.[210,257,295] The nuclear spin Hamiltonian operator for a homonuclear pair of spin-1/2 nuclei in a stationary sample is:

$$\begin{aligned} h^{-1}\hat{\mathscr{H}} &= -(2\pi)^{-1}\gamma\hat{\mathbf{I}}(1-\underline{\boldsymbol{\sigma}}_{\mathrm{I}})\mathbf{B}_0 - (2\pi)^{-1}\gamma\hat{\mathbf{S}}(1-\underline{\boldsymbol{\sigma}}_{\mathrm{S}})\mathbf{B}_0 \\ &\quad + \hat{\mathbf{I}}\cdot\underline{\mathbf{J}}\cdot\hat{\mathbf{S}} + \hat{\mathbf{I}}\cdot\underline{\mathbf{D}}\cdot\hat{\mathbf{S}} \quad . \end{aligned} \tag{7.5}$$

After breaking the interaction tensors into their isotropic, symmetric, and antisymmetric components, and dropping nonsecular[8] terms, the effects of MAS in averaging orientation dependencies can be included. It is well known that all terms in the secular Hamiltonian containing $\underline{\mathbf{J}}^{\mathrm{sym}}$ and $\underline{\mathbf{D}}$ average to zero, and also that the secular part of $\hat{\mathbf{I}} \cdot \underline{\boldsymbol{\sigma}}_{\mathrm{I}} \cdot \mathbf{B}_0$ is averaged to $\sigma_{\mathrm{I}} \hat{I}_z$ when $\mathbf{B}_0$ is along the laboratory Z axis (I am using σ_{I} as notation for the isotropic shielding to avoid using the clumsy double subscript $\sigma_{\mathrm{iso,I}}$).[4] Therefore, the secular Hamiltonian under MAS can be defined as:

$$\begin{aligned} h^{-1}\hat{\mathcal{H}}_0^{\mathrm{MAS}} = \quad & -\nu_{\mathrm{L}}\left[(1-\sigma_{\mathrm{I}})\hat{I}_z + (1-\sigma_{\mathrm{S}})\hat{S}_z\right] \\ & + J_{\mathrm{iso}}\hat{I}_z\hat{S}_z + \frac{1}{2}J_{\mathrm{iso}}\left(\hat{I}_+\hat{S}_- + \hat{I}_-\hat{S}_+\right) \\ & + \hat{\mathbf{I}} \cdot \underline{\mathbf{J}}^{\mathrm{anti,MAS}} \cdot \hat{\mathbf{S}} \quad , \end{aligned} \tag{7.6}$$

where $\nu_{\mathrm{L}} = (2\pi)^{-1}\gamma B_0$, and $\underline{\mathbf{J}}^{\mathrm{anti,MAS}}$ is the MAS average of $\underline{\mathbf{J}}^{\mathrm{anti}}$, and an infinitely fast MAS rate is assumed. Lineshape simulations for solid samples generally neglect the term containing $\underline{\mathbf{J}}^{\mathrm{anti,MAS}}$; however, Andrew and Farnell have presented a theory including effects from the antisymmetric portion of $\underline{\mathbf{J}}$ on solid-state NMR spectra from a pair of spin-1/2 nuclei in a single crystal undergoing MAS.[4] We first review Andrew and Farnell's results for NMR spectra from a single crystal, and then extend the theory to include the orientational distribution of a powder sample. Methods for analyzing the resultant powder pattern in terms of the components of $\underline{\mathbf{J}}^{\mathrm{anti}}$ are then discussed.

7.2.1 The Antisymmetric J-coupling Hamiltonian

Starting with a stationary single crystal in the lab frame, the only secular terms in the antisymmetric J-coupling Hamiltonian between spins I and S are the two

involving $J_{YX}^{anti,L}$:

$$\begin{aligned} h^{-1}\hat{\mathcal{H}}^{anti} &= \hat{\mathbf{I}} \cdot \underline{\mathbf{J}}^{anti,L} \cdot \hat{\mathbf{S}} \\ h^{-1}\hat{\mathcal{H}}_0^{anti} &= J_{YX}^{anti,L}\left(\hat{I}_X\hat{S}_Y + \hat{I}_Y\hat{S}_X\right) \\ &= i\frac{1}{2}J_{YX}^{anti,L}\left(\hat{I}_+\hat{S}_- - \hat{I}_-\hat{S}_+\right) . \end{aligned} \tag{7.7}$$

Because $\hat{\mathcal{H}}_0^{anti}$ contains only the flip-flop operator involving spins I and S, it has a negligible effect on the energy levels unless the spins I and S have nearly equal chemically shifted Zeeman interactions; accordingly, $\underline{\mathbf{J}}^{anti}$ only affects NMR spectra from AB spin systems. Comparison to Equation 7.6 shows that $\hat{\mathcal{H}}_0^{anti}$ is similar in format to the flip-flop operator term involving J_{iso}, and will therefore have a similar effect on the energy levels. The additional antisymmetric coupling term will not have exactly the same action however, because it is an imaginary operator and has an opposite sign in the spin-operator term. The only step remaining before we can predict spectra using the Hamiltonian in Equation 7.6 is determination of the MAS average of $J_{YX}^{anti,L}$.

Under MAS, the orientation of each crystallite will become time dependent, so it is convenient to consider the tensor in the lab frame, $\underline{\mathbf{J}}^{anti,L}$, as being derived from its representation in the crystallite axis system depicted in Figure 7.1, $\underline{\mathbf{J}}^{anti,C}$, using direction cosines:[296]

$$J_{YX}^{anti,L} = \begin{bmatrix} \left(a_{Yx}a_{Xy} - a_{Yy}a_{Xx}\right) J_{yx}^{anti,C} \\ + \left(a_{Yx}a_{Xz} - a_{Yz}a_{Xx}\right) J_{zx}^{anti,C} \\ + \left(a_{Yy}a_{Xz} - a_{Yz}a_{Xy}\right) J_{zy}^{anti,C} \end{bmatrix} . \tag{7.8}$$

In Equation 7.8, each a_{Uv} is the cosine of the angle between coordinate-axis U

All other terms are of the form $J_{zz}\hat{I}_i\hat{S}_z$ or $J_{zz}\hat{I}_z\hat{S}_i$ (where i = x or y), which are nonsecular. See Appendix 17.5 of reference 8 or Chapter 3 of reference 11 for an explanation of why such terms do not affect the energy levels.

of the lab frame and coordinate-axis v of the crystallite frame. If some external motion causes the molecular orientation to change, each direction cosine will be time dependent. After including expressions for the time dependence of each a_{Uv}, the average value of $J_{YX}^{anti,L}$ under external motion can be derived (see appendix 5 of reference 10 for an instructive example where U is the laboratory Z axis and the external motion is MAS). Under isotropic tumbling the time average of $J_{YX}^{anti,L}$ is zero, but not for a solid undergoing MAS.[4] It is convenient to use the notation $A(\Theta)$ for the average value of $J_{YX}^{anti,L}$ under MAS, because it acts as an effective antisymmetric coupling constant which differs for each orientation,Θ , of the crystallite.[4] The effect of $\underline{\mathbf{J}}^{anti}$ is therefore to add a second coupling term to the secular Hamiltonian for an AB spin system under MAS:

$$h^{-1}\hat{\mathscr{H}}_0^{anti} = i\frac{1}{2}A(\Theta)\left(\hat{I}_+\hat{S}_- - \hat{I}_-\hat{S}_+\right) . \tag{7.9}$$

Andrew and Farnell have provided an expression for the effective antisymmetric coupling constant in a crystallite undergoing MAS, see equation 39 of reference 4. Application of a few algebraic manipulations produces an analogous, but slightly simpler, form for $A(\Theta)$:

$$A(\Theta) = 1/\sqrt{3}\begin{bmatrix} (\sin\xi_y \sin\xi_x)\, J_{yx}^{anti,C} \\ +(\sin\xi_z \sin\xi_x)\, J_{zx}^{anti,C} \\ +(\sin\xi_z \sin\xi_y)\, J_{zy}^{anti,C} \end{bmatrix} . \tag{7.10}$$

Equation 7.10 makes use of the coordinate system and definitions shown in Figure 7.1. As described in the previous section, the components of $\underline{\mathbf{J}}^{anti,C}$ are those in the crystallite reference frame shown in Figure 7.1, which could be, for example, the PAS of $\underline{\mathbf{J}}^{sym}$. While the depiction in Figure 7.1 is for the crystallite axis system at time zero, all angles in Equation 7.10 are constant during the motion of the

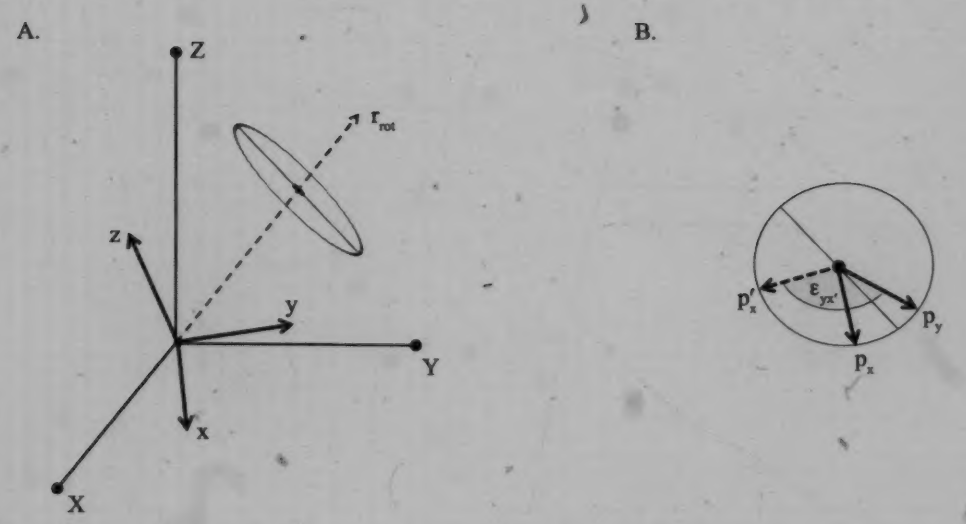

Figure 7.1: A. Coordinate system and conventions used in the expressions for the $A(\Theta)$ distribution. The lab frame is defined by the axes X, Y, Z; the axis of sample rotation is $\vec{r}_{rot}$, which is at the "magic angle" of $\cos^{-1}(1/\sqrt{3})$ relative to the Z axis; and the crystallite axis system in which $\underline{\mathbf{J}}$ is represented is described with the vectors x, y, z. Angles given as ξ_a are those between axis a of the crystallite frame and $\vec{r}_{rot}$. B. Normalized projections of the crystallite axes x, y, z on the plane perpendicular to $\vec{r}_{rot}$ shown in A are labelled p_x, p_y, and p_z. Rotation of these projected vectors by -90°about $\vec{r}_{rot}$ are annotated as the corresponding primed vectors p'_x, p'_y, p'_z; and angles given as $\varepsilon_{ab'}$ are those between p_a and p'_b ($\varepsilon_{yx'}$ is shown as an example).

rotor, reflecting the fact that the value of $A(\Theta)$ in each crystallite is independent of time. Furthermore, the rotational independence of the expression requires that any crystallites whose initial orientations are related to each other by rotation around the sample's spinning axis are characterized by the same value of $A(\Theta)$. However, any crystallites whose orientations do not become superimposed by the motion of the rotor will exhibit a different value of $A(\Theta)$, and a powder will therefore be characterized by a distribution of these effective coupling constants.

It is interesting to contrast the effects of MAS on $\underline{\mathbf{J}}^{\text{anti}}$ to its effect on the other anisotropic terms in the secular Hamiltonian. By defining $\underline{\boldsymbol{\sigma}}^{\text{sym}}$ analogously to the

definition of $\underline{\mathbf{J}}^{\mathrm{sym}}$ in Equation 7.3, the only orientation dependence in the secular Hamiltonian, discounting $\underline{\mathbf{J}}^{\mathrm{anti}}$, is contained in terms involving $\underline{\boldsymbol{\sigma}}^{\mathrm{sym}}$, $\underline{\mathbf{J}}^{\mathrm{sym}}$, and $\underline{\mathbf{D}}$. For these more familiar terms, the secular Hamiltonian's dependence on crystallite orientation is encoded in direction cosines between the applied magnetic field and the principal component axes of the involved tensor, i.e., terms of the form a_{Zv}.[4] Because the average squared value under MAS (or in solution) for this form of direction cosine, $\langle a_{\mathrm{Zv}}^2 \rangle$, is 1/3 for any crystallite orientation, the average of each secular Hamiltonian term involving $\underline{\boldsymbol{\sigma}}^{\mathrm{sym}}$, $\underline{\mathbf{J}}^{\mathrm{sym}}$, and $\underline{\mathbf{D}}$ is zero.[4,10] This averaging explains why these three terms need not be included in the Hamiltonian, and do not affect spectra of samples undergoing MAS (at a sufficiently rapid rate). The direction cosines describing the value of $J_{\mathrm{YX}}^{\mathrm{anti,L}}$ are obviously not of the same form, and this explains why the effect of MAS on $\underline{\mathbf{J}}^{\mathrm{anti}}$ differs from its effect on $\underline{\boldsymbol{\sigma}}^{\mathrm{sym}}$, $\underline{\mathbf{J}}^{\mathrm{sym}}$, and $\underline{\mathbf{D}}$; accordingly, the average value of $J_{\mathrm{YX}}^{\mathrm{anti,L}}$ under MAS is not zero, but a constant, $A(\Theta)$, that differs for each nondegenerate crystallite orientation.

7.2.2 The $A(\Theta)$ Distribution

To predict NMR spectra using the above Hamiltonian operator it is necessary to determine the shape of the $A(\Theta)$ distribution, and this was investigated here using numerical powder averaging. In order to determine a more general relationship, it is convenient to scale Equation 7.10 by the largest component of $\underline{\mathbf{J}}^{\mathrm{anti,C}}$. Considering first the case when $J_{\mathrm{zy}}^{\mathrm{anti,C}}$ is the largest element,

$$\begin{aligned} A(\Theta) &= J_{\mathrm{zy}}^{\mathrm{anti,C}}(1/\sqrt{3}) \begin{bmatrix} (\sin\xi_{\mathrm{y}} \sin\xi_{\mathrm{x}} \cos\varepsilon_{\mathrm{yx'}}) c_{\mathrm{yx}} \\ +(\sin\xi_{\mathrm{z}} \sin\xi_{\mathrm{x}} \cos\varepsilon_{\mathrm{zx'}}) c_{\mathrm{zx}} \\ +(\sin\xi_{\mathrm{z}} \sin\xi_{\mathrm{y}} \cos\varepsilon_{\mathrm{zy'}}) \end{bmatrix} \\ &= J_{\mathrm{zy}}^{\mathrm{anti,C}} \times f_{\mathrm{zy}}(\Theta; c_{\mathrm{yx}}, c_{\mathrm{zx}}) \ , \end{aligned} \tag{7.11}$$

where $f_{zy}(\Theta; c_{yx}, c_{zx})$ is a function of the crystallite orientation, which is again denoted byΘ . The function $f_{zy}(\Theta; c_{yx}, c_{zx})$ only involves the ratio of elements in $\underline{\mathbf{J}}^{anti,C}$ through the parameters $c_{ij} = J_{ij}^{anti,C}/J_{zy}^{anti,C}$; note that while the theoretical range for these parameters is $-1 \leq c_{ij} \leq 1$, all results were found to be independent of the sign of the c_{ij} constants. See Section 7.7 for specific details on the numerical calculations. As shown in Figure 7.2A, all values of f_{zy} between $\pm 1/\sqrt{3}$ are equally probable when $J_{zy}^{anti,C}$ is the only component of $\underline{\mathbf{J}}^{anti,C}$, while all values in the range ± 1 are populated equally when $J_{yx}^{anti,C} = J_{zx}^{anti,C} = J_{zy}^{anti,C}$. For all other values of the c_{ij} constants, the upper and lower limits of f_{zy} were found to be intermediate between the extremes of $\pm 1/\sqrt{3}$ and ± 1 mentioned above, and all values of the distribution were also found equally probable. There appears to be no obvious connection between the specific limits of f_{zy} and the c_{ij} constants, except in the two cases of $c_{yx} = c_{zx} = 0$ or 1. Results obtained under the assumption that either $J_{yx}^{anti,C}$ or $J_{zx}^{anti,C}$ are the largest component of $\underline{\mathbf{J}}^{anti,C}$ are entirely analogous. In summary, a powdered sample is populated equally by crystallites displaying all values of $A(\Theta)$ between -A_{max} and +A_{max}, where A_{max} is between 1 and $1/\sqrt{3}$ of the largest component of $\underline{\mathbf{J}}^{anti,C}$.

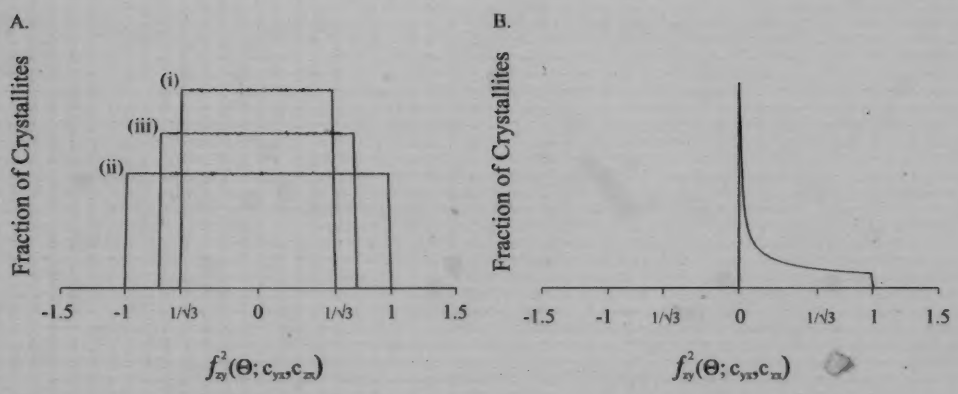

Figure 7.2: A. Numerically generated plots of $f_{zy}(\Theta; c_{yx}, c_{zx})$ versus fraction of crystallites displaying that value. (i) The smallest range of the f_{zy} distribution, $\pm 1/\sqrt{3}$, is found with the parameters $c_{yz} = c_{zx} = 0$. (ii) The largest range of the f_{zy} distribution, ± 1, occurs when $c_{yz} = c_{zx} = 1$. (iii) Example of the range found for the f_{zy} distribution with intermediate values of the c_{ij} constants, in this plot, $c_{yz} = 0$ and $c_{zx} = 0.8$. B. Plot of $f^2_{zy}(\Theta; c_{yx}, c_{zx})$, with parameters $c_{yz} = c_{zx} = 1$, the same as in A(ii).

7.2.3 NMR Spectra from a Single Crystal

From the above considerations, the secular Hamiltonian for one crystallite containing an isolated AB spin pair under fast MAS averaging must incorporate the usual terms involving isotropic nuclear magnetic shieldings for both nuclei, and the isotropic J coupling; additionally, it must include the antisymmetric J-coupling term defined above:

$$\begin{aligned} h^{-1}\hat{\mathscr{H}}_0^{\mathrm{MAS}} = \quad & -\nu_{\mathrm{L}}\left[(1-\sigma_{\mathrm{I}})\hat{I}_z + (1-\sigma_{\mathrm{S}})\hat{S}_z\right] \\ & + J_{\mathrm{iso}}\hat{I}_z\hat{S}_z + \frac{1}{2}J_{\mathrm{iso}}\left(\hat{I}_+\hat{S}_- + \hat{I}_-\hat{S}_+\right) \\ & + i\frac{1}{2}A(\Theta)\left(\hat{I}_+\hat{S}_- - \hat{I}_-\hat{S}_+\right). \end{aligned} \tag{7.12}$$

To predict the NMR spectrum resulting from this Hamiltonian, one must first find the energy levels. For spin-1/2 nuclei, taking the Zeeman states as basis functions,

the non-zero elements of the Hamiltonian matrix are the diagonal ones,

$$\begin{aligned}
\langle\alpha\alpha|h^{-1}\hat{\mathscr{H}}_0^{\mathrm{MAS}}|\alpha\alpha\rangle &= -\nu_{\mathrm{L}}\left[1-\frac{1}{2}(\sigma_{\mathrm{I}}+\sigma_{\mathrm{S}})\right]+\frac{1}{4}J_{\mathrm{iso}}\,,\\
\langle\alpha\beta|h^{-1}\hat{\mathscr{H}}_0^{\mathrm{MAS}}|\alpha\beta\rangle &= +\nu_{\mathrm{L}}\left[\frac{1}{2}(\sigma_{\mathrm{I}}-\sigma_{\mathrm{S}})\right]-\frac{1}{4}J_{\mathrm{iso}}\,,\\
\langle\beta\alpha|h^{-1}\hat{\mathscr{H}}_0^{\mathrm{MAS}}|\beta\alpha\rangle &= -\nu_{\mathrm{L}}\left[\frac{1}{2}(\sigma_{\mathrm{I}}-\sigma_{\mathrm{S}})\right]-\frac{1}{4}J_{\mathrm{iso}}\,,\\
\langle\beta\beta|h^{-1}\hat{\mathscr{H}}_0^{\mathrm{MAS}}|\beta\beta\rangle &= +\nu_{\mathrm{L}}\left[1-\frac{1}{2}(\sigma_{\mathrm{I}}+\sigma_{\mathrm{S}})\right]+\frac{1}{4}J_{\mathrm{iso}}\,; \qquad (7.13)
\end{aligned}$$

and two off-diagonal entries which contain contributions from J_{iso} and $A(\Theta)$:

$$\begin{aligned}
\langle\beta\alpha|h^{-1}\hat{\mathscr{H}}_0^{\mathrm{MAS}}|\alpha\beta\rangle &= \frac{1}{2}\Big[J_{\mathrm{iso}}-iA(\Theta)\Big]\,,\\
\langle\alpha\beta|h^{-1}\hat{\mathscr{H}}_0^{\mathrm{MAS}}|\beta\alpha\rangle &= \frac{1}{2}\Big[J_{\mathrm{iso}}+iA(\Theta)\Big]\,. \qquad (7.14)
\end{aligned}$$

Both $|\alpha\alpha\rangle$ and $|\beta\beta\rangle$ are eigenfunctions of $\hat{\mathscr{H}}_0^{\mathrm{MAS}}$, and their eigenvalues are simply given by the first and last expressions of Equation 7.13. The two remaining eigenfunctions can be obtained in the usual way[295] by diagonalizing the 2 x 2 submatrix containing the four remaining non-zero matrix elements. Resulting from this diagonalization is the set of energy levels and wave functions given in Table 7.1, where the following definitions have been used to simplify the expressions:

$$C = \sqrt{J_{\mathrm{iso}}^2+A^2(\Theta)+\Delta_s^2}\,, \qquad (7.15)$$

$$\Delta_s = \nu_{\mathrm{L}}(\sigma_{\mathrm{I}}-\sigma_{\mathrm{S}})\,, \qquad (7.16)$$

$$Q = \sqrt{2C(C-\Delta_s)}\,. \qquad (7.17)$$

Here,Δ_s is the difference between the magnetic shieldings of the two sites, measured in Hz. All results reduce to match those of the classic expressions for an AB spin system in the limit of $A(\Theta)=0$.

Table 7.1: Energy levels and wavefunctions for an AB spin system under MAS, including the effects of $\underline{\mathbf{J}}^{\text{anti}}$.

Wave Function[a]	Energy Level[a]	m_T[a]
$\psi_1 = \lvert\alpha\alpha\rangle$	$E_1/h = -\nu_L\left[1 - \frac{1}{2}(\sigma_I + \sigma_S)\right] + \frac{1}{4}J_{iso}$	+1
$\psi_2 = Q^{-1}\left(\left[J_{iso} + iA(\Theta)\right]\lvert\alpha\beta\rangle + \left[C - \Delta_s\right]\lvert\beta\alpha\rangle\right)$	$E_2/h = -\frac{1}{4}J_{iso} + \frac{1}{2}C$	0
$\psi_3 = Q^{-1}\left(\left[C - \Delta_s\right]\lvert\alpha\beta\rangle - \left[J_{iso} - iA(\Theta)\right]\lvert\beta\alpha\rangle\right)$	$E_3/h = -\frac{1}{4}J_{iso} - \frac{1}{2}C$	0
$\psi_4 = \lvert\beta\beta\rangle$	$E_4/h = +\nu_L\left[1 - \frac{1}{2}(\sigma_I + \sigma_S)\right] + \frac{1}{4}J_{iso}$	-1

[a]See text for definitions of constants; analogous expressions for the wave functions and energy levels may be found in reference 4.

Table 7.2: Transition frequencies and intensities for an AB spectrum, incorporating isotropic chemical shifts and the full $\underline{\mathbf{J}}$ tensor.

Transition	Frequency[a]	Relative Intensity[a]
$\nu_{3,4}$	$\nu_L\left[1 - \frac{1}{2}(\sigma_I + \sigma_S)\right] + \frac{1}{2}C + \frac{1}{2}J_{iso}$	$1 - J_{iso}/C$
$\nu_{1,2}$	$\nu_L\left[1 - \frac{1}{2}(\sigma_I + \sigma_S)\right] + \frac{1}{2}C - \frac{1}{2}J_{iso}$	$1 + J_{iso}/C$
$\nu_{2,4}$	$\nu_L\left[1 - \frac{1}{2}(\sigma_I + \sigma_S)\right] - \frac{1}{2}C + \frac{1}{2}J_{iso}$	$1 + J_{iso}/C$
$\nu_{1,3}$	$\nu_L\left[1 - \frac{1}{2}(\sigma_I + \sigma_S)\right] - \frac{1}{2}C - \frac{1}{2}J_{iso}$	$1 - J_{iso}/C$

[a]See text for definitions of constants.

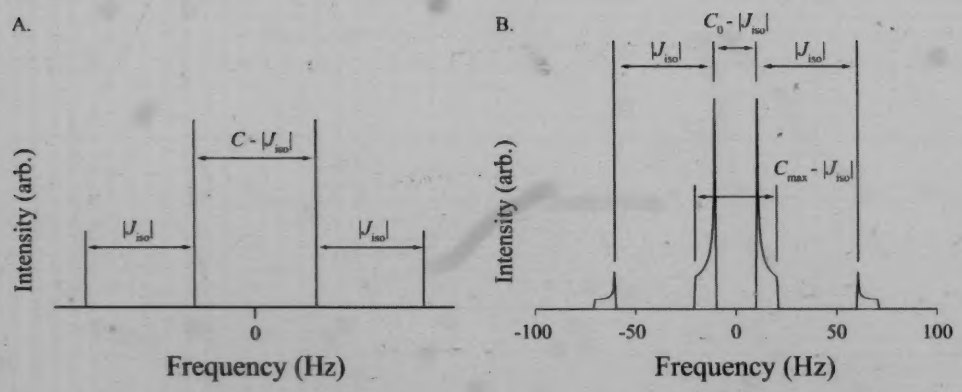

Figure 7.3: A. Numerically generated plots of $f_{zy}(\Theta; c_{yx}, c_{zx})$ versus fraction of crystallites displaying that value. (i) The smallest range of the f_{zy} distribution, $\pm 1/\sqrt{3}$, is found with the parameters $c_{yz} = c_{zx} = 0$.

The allowed transitions are those where m_T, the eigenvalue of the operator for the z-component of total spin angular momentum $\left(\hat{I}_z + \hat{S}_z\right)$, changes by ± 1,[295] and values of m_T for each wave function are reported in Table 7.1. Frequencies for each allowed transition are given in Table 7.2. Relative intensities for each transition may be determined from the absolute squares of the matrix elements of $\hat{F}_- = \hat{I}_- + \hat{S}_-$ between the involved wave functions,[295] and are also reported in Table 7.2. The spectrum expected from a single crystal undergoing MAS is presented in Figure 7.3A, and is analogous to the textbook example of an AB spectrum in solution (where $\underline{\mathbf{J}}^{anti}$ has no effect); however, for a solid sample under MAS, the splitting between the two central lines is increased when $A(\Theta)$ is nonzero. It is interesting to note that when $A(\Theta)$ is of substantial magnitude compared with J_{iso}, the relative intensities of the outer two transitions increase relative to the case when $A(\Theta)$ is negligible (for the same ratio of J_{iso} to the chemical shift difference between the two sites).

7.2.4 NMR Spectra from Powdered Samples

Because each crystallite of a powder has a different value of $A(\Theta)$, each will produce a different four-line NMR spectrum. The separation between the two inner peaks is $C - |J_{iso}|$, and because C is a function of A^2, the inner peaks will form powder patterns. The outer two peaks will also have a lineshape because, in every crystallite, each is separated by J_{iso} from the respective inner peak. The smallest separation between the inner two peaks occurs for crystallites with $A^2(\Theta) = 0$, designated as $C = C_0$ in Figure 7.3B, and this will also be the most intense portion of the lineshape as it is the most probable value of $A^2(\Theta)$. Crystallites with increasing values of $A^2(\Theta)$ will produce NMR spectra with an increasing separation between the inner peaks, but with decreasing intensity because of the smaller probability of $A^2(\Theta)$, see Figure 7.2B. The two outer peaks of each crystallite's spectrum will mimic that of the inner two, producing the total NMR spectrum given in Figure 7.3B.

The form of the spectrum in Figure 7.3 illustrates the information that can be derived from it. The spacings between the most intense parts of the four lineshapes are independent of the antisymmetric components of $\underline{\mathbf{J}}$, so these can be analyzed according to the methods used for AB NMR spectra of solution samples.[295,297,298] Because the outer two peaks are generally of too small an intensity to measure, it is usually necessary to obtain NMR spectra at two applied magnetic field strengths (or from two isotopomers) to separate the value of J_{iso} from that ofΔ_{g}. The largest splitting observed between the inner two transitions of Figure 7.3B occurs for crystallites where $C = C_{max}$, from which Equation 7.15 can be solved for A_{max}. And, as noted above, the absolute value of the largest of the three components of $\underline{\mathbf{J}}^{anti,C}$ is between $1A_{max}$ and $\sqrt{3}A_{max}$. Interestingly, it is not necessary to fit the entire lineshape, because all of the information comes from the breadth of the peak. Analysis of the NMR lineshape from an AB spin system under MAS therefore provides the

values of J_{iso}, Δ_s, and a measure of the largest component of $\underline{\mathbf{J}}^{\mathrm{anti,C}}$.

It is worth noting that symmetry requirements on the number of components in $\underline{\mathbf{J}}^{\mathrm{anti,C}}$, see below, have the possibility to fix the values of the c_{ij} constants and thereby reduce the noted range of $1A_{\mathrm{max}}$ to $\sqrt{3}A_{\mathrm{max}}$ that experiments can place on the largest component of $\underline{\mathbf{J}}^{\mathrm{anti,C}}$. We also note that the above results are independent of the choice used for the crystallite axis system. The PAS of $\underline{\mathbf{J}}^{\mathrm{sym}}$ can be used, but any crystallite axis system related by a set of three Euler angles could be chosen; accordingly, the experiment would provide an upper limit on the largest component of $\underline{\mathbf{J}}^{\mathrm{anti}}$ transformed to the new coordinate system. As the conclusions must remain valid under a change of the crystallite coordinate system, the final result is an upper limit of $\sqrt{3}A_{\mathrm{max}}$ on the largest component of $\underline{\mathbf{J}}^{\mathrm{anti}}$ as represented in any coordinate system. No orientation information regarding $\underline{\mathbf{J}}^{\mathrm{anti}}$ is produced by the experiment.

7.3 Selection of Appropriate Spin Systems and Compounds

In this section, we seek to establish some practical requirements for the observation of spectral features induced by $\underline{\mathbf{J}}^{\mathrm{anti}}$. There are several requirements which must be satisfied to ensure the feasibility of measuring $\underline{\mathbf{J}}^{\mathrm{anti}}$. Even if all the requirements are satisfied, there is no guarantee that $\underline{\mathbf{J}}^{\mathrm{anti}}$ will be of significant magnitude to be measured unambiguously. The requirements may be divided into those which concern the nuclear spin interactions of the nucleus to be observed, and those that describe the structural and symmetry properties of the molecule to be studied. The following discussion aims to demonstrate that after consideration of all requirements, only a small fraction of molecules are likely to provide an observation of $\underline{\mathbf{J}}^{\mathrm{anti}}$ using the present method. The discussion is focussed on powdered samples; however, measurement of $\underline{\mathbf{J}}^{\mathrm{anti}}$ from a single crystal has many of the same general requirements.

The first requirement is that a chemical system must be found for which the two nuclei are strongly J coupled and for which their isotropic chemical shift difference is as small as possible. This requirement may be understood by considering the governing Hamiltonian, Equation 7.12, where it may be seen that the only occurrence of A is as the coefficient of a flip-flop type operator. And, in the usual fashion, a flip-flop operator only affects the energy levels when the two involved spins have Larmor frequencies which do not differ by much more than the magnitude of its coefficient. This behaviour is also encoded in the energy-level expressions through the value of C, Equation 7.15, where it may be seen that the influence of A on the spectrum increases as the magnitude of A increases relative to the chemical shift difference. Because of the necessity of a small difference in chemical shifts, a homonuclear spin pair will be required. A pair of magnetically equivalent nuclei, which constitute an A_2 spin pair and give rise to identical chemical shifts, is not a suitable spin pair since J coupling between these nuclei will not manifest itself in the NMR spectrum. Hence, what is required is an isolated pair of bonded nuclei which are nearly (but not exactly) crystallographically equivalent, so they will have very similar isotropic chemical shifts, but are likely to have a large indirect nuclear spin-spin coupling interaction. Since the chemical shift difference is smaller in Hz at lower applied magnetic field strengths, in some cases the observation of $\underline{\mathbf{J}}^{\mathrm{anti}}$ will only be possible at low applied magnetic field strengths. Measurement of $\underline{\mathbf{J}}^{\mathrm{anti}}$ is therefore one of the unusual cases where it is advisable to use the lowest possible external magnetic field.

The second requirement within the present strategy is that one must have a chemical system for which there is an effectively isolated pair of spin-1/2 nuclei. Quadrupolar nuclei are not feasible candidates due to the typically dominant quadrupolar interaction; however, it is possible that another method for measuring antisymmetric J coupling may involve quadrupolar nuclei as the quadrupolar inter-

action was taken advantage of to estimate the antisymmetric part of the chemical shift tensor by Wi and Frydman.[293] Isotopes such as ^{1}H, ^{19}F, and possibly $^{203/205}$Tl will likely not be suitable due to strong homonuclear dipolar couplings preventing them from forming isolated spin pairs. Lastly, because of the fact that spin *pairs* must be observed, the spectral intensity will scale with natural abundance squared, and as such, natural abundance will play a more important role in selecting a nucleus (unless isotopic labelling is available).

Although Abragam states that the components of $\underline{\mathbf{J}}^{\mathrm{anti}}$ are expected to be negligible relative to the symmetric part of $\underline{\mathbf{J}}$,[299,300] multiconfigurational self-consistent field calculations on ClF_3 and OF_2 have indicated that the magnitudes of $\underline{\mathbf{J}}^{\mathrm{anti}}$ elements are comparable to those of the principal components of $\underline{\mathbf{J}}^{\mathrm{sym}}$ in these compounds.[301] Thus, a spin pair with a large value of J_{iso} favours the likelihood of there being an antisymmetric component of substantial magnitude. This requirement rules out certain spin pairs including ^{13}C and ^{15}N since, e.g., in a magnetic field of 4.7 T, the value of $^{1}J_{\mathrm{iso}}(^{13}\mathrm{C},^{13}\mathrm{C})$ would have to be well in excess of 50 Hz for a spin pair with a chemical shift difference of 1 ppm. Such a situation is not likely given that one-bond carbon-carbon coupling constants are typically on the order of 50 Hz.[302] Because J_{iso} values generally become larger moving down any group in the periodic table, the heavier elements present the best chance of possessing observable $\underline{\mathbf{J}}^{\mathrm{anti}}$ components.

Practically, one must be concerned with the chemical shift anisotropy of the nuclei in the AB spin pair. Heavier nuclei such as ^{199}Hg and ^{207}Pb tend to have substantial CS tensor spans.[303,304] When carrying out MAS NMR experiments on powdered samples, this fact introduces the additional complication that the spectral intensity is distributed over a large spectral width in the form of spinning sidebands. Thus, not only would a large span reduce the effective signal-to-noise ratio of the NMR spectrum, but it would also complicate the appearance and interpretation of

the spectrum. Hence it is preferable to find a system for which the nuclei have relatively small CS tensor spans. This requirement is not critical, especially if a single-crystal NMR experiment is to be performed. However, this discussion is focussed on measurements made using powdered samples.

The molecule under study must be of sufficiently low symmetry about the bond axis of the coupled nuclei to ensure that the antisymmetric component of $\underline{\mathbf{J}}$ is not forced to be zero by symmetry. The number of symmetry-allowed components in $\underline{\mathbf{J}}^{\mathrm{anti}}$ under various point groups is presented in Table 7.3 (see also references 20 and 30).

While the anisotropy of the symmetric part of $\underline{\boldsymbol{\sigma}}$ may pose a challenge in the acquisition of high-quality NMR spectra of the AB spin pair, we do not expect the antisymmetric component of $\underline{\boldsymbol{\sigma}}$ to hamper or influence the measurement of $\underline{\mathbf{J}}^{\mathrm{anti}}$ by this method. The effect of $\underline{\boldsymbol{\sigma}}^{\mathrm{anti}}$ on NMR lineshapes is generally expected to be very small.[273,289,290] However, in some cases it is possible for the inclusion of extra terms in the Hamiltonian to magnify effects from the typically nonsecular terms involving $\underline{\boldsymbol{\sigma}}^{\mathrm{anti}}$, e.g., a strong quadrupolar interaction is known to have such an effect.[293] Inspection of the wave functions in Table 1 shows that this is not the case with $\hat{\mathscr{H}}_0^{\mathrm{anti,MAS}}$, as terms in the Hamiltonian containing $\underline{\boldsymbol{\sigma}}^{\mathrm{anti}}$ remain nonsecular. Accordingly, we do not expect the predicted effects of $\underline{\mathbf{J}}^{\mathrm{anti}}$ to be obscured by the presence of $\underline{\boldsymbol{\sigma}}^{\mathrm{anti}}$ terms.

In the present work, the nuclei deemed most suitable for a definitive measurement of $\underline{\mathbf{J}}^{\mathrm{anti}}$ are ^{29}Si, ^{31}P, ^{77}Se, $^{111/113}$Cd, $^{115/117/119}$Sn, $^{123/125}$Te and ^{129}Xe. There is also a possibility that some heavier nuclei could provide valuable results, particularly if single crystal spectra are investigated using MAS.

Table 7.3: Number of independent components of $\underline{\mathbf{J}}^{\text{anti}}$ for each point group, assuming the two nuclei are not exchanged by a symmetry operation (condensed from Table 3.2).

Point Group Symmetry About the Two Coupled Nuclei	Number of Unique Antisymmetric Components
C_1	3
C_s, C_n $(n > 2)$	1
all others	0

7.4 Data Collection and Analysis

Now that the most promising candidates for the observation of homonuclear antisymmetric J coupling have been narrowed down, suitable compounds must be identified. Tin seems to be the most promising element due to the high receptivities of the ^{119}Sn and ^{117}Sn isotopes, in addition to moderate chemical shift anisotropies and a well-developed synthetic chemistry.

7.4.1 Tin-119 Solid-State NMR Spectroscopy of Hexa(*p*-tolyl)ditin

Many ditin compounds of the type R_3Sn-SnR_3 possess magnetically equivalent tin atoms which are related by an inversion centre. Others have C_{3v} symmetry, which by symmetry require all elements of $\underline{\mathbf{J}}^{\text{anti}}$ to be zero.[20,30] One candidate that satisfies the stringent requirements is hexa(*p*-tolyl)ditin, shown in Figure 7.4, which has two crystallographically non-equivalent tin atoms.[305] Solution ^{119}Sn NMR in $CDCl_3$ has provided a value of δ_{iso} = -141.9 ppm for the then chemically equivalent tin atoms, and a value of $^1J_{\text{iso}}(^{119}\text{Sn},^{119}\text{Sn})$ of 4570 Hz.[305]

The ^{119}Sn CP/MAS NMR spectrum of solid powdered hexa(*p*-tolyl)ditin acquired at 7.05 T is presented in Figure 7.5A; ^{119}Sn and ^{117}Sn CP/MAS spectra were also obtained at 4.70 T (not shown). The form of the spectrum, which appears more complicated than the four-line ideal spectrum presented in Figure 7.3, is due

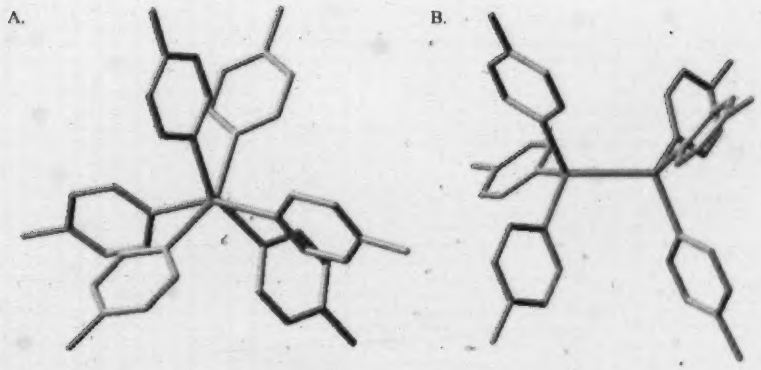

Figure 7.4: Structure of hexa(*p*-tolyl)ditin. A. View along the tin-tin bond. B. Side view. Hydrogen atoms are omitted for clarity.

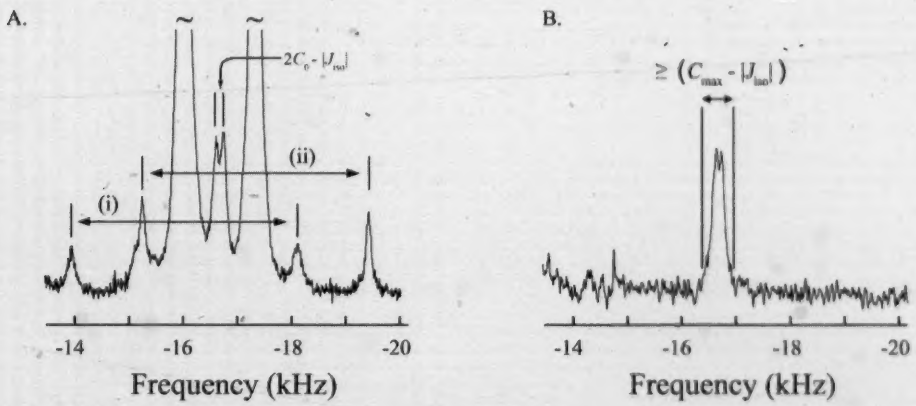

Figure 7.5: A. Tin-119 VACP/MAS spectrum of hexa(*p*-tolyl)ditin obtained at 7.05 T. The two dominant peaks result from the uncoupled nuclei, and are therefore far more intense than peaks from the coupled isotopomers. The splitting (i) is equal to $^1J_{iso}(^{119}Sn,^{117}Sn)$ for site 1 and the splitting (ii) is $^1J_{iso}(^{119}Sn,^{117}Sn)$ for site 2. The splitting corresponding to $C_0 - |J_{iso}(^{119}Sn,^{119}Sn)|$ is also marked in the figure. B. Tin-119 POST-C7 spectrum of hexa(*p*-tolyl)ditin also obtained at 7.05 T under MAS, where the double-quantum pulse sequence filters out all but homonuclear spin pairs, leaving only the central part of the AB pattern. The edges of the lineshape provide a maximum value for $C_0 - |J_{iso}(^{119}Sn,^{119}Sn)|$, and therefore of the largest component of $\underline{\mathbf{J}}^{anti}$.

to the fact that the ^{119}Sn isotope is not 100% abundant. We also note that nearly all of the spectral intensity is concentrated in the centrebands, as ^{119}Sn CP NMR spectra of a stationary sample of hexa(*p*-tolyl)ditin indicated a CS tensor span for tin of less than 200 ppm. Values for the NMR parameters derived from these spectra are presented in Table 7.4. The isotropic chemical shifts of the two Sn sites in hexa(*p*-tolyl)ditin are easily determined as 142.5 and 154.2 ppm from the peaks of the uncoupled ^{119}Sn nuclei, providing a value for Δ_s of 1310 ± 20 Hz. In Figure 7.5A, the splittings (i) and (ii) between the outer two pairs of lines reflect the couplings of sites 1 and 2 to ^{117}Sn nuclei. These two couplings are found to be the same (as expected), and the spectra yield a final value of 4175 ± 20 Hz for $^1J_{\rm iso}(^{119}{\rm Sn},^{117}{\rm Sn})$ in hexa(*p*-tolyl)ditin. Because isotope effects are expected to be insubstantial here,[306] a value for $^1J_{\rm iso}(^{119}{\rm Sn},^{119}{\rm Sn})$ of 4368 Hz may be obtained through multiplication by the ratio of the magnetogyric ratios, $\gamma(^{119}{\rm Sn})/\gamma(^{117}{\rm Sn})$.[151] The splitting $C_0 - |J_{\rm iso}|$, see Figure 7.5A, is 140 ± 50 Hz, which agrees within error with the splitting of 192 ± 7 Hz expected from the above values of $J_{\rm iso}$, and Δ_s. Note that for molecules containing two ^{119}Sn nuclei, the two outer transitions are not observed in the ^{119}Sn NMR spectrum shown in Figure 7.5A. Because the integrated intensity of each of the transitions is approximately 2.2% of each of the inner transitions, it would be extremely difficult to observe them. It would be possible to observe effects of $\underline{\mathbf{J}}^{\rm anti}$ solely from the inner transitions; however, spectral crowding by peaks from the other isotopomers prevents observation of the entire line shape and could be responsible for obscuring the effects of $\underline{\mathbf{J}}^{\rm anti}$.

In an effort to determine some line shape for the inner two peaks, a two-dimensional *J*-resolved ^{119}Sn NMR experiment was obtained at 4.70 T.[307,308] In the *J*-resolved experiment, heteronuclear dipolar interactions as well as anisotropic chemical shifts are refocussed at the top of the echo, thereby providing better resolution in the indirect ($F1$) dimension.[307] Furthermore, because the peaks from

Table 7.4: Tin-119 NMR parameters determined for hexa(*p*-tolyl)ditin.

Parameter		Value
δ_{iso}(site 1)	/ppm	-142.5 ± 0.2
δ_{iso}(site 2)	/ppm	-154.1 ± 0.2
$^1J_{iso}(^{119}Sn,^{119}Sn)$	/Hz	4368 ± 20
$^1\underline{J}^{anti}(^{119}Sn,^{119}Sn)$ elements	/Hz	$\lesssim 2900$

the AB pattern are separated along the $F1$ dimension, this experiment presents the opportunity to observe some anisotropic line shape that could be obscured in the one-dimensional spectrum. Shown in Figure 7.6 is a 2D J-resolved ^{119}Sn CP/MAS NMR spectrum of hexa(*p*-tolyl)ditin. The projection of this spectrum onto the isotropic dimension corresponds to the one-dimensional CP/MAS spectrum. In the indirect J-resolved dimension, the splitting $C_0 - |J_{iso}(^{119}Sn,^{119}Sn)|$ is much better resolved than it is in the isotropic dimension, and therefore provides a more accurate measurement. The precision of the measurement in the indirect dimension is limited by the number of points which define the spectrum. In the spectrum shown in Figure 7.6, 16 points define the 200 Hz spectral window in the indirect dimension, thereby providing one data point every 12.5 Hz. The splitting $C_0 - |J_{iso}(^{119}Sn,^{119}Sn)|$ is 85.0 ± 12.5 Hz, which compares favourably with the splitting of 87 ± 5 Hz expected from J_{iso} and the$\Delta_s = 875 \pm 20$ Hz measured from the 1D spectrum acquired at the same applied field strength. Unfortunately, when the signal is spread out into two dimensions, the signal-to-noise ratio of the inner two peaks of the AB spectrum is reduced such that any lineshape present would not be detected.

Another method of decongesting the spectral overlap seen in Figure 7.5A is to use a double-quantum filter, DQF, to remove any peaks that do not arise from a homonuclear spin pair. The spectrum shown in Figure 7.5B is an example of this method where we have used the POST-C7 experiment which leaves only peaks from

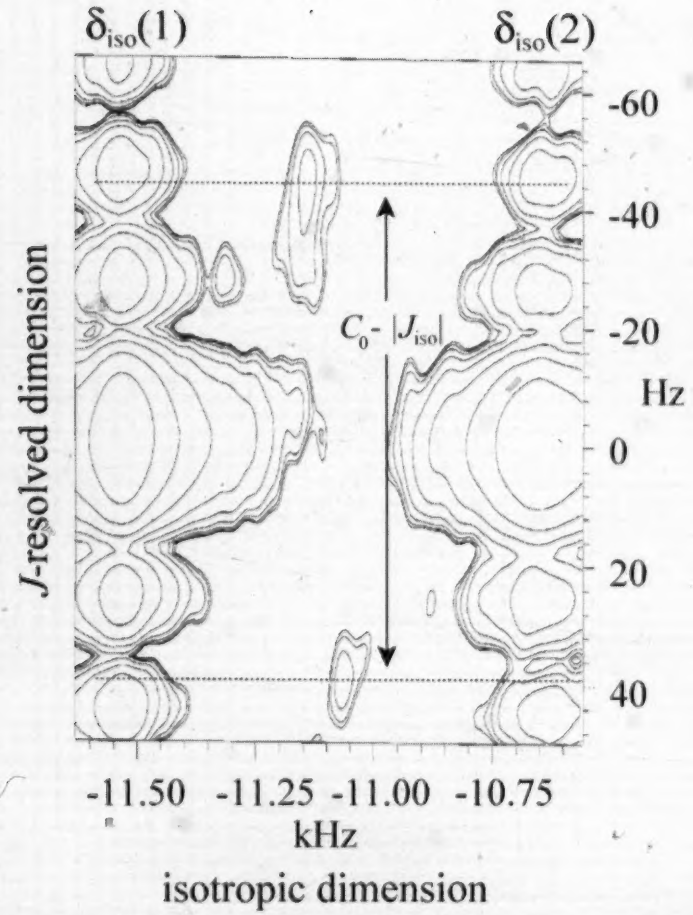

Figure 7.6: 2D J-resolved ^{119}Sn CP/MAS NMR spectrum of hexa(*p*-tolyl)ditin obtained at 4.70 T. The splitting $C_0 - |J_{iso}(^{119}Sn, ^{119}Sn)|$ is easily resolved in the second dimension.

^{119}Sn nuclei that are relatively strongly dipolar coupled to one another.[309,310] The spectrum in Figure 7.5B therefore corresponds to that of 7.5A, except that only the inner two peaks from the AB spin system remain. Because of the low natural abundance of ^{119}Sn spin pairs and the loss of signal during the POST-C7 pulse sequence, sufficient signal to noise was difficult to obtain; however, after three days of acquisition the spectrum was resolved well enough to be useful. Before providing

a concrete evaluation, we note that A_{max} only produces a significant effect on the spectrum when its magnitude is comparable to both J_{iso} andΔ_s. For example, the breadth of the each of the inner peaks of Figure 7.5B, $C_{max} - C_0$, would only be 11 Hz if A_{max} were 450 Hz (10% of J_{iso}). Comparing the DQF spectrum to the theoretical form of Figure 7.3B shows that the edges of the peaks in the DQF spectrum provide an upper limit to C_{max}, and therefore an upper limit on the largest element of $\underline{\mathbf{J}}^{anti}$. The breadth of the AB doublet is 500 Hz, which translates into a value of 1700 Hz for A_{max}, and A_{max} is from 1 to $1/\sqrt{3}$ of the largest element of $\underline{\mathbf{J}}^{anti}$. The DQF spectrum therefore provides an upper limit of 2900 Hz for the largest element of $\underline{\mathbf{J}}^{anti}$ in hexa(*p*-tolyl)ditin.

In cases where a peak shoulder is directly observed, an exact value of A_{max} can be extracted; however, only the peak width can be determined from the presented spectrum of hexa(*p*-tolyl)ditin, and therefore only an upper limit on A_{max} can be reported. It should also be noted that line broadening from other sources acts to increase the upper limit provided by this analysis. For example, the sample calculation presented in the preceding paragraph shows that even if A_{max} were zero in this compound, line broadening causing an apparent increase in $C_{max} - C_0$ of only 11 Hz would lead to an upper limit of 450 Hz for A_{max}. Because of interference from line-broadening effects, the actual value of $\underline{\mathbf{J}}^{anti}$ elements may be anywhere between 0 and the upper limit of 2900 Hz. Despite the limitations of analyzing a spectrum for which the theoretically expected shoulder is not observed, it is interesting that we can place a definite upper limit on $\underline{\mathbf{J}}^{anti}$ elements.

7.5 Experimental and Theoretical Implications

Given that quantum chemical calculations have shown that the magnitudes of $\underline{\mathbf{J}}^{anti}$ elements have the potential to be comparable to those of $\underline{\mathbf{J}}^{sym}$,[301] it is important to consider their effect on NMR spectra. Effects from $\underline{\mathbf{J}}^{anti}$ have generally been

ignored in spectral analysis, despite the fact that Andrew and Farnell have predicted measureable effects on AB spectra from single crystals spinning at the magic angle.[4] Aside from interest in $\underline{\mathbf{J}}^{\mathrm{anti}}$ itself, it is important to consider whether the presence of large elements in $\underline{\mathbf{J}}^{\mathrm{anti}}$ could lead to errors when analyzing AB spectra of powders undergoing MAS. While an observable difference in peak position is predicted for each crystallite, it is found here that the most probable frequency, i.e., the highest part of each peak, is independent of $\underline{\mathbf{J}}^{\mathrm{anti}}$. Therefore, one need not worry about $\underline{\mathbf{J}}^{\mathrm{anti}}$ introducing errors in determinations of the other NMR observables under these conditions.

While the above theory shows that it is possible to analyze spectra independently of $\underline{\mathbf{J}}^{\mathrm{anti}}$, the discussion also presents a strategy for its measurement. The fundamental reason for measuring the antisymmetric parts of NMR interaction tensors, and indeed for measuring the anisotropic symmetric parts, is to make use of the fact that up to nine independent elements are available for a given interaction tensor (see Equation 7.1). Routine use is made of the isotropic portions of the chemical shift and J-coupling tensors; the availability of up to eight more parameters to describe a given interaction signifies the opportunity to provide much more complete descriptions of the nuclear environment.

The potential existence of sizable antisymmetric contributions to $\underline{\mathbf{J}}$ also has other important implications. For example, the different mechanisms which contribute to J coupling are listed in Table 7.5, where it may be seen that each mechanism possesses different symmetry properties.[311] Because $\underline{\mathbf{J}}^{\mathrm{anti}}$ contains no contribution from the Fermi-contact (FC) coupling mechanism, measurement of an antisymmetric component of $\underline{\mathbf{J}}$ would represent some of the most convincing experimental evidence for non-FC contributions to the indirect spin-spin coupling. Furthermore, it is noted that in principle the antisymmetric part of $\underline{\mathbf{J}}$ contributes to nuclear spin relaxation although its effect has never been observed experimentally.[191,294] While the ex-

Table 7.5: Relationships between the mechanisms which contribute to $\underline{\mathbf{J}}$ and the symmetry properties of $\underline{\mathbf{J}}$[311]

Mechanism	Isotropic	Symmetric	Antisymmetric
DSO	√	√	√
PSO	√	√	√
FC	√	X	X
SD	√	√	√
FC × SD	X	√	X

perimental strategy described herein is applicable to tightly coupled homonuclear spin pairs, antisymmetric J coupling is a general phenomenon which will in principle affect nuclear spin relaxation even in situations where it cannot be measured directly.

7.6 Conclusions

The present work has described an experimental strategy for measuring the antisymmetric part of indirect nuclear spin-spin coupling tensors for tightly coupled (AB) homonuclear spin pairs in solid samples undergoing MAS. Considerations for identifying appropriate spin systems and chemical compounds have been developed, and we also note that modern quantum-chemical calculations would likely be helpful in selecting suitable candidate molecules. Analysis of spectra from samples undergoing MAS, which averages all interactions other than $\underline{\mathbf{J}}^{anti}$ to their isotropic values, appears to be an ideal strategy. $\underline{\mathbf{J}}^{anti}$ would affect spectra from stationary samples, but it would be difficult to separate $\underline{\mathbf{J}}^{anti}$ from the orientationally dependent $\underline{\mathbf{J}}^{sym}$ and $\underline{\mathbf{D}}$ interactions (even with single crystal data). The effect of $\underline{\mathbf{J}}^{anti}$ components on NMR lineshapes from powdered samples undergoing MAS is derived, and the method of spectral analysis discussed. The main finding is that NMR peak shapes from AB spin systems will be affected, but that the most intense portion of the

spectra may be analyzed independent of $\underline{\mathbf{J}}^{\mathrm{anti}}$. It is also found that $\underline{\mathbf{J}}^{\mathrm{anti}}$ must be comparable in magnitude to J_{iso} and the difference in chemical shifts between the two sites to affect the NMR spectra. In particular, the method of analysis allows one to determine a measure of the largest element of $\underline{\mathbf{J}}^{\mathrm{anti}}$. Using this approach, the ^{119}Sn NMR spectrum of hexa(*p*-tolyl)ditin was analyzed to show that all elements of $\underline{\mathbf{J}}^{\mathrm{anti}}$ in this compound must be smaller than 2900 Hz.

7.7 Experimental Details

Hexa-(*p*-tolyl)ditin was synthesized as a white powder following a procedure adapted from references 312 and 313. The compound was recrystallized from benzene, which apparently affords the type-B polymorph.[305] Tin-119 VACP/MAS NMR spectra of powdered samples of hexa(*p*-tolyl)ditin were acquired at a frequency of 74.63 MHz using a Chemagnetics CMX Infinity 200 spectrometer, or at 112.01 MHz with a Bruker Avance 300 spectrometer. Tin-117 VACP/MAS NMR spectra were acquired at 71.31 MHz using a Chemagnetics CMX Infinity 200 spectrometer. A 4 mm DR MAS probe was used for all experiments. Tetracyclohexyltin was used as a setup sample and secondary chemical shift reference, as δ_{iso}= 97.35 ppm with respect to a solution of $SnMe_4$ at 0 ppm.[314,315] All ^{119}Sn and ^{117}Sn CP/MAS experiments used a 40 s recycle delay, 5-6 ms contact times, and either 2.40 μs (at 4.70 T) or 4.00 μs $\pi/2$ pulses. High-power proton decoupling ($\gamma B_1/2\pi > 60$ kHz) was used for all experiments. The POST-C7 pulse sequence was used to provide a double-quantum filtered ^{119}Sn spectrum;[309,310] an MAS rate of 8.929 kHz and an experimentally optimized ^{119}Sn B_1 field near the theoretical maximum of 62.5 kHz was applied. The DQ conversion efficiency of the POST-C7 sequence was found to be approximately half the theoretical value of 47% for the 895.96 μs DQ excitation block used.[316] Heteronuclear decoupling was applied only during the acquisition period of the POST-C7 experiment.[48] Two-dimensional *J*-resolved ^{119}Sn MAS NMR spectra

were acquired using similar parameters, with 16 points acquired in the indirect dimension, a spectral window of 200 Hz in the indirect dimension, and 128 scans per increment.[307,308]

Numerical calculations of the $A(\Theta)$ distribution and its effect on NMR spectra were performed with purpose-built C code. The powder distribution was generated by calculating the value of $f_{zy}(\Theta; c_{yx}, c_{zx})$, see Equation 7.11, for a large set of crystallite orientations; orientations were generated in the rotor frame, to take advantage of the above-noted rotational symmetry of $f_{zy}(\Theta; c_{yx}, c_{zx})$ about the axis of sample rotation. Specifically, crystallites were initially aligned with z along $\vec{r}_{rot}$, then rotated about $\vec{r}_{rot}$ through the angle α (where $0 < \alpha < 2\pi$), and then about the initial y axis through the angle β (where $0 < \beta < \pi$). A total of 832039 crystallite orientations were used, where the α and β Euler angles were sampled according to the Zaremba-Conroy-Wolfsberg, ZCW, distribution.[317–319] Each ξ_a and $\varepsilon_{ab'}$ angle in Equation 7.11 was then calculated using standard linear algebra, and used to create plots of $f_{zy}(\Theta; c_{yx}, c_{zx})$, $f^2_{zy}(\Theta; c_{yx}, c_{zx})$, or the NMR spectral frequencies.

Angular distribution set provided by the Laboratory for Biomolecular NMR spectroscopy, University of Aarhus, Aarhus DK (*http://bionmr.chem.au.dk/download/simpson/crystal_files/*).

Chapter 8

Concluding Remarks and Future Outlook

A range of investigations have been completed using solid-state NMR as the principal means of research. While somewhat diverse in nature, all the projects have a common element: they aim to provide data and insight into the relationship between molecular structure, chemical bonding and the NMR observables. Hopefully, the results obtained here will be applicable to the investigation of new problems. Probably the most progress towards investigating the bonding/observable relationship was obtained in the investigation of (η^2-diphenylacetylene)$Pt(PPh_3)_2$ presented in Chapter 6. The η^2-bonding of an unsaturated-carbon ligand to a late transition metal is well understood in the chemistry literature. The investigation presented in this thesis provides a more comprehensive than heretofore available description of ligand-atom CS tensor changes upon coordination to a metal. Some insight into the origin of these magnetic shielding changes was also provided. Certainly, the π^* virtual molecular orbitals of the free ligand, important to perturbation-theory derivations of nuclear magnetic shielding, are no longer available after metal coordination; however, theoretical arguments show that the electronic structure local

to the platinum atom (and therefore nonlocal to the ligand) have a large effect on the shielding. Since magnetic shielding results from induction of an electron current density in the molecule by the magnetic field, it makes sense that when the electronic structure of the metal atom is such that a significant current density is induced near Pt, it can have an effect on the neighbouring orbitals. Despite the fact that electron density or hybridization at the atom of interest are often invoked in explanations of magnetic shielding, there are nonlocal contributions to the shielding that must also be considered. The investigation of aurocyanides presented in Chapters 4 and 5 also depended on an interpretation of the effect of bonding on chemical shifts. In this case, an empirical correlation between intermolecular metallophilic bonding and the isotropic carbon-13 chemical shift was determined. Theoretical explanation of the relationship between this type of intermolecular bonding and the chemical shift would probably be much more subtle than in the stronger η^2-bonding discussed above. Empirical relationships of the type found for aurophilic bonding provide tools with which to solve chemical and structural problems.

The investigation of antisymmetry in $\underline{\mathbf{J}}$ can, in some ways, be viewed as the precursor to these other projects. In most cases, before empirical trends and their theoretical explanations can be developed, experimental theory and methodology must first be explored. The indirect spin-spin coupling described by $\underline{\mathbf{J}}$ is a measure of the electron polarization that propagates along chemical bonds; therefore, this interaction is a sensitive probe of bonding. We don't yet know what chemical insight we will be able to derive from this information, but one might expect comprehensive data on the nuclear environment to be encoded in the elements of $\underline{\mathbf{J}}^{\mathrm{anti}}$. My main area of study was in the field of solid-state NMR, but I have done my best to apply this sensitive experimental technique in order to learn about other areas of chemistry.

8.1 Future Studies

Hopefully, the introduction to cyanoaurate coordination polymers in Chapter 4 has effectively communicated the potential of these materials to possess properties that are both interesting and of practical use. It is hoped that the SSNMR studies begun in this thesis will provide a set of tools with which to investigate the structure and function of these fascinating materials. The simplest cyanoaurate coordination polymer is the parent material AuCN, and its study (Chapter 5) provides an example of the information that can be obtained using SSNMR. Probably the most useful application of SSNMR to cyanoaurate coordination polymers would be the study of systems in which full structural characterization by diffraction is not possible. For example, several examples of zeolite-like vapour absorption have been observed, and while structures for some of the more stable absorption complexes have been determined, others remain unavailable.

The behaviour displayed by $Zn[Au(CN)_2]$ in the solid state makes this material a particularly promising one for NMR study. Crystal structures of four polymorphs, labelled α, β, γ, and δ, have been determined using X-ray diffraction of either single-crystal or powdered samples.[74] Exposure of any of these four polymorphs to concentrated ammonia vapour results in a white powder of unknown structure, which, after standing in air for one minute, generates the yellow powder $\{Zn(NH_3)_2[Au(CN)_2]_2\}$. Further standing (30 min.) results in regeneration of the starting material $Zn[Au(CN)_2]$ (mixtures of α and δ polymorphic forms). The crystal structure of the intermediate material $\{Zn(NH_3)_2[Au(CN)_2]_2\}$ was determined by fitting the powder XRD pattern to a theoretical structure; the analogous material $\{Cd(NH_3)_2[Au(CN)_2]_2\}$, which displays a similar powder XRD pattern, was used as a starting structure. However, the broadness of peaks in the diffraction pattern indicated that some disorder was present. The identity of the other intermediate, the white material present under concentrated ammonia vapour, remains

unknown. SSNMR could provide useful complementary data in further characterizing these two ammonia absorption complexes. The carbon isotropic chemical shifts should be quite sensitive to the vapour absorption, as there is a significant change in the aurophilic bonding upon ammonia absorption. It is also possible that some insight into the absorption/desorption process could be obtained using SSNMR—in particular, desorption in the necessary temperature range could be effected using variable-temperature NMR experiments. The presence of ammonia in the structures is a significant advantage in the acquisition of SSNMR data, as the ^{13}C and ^{15}N relaxation times would certainly be much shorter than those for most of the compounds studied in this thesis; this advantage combined with the ability to perform CP from the protons would greatly facilitate such a study. Assignment of ^{13}C and ^{15}N isotropic chemical shifts in the complicated network structures could be performed with the 2D homonuclear dipolar recoupling $SR26_4^{11}$ experiment applied in the study of AuCN. Given the dependence of the signal intensity on the internuclear distance of each spin pair, it is possible that the NMR crystallography method utilizing ^{29}Si-^{29}Si $SR26_4^{11}$ experiments pioneered by Brouwer et al. on zeolites could provide a very complete description of the structure.[49,50] Additionally, the increased signal intensity available when using CP may allow correlation of chemical shifts in directly bonded C and N atoms using $^{13}C \rightarrow {}^{15}N$ CP HETCOR experiments. Testing and benchmarking of such ^{13}C,^{15}N HETCOR experiments for cyanides would no doubt find application in a wide variety of cyanide containing materials. For example, such experiments could clarify interpretation of the ^{15}N isotropic chemical shifts observed in AuCN, and provide further information on its structure (and the intermediates described in Chapter 5). Of course, SSNMR studies of $\{Zn(NH_3)_2[Au(CN)_2]_2\}$ polymorphs and ammonia absorption complexes is just one possible application, of which the wide array of cyanoaurate coordination polymers should provide a long list.

Because metallophilic bonding is shown to affect neighbouring-atom isotropic chemical shifts, the obvious next step is to question under which other conditions this occurs. In Chapter 4, it was mentioned that residual dipolar coupling between ^{31}P and ^{197}Au has been observed in several gold(I) phosphines. This is interesting in and of itself, given the rarity of magnetic resonance effects observed for ^{197}Au and the special position of Au in relativistic theory. One of these molecules, ClAu(Ph_2)P-CH_2-P(Ph_2)AuCl or bis(diphenylphosphino)methane-di(chloro-gold(I)), is known to crystallize in two structures with distinct molecular conformations.[320,321] In one polymorph the P-Au-Cl vectors are arranged *trans* to each other,[321] while in the other they are in a *cis* arrangement, forming a 3.34 Å aurophilic bond.[320] Acquisition of the ^{31}P SSNMR spectrum under MAS should allow one to determine how the effect of aurophilic bond formation on neighbouring-atom $\delta_{iso}(^{31}P)$ compares to the effects observed for $\delta_{iso}(^{13}C)$ in the cyanoaurate materials. In the Wasylishen group, Jerrod Dwan has begun work on investigating these compounds, in addition to further characterizing the $^1J_{iso}(^{197}Au,^{31}P)$ coupling interaction in the other gold(I) phosphines.

The investigation of effects from η^2-coordination to platinum on ^{13}C chemical shift tensors in diphenylacetylene provided interesting and practical empirical data. Additionally, it provided me with the opportunity to investigate the theoretical description of magnetic shielding using DFT calculations. This is excellent experience which has provided me with a useful background for future investigation of problems in NMR. In general, the number of significant terms in the expansion of the perturbation-theory expression precludes simple insights from being obtained; however, there are interesting cases where such an investigation is fruitful. For example, the theory underlying indirect spin-spin couplings is not very different from that governing magnetic shielding, and I have applied similar principles in analyzing some prototype systems. One mechanism for J coupling, the Fermi-contact (FC)

mechanism, is relatively simple in format and has previously been applied to the explanation of J couplings using LCAO-MO theory.[279] I have made strides towards an explanation of unusual NMR parameters in some simple stannanes (tin analogues of methane). For example, the value of $^1J_{iso}(^{119}Sn,^1H)$ in SnH_3^+, $\pm$ 2907 Hz, is much larger than the value observed in SnH_3^-, $\pm$ 101 Hz. DFT calculations of the J coupling indicate that the only significant coupling mechanism is the FC contribution, which shows that a simple LCAO-MO theory explanation may be possible. Because the perturbation-theory expansion of the FC term includes only occupied MOs with s-character, it is relatively straightforward to predict the important contributions to J_{iso} using an MO diagram. In this particular case, approximately the same magnitude J_{iso} contribution occurs in both SnH_3^+ and SnH_3^- from terms involving the occupied fully-symmetric MO (linear combination of s-orbitals on all atoms). In planar SnH_3^+, there are no other frontier MOs with s-character, but in pyramidal SnH_3^-, the lone-pair MO has s-character of opposite phase to the fully symmetric MO; therefore, the lone-pair MO causes equal and opposite contributions to J_{iso}. The net result is a large J_{iso} for SnH_3^+, but a small J_{iso} for SnH_3^-. I am also attempting to use MO interpretations of NMR parameters to explain unusual results in DFT calculations of magnetic shielding in the Sn analogue of carbene, $:SnH_2$. DFT calculations indicate that the relativistically originated spin-orbit contribution to the $^{119/117}Sn$ magnetic shielding in this hypothetical molecule is unusually large when compared to other tin molecules. I have not yet determined a fully formed theory to explain this result, but after talking with Prof. Pekka Pyykkö at a conference this past summer, I believe I am now headed down the correct path. These interpretations of NMR parameters are examples of problems that can be solved using the experience obtained in the investigation of (η^2-diphenylacetylene)$Pt(PPh_3)_2$ presented in Chapter 6. I believe that this methodology is something that I will have the opportunity to apply many times in my research career, and hopefully the

literature reports of these interpretations will stimulate ideas in other researchers as well.

The investigation of antisymmetry in the indirect spin-spin coupling tensor presented in Chapter 7 is at the early stages of the field. There are still many unknowns regarding $\underline{\mathbf{J}}^{\mathrm{anti}}$, and extensions of the presented methodology or development of other experimental methods could shed further light on its properties and uses. In particular, I believe that experimental investigation of more example molecules using the methodology developed here could prove profitable. Literature searches have yielded a few promising candidates, and some initial steps have already been undertaken. The largest known J_{iso} coupling constant is the value of ${}^{1}J_{\mathrm{iso}}({}^{199}\mathrm{Hg},{}^{199}\mathrm{Hg}) = 284100(860)$ Hz observed for $\left\{\left[\mathrm{Hg_2}(\text{18-crown-6})(\mathrm{Me_2SO})(\mu\text{-}\mathrm{Me_2SO})\right](\mathrm{O_3SCF_3})_2\right\}_2$ in dichloromethane.[322] Given the extremely large value of J_{iso}, it would be interesting to attempt to measure $\underline{\mathbf{J}}^{\mathrm{anti}}$ in this molecule. I synthesized a sample of the material, but attempts at observing the corresponding ${}^{199}\mathrm{Hg}$ MAS NMR spectrum yielded no signal. We suspect that this is due to dispersal of the spinning sidebands (NMR peaks) over a large spectral range, leaving too little signal in each for facile observation. Variable-temperature relaxation experiments of a sample dissolved in dichloromethane confirmed this theory, and it it unlikely we will be able to obtain a useful spectrum with our current hardware. However, newer generations of spectrometer, particularly the new "very fast spinning" MAS probes, could provide a route to observing the signal. Interesting homonuclear metal-metal bonds are formed by some complexes of the "scorpionate" ligands, and these could also provide a means for observing $\underline{\mathbf{J}}^{\mathrm{anti}}$. A promising example with favourable NMR properties is $\{[\mathrm{HB}(3,5\text{-}\mathrm{Me_2pz})_3]\mathrm{Cd}\}_2$, in which a value of ${}^{1}J_{\mathrm{iso}}({}^{113}\mathrm{Cd},{}^{111}\mathrm{Cd}) = 20646$ Hz has been observed in chloromethane solution.[323] Aside from further experimental work, investigation of $\underline{\mathbf{J}}^{\mathrm{anti}}$ in these compounds using quantum chemical calculations could also provide interesting insights.

Bibliography

[1] Wheelwright, P. *The Presocratics;* Prentice Hall: Saddle River, NJ, US, 1966.

[2] Harris, K. J.; Wasylishen, R. E. *Inorg. Chem.* **2009,** *48,* 2316-2332.

[3] Harris, K. J.; Bernard, G. M.; McDonald, C.; McDonald, R.; Ferguson, M. J.; Wasylishen, R. E. *Inorg. Chem.* **2006,** *45,* 2461-2473.

[4] Andrew, E. R.; Farnell, L. F. *Mol. Phys.* **1968,** *15,* 157-165.

[5] Harris, K. J.; Bryce, D. L.; Wasylishen, R. E. *Can. J. Chem.* in press.

[6] Griffiths, D. J. *Introduction to Quantum Mechanics;* Prentice Hall: Saddle River, NJ, US, 1995.

[7] Farrar, T. C.; Harriman, J. E. *Density Matrix Theory and its Applications in NMR Spectroscopy;* The Farragut Press: Madison, WI, US, 2nd ed.; 1995.

[8] Levitt, M. H. *Spin Dynamics: Basics of Nuclear Magnetic Resonance;* John Wiley and Sons: Chichester, UK, 2001.

[9] Hore, P. J.; Jones, J. A.; Wimperis, S. NMR: The Toolkit. In *Oxford Chemistry Primers*, Vol. 92; Compton, R. G., Ed.; Oxford University Press: Oxford, UK, 2000.

[10] Harris, R. K. *Nuclear Magnetic Resonance Spectroscopy: A Physicochemical View;* Pearson Education Limited: Essex, UK, 1987.

[11] Slichter, C. P. *Principles of Magnetic Resonance;* Springer-Verlag: Berlin, DE, 3rd ed.; 1989.

[12] Duer, M. J. *Introduction to Solid-State NMR Spectroscopy;* Blackwell Publishing: Oxford, UK, 2004.

[13] Fukushima, E.; Roeder, S. B. W. *Experimental Pulse NMR: A Nuts and Bolts Approach;* Addison-Wesley: Reading, US, 1981.

[14] Hull, W. E. Experimental Aspects of Two-Dimensional NMR. In *Two-Dimensional NMR Spectroscopy: Applications for Chemists and Biochemists*, 2nd ed.; Croasmun, W. R.; Carlson, R. M. K., Eds.; VCH Publishers: New York, US, 1994.

[15] Rabenstein, D. L.; Nakashima, T. T. Nuclear Magnetic Resonance Spectroscopy and its Application to Trace Analysis. In *Trace Analysis: Spectroscopic Methods for Molecules*; Christian, G. D.; Callis, J. B., Eds.; John Wiley and Sons: New York, US, 1986.

[16] Keeler, J. *Understanding NMR Spectroscopy;* John Wiley and Sons: Chichester, UK, 2005.

[17] Mason, J. *Solid State Nucl. Magn. Reson.* **1993,** *2*, 285-288.

[18] Bhagavantam, S. *Crystal Symmetry and Physical Properties;* Academic Press: London, UK, 1966.

[19] Buckingham, A. D.; Malm, S. M. *Mol. Phys.* **1971,** *22*, 1127.

[20] Robert, J. B.; Wiesenfeld, L. *Phys. Rep.* **1982,** *86*, 363-401.

[21] Raynes, W. T. Theoretical and Physical Aspects of Nuclear Shielding. In *Nuclear Magnetic Resonance (Specialist Periodical Reports)*, Vol. 7; Abraham, R. J., Ed.; The Chemical Society: Oxford, UK, 1978.

[22] Solum, M. S.; Facelli, J. C.; Michl, J.; Grant, D. M. *J. Am. Chem. Soc.* **1986,** *108,* 6464-6470.

[23] Jameson, A. K.; Jameson, C. J. *Chem. Phys. Lett.* **1987,** *134,* 461-466.

[24] Eichele, K.; Wasylishen, R. "WSOLIDS", Version 2.0.18.

[25] Wasylishen, R. E. Dipolar and Indirect Coupling Tensors in Solids. In *Encyclopedia of Nuclear Magnetic Resonance*, Vol. 3; Grant, D. M.; Harris, R. K., Eds.; John Wiley and Sons: Chichester, UK, 1996.

[26] Ishii, Y.; Terao, T.; Hayashi, S. *J. Chem. Phys.* **1997,** *107,* 2760-2774.

[27] Nakai, T.; Ashida, J.; Terao, T. *Mol. Phys.* **1989,** *67,* 839-847.

[28] Millar, J. M.; Thayer, A. M.; Zax, D. B.; Pines, A. *J. Am. Chem. Soc.* **1986,** *108,* 5113-5116.

[29] Wasylishen, R. E. Indirect Nuclear Spin-Spin Coupling Tensors. In *Encyclopedia of Nuclear Magnetic Resonance*, Vol. 9; Grant, D. M.; Harris, R. K., Eds.; John Wiley and Sons: Chichester, UK, 2002.

[30] Buckingham, A. D.; Pyykkö, P.; Robert, J. B.; Wiesenfeld, L. *Mol. Phys.* **1982,** *46,* 177-182.

[31] Man, P. P. Quadrupolar Interactions. In *Encyclopedia of Nuclear Magnetic Resonance*, Vol. 6; Grant, D. M.; Harris, R. K., Eds.; John Wiley and Sons: Chichester, UK, 1996.

[32] Power, W. P.; Wasylishen, R. E. *Annu. Rep. NMR Spectrosc.* **1991,** *23,* 1-83.

[33] Eichele, K.; Wasylishen, R. E. *J. Magn. Reson., Ser. A* **1994,** *106,* 46-56.

[34] van Willigen, H.; Griffin, R. G.; Haberkorn, R. A. *J. Chem. Phys.* **1977,** *67,* 5855-5860.

[35] Lumsden, M. D.; Wu, G.; Wasylishen, R. E.; Curtis, R. D. *J. Am. Chem. Soc.* **1993,** *115,* 2825-2832.

[36] Curtis, R. D.; Hilborn, J. W.; Wu, G.; Lumsden, M. D.; Wasylishen, R. E.; Pincock, J. A. *J. Phys. Chem.* **1993,** *97,* 1856-1861.

[37] Rose, M. E. *Elementary Theory of Angular Momentum;* John Wiley & Sons: New York, US, 1967.

[38] Hodgkinson, P. *Prog. Nucl. Magn. Reson. Spectrosc.* **2005,** *46,* 197-221.

[39] Engelke, F. Cross Polarization in Rotating Solids: Spin-1/2 Nuclei. In *Encyclopedia of Nuclear Magnetic Resonance,* Vol. 3; Grant, D. M.; Harris, R. K., Eds.; John Wiley and Sons: Chichester, UK, 1996.

[40] Andrew, R. E. Magic Angle Spinning. In *Encyclopedia of Nuclear Magnetic Resonance,* Vol. 5; Grant, D. M.; Harris, R. K., Eds.; John Wiley and Sons: Chichester, UK, 1996.

[41] Herzfeld, J.; Berger, A. E. *J. Chem. Phys.* **1980,** *73,* 6021-6030.

[42] Harris, R. K.; Olivieri, A. C. Spinning Sideband Analysis for Spin-1/2 Nuclei. In *Encyclopedia of Nuclear Magnetic Resonance,* Vol. 9; Grant, D. M.; Harris, R. K., Eds.; John Wiley and Sons: Chichester, UK, 2002.

[43] Schnell, I. *Prog. Nucl. Magn. Reson. Spectrosc.* **2004,** *45,* 145-207.

[44] Griffiths, J. M.; Bennett, A. E.; Griffin, R. G. Homonuclear Recoupling Schemes in MAS NMR. In *Encyclopedia of Nuclear Magnetic Resonance,* Vol. 4; Grant, D. M.; Harris, R. K., Eds.; John Wiley and Sons: Chichester, UK, 1996.

[45] Levitt, M. H. Symmetry-Based Pulse Sequences in Magic-Angle Spinning Solid-State NMR. In *Encyclopedia of Nuclear Magnetic Resonance,* Vol. 9;

Grant, D. M.; Harris, R. K., Eds.; John Wiley and Sons: Chichester, UK, 2002.

[46] Kristiansen, P. E.; Carravetta, M.; Lai, W. C.; Levitt, M. H. *Chem. Phys. Lett.* **2004,** *390,* 1-7.

[47] Kristiansen, P. E.; Carravetta, M.; van Beek, J. D.; Lai, W. C.; Levitt, M. H. *J. Chem. Phys.* **2006,** *124,* 234510.

[48] Marin-Montesinos, I.; Brouwer, D. H.; Antonioli, G.; Lai, W. C.; A., B.; Levitt, M. H. *J. Magn. Reson.* **2005,** *177,* 307-317.

[49] Brouwer, D. H.; Kristiansen, P. E.; Fyfe, C. A.; Levitt, M. H. *J. Am. Chem. Soc.* **2005,** *127,* 542-543.

[50] Brouwer, D. H.; Darton, R. J.; Morris, R. E.; Levitt, M. H. *J. Am. Chem. Soc.* **2005,** *127,* 10365-10370.

[51] Jones, P. G. *Gold Bull.* **1981,** *14,* 102-118.

[52] Jones, P. G. *Gold Bull.* **1983,** *16,* 114-124.

[53] Jones, P. G. *Gold Bull.* **1986,** *19,* 46-56.

[54] Scherbaum, F.; Grohmann, A.; Huber, B.; Krüger, C.; Schmidbaur, H. *Angew. Chem., Int. Ed.* **1988,** *27,* 1544-1546.

[55] Schmidbaur, H. *Chem. Soc. Rev.* **1995,** *24,* 391-400.

[56] Pyykkö, P. *Chem. Rev.* **1997,** *97,* 597-636.

[57] Pyykkö, P. *Angew. Chem. Int. Ed. Engl.* **2004,** *43,* 4412-4456.

[58] Pyykkö, P.; Zhao, Y.-F. *Angew. Chem. Int. Ed. Engl.* **1991,** *30,* 604-605.

[59] Runeberg, N.; Schütz, M.; Werner, H.-J. *J. Chem. Phys.* **1999,** *110,* 7210-7215.

[60] Magnko, L.; Schweizer, M.; Rauhut, G.; Schütz, M.; Stoll, H.; Werner, H.-J. *Phys. Chem. Chem. Phys.* **2002,** *4,* 1006-1013.

[61] Braga, D.; Grepioni, F.; Desiraju, G. R. *Chem. Rev.* **1998,** *98,* 1375-1405.

[62] Leznoff, D. B.; Lefebvre, J. *Gold Bull.* **2005,** *38,* 47-54.

[63] Katz, M. J.; Sakai, K.; Leznoff, D. B. *Chem. Soc. Rev.* **2008,** *37,* 1884-1895.

[64] Gade, L. H. *Angew. Chem., Int. Ed.* **1997,** *36,* 1171-1173.

[65] Yam, V. W.-W.; Lo, K. K.-W. *Chem. Soc. Rev.* **1999,** *28,* 323-334.

[66] Yam, V. W.-W.; Cheng, E. C.-C. *Top. Curr. Chem.* **2007,** *281,* 269-309.

[67] Yam, V. W.-W.; Cheng, E. C.-C. *Chem. Soc. Rev.* **2008,** *37,* 1806-1813.

[68] Assefa, Z.; Omary, M. A.; McBurnett, B. G.; Mohamed, A. A.; Patterson, H. H.; Staples, R. J.; Fackler Jr., J. P. *Inorg. Chem.* **2002,** *41,* 6274-6280.

[69] White-Morris, R. L.; Olmstead, M. M.; Jiang, F. L.; Tinti, D. S.; Balch, A. L. *J. Am. Chem. Soc.* **2002,** *124,* 2327-2336.

[70] Bariáin, C.; Matías, I. R.; Romeo, I.; Garrido, J.; Laguna, M. *Appl. Phys. Lett.* **2000,** *77,* 2274-2276.

[71] Rawashdeh-Omary, M. A.; Omary, M. A.; Fackler Jr., J. P.; Galassi, R.; Pietroni, B. R.; Burini, A. *J. Am. Chem. Soc.* **2001,** *123,* 9689-9691.

[72] Fernández, E. J.; López-de Luzuriaga, J. M.; Monge, M.; Olmos, M. E.; Pérez, J.; Laguna, A.; Mohamed, A. A.; Fackler Jr., J. P. *J. Am. Chem. Soc.* **2003,** *125,* 2022-2023.

[73] Lefebvre, J.; Batchelor, R. J.; Leznoff, D. B. *J. Am. Chem. Soc.* **2004,** *126,* 16117-16125.

[74] Katz, M. J.; Ramnial, T.; Yu, H.-Z.; Leznoff, D. B. *J. Am. Chem. Soc.* **2008,** *130,* 10662-10673.

[75] Vickery, J. C.; Olmstead, M. M.; Fung, E. Y.; Balch, A. L. *Angew. Chem., Int. Ed.* **1997,** *36,* 1179-1181.

[76] Yam, V. W.-W.; Li, C.-K.; Chan, C.-L. *Angew. Chem., Int. Ed.* **1998,** *37,* 2857-2859.

[77] Li, C.-K.; Lu, X.-X.; Wong, K. M.-C.; Chan, C.-L.; Zhu, N. Y.; Yam, V. W.-W. *Inorg. Chem.* **2004,** *43,* 7421-7430.

[78] La Brooy, S. R.; Linge, H. G.; Walker, G. S. *Miner. Eng.* **1994,** *7,* 1213-1241.

[79] Ahmad, S. *Coord. Chem. Rev.* **2004,** *248,* 231-243.

[80] Rawashdeh-Omary, M. A.; Omary, M. A.; Patterson, H. H. *J. Am. Chem. Soc.* **2000,** *122,* 10371-10380.

[81] Rawashdeh-Omary, M. A.; Omary, M. A.; Patterson, H. H.; Fackler Jr., J. P. *J. Am. Chem. Soc.* **2001,** *123,* 11237-11247.

[82] Che, C.-M.; Wong, W.-T.; Lai, T.-F.; Kwong, H.-L. *J. Chem. Soc., Chem. Commun.* **1989,** 243-244.

[83] Dong, W.; Sun, Y.-Q.; Yu, B.; Zhou, H.-B.; Song, H.-B.; Liu, Z.-Q.; Wang, Q.-M.; Liao, D.-Z.; Jiang, Z.-H.; Yan, S.-P.; Cheng, P. *New J. Chem.* **2004,** *28,* 1347-1351.

[84] Paraschiv, C.; Andruh, M.; Ferlay, S.; Hosseini, M. W.; Kyritsakas, N.; Planeix, J.-M.; Stanica, N. *Dalton Trans.* **2005,** 1195-1202.

[85] Siemeling, U.; Rother, D.; Bruhn, C.; Fink, H.; Weidner, T.; Träger, F.; Rothenberger, A.; Fenske, D.; Priebe, A.; Maurer, J.; Winter, R. *J. Am. Chem. Soc.* **2005,** *127,* 1102-1103.

[86] Xu, G.-F.; Liu, Z.-Q.; Zhou, H.-B.; Guo, Y.; Liao, D.-Z. *Aust. J. Chem.* **2006,** *59,* 640-646.

[87] Zhou, H.-B.; Wang, S.-P.; Liu, Z.-Q.; Liao, D.-Z.; Jiang, Z.-H.; Yan, S.-P.; Cheng, P. *Inorg. Chim. Acta* **2006,** *359,* 533-540.

[88] Chen, J.-X.; Zhang, W.-H.; Tang, X.-Y.; Ren, Z.-G.; Li, H.-X.; Zhang, Y.; Lang, J.-P. *Inorg. Chem.* **2006,** *45,* 7671-7680.

[89] Madalan, A. M.; Avarvari, N.; Andruh, M. *Cryst. Growth Des.* **2006,** *6,* 1671-1675.

[90] Katz, M. J.; Shorrock, C. J.; Batchelor, R. J.; Leznoff, D. B. *Inorg. Chem.* **2006,** *45,* 1757-1765.

[91] Qu, J.; Gu, W.; Liu, X. *J. Coord. Chem.* **2008,** *61,* 618-626.

[92] Katz, M. J.; Michaelis, V. K.; Aguiar, P. M.; Yson, R.; Lu, H.; Kaluarachchi, H.; Batchelor, R. J.; Schreckenbach, G.; Kroeker, S.; Patterson, H. H.; Leznoff, D. B. *Inorg. Chem.* **2008,** *47,* 6353-6363.

[93] Lefebvre, J.; Tyagi, P.; Trudel, S.; Pacradouni, V.; Kaiser, C.; Sonier, J. E.; Leznoff, D. B. *Inorg. Chem.* **2009,** *48,* 55-67.

[94] Korčok, J. L.; Katz, M. J.; Leznoff, D. B. *J. Am. Chem. Soc.* **2009,** *131,* 4866-4871.

[95] Katz, M. J.; Aguiar, P. M.; Batchelor, R. J.; Bokov, A. A.; Ye, Z.-G.; Kroeker, S.; Leznoff, D. B. *J. Am. Chem. Soc.* **2006,** *128,* 3669-3676.

[96] Katz, M. J.; Kaluarachchi, H.; Batchelor, R. J.; Bokov, A. A.; Ye, Z.-G.; Leznoff, D. B. *Angew. Chem., Int. Ed.* **2007,** *46,* 8804-8807.

[97] Dong, W.; Zhu, L.-N.; Sun, Y.-Q.; Liang, M.; Liu, Z.-Q.; Liao, D.-Z.; Jiang, Z.-H.; Yan, S.-P.; Cheng, P. *Chem. Commun.* **2003,** 2544-2545.

[98] Colacio, E.; Lloret, F.; Kivekäs, R.; Ruiz, J.; Suárez-Varela, J.; Sundberg, M. R. *Chem. Commun.* **2002,** 592-593.

[99] Chu, I. K.; Shek, I. P. Y.; Siu, K. W. M.; Wong, W.-T.; Zuo, J.-L.; Lau, T.-C. *New J. Chem.* **2000,** *24,* 765-769.

[100] Leznoff, D. B.; Xue, B.-Y.; Patrick, B. O.; Sanchez, V.; Thompson, R. C. *Chem. Commun.* **2001,** 259-260.

[101] Leznoff, D. B.; Xue, B.-Y.; Stevens, C. L.; Storr, A.; Thompson, R. C.; Patrick, B. O. *Polyhedron* **2001,** *20,* 1247-1254.

[102] Leznoff, D. B.; Xue, B.-Y.; Batchelor, R. J.; Einstein, F. W. B.; Patrick, B. O. *Inorg. Chem.* **2001,** *40,* 6026-6034.

[103] Shorrock, C. J.; Xue, B.-Y.; Kim, P. B.; Batchelor, R. J.; Patrick, B. O.; Leznoff, D. B. *Inorg. Chem.* **2002,** *41,* 6743-6753.

[104] Niel, V.; Thompson, A. L.; Muñoz, M. C.; Galet, A.; Goeta, A. S. E.; Real, J. A. *Angew. Chem., Int. Ed.* **2003,** *42,* 3760-3763.

[105] Colacio, E.; Lloret, F.; Kivekäs, R.; Suárez-Varela, J.; Sundberg, M. R.; Uggla, R. *Inorg. Chem.* **2003,** *42,* 560-565.

[106] Shorrock, C. J.; Jong, H.; Batchelor, R. J.; Leznoff, D. B. *Inorg. Chem.* **2003,** *42,* 3917-3924.

[107] Stender, M.; White-Morris, R. L.; Olmstead, M. M.; Balch, A. L. *Inorg. Chem.* **2003,** *42,* 4504-4506.

[108] Vitoria, P.; Muga, I.; Gutiérrez-Zorrilla, J. M.; Luque, A.; Román, P.; Lezama, L.; Zúniga, F. J.; Beitia, J. I. *Inorg. Chem.* **2003,** *42,* 960-969.

[109] Zhou, H.-B.; Wang, S.-P.; Dong, W.; Liu, Z.-Q.; Wang, Q.-L.; Liao, D.-Z.; Jiang, Z.-H.; Yan, S.-P.; Cheng, P. *Inorg. Chem.* **2004,** *43,* 4552-4554.

[110] Galet, A.; Muñoz, M. C.; Martínez, V.; Real, J. A. *Chem. Commun.* **2004,** 2268-2269.

[111] Leznoff, D. B.; Shorrock, C. J.; Batchelor, R. J. *Gold. Bull.* **2007,** *40,* 36-39.

[112] Lefebvre, J.; Callaghan, F.; Katz, M. J.; Sonier, J. E.; Leznoff, D. B. *Chem.–Eur. J.* **2006,** *12,* 6748-6761.

[113] Geisheimer, A. R.; Katz, M. J.; Batchelor, R. J.; Leznoff, D. B. *CrystEngComm* **2007,** *9,* 1078-1083.

[114] Katz, M. J.; Kaluarachchi, H.; Batchelor, R. J.; Schatte, G.; Leznoff, D. B. *Cryst. Growth Des.* **2007,** *7,* 1946-1948.

[115] Lefebvre, J.; Chartrand, D.; Leznoff, D. B. *Polyhedron* **2007,** *26,* 2189-2199.

[116] Lefebvre, J.; Trudel, S.; Hill, R. H.; Leznoff, D. B. *Chem.–Eur. J.* **2008,** *14,* 7156-7167.

[117] Avalle, P.; Harris, R. K.; Hanika-Heidl, H.; Fischer, R. D. *Solid State Sci.* **2004,** *6,* 1069-1076.

[118] Poll, E.-M.; Schütze, J.-U.; Fischer, R. D.; Davies, N. A.; Apperley, D. C.; Harris, R. K. *J. Organomet. Chem.* **2001,** *621,* 254-260.

[119] Poll, E.-M.; Olbrich, F.; Samba, S.; Fischer, R. D.; Avalle, P.; Apperley, D. C.; Harris, R. K. *J. Solid State Chem.* **2001,** *157,* 324-338.

[120] Poll, E.-M.; Samba, S.; Fischer, R. D.; Olbrich, F.; Davies, N. A.; Avalle, P.; Apperley, D. C.; Harris, R. K. *J. Solid State Chem.* **2000,** *152,* 286-301.

[121] Siebel, E.; Fischer, R. D.; Davies, N. A.; Apperley, D. C.; Harris, R. K. *J. Organomet. Chem.* **2000,** *604,* 34-42.

[122] Bowmaker, G. A.; Churakov, A. V.; Harris, R. K.; Oh, S.-W. *J. Organomet. Chem.* **1998,** *550,* 89-99.

[123] Brimah, A. K.; Schwarz, P.; Fischer, R. D.; Davies, N. A.; Harris, R. K. *J. Organomet. Chem.* **1998,** *568,* 1-12.

[124] Schwarz, P.; Siebel, E.; Fischer, R. D.; Davies, N. A.; Apperley, D. C.; Harris, R. K. *Chem.–Eur. J.* **1998,** *4,* 919-926.

[125] Siebel, E.; Fischer, R. D.; Kopf, J.; Davies, N. A.; Apperley, D. C.; Harris, R. K. *Inorg. Chem. Commun.* **1998,** *1,* 346-349.

[126] Schütze, J.-U.; Eckhardt, R.; Fischer, R. D.; Apperley, D. C.; Davies, N. A.; Harris, R. K. *J. Organomet. Chem.* **1997,** *534,* 187-194.

[127] Davies, N. A.; Harris, R. K.; Olivieri, A. C. *Mol. Phys.* **1996,** *87,* 669-677.

[128] Eller, S.; Schwarz, P.; Brimah, A. K.; Fischer, R. D.; Apperley, D. C.; Davies, N. A.; Harris, R. K. *Organometallics* **1993,** *12,* 3232-3240.

[129] Behrens, U.; Brimah, A. K.; Soliman, T. M.; Fischer, R. D.; Apperley, D. C.; Davies, N. A.; Harris, R. K. *Organometallics* **1992,** *11,* 1718-1726.

[130] Apperley, D. C.; Davies, N. A.; Harris, R. K.; Brimah, A. K.; Eller, S.; Fischer, R. D. *Organometallics* **1990,** *9,* 2672-2676.

[131] Wu, G.; Wasylishen, R. E. *J. Phys. Chem.* **1993,** *97,* 7863-7869.

[132] Schubert, R. J.; Range, K.-J. *Z. Naturforsch., B: Chem. Sci.* **1990,** *45,* 1118-1122.

[133] Rosenzweig, A.; Cromer, D. T. *Acta. Cryst.* **1959,** *12,* 709-712.

[134] Blom, N.; Ludi, A.; Bürgi, H.-B.; Tichý, K. *Acta Crystallogr., Sect. C: Cryst. Struct. Commun.* **1984,** *40,* 1767-1769.

[135] Veshtort, M.; Griffin, R. G. *J. Magn. Reson.* **2006,** *178,* 248-282.

[136] Clayden, N. J.; Dobson, C. M.; Lian, L.-Y.; Smith, D. J. *J. Magn. Reson.* **1986,** *69,* 476-487.

[137] Friesen, K. J.; Wasylishen, R. E. *J. Magn. Reson.* **1982,** *48,* 152-154.

[138] Eichele, K.; Wasylishen, R. E. *Solid State Nucl. Magn. Reson.* **1992,** *1,* 159-163.

[139] Barszczewicz, A.; Helgaker, T.; Jaszuński, M.; Jørgensen, P.; Ruud, K. *J. Magn. Reson., Ser. A* **1995,** *114,* 212-218.

[140] Bryce, D. L.; Wasylishen, R. E. *Inorg. Chem.* **2002,** *41,* 4131-4138.

[141] Harris, R. K.; Becker, E. D.; Cabral de Menezes, S. M.; Goodfellow, R.; Granger, P. *Pure Appl. Chem.* **2001,** *73,* 1795-1818.

[142] Barron, P. F.; Engelhardt, L. M.; Healy, P. C.; Oddy, J.; White, A. H. *Aust. J. Chem.* **1987,** *40,* 1545-1555.

[143] Attar, S.; Bearden, W. H.; Alcock, N. W.; Alyea, E. C.; Nelson, J. H. *Inorg. Chem.* **1990,** *29,* 425-433.

[144] Berners-Price, S. J.; Colquhoun, L. A.; Healy, P. C.; Byriel, K. A.; Hanna, J. V. *J. Chem. Soc., Dalton Trans.* **1992,** 3357-3363.

[145] Baker, L.-J.; Bowmaker, G. A.; Healy, P. C.; Skelton, B. W.; White, A. H. *J. Chem. Soc., Dalton Trans.* **1992,** 989-997.

[146] Angermair, K.; Bowmaker, G. A.; de Silva, E. N.; Healy, P. C.; Jones, B. E.; Schmidbaur, H. *J. Chem. Soc., Dalton Trans.* **1996,** 3121-3129.

[147] de Silva, E. N.; Bowmaker, G. A.; Healy, P. C. *J. Mol. Struct.* **2000,** *516,* 263-272.

[148] Healy, P. C.; Loughrey, B. T.; Bowmaker, G. A.; Hannac, J. V. *Dalton Trans.* **2008,** 3723-3728.

[149] Faltens, M. O.; Shirley, D. A. *J. Chem. Phys.* **1970,** *53,* 4249-4264.

[150] Olivieri, A. *Solid State Nucl. Magn. Reson.* **1992,** *1,* 345-353.

[151] Jameson, C. J. Spin-Spin Coupling. In *Multinuclear NMR*; Mason, J., Ed.; Plenum Press: New York, US, 1987.

[152] Bradley, R. S.; Munro, D. C.; Spencer, P. N. *Trans. Faraday Soc.* **1969,** *65,* 1920.

[153] Prof. Daniel Leznoff, Simon Fraser University. *Private communication.*

[154] Jones, L. H.; Smith, J. M. *J. Chem. Phys.* **1964,** *41,* 2507.

[155] Earl, W. L.; VanderHart, D. L. *J. Magn. Reson.* **1982,** *48,* 35-54.

[156] Peersen, O. B.; Wu, X. L.; Kustanovich, I.; Smith, S. O. *J. Magn. Reson., Ser. A* **1993,** *104,* 334-339.

[157] Hartmann, S. R.; Hahn, E. L. *Phys. Rev.* **1962,** *128,* 2042-2053.

[158] Pines, A.; Gibby, M. G.; Waugh, J. S. *J. Chem. Phys.* **1972,** *56,* 1776-1777.

[159] Pines, A.; Gibby, M. G.; Waugh, J. S. *J. Chem. Phys.* **1973,** *59,* 569-590.

[160] Pines, A.; Gibby, M. G.; Waugh, J. S. *Chem. Phys. Lett.* **1972,** *15,* 373-376.

[161] Bennett, A. E.; Rienstra, C. M.; Auger, M.; Lakshmi, K. V.; Griffin, R. G. *J. Chem. Phys.* **1995,** *103,* 6951-6958.

[162] Bryce, D. L.; Bernard, G. M.; Gee, M.; Lumsden, M. D.; Eichele, K.; Wasylishen, R. E. *Can. J. Anal. Sci. Spectrosc.* **2001,** *46,* 46-82.

[163] Ahrland, S.; Dreisch, K.; Norén, B.; Oskarsson, Å. *Mater. Chem. Phys.* **1993,** *35,* 281-289.

[164] Pathaneni, S. S.; Desiraju, G. R. *J. Chem. Soc., Dalton Trans.* **1993,** 319-322.

[165] Beeler, A. J.; Orendt, A. M.; Grant, D. M.; Cutts, P. W.; Michl, J.; Zilm, K. W.; Downing, J. W.; Facelli, J. C.; Schindler, M. S.; Kutzelnigg, W. *J. Am. Chem. Soc.* **1984,** *106,* 7672-7676.

[166] Dickson, R. M.; McKinnon, M. S.; Britten, J. F.; Wasylishen, R. E. *Can. J. Chem.* **1987,** *65,* 941-946.

[167] Ramsey, N. F. *Phys. Rev.* **1950,** *78,* 699-703.

[168] Fischer, P.; Ludi, A.; Patterson, H. H.; Hewat, A. W. *Inorg. Chem.* **1994,** *33,* 62-66.

[169] Fischer, P.; Mesot, J.; Lucas, B.; Ludi, A.; Patterson, H.; Hewat, A. *Inorg. Chem.* **1997,** *36,* 2791-2794.

[170] Nomura, Y.; Takeuchi, Y.; Nakagawa, N. *Tetrahedron Lett.* **1969,** 639.

[171] Autschbach, J.; Ziegler, T. Relativistic Computation of NMR Shieldings and Spin-Spin Coupling Constants. In *Encyclopedia of Nuclear Magnetic Resonance*, Vol. 9; Grant, D. M.; Harris, R. K., Eds.; John Wiley and Sons: Chichester, UK, 2002.

[172] Bertinotti, C.; Bertinotti, A. *Acta Crystallogr., Sect. B* **1970,** *26,* 422.

[173] Bowmaker, G. A.; Kennedy, B. J.; Reid, J. C. *Inorg. Chem.* **1998,** *37,* 3968-3974.

[174] Hibble, S. J.; Cheyne, S. M.; Hannon, A. C.; Eversfield, S. G. *Inorg. Chem.* **2002,** *41,* 4990-4992.

[175] Hibble, S. J.; Eversfield, S. G.; Cowley, A. R.; Chippindale, A. M. *Angew. Chem., Int. Ed.* **2004,** *43,* 628-630.

[176] Hibble, S. J.; Cheyne, S. M.; Hannon, A. C.; Eversfield, S. G. *Inorg. Chem.* **2002,** *41,* 1042-1044.

[177] Hibble, S. J.; Hannon, A. C.; Cheyne, S. M. *Inorg. Chem.* **2003,** *42,* 4724-4730.

[178] Reckeweg, O.; Simon, A. *Z. Naturforsch., B: Chem. Sci.* **2002,** *57,* 895-900.

[179] Reckeweg, O.; Lind, C.; Simon, A.; DiSalvo, F. J. *Z. Naturforsch., B: Chem. Sci.* **2003,** *58,* 155-158.

[180] Wang, J.; Collins, M. F.; Johari, G. P. *Phys. Rev. B* **2002,** *65,* 180103.

[181] Sawaguchi, T.; Yamada, T.; Okinaka, Y.; Itaya, K. *J. Phys. Chem.* **1995,** *99,* 14149-14155.

[182] Yamada, T.; Sekine, R.; Sawaguchi, T. *J. Chem. Phys.* **2000,** *113,* 1217-1227.

[183] Kroeker, S.; Wasylishen, R. E.; Hanna, J. V. *J. Am. Chem. Soc.* **1999,** *121,* 1582-1590.

[184] Hakala, M. O.; Pyykkö, P. *Chem. Commun.* **2006,** 2890-2892.

[185] Zaleski-Ejgierd, P.; Hakala, M.; Pyykkö, P. *Phys. Rev. B* **2007,** *76,* 094104.

[186] Okinaka, Y.; Smith, L. E. "Preparation of Gold Cyanide", 1980 U.S.A. Patent #4,222,996.

[187] The samples used in the 2002 study were still present in our lab, and a check of their IR spectra revealed a single resonance for each of the 99% labeled samples (dilabeled ^{13}C,^{15}N as well as monolabeled ^{15}N and ^{13}C materials).

[188] Bak, M.; Rasmussen, J. T.; Nielsen, N. C. *J. Magn. Reson.* **2000,** *147,* 296-330.

[189] Anet, F. A. L.; O'Leary, D. J. *Concepts Magn. Res.* **1991,** *3,* 193-214.

[190] The sample of AuCN used for the variable temperature and ^{197}Au NQR experiments was an initial preparation not corresponding exactly to those discussed in the text. While this sample was not characterized as fully as the presented samples, it was prepared in an analogous way, and its ^{13}C MAS NMR spectrum was consistent with those of the final samples.

[191] Spiess, H. W. Rotation of Molecules and Nuclear Spin Relaxation. In *NMR Basic Principles and Progress,* Vol. 15; Diehl, P.; Fluck, E.; Kosfeld, R., Eds.; Springer-Verlag: Berlin, DE, 1978.

[192] Goodwin, A. L.; Kennedy, B. J.; Kepert, C. J. *J. Am. Chem. Soc.* **2009,** *131,* 6334-6335.

[193] Mingos, D. M. P. Bonding of Unsaturated Organic Molecules to Transition Metals. In *Comprehensive Organometallic Chemistry,* Vol. 3; Wilkinson, G., Ed.; Pergamon: Oxford, UK, 1982.

[194] Hartley, F. R. Platinum. In *Comprehensive Organometallic Chemistry,* Vol. 6; Wilkinson, G., Ed.; Pergamon: Oxford, UK, 1982.

[195] Young, G. B. Platinum-Carbon π-Bonded Complexes. In *Comprehensive Organometallic Chemistry II*, Vol. 9; Puddephatt, R. J., Ed.; Pergamon: Oxford, UK, 1995.

[196] Mann, B. E.; Taylor, B. F. *^{13}C NMR Data for Organometallic Compounds;* Academic Press: London, UK, 1981.

[197] Cooper, D. G.; Powell, J. *Inorg. Chem.* **1976,** *15,* 1959-1968.

[198] Chaloner, P. A.; Davies, S. E.; Hitchcock, P. B. *Polyhedron* **1997,** *16,* 765-776.

[199] Boag, N. M.; Green, M.; Grove, D. M.; Howard, J. A. K.; Spencer, J. L.; Stone, F. G. A. *J. Chem. Soc., Dalton Trans.* **1980,** 2170-2181.

[200] Walraff, G. M. Ph.D. thesis, University of Utah, Salt Lake City, UT, US, 1985.

[201] Bernard, G. M.; Wasylishen, R. E. NMR Studies of Ligand Nuclei in Organometallic Compounds—New Information from Solid-State NMR Techniques. In *Physical Organometallic Chemistry*, Vol. 3; Gielen, M.; Willem, R.; Wrackmeyer, B., Eds.; John Wiley & Sons: West Sussex, UK, 2002.

[202] Huang, Y.; Gilson, D. F. R.; Butler, I. S. *J. Chem. Soc., Dalton Trans.* **1992,** 2881-2883.

[203] Gay, I. D.; Young, G. B. *Organometallics* **1996,** *15,* 2264-2269.

[204] Havlin, R.; McMahon, M.; Srinivasan, R.; Le, H.; Oldfield, E. *J. Phys. Chem. A* **1997,** *101,* 8908-8913.

[205] Ding, S.; McDowell, C. A. *Chem. Phys. Lett.* **1997,** *268,* 194-200.

[206] Challoner, R.; Sebald, A. *Solid State Nucl. Magn. Reson.* **1995,** *4,* 39-45.

[207] Bernard, G. M.; Wasylishen, R. E.; Phillips, A. D. *J. Phys. Chem. A* **2000,** *104,* 8131-8141.

[208] Bernard, G. M.; Wu, G.; Wasylishen, R. E. *J. Phys. Chem. A* **1998,** *102,* 3184-3192.

[209] Glanville, J. O.; Stewart, J. M.; Grim, S. O. *J. Organomet. Chem.* **1967,** *7,* P9-P10.

[210] Zilm, K. W.; Grant, D. M. *J. Am. Chem. Soc.* **1981,** *103,* 2913-2922.

[211] Cross, V. R.; Waugh, J. S. *J. Magn. Reson.* **1977,** *25,* 225.

[212] Bernard, G. M.; Wasylishen, R. E. *Solid State Nucl. Magn. Reson.* **2002,** *21,* 86-104.

[213] Wiberg, K. B.; Hammer, J. D.; Zilm, K. W.; Keith, T. A.; Cheeseman, J. R.; Duchamp, J. C. *J. Org. Chem.* **2004,** *69,* 1086-1096.

[214] Farrar, T. C.; Jablonsky, M. J.; Schwartz, J. L. *J. Phys. Chem.* **1994,** *98,* 4780-4786.

[215] Dedieu, A. *Chem. Rev.* **2000,** *100,* 543-600.

[216] Frenking, G.; Fröhlich, N. *Chem. Rev.* **2000,** *100,* 717-774.

[217] Autschbach, J.; Ziegler, T. Relativistic Computation of NMR Shieldings and Spin-Spin Coupling Constants. In *Encyclopedia of Nuclear Magnetic Resonance*, Vol. 9; Grant, D. M.; Harris, R. K., Eds.; John Wiley & Sons: Chichester, UK, 2002.

[218] Cornwell, C. D. *J. Chem. Phys.* **1966,** *44,* 874.

[219] Grutzner, J. B. Chemical Shift Theory: Orbital Symmetry and Charge Effects on Chemical Shifts. In *Recent Advances in Organic NMR Spectroscopy*; Lambert, J. B.; Rittner, R., Eds.; Norell Press: Landisville, US, 1987.

[220] Dahn, H. *J. Chem. Educ.* **2000,** *77,* 905-909.

[221] Schreckenbach, G.; Ziegler, T. *J. Phys. Chem.* **1995,** *99,* 606-611.

[222] Schreckenbach, G. Ph.D. thesis, University of Calgary, Calgary, AB, Canada, 1996.

[223] Schreckenbach, G.; Ziegler, T. *Int. J. Quantum Chem.* **1996,** *60,* 753-766.

[224] Wiberg, K. B.; Hammer, J. D.; Zilm, K. W.; Cheeseman, J. R.; Keith, T. A. *J. Phys. Chem. A* **1998,** *102,* 8766-8773.

[225] Wiberg, K. B.; Hammer, J. D.; Zilm, K. W.; Cheeseman, J. R. *J. Org. Chem.* **1999,** *64,* 6394-6400.

[226] Blake, D. M.; Roundhill, D. M. *Inorg. Synth.* **1978,** *18,* 120-124.

[227] Sheldrick, G. M. *SHELXL-93, A Program for Crystal Structure Determination;* University of Göttingen: Göttingen, DE, 1993.

[228] Bak, M.; Rasmussen, J. T.; Nielsen, N. C. *J. Magn. Reson.* **2000,** *147,* 296-330.

[229] Opella, S. J.; Frey, M. H. *J. Am. Chem. Soc.* **1979,** *101,* 5854-5856.

[230] Zanin, I. E.; Antipin, M. Y.; Struchkov, Y. T. *Sov. Phys. Crystallogr. (Engl. Transl.)* **1991,** *36,* 219-224.

[231] "ADF2004.01", SCM, Theoretical Chemistry, Vrije Universiteit, Amsterdam, The Netherlands, http://www.scm.com.

[232] te Velde, G.; Bickelhaupt, F. M.; Baerends, E. J.; Fonseca Guerra, C.; van Gisbergen, S. J. A.; Snijders, J. G.; Ziegler, T. *J. Comput. Chem.* **2001,** *22,* 931-967.

[233] Fonseca Guerra, C.; Snijders, J. G.; te Velde, G.; Baerends, E. J. *Theor. Chem. Acc.* **1998,** *99,* 391-403.

[234] Wolff, S. K.; Ziegler, T.; van Lenthe, E.; Baerends, E. J. *J. Chem. Phys.* **1999,** *110,* 7689-7698.

[235] Wolff, S. K.; Ziegler, T. *J. Chem. Phys.* **1998,** *109,* 895-905.

[236] Ditchfield, R. *Mol. Phys.* **1974,** *27,* 789-807.

[237] Wolinski, K.; Hinton, J. F.; Pulay, P. *J. Am. Chem. Soc.* **1990,** *112,* 8251-8260.

[238] Vosko, S. H.; Wilk, L.; Nusair, M. *Can. J. Phys.* **1980,** *58,* 1200-1211.

[239] Becke, A. D. *Phys. Rev. A* **1988,** *38,* 3098-3100.

[240] Perdew, J. P. *Phys. Rev. B* **1986,** *33,* 8822-8824.

[241] Perdew, J. P. *Phys. Rev. B* **1986,** *34,* 7406.

[242] Duncan, J. L. *Mol. Phys.* **1974,** *28,* 1177-1191.

[243] Harada, J.; Ogawa, K. *J. Am. Chem. Soc.* **2004,** *126,* 3539-3544.

[244] van Lenthe, E.; Baerends, E. J.; Snijders, J. G. *J. Chem. Phys.* **1993,** *99,* 4597-4610.

[245] van Lenthe, E.; Baerends, E. J.; Snijders, J. G. *J. Chem. Phys.* **1994,** *101,* 9783-9792.

[246] Kalinowski, H.-O.; Berger, S.; Braun, S. *Carbon-13 NMR Spectroscopy;* John Wiley & Sons: Chichester, UK, 1988.

[247] Moss, W. N.; Goroff, N. S. *J. Org. Chem.* **2005,** *70,* 802-808.

[248] Rubin, M.; Trofimov, A.; Gevorgyan, V. *J. Am. Chem. Soc.* **2005,** *127,* 10243-10249.

[249] Davies, B. W.; Payne, N. C. *J. Organomet. Chem.* **1975,** *99,* 315-328.

[250] Farrugia, L. J. *J. Appl. Crystallogr.* **1997,** *30,* 565.

[251] Günther, H. *Angew. Chem., Int. Ed. Engl.* **1972,** *11,* 861-948.

[252] Günther, H. *NMR Spectroscopy: Basic Principles, Concepts, and Applications in Chemistry;* John Wiley & Sons: Chichester, UK, 2nd ed.; 1995.

[253] Wrackmeyer, B. *Z. Naturforsch., B: Chem. Sci.* **1997,** *52,* 1019-1021.

[254] Lynden-Bell, R. M.; Sheppard, N. *Proc. R. Soc. London, Ser. A* **1962,** *269,* 385-403.

[255] McFarlane, W. *J. Chem. Soc. A* **1967,** 1922-1923.

[256] Anderson, D. W.; Ebsworth, E. A. V.; Rankin, D. W. H. *J. Chem. Soc., Dalton Trans.* **1973,** 2370-2373.

[257] VanderHart, D. L.; Gutowsky, H. S. *J. Chem. Phys.* **1968,** *49,* 261-271.

[258] Dewar, J. S. *Bull. Soc. Chim. Fr.* **1951,** *18,* C71.

[259] Chatt, J.; Duncanson, L. A. *J. Chem. Soc.* **1953,** 2939-2947.

[260] Nelson, J. H.; Wheelock, K. S.; Cusachs, L. C.; Jonassen, H. B. *J. Am. Chem. Soc.* **1969,** *91,* 7005.

[261] Nelson, J. H.; Jonassen, H. B. *Coord. Chem. Rev.* **1971,** *6,* 27.

[262] Seebach, D. *Angew. Chem., Int. Ed. Engl.* **1979,** *18,* 239-258.

[263] Zilm, K. W.; Conlin, R. T.; Grant, D. M.; Michl, J. *J. Am. Chem. Soc.* **1980,** *102,* 6672-6676.

[264] Hansen, P. E.; Poulsen, O. K.; Berg, A. *Org. Magn. Reson.* **1979,** *12,* 43-49.

[265] Müller, H. S. P.; Gerry, M. C. L. *J. Chem. Phys.* **1995,** *103,* 577-583.

[266] Frydman, L. *Annu. Rev. Phys. Chem.* **2001,** *52,* 463-498.

[267] Tjandra, N.; Bax, A. *Science* **1997,** *278,* 1111-1114.

[268] Tolman, J. R.; Flanagan, J. M.; Kennedy, M. A.; Prestegard, J. H. *Proc. Natl. Acad. Sci. US* **1995,** *92,* 9279-9283.

[269] Prestegard, J. H.; Al-Hashimi, H. M.; Tolman, J. R. *Quart. Rev. Biophys.* **2000,** *33,* 371-424.

[270] Simon, B.; Sattler, M. *Angew. Chem., Int. Ed.* **2002,** *41,* 437-440.

[271] de Alba, E.; Tjandra, N. *Prog. Nucl. Magn. Reson. Spectrosc.* **2002,** *40,* 175-197.

[272] Bryce, D. L.; Grishaev, A.; Bax, A. *J. Am. Chem. Soc.* **2005,** *127,* 7387-7396.

[273] Haeberlen, U. High Resolution NMR in Solids: Selective Averaging. In *Advances in Magnetic Resonance, Supplement 1*; Waugh, J. S., Ed.; Academic Press: New York, US, 1976.

[274] Vaara, J.; Jokisaari, J.; Wasylishen, R. E.; Bryce, D. L. *Prog. Nucl. Magn. Reson. Spectrosc.* **2002,** *41,* 233-304.

[275] Bryce, D. L.; Wasylishen, R. E. *Acc. Chem. Res.* **2003,** *36,* 327-334.

[276] Autschbach, J.; Ziegler, T. *J. Chem. Phys.* **2000,** *113,* 936-947.

[277] Autschbach, J.; Ziegler, T. *J. Chem. Phys.* **2000,** *113,* 9410-9418.

[278] Dickson, R. M.; Ziegler, T. *J. Phys. Chem.* **1996,** *100,* 5286-5290.

[279] Khandogin, J.; Ziegler, T. *Spectrochim. Acta.* **1999,** *55A,* 607-624.

[280] Bryce, D. L.; Wasylishen, R. E. *Inorg. Chem.* **2002,** *41,* 3091-3101.

[281] Bryce, D. L.; Wasylishen, R. E. *J. Am. Chem. Soc.* **2000,** *122,* 3197-3205.

[282] Bryce, D. L.; Wasylishen, R. E.; Autschbach, J.; Ziegler, T. *J. Am. Chem. Soc.* **2002,** *124,* 4894-4900.

[283] Autschbach, J.; Le Guennic, B. *J. Chem. Ed.* **2007,** *84,* 156.

[284] Autschbach, J. *Coord. Chem. Rev.* **2007,** *251,* 1796.

[285] Autschbach, J. The Calculation of NMR Parameters in Transition Metal Complexes. In *Structure and Bonding: Principles and Applications of Density Functional Theory in Inorganic Chemistry I,* Vol. 112; Kaltsoyanis, N.; McGrady, J. E., Eds.; Springer-Verlag: Berlin, DE, 2004.

[286] Helgaker, T.; Jaszuński, M.; Pecul, M. *Prog. Nucl. Magn. Reson. Spectrosc.* **2008,** *53,* 249-268.

[287] Krivdin, L. B.; Contreras, R. H. *Annu. Rep. Nucl. Magn. Reson. Spectrosc.* **2007,** *61,* 133-245.

[288] Helgaker, T.; Jaszuński, M.; Ruud, K. *Chem. Rev.* **1999,** *99,* 293-352.

[289] Schneider, R. F. *J. Chem. Phys.* **1968,** *48,* 4905-4909.

[290] Ding, S. W.; Ye, C. H. *Chem. Phys. Lett.* **1990,** *170,* 277-282.

[291] Anet, F. A. L.; O'Leary, D. J.; Wade, C. G.; Johnson, R. D. *Chem. Phys. Lett.* **1990,** *171,* 401-405.

[292] Chenon, M. T.; Coupry, C.; Werbelow, L. G. *J. Phys. Chem.* **1992,** *96,* 561-566.

[293] Wi, S.; Frydman, L. *J. Chem. Phys.* **2002,** *116,* 1551-1561.

[294] Blicharski, J. S. *Z. Naturforsch.* **1972,** *27A,* 1355.

[295] Corio, P. L. *Structure of High-Resolution NMR Spectra;* Academic Press: New York, US, 1966.

[296] Nye, J. F. *Physical Properties of Crystals: Their Representation by Tensors and Matrices;* Oxford University Press: Oxford, UK, 1985.

[297] Hahn, E. L.; Maxwell, D. E. *Phys. Rev.* **1952,** *88,* 1070.

[298] Anderson, W. A. *Phys. Rev.* **1956,** *102,* 151.

[299] Abragam, A. Principles of Nuclear Magnetism. In *International Series of Monographs in Physics*; Adair, R. K.; Elliott, R. J.; Marshall, W. C.; Wilkinson, D. H., Eds.; Clarendon Press: Oxford, UK, 1961.

[300] Abragam, A.; Goldman, M. Nuclear Magnetism: Order and Disorder. In *International Series of Monographs on Physics*; Krumhansl, J. A.; Marshall, W.; Wilkinson, D. H., Eds.; Clarendon Press: Oxford, UK, 1982.

[301] Bryce, D. L.; Wasylishen, R. E. *J. Am. Chem. Soc.* **2000,** *122,* 11236-11237.

[302] Wasylishen, R. E. . In *Annual Reports on NMR Spectroscopy*; Webb, G. A., Ed.; Academic Press: London, UK, 1977.

[303] Ambrosius, F.; Klaus, E.; Schaller, T.; Sebald, A. *Z. Naturforsch.* **1995,** *50A,* 423-428.

[304] van Bramer, S. E.; Glatfelter, A.; Bai, S.; Dybowski, C.; Neue, G. *Concepts Magn. Reson.* **2002,** *14,* 365-387.

[305] Schneider, C.; Dräger, M. *J. Organomet. Chem.* **1991,** *415,* 349-362.

[306] Jameson, C. J. The Dynamic and Electronic Factors in Isotope Effects on NMR Parameters. In *Isotopes in the Physical and Biomedical Sciences,* Vol. 2; Buncel, E.; Jones, J. R., Eds.; Elsevier: Amsterdam, NL, 1991.

[307] Wu, G.; Wasylishen, R. E. *Inorg. Chem.* **1992,** *31,* 145-148.

[308] Wu, G.; Wasylishen, R. E. *Organometallics* **1992,** *11,* 3242-3248.

[309] Lee, Y. K.; Kurur, N. D.; Helmle, M.; Johannessen, O. G.; Nielsen, N. C.; Levitt, M. H. *Chem. Phys. Lett.* **1995,** *242,* 304-309.

[310] Hohwy, M.; Jakobsen, H. J.; Edén, M.; Levitt, M. H.; Nielsen, N. C. *J. Chem. Phys.* **1998,** *108,* 2686-2694.

[311] Buckingham, A. D.; Love, I. *J. Magn. Reson.* **1970,** *2,* 338.

[312] Krause, E. *Ber.* **1918,** *51,* 912-914.

[313] Krause, E.; Becker, R. *Ber.* **1920,** *53B,* 173-190.

[314] Lippmaa, E. T.; Alla, M. A.; Pehk, T. J. *J. Am. Chem. Soc.* **1978,** *100,* 1929-1931.

[315] Harris, R. K.; Sebald, A. *Magn. Reson. Chem.* **1987,** *25,* 1058-1062.

[316] Graf, R.; Demco, D. E.; Hafner, S.; Spiess, H. W. *Solid State Nucl. Magn. Reson.* **1998,** *12,* 139-152.

[317] Zaremba, Z. K. *Ann. Mat. Pura. Appl.* **1966,** *73,* 293.

[318] Conroy, H. *J. Chem. Phys.* **1967,** *47,* 5307.

[319] Cheng, V. B.; Suzukawa, Jr., H. H.; Wolfsberg, M. *J. Chem. Phys.* **1973,** *59,* 3992.

[320] Schmidbaur, H.; Wohlleben, A.; Wagner, F.; Orama, O.; Huttner, G. *Chem. Ber.* **1977,** *110,* 1748.

[321] Healy, P. C. *Acta Crystallogr., Sect. E: Struct. Rep. Online* **2003,** *59,* m1112-m1114.

[322] Malleier, R.; Kopacka, H.; Schuh, W.; Wurst, K.; Peringer, P. *Chem. Commun.* **2001,** 51-52.

[323] Reger, D. L.; Mason, S. S.; Rheingold, A. L. *J. Am. Chem. Soc.* **1993,** *115,* 10406-10407.